Università degli Studi di Catania | *Ministero dell'Istruzione* | *Fondo Sociale Europeo*

On seismic design and advanced numerical modelling of flexible cantilever walls under earthquake loading including cyclic mobility

By

Giovanni Li Destri Nicosia

Dottorato di Ricerca in Ingegneria Geotecnica Ciclo XXII

Coordinator: Prof. Michele Maugeri

Supervisor: Prof. Michele Maugeri

Dicembre , 2010

ABSTRACT

Pseudostatic design methods for seismic design of retaining structures are very widely spread in aseismic design codes worldwide. These methods are based on a crude simplification of reality, nevertheless observational evidence of earth retaining structures designed using simplified methods based on limit equilibrium show their good overall performance except for some situations where saturated granular backfill is present. The aim of this work is first to critically describe the main tools available today for the analysis and seismic design of flexible retaining structures. Secondly to apply different methodology to a practical benchmark study case describing all issues related to the correct application of simplified methodologies and issues regarding the sophisticated numerical approaches. Finally results obtained by the simplified and the sophisticated approaches are evaluated and compared Differences, advantages and disadvantages between the simplified and the more sophisticated approaches are illustrated along with those between the numerical analysis themselves.
Analyses are performed for the case of dry and saturated backfill for both simplified and numerical approach and the effectiveness of the simplified method comparing to numerical analyses is assessed in both cases.
A good agreement between Finite Elements (DYNAFLOW) and Finite Difference (FLAC) approach was reached for the case of dry backfill and a special numerical application of the pseudodynamic approach is also presented. For its relatively simple implementation and the fairly good agreement with more sophisticated analysis shown for the benchmark case configuration considered, such procedure appears to be an effective tool and good alternative to classical pseudostatic approach for the seismic design/assesments of retaining structures in earthquake prone regions. Time history analyses on the other hand are time consuming require a more experienced user and the additional task to selected a representative set of spectrum compatible accelegrams.
The case study of saturated backfill included in the present work presents a simplified methodology to assess liquefaction potential and the comparison with more sophisticated analyses (OPENSEES and FLAC) allows some considerations on the limits and strength of such methodology.

Keywords: flexible retaining structures; pseudostatic methods, FEM, FDM, cyclic mobility;

ACKNOWLEDGEMENTS

I would like to thank all those who gave me support for carrying out this Thesis including Professor Maugeri from the University of Catania, Eric Parker from D'Appolonia SpA, Professor A. Elgamal from UCSD for his support on Opensees PDMY model, Prof A Pecker and Prof J H Prevost for their support on Dynaflow, Dr Carlo Lai from Eucentre and Dr John Perry from Mott MacDonald LtD.

TABLE OF CONTENTS

LIST OF FIGURES

Page

LIST OF TABLES

Page

1 INTRODUCTION.

Earthquake resistant design of earth retaining structures like retaining walls is an important issue to reduce the devastating effect of earthquake hazard. The seismic behaviour of retaining structures under seismic conditions is a complex soil structure interaction phenomenon even if the case of gravitational loading alone is considered. The case of earthquake loading is even more complex to address.

Despite such complexity, due to the widespread presence of retaining type of structures many studies and investigations are among the first in geotechnical engineering and as a result there are several categories of design/analysis methodologies available for both static and seismic design of flexible retaining structures which are briefly described in the following. A correct and efficient use of each methodology requires an understanding of the underlying hypothesys.

For engineering design reference codes such as European EC8, the new Italian seismic code (Allegato 4, OPCM No. 3274 e 3316) or Italian Building Code (D.M. 14/01/2008) for routine day to day design of retaining walls, advocate the use of simplified design methodologies based on limit equilibrium and pseudostatic methods. The application of these simplified methodologies requires an understanding of the possible failure mechanisms and the most convenient yet safe approach to evaluate the limit loads.

An alternative approach for seismic design/assessment of retaining structures is that based on numerical methods and a variety of methodologies are available. In this respect it is important to illustrate which are advantages and limitations of each type of method. Even if an in depth descriptions of numerical analysis is not the purpose of this work, to illustrate advantegs and limitations of different methodologies, it is of interest to have a picture of the main framework in which Finite Elements and Finite Difference methods can be placed. Three numerical codes are used in this work two based on Finite Elements Method (DYNAFLOW and Opensees) and one based of Finite Differences Method (FLAC). The theory beyond these numerical tools is very vast and their correct engineering application requires a clear idea on the main limits beyond the modelling and the solution process. For this reason a wide range of topics such as non linear cyclic soil behaviour or plane wave propagation theory, non linear iterative solution strategies and probabilistic hazard assessment for seismi input selection must be correctly understood.

Following an empirical approach, the methodology of this work is based on the choice of a design benchmark reference problem, on the application of pseudostatic and more refined numerical tools and finally on the analysis of the results obtained using different methodologies. The conclusions of this application are intended to give some guidance for choosing the most convenient method for assessment and design of flexible retaining structures under earthquake loading and for understanding the reasons of the limitations of the results obtained. Since performance of flexible retaining structure under earthquake loading has been poor [Gazetas et al, 2004] for the case of saturated backfill, both cases of saturated and unsaturated backfill are considered.

The work is structured in the following way: in the next Chapter a review of case histories of documented failures of earth retaining structures is outlined, in Chapter 3 a review of available methods for earth retaining structures seismic analysis/design is presented, Chapter 4 contains a description of a wide range of general modelling issues for geotechnical earthquake engineering, in Chapter 5 the model analysed is described and the pseudostatic code based design approach applied. In Chapter 6 the methodology for the selection of the accelerograms and the input accelerograms is introduced. In Chapter 7 and Chapter 8 a description of the numerical models used for the analyses is done and the results of the numerical analysis are presented respectively for the dry and saturated cases. Chapter 9 contains the conclusions.

2 CASE HISTORIES AND MOTIVATION.

Field observation and reporting of damage caused by earthquake allows engineers to learn about limitations of design practice and to identify most critical failure mechanisms and the causes behind them. Several examples of failures of retaining structures under earthquake loading from literature are described in the following sections.

2.1 Damage to earth structures by the Niigata Earthquake 1964.

On June 16, 1964 a great earthquake occurred at Niigata Prefecture, Japan. Soil formation in this area consists chiefly of recent alluvial deposit and recently deposited artificial fill which are composed of relatively uniform, loose and saturated sand. The vibration due to earthquake induced the liquefaction of saturated loose sand and caused much damage to earth structure and foundation.
Structures in harbours and revetments of river banks were also moved, sttled or overturned by the earthquake, since the grounds were liquefied. Almost all structures in Niigata Harbour suffered severely and those of Sakata Harbour were also damaged. Figure 2.1 [Kawakami and Asada, 1966] shows the appearance of damaged Yamashita Wharf in Niigata Harbour, namely the quaywall of steel sheet piles was pushes out 36 cm, the ground behind the concrete anchor plate was subsided and the bed of the sea was heaved up by about 100 cm. This damage was caused by the increase of earth pressure acted on back of sheet piles and the decrease of the resistance of anchor plate of tie rod against sliding, due to liquefaction of sandy backfill.

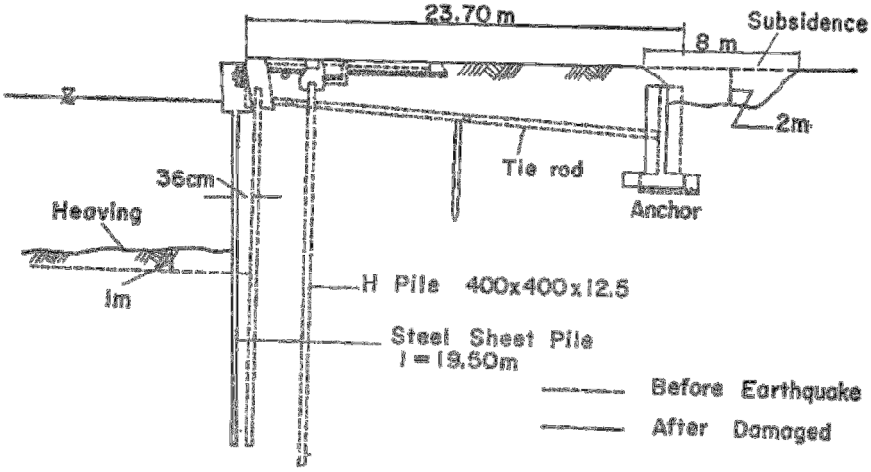

Figure 2.1 Cross section of Konakano No. 1 Quaywall in Port of Hachinoe [Kawakami and Asada, 1966]

2.2 Sheet pile walls damage from the Tokachioki Earthquake 1968.

Port and harbour facilities in the southern part of Hokkaido and the northern part of Honshu were damaged by the 1968 Tokachioki earthquake on May 16, 1968 with total sum of damage estimated approximately 5 million U.S. Dollars.
Hayashi and Katayama [Hayashi and Katayama, 1970] include description of damages to several types of port and harbour facilities including caisson breakwaters, gravity types of quay wall and sheetpile bulkhead quay walls with and without batter anchor piles. There were few large-sized mooring facilities which suffered heavy damage and comparatively heavy damage was encountered in lighter's wharves and sea walls.
Generally speaking, damage to mooring systems and sea walls were similar to those encountered in other previous earthquakes, i.e. swelling of front lines, settlements and cracking of aprons.

- Damage to sheetpile bulkhead:

Typical features of the damage to sheetpile bulkhead were a forward tilting of the wall due to insufficient anchor resistance , development of tension cracks above the anchor in parallel direction to the front line and settlement of backfill surface. In some cases, local breakage of fixation of tie rod to anchor was observed. As an example of heavily damaged sheetpile bulkhead Figure 2.2 shows the largest deformation of Konakano sheetpile bulkhead quay wall. The seaward movement of the front line was about 1 m, a concrete coping of sheetpile was broken with a relative settlement of the apron to the coping was 65 cm.
Cross section of such quaywall, before and after the earthquake are shown in Figure 2.3.

Calculated factor of safety for twenty cases of sheetpile shows that for eight of those cases in which factor of safety was less than one for insufficient embedment depth, there was no damage due to bending of sheetpiles or breaking of tie rods showing that current design method for embedment was conservative, but in the bulkheads of such sheetpiles a swelling of front lines ranging from 10 to 30 cm was observed due to the movements of anchor plates.

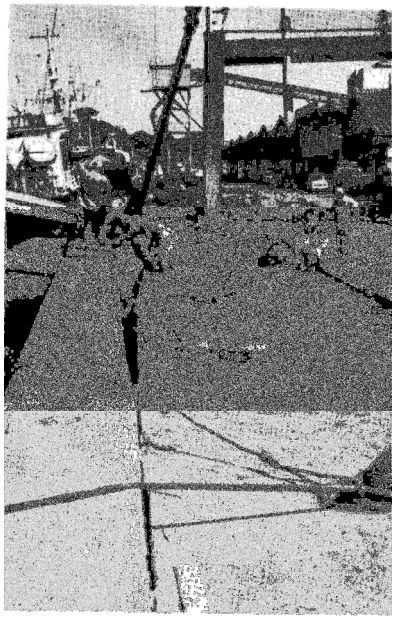

Figure 2.2 Damage to Konakano No. 1 sheetpile quaywall in Port of Hachinoe [Hayashi and Katayama, 1970]

Records from Niigata earthquake indicate that even for case with safety factor of safety higher than one have sometime shown insufficient anchor resistance and in addition anchoring, is installed in a position most susceptible of soil liquefaction.

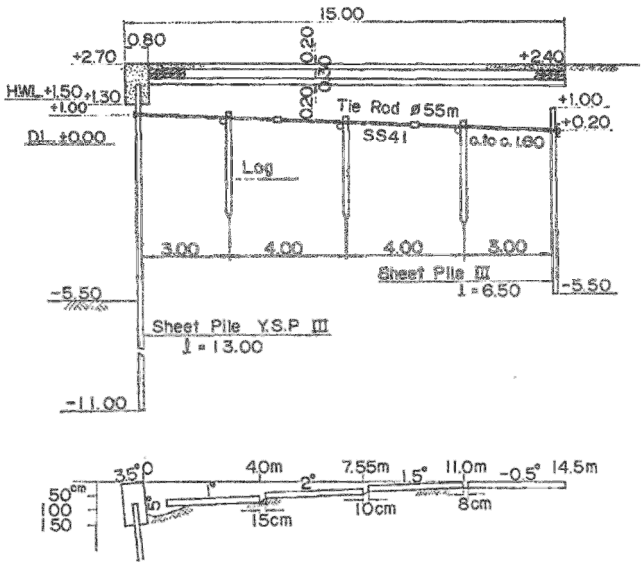

Figure 2.3 Cross section of Konakano No. 1 Quaywall in Port of Hachinoe [Hayashi and Katayama, 1970]

- Damage to sheetpile bulkhead with batter anchor piles:

This type of facilities were more recently introduced hence it had not been subjected to any strong earthquake before. Two facilities of this type were subjected to the earthquake. There was no damage in one case. In the other case of the -5.5m quaywall of Kitahama Pier in Port of Hakodate, however, the fixation point of the sheetpile anchor piles was broken. Cross sections, before and after the earthquake, of the latter structure are shown in Figure 2.4.

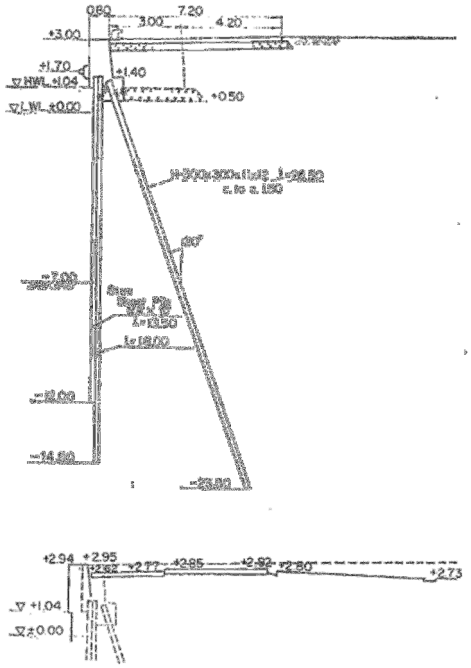

Figure 2.4 Cross section of Konakano No. 1 Quaywall in Port of Hachinoe [Hayashi and Katayama, 1970]

2.3 Sheet pile walls damage from the Nihonkai Chubu Earthquake 1983.

The epicenter of the 1983 Nihonkai Chubu Earthquake was located in the Japan Sea, called 'Nihonkai' in Japanese. With the shallow focal depth of 14km, the earthquake caused tsunami killing 100 people.

Iai and Kameoka [Iai and Kameoka, 1993] report a case history regarding the failure of a sheetpile quay wall placed in Ohama No. 2 Wharf in Akita port, along the Omono river. Most of the quay walls along such river were constructed with a backfilling method and suffered damage due to the liquefaction of the backfill.

At the time of the earthquake, the quay wall at Ohama No. 2 Wharf had such a cross section as shown in Figure 2.5. As indicated in this figure, the quay wall was constructed with a backfilling method. The earthquake at the quay wall and induced such deformations as shown in the same figure with the broken lines.

An eyewitness, a truck driver who had narrowly escaped from Ohama No. 2 Wharf shown in Figure 2.6, identified that the quay wall gradually deformed during the earthquake.

The deformations ions in the sheet pile and the anchor, plotted along the face line of the quay wall are shown in Figure 2.7. In this figure, the typical deformed cross sections are shown in Figure 2.7 (a) with alphabets indicating the locations shown at the top row in Figure 2.7 (b); the sections A and B and the approaches at the both ends. The cross section shown earlier in Figure 2.5 is of the section A but those of the section B and the approaches are slightly different from this. The horizontal displacements at the top of the sheet pile wall, shown in the top row in Figure 2.7 (b), are obviously constrained by the structures at the approaches at both ends of the of the Ohama No. 2 Wharf. The dent shown on the second row in Figure 2.7 (b) at the left end of section B was due to the effect of the truck shown in Figure 2.6.
The horizontal displacement at the top of the sheet pile in section A range from about 1.1 to 1.8 m. The settlements at the middle part of the apron, which are indicated by the broken lines in Figure 2.5, are about 1.4m, being almost the same as the horizontal displacements of the sheet pile wall. The displacement at the top of the sheet pile wall are evidently associated with those of the anchor piles as shown in the third row in Figure 2.7; the anchors were pulled by the sheet piles toward the sea, accordingly inclined, as shown in the fourth row in Figure 2.7(b), presumably due to the reduced resistance in the liquefied backfill sand.

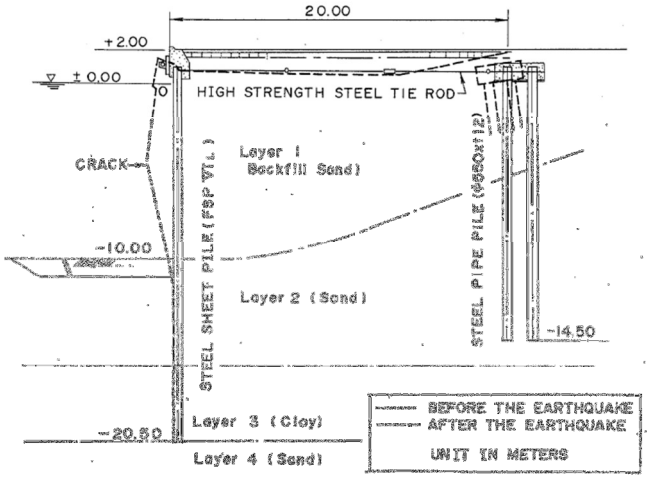

Figure 2.5 Cross section of a quay wall at Ohama No.2 Wharf [Iai and Kameoka, 1993]

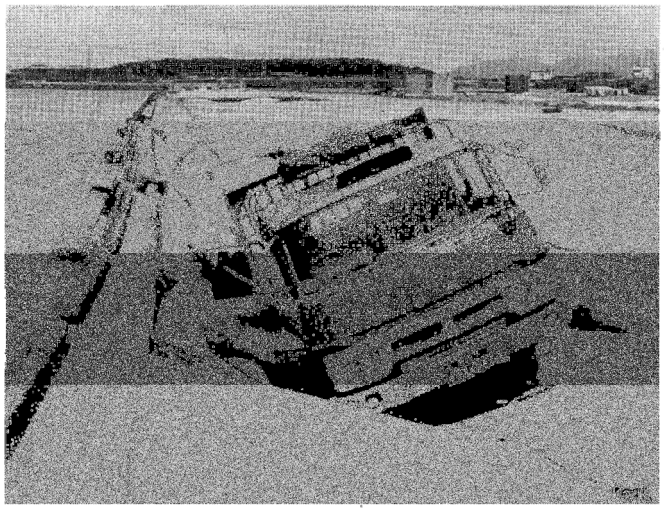

Figure 2.6 Damage at Ohama No. 2 Wharf [Iai and Kameoka, 1993]

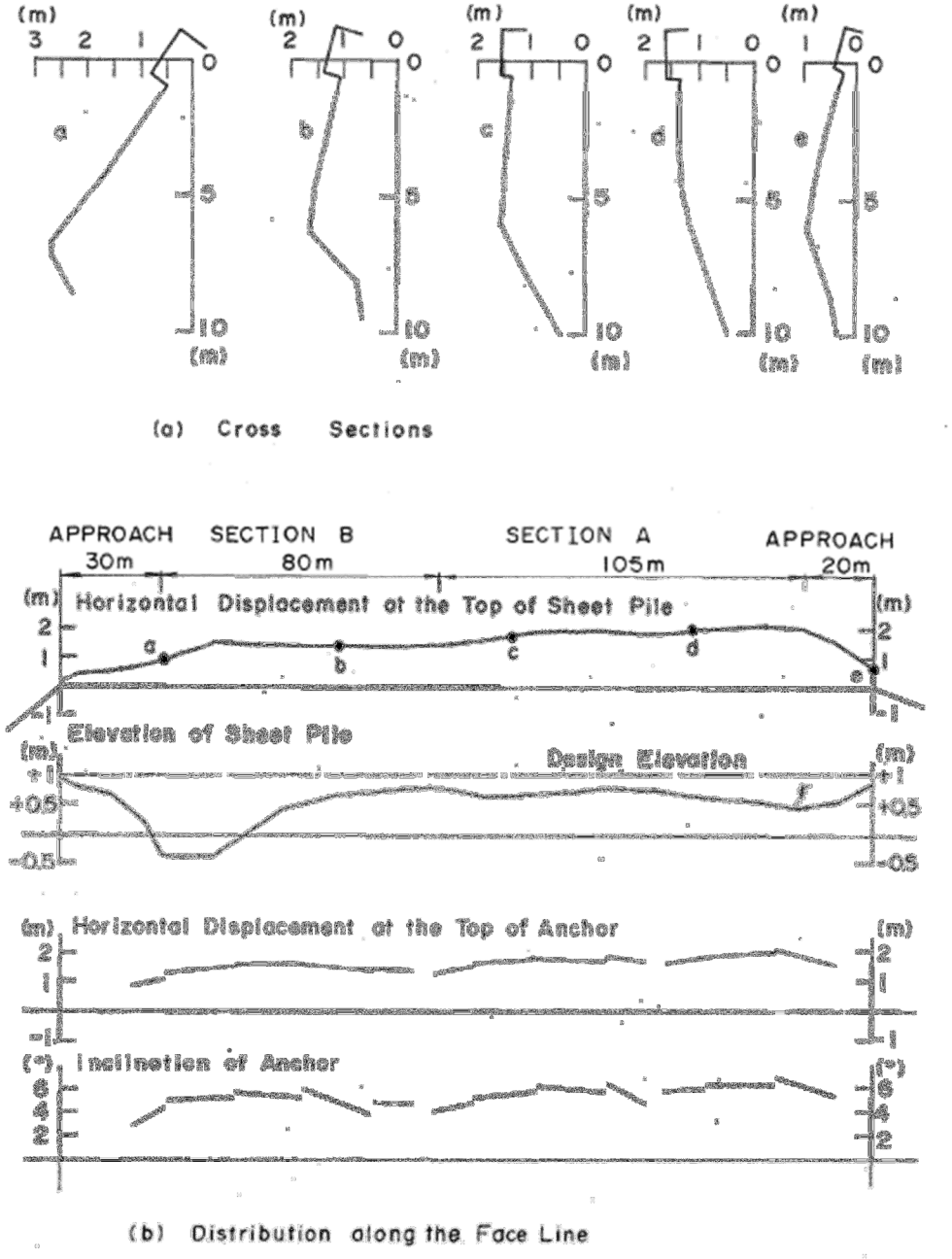

Figure 2.7 Deformation along the face line at Ohama No. 2 Wharf (a) Cross section, (b) Distribution along the face line [Iai and Kameoka, 1993]

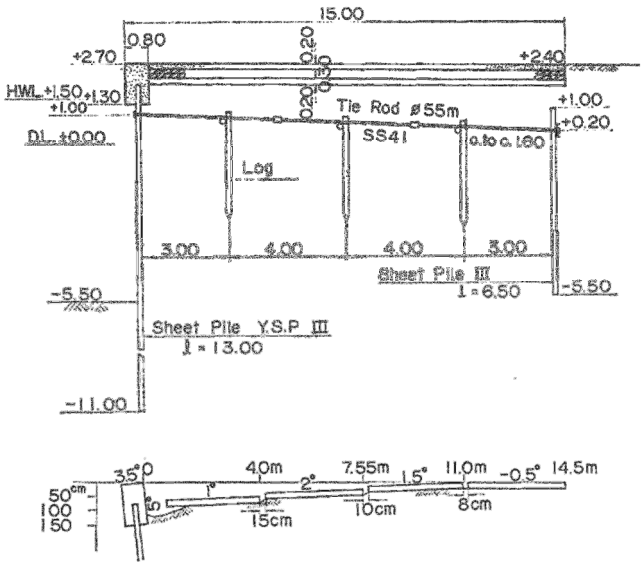

Figure 2.8 Cross section of Konakano No. 1 Quaywall in Port of Hachinoe [Hayashi and Katayama, 1970]

2.4 Damage to earth structures caused by the 1995 Hanshin-Awaji Earthquake

The January 17, 1995m Hansin-Awaji earthquake, registered at a magnitude of 7.2 (JMA) delivered a totally unexpected and devastating shock to the densely populated Kobe-Osaka corridor squeezed between the Osaka Bayand the Rokko mountain. Human casualty turned out to be extremely high in the Hansin-Hawaji earthquake disaster. In fact, a toll of approximately 5.500 deaths reported in this disaster is not acceptable by any stand.
Kimura [Kimura, 1996] estimate total damage to quays walls in Kobe harbour to be of great size as all of the 186 walls were damaged.
The NCEER (National Centre for Earthquake Engineering Research) report by Ballantyne [Ballantyne et al. , 1995] concentrates on performance of electric facilities, gas delivery systems, hospitals, telecommunication facilities and transportation systems subjected to this earthquakes. The Motoyama Water purification plant had damage to two segments of pipelines, the retaining wall alongside the Simiyoshi River moved, breaking the intake box overflow line Figure 2.9.

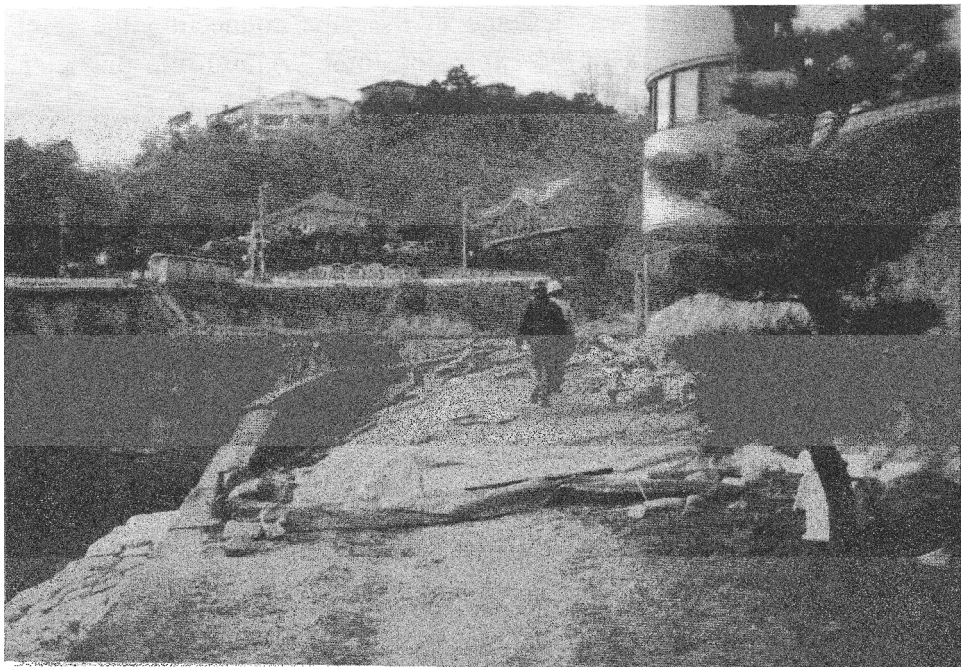

Figure 2.9 Cracked retaining wall (left) at Motoyama water purification plant intake box

The Higashinada Wastewater Treatment Plant is the City of Kobe's largest plant, providing one third of the city's treatment capacity. A location map is shown in Figure 2.10. The facility was heavily damaged when the seawall along the south side of the plant adjacent to the channel moved as much as 3m towards the water as a result of liquefaction. As a result of the movement, the entire site settled an average of one meter. The seawall on the north moved up to 1m south. Liquefaction induced lateral spread and settlement were most sever within a distance of 100m south of the seawall along the southern margin of the channel. Horizontal displacements of 3m and settlements as large as 2 m were observed within the plant site.

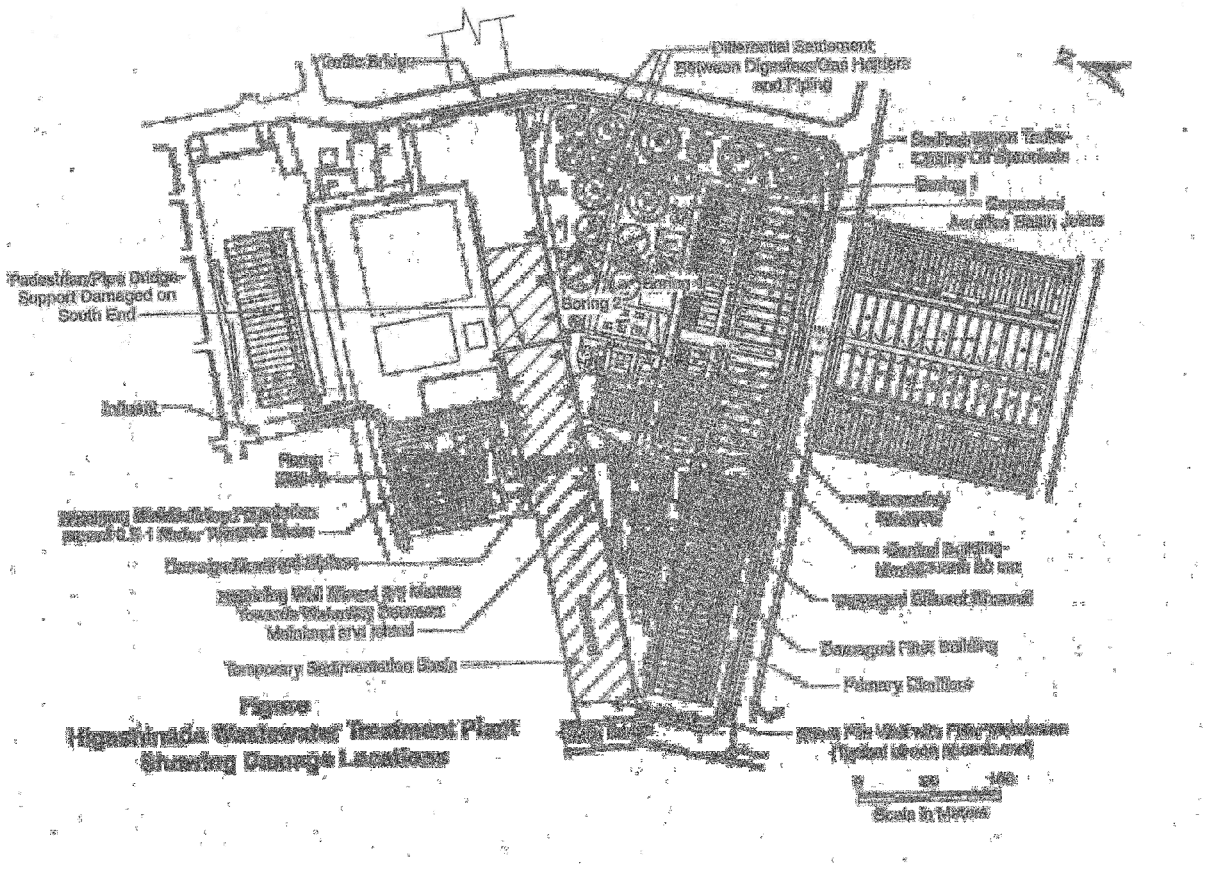

Figure 2.10 Higashinada Wastewater Plant Site Plan

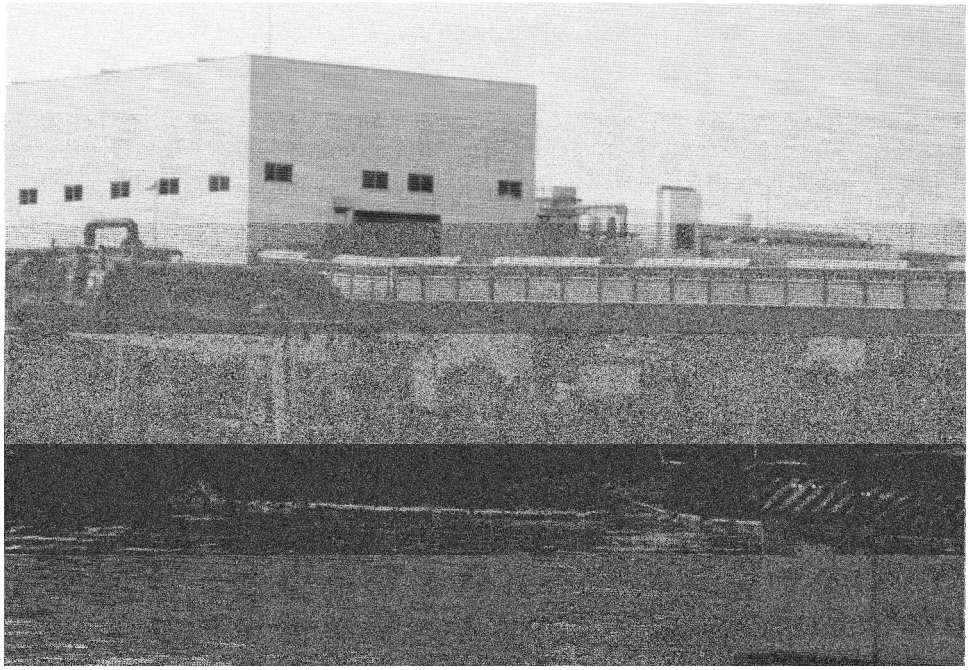

Figure 2.11 Retaining wall along the Inlet between the Island and the mainland moved toward the water (north) 2 to 3 m

2.5 Retaining wall damage from the Kocaeli (Izmit) Earthquake 1999, Turkey.

In 1999, Turkey was struck by a destructive earthquake the occurred on the western extension of the 1500 km long North Anatolian Fault (NAF). The earthquake hit the most densely populated urban environments, namely Kocaeli and Sakarya provinces, situated on an alluvial fan at the western part of the NAF with magnitude (M_w) 7.4. It also provided some of the most extensive strong ground motion data set ever recorded in Turkey within about 130 Km of the surface fault rupture.
Surface faulting propagated eastward , starting form the Marmara region, while damaging the transportation infrastructure such as viaduct, bridges, bridge approaches and roadways such as the Trans European Motorways (TEM). At several locations westward of the town of Arifiye, the surface fault intersected the TEM and the bridge overpass in Arifiye, located less than 50km eastward of the epicentre collapsed due to tectonic movement along the fault zone.
Beyond the serious collapse of the bridge deck [Pamuk, 2004], the northern bridge approach fill (or ramp) that was reinforced with a pair of mechanically stabilized earth walls (MSEW) was also damaged due to excessive tectonic movement along the fault zone during the main shock of the earthquake. Major damage to the walls was not from seismic design but a combination of adverse effects by the nearby fault movement and, possibly, bearing capacity problems associated with underlying foundation soil.
Around 12 people died for a bus passing below the bridge crashed into one the collapsed decks, preliminary repairs cost was around 40 millions dollars and 4% of it was for the demolition and reconstruction of the severely damaged Arifiye Overpass and its reinforced earth abutment system. The closest recording station to the Arifiye Bridge was Sakarya station (SKR), located between downtown Adapazar and Arifiye, for about 4 km northward from the bridge site. The largest peak horizontal ground acceleration of about 0.4g (EW direction) and peak vertical ground acceleration of 0.26g were recorded at this station during the main shock of the Kocaeli earthquake. A clear evidence of impulsive motion (fling) can be observed from the velocity and displacement curves of Figure 2.12

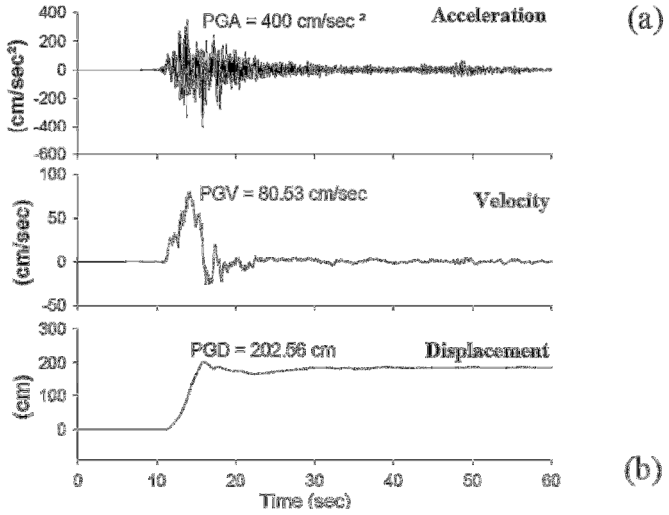

Figure 2.12 Accelerograms recordings at Adapazari station (SKR) and calculated velocity and displacement time histories.

Unseating of the bridge decks and the damage of the walls of the reinforced approach fill (Figure 2.13, Figure 2.14) were the result of the static displacements due to fault traversing the bridge and its associated strong near-field effects. The presence of the drainage culvert also influences the behaviour of the approach fill. In fact because the vertical displacement at E2 was larger than W2, the approach ramp tilted eastward in the cross section as if the presence of the rigid culvert prevented interaction between the ramp and its foundation, therefore, the walls could not accommodate the underlying ground deformations that was induced by the fault rupture. Beside the panel cracks and separation at these locations, generally speaking the overall performance of the reinforced wall was satisfactory.

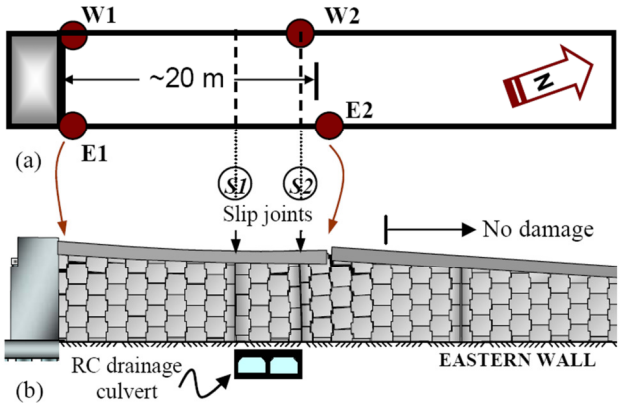

Figure 2.13 MSE bridge approach (a) plan view of approach fill with damage concentration; (b) schematic of eastern wall after the earthquake.

(a)

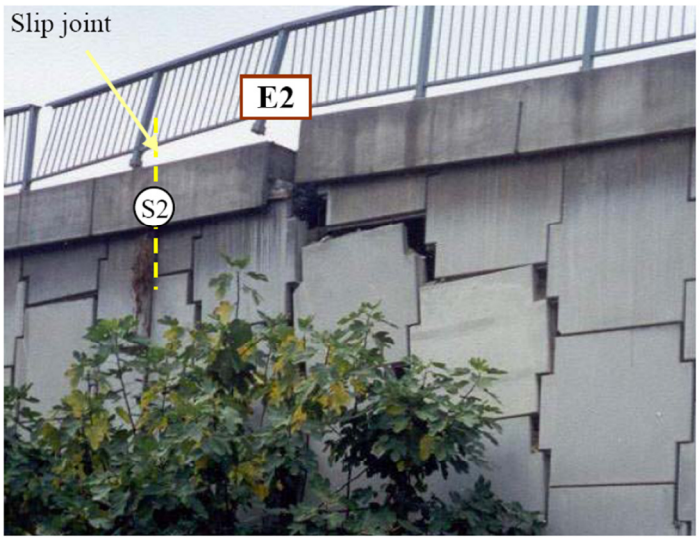

(b)

Figure 2.14 Damage detail for (a) E1 and (b) E2 on eastern MSEW face (phots after Ozbakir)

2.6 Damage to earth structures caused by the 2004 Niigata-Ken Chuetsu Earthquake

Koseki [Koseki et al, 2005] reports cases in which Embankments and retaining walls for railways, roads and building estates suffered serious damage as a consequence of the 2004 October 23, Niigata-ken Chuetsu earthquake. Such damage was observed at sites where concentration of ground water flow in the subsoil layer may have taken place and/or the fill material may have been partly saturated. River dikes suffered less damage due possibly to less liquefiable conditions of subsoil layers below river dikes in severely-shaken regions. Figure 2.15 shows failure of a gravity type retaining wall along National Highway Route 17 at Kamikatagai, Ojiya city. This wall had been constructed in parallel with a railway embankment, which also suffered from sliding failure Its reconstruction (Figure 2.16) after the earthquake was executed by using the reinforced soil retaining wall with a full height rigid facing.

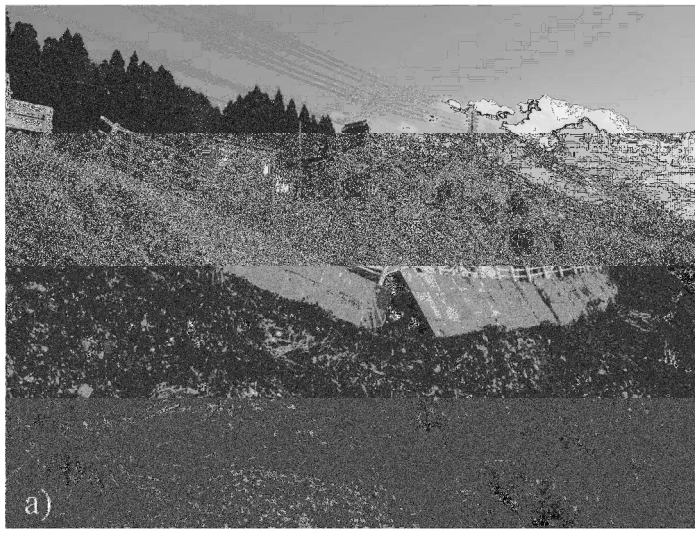

Figure 2.15 Damage of retaining wall along National Highway Route 17

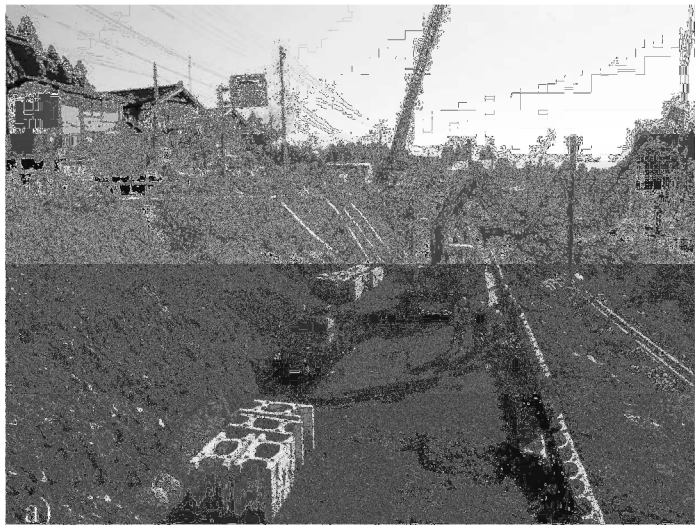

Figure 2.16 Reconstruction of damaged retaining wall along National Highway Route 17

2.7 Conclusions

The performance of retaining walls during earthquakes has been found to depend profoundly on the existence of water and the presence of loose cohesionless soils in the supported soil and foundations. Earthquake reality have shown that harbour quay walls made up of either caissons gravity walls or, especially, of passively anchored sheet-pile walls, are quite vulnerable to strong seismic shaking, mainly as a result of strength degradation of saturated cohesionless soils in the backfill and the foundation. This vulnerability was amply demonstrated in the 1995 Kobe earthquake as well as many previous and subsequent earthquakes.

Such behavior [Gazetas et al, 2004] is contrary to the behavior of flexible retaining walls such as the semi-gravity type L-shaped walls, Prestressed-Anchor piled (PAP) walls, and reinforced Soil (RS) walls, retaining non saturated cohesionless soils or saturated clayey soils. These types of walls have behaved particularly (and sometime surprisingly) well during many recent earthquakes as Loma Prieta (1989), Northridge (1994), Kobe (1995), Chi-Chi (1999), Kocalei (1999) and Athens (1999) earthquakes.

3 FRAMEWORK: ANALYSIS AND DESIGN PRINCIPLES.

Interaction between earth retaining structures and surrounding soil is a complex phenomenon for both static and seismic case. This maybe the main reason for which available analysis-design methods present different degree of complexity as it is difficult to account for all aspects at once. Under static loading it was shown [Rowe, 1957] that wall flexibility leads to important pressure redistribution along the wall and for dense granular fills to consider the effect such redistribution becomes important to accurately evaluate the reduction of bending moment acting on the wall. Presence of anchoring systems may also affect strongly the behaviour of flexible structures in that limiting displacements, anchoring systems may prevent active pressure conditions from developing and elastic soil behaviour modelling maybe appropriate. On the other hand for unanchored structures larger displacements may occur and the occurrence of plastic zones may become important [Faccioli *et al.*, 1996].

In the present chapter a review of available methodologies for the earthquake resistant design of flexible retaining structures is done. Under a didactical point of view it is useful to group different methods depending on specific criteria. A possible classification can be done with respect to the way seismic force is considered. In this case three groups can be identified as follow based on the way seismic input is prescribed:

- Pseudostatic methods: earthquake force is modelled using an equivalent constant additional uniform acceleration as in Monobe-Okabe method [Mononobe and Matsuo,1929] and its variants (e.g. Prakash *et al.* [1966]). Several solutions based on limit equilibrium (e.g. Rao and Choudhury [2005]), limit analysis (e.g. Lancellotta [2007]) or method of characteristics (e.g. Sokolwskii, [1965]) are available.

- Pseudo-dynamic methods: in which the effect of the input accelerogramm is considered in a simplified way. For flexible retaining structures this approach can be divided in two: either based on rigid block method [Newmark, 1965] as maybe the case of Towata and Islam [1987] where emphasis is put on displacement analysis or subgrade reaction method as the case of Richards *et al.* [1999].

- Complete dynamic analysis: imply the integration of the equation of motion considering the complete input accelerogramm. Solution can be analytical as the one of Veletsos and Younan [1994a, 1994b, 1997, 2000], Wood [1973], Scott [1973] or

numerical based on Finite Element Methods (FEM) as the case of Psarropoulos *et al*, [2005], Madhabushi and Zeng [2006 and 2007] or Finite Difference Method (FDM) as the case of Green and Ebeling [2002].

Another classification can be done with respect to the retaining structure displacements and correlated soil material modelling assumptions:

- Limit state analysis: in which relative soil-wall motion is high enough to lead to soil yielding. A failure mechanism occurs. Example is given by Mononobe-Okabe method [Mononobe and Matsuo,1929] and its variants.
- Linear elastic analysis: where limited wall-soil movement allows for linear elastic assumption. Example are given by Wood [1973], Scott [1973], Veletsos and Younan [1994a, 1994b, 1997,2000].
- Intermediate cases: where non linear soil material behaviour is allowed but no failure mechanism is assumed a priori. This is the case of Richards et al. [1999], or Siller et al. [1991] as well as the case of numerical solutions based on FEM of FDM as above.

In the following paragraphs the different approaches will be examined starting from pseudostatic as it is the most used (and sometimes abused) method. Finally tentative conclusions regarding the advantage and limitations of each method will be outlined.

3.1 Pseudostatic approach.

In this paragraph the pseudostatic approach for seismic design of (flexible) earth retaining structures is introduced. Special consideration is given regarding the displacement required for formation of rupture mechanisms and several solutions approaches are presented.

3.1.1 Active and Passive Lateral Earth Pressure: static case

Vertical or near-vertical slopes of soil are supported by retaining walls, cantilever sheet-pile walls, sheet pile bulkheads, braced cuts and other similar structures. The proper design of those structures requires and estimation of lateral earth pressure which is a function of several factors such as the type and amount of wall movement, the strength parameters of the soil, the unit weight of the soil and the drainage conditions in the backfill. A very intuitive definition of active and passive state can be made with reference to wall-soil movement as is shown in Figure 3.1

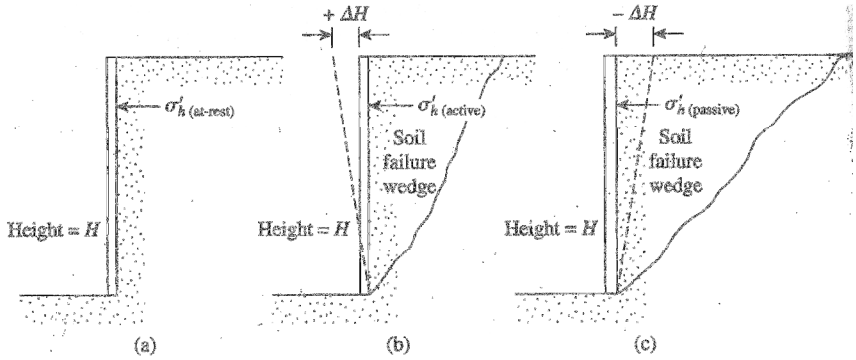

Figure 3.1 Relative soil wall displacements for rest a), active b) –passive c) states [Das B.M. , 2007]

Experimental results showing evidence of active thrust and passive resistance for a gravity wall is shown in Figure 3.2. Stress paths in the q-p plane for a granular soil element going from at rest conditions to active state or passive state are shown in Figure 3.3

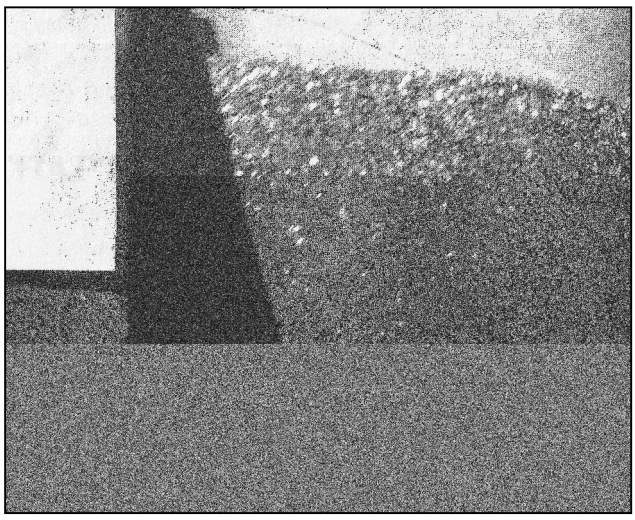

Figure 3.2 Movement of "soil" surrounding model retaining wall [Lambe, T.W., Whitman, V. W, 1979]

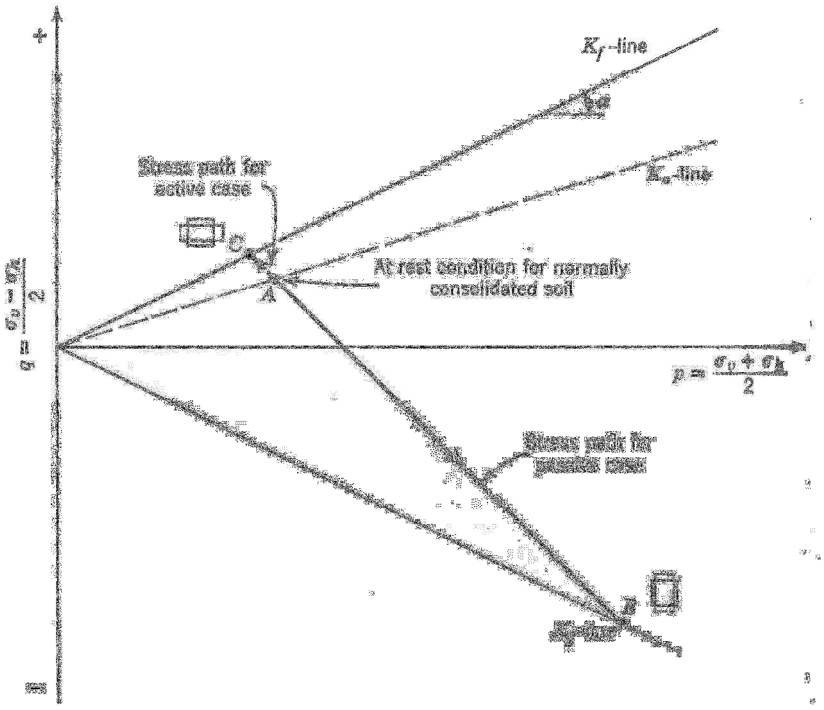

Figure 3.3 Stress paths from at rest conditions to active or passive state [Lambe, T.W., Whitman, V. W, 1979]

Considering (Figure 3.4 a) a horizontal surface of semi-infinite mass of cohesionless soil with a unit weight γ, at depth z below AB, the vertical pressure below ab is $p_0 = \gamma \cdot z$. After deposition of this mass of soil, the value of the lateral earth pressure p_h corresponds to the at

rest value $p_h = p_0 = K_0 \cdot p_v$. Since the element is symmetrical with respect to the vertical plane, the normal stress on *ab* is a principal stress. In Figure 3.4d representing the stress state in the plane, the at-rest condition corresponds to circle I.

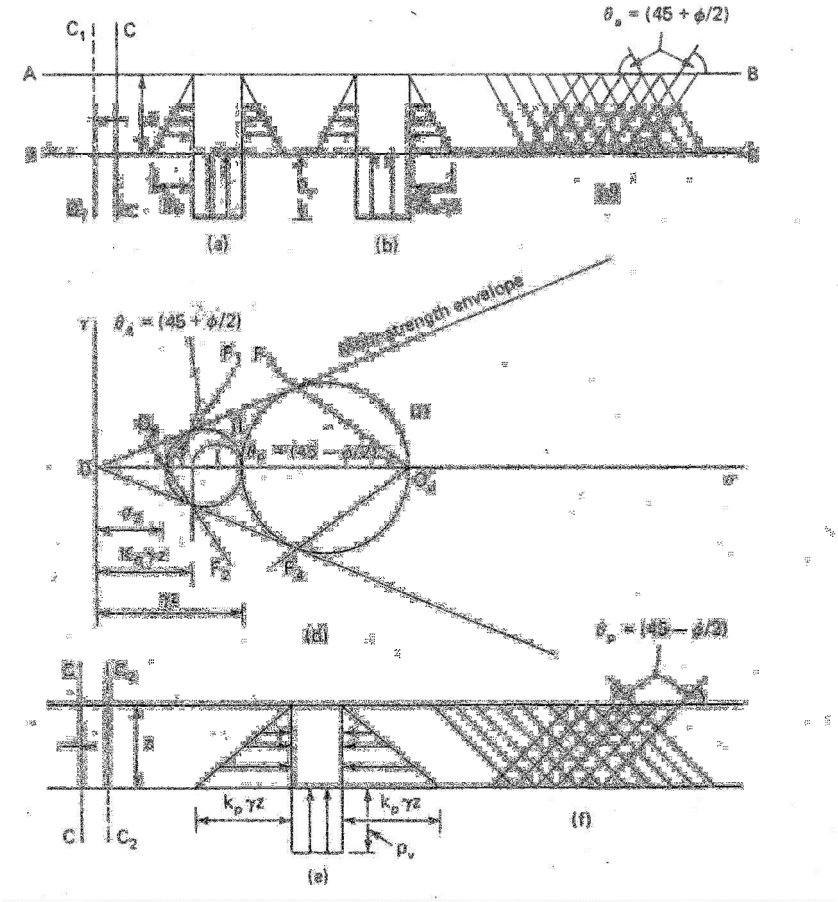

Figure 3.4 (a) At rest conditions (b,c) Rankine's states of plastic equilibrium illustrating active conditions (*d*) Mohr stress and strength diagrams (*e,f* illustrating passive conditions) [Prakash, S., 1981]

As the soil mass stretches (Figure 3.4a), plane *cc* moves to the left to position c_1c_1, lateral pressure decreases and (Figure 3.4d) the diameter of the stress circle increases. According to the MohrCoulomb failure criteria, the greatest diameter that a MohrCircle can have is when the Mohr Circle (II) is tangential to the Mohr strength envelope. The origin of planes is O_p, and O_pF_1 and O_pF_2 are failure planes inclined at 45°+φ'/2 each, to the major principal planes. A relationship between major and minor principal stresses at incipient failure is given by

$$K_a = \frac{P_h}{P_v} = \frac{1-\sin\phi}{1+\sin\phi} \tag{3.1}$$

Where K_a is the *coefficient of active earth pressure*. Once the soil mass stretches and lateral earth pressure reduces to active conditions, further stretching of the mass has no effect on p_h

and sliding occurs along planes parallel to O_pF_1 and O_pF_2. The vertical traces of such planes shown in Figure 3.4c, constitute the *shear pattern*.
If the wall face is smooth and vertical and deformation conditions for plastic equilibrium is satisfied, the above concepts regarding plastic equilibrium can be applied to determine the active thrust on retaining walls and similar problems.
Similarly if the soil mass is compressed and section *cc* moves to c_2c_2, the Mohr Coulomb circle corresponding to this state of stress is shown by circle III (Figure 3.4, d). Failure planes are in directions of $O_p'F_3$ and $O_p'F_4$ and are inclined 45°-φ'/2 with respect to the horizontal. The shear pattern is sketched in Figure 3.4 f and the ratio between vertical and horizontal principal stresses at incipient failure is given by

$$K_p = \frac{P_h}{P_v} = \frac{1+\sin\phi}{1-\sin\phi} \tag{3.2}$$

Once again it is noted that once the passive Rankine passive resistance has been mobilized, further compression of the soil causes no increase in soil resistance and slippage occurs along the failure planes.
The strain or relative displacement (ΔH/H) required for mobilization of limit states changes depending whether it is active or passive state and depends also on the type of soil. In Figure 3. 5 results of triaxial tests on dry granular soil [Lambe, Whitman 1979] show that the strain level required in order to achieve full mobilization of active state in dense sand is around -0.5% while full mobilization of passive resistance requires around 2% strain.

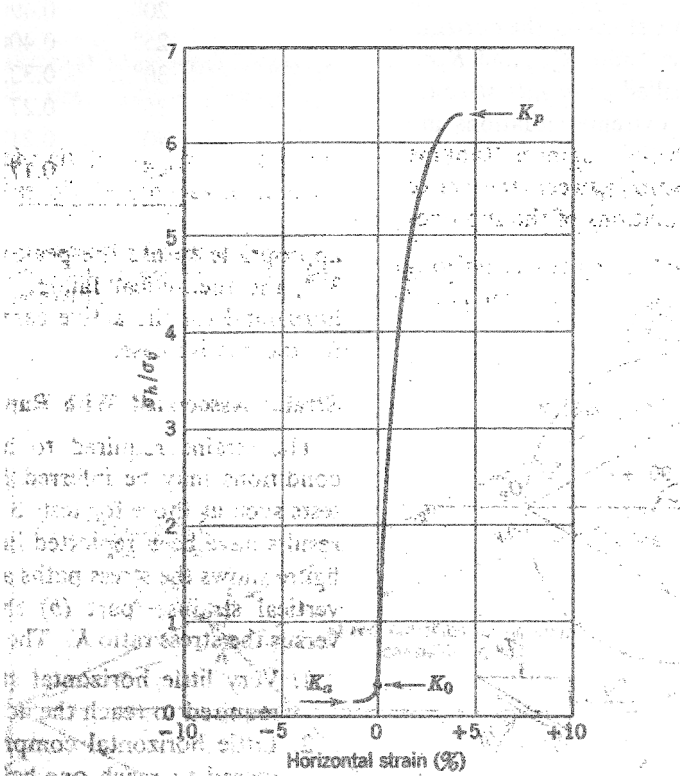

Figure 3. 5 Strains required to reach passive and active state in dense sand [Lambe, T.W., Whitman, V. W, 1979]

Consequently, as outlined by Clough and Duncan [1991], the magnitude of relative displacement (ΔH/H) required for mobilization changes accordingly and can be assumed for loose sand of the order of 1% for passive case and 0.1% for active case.

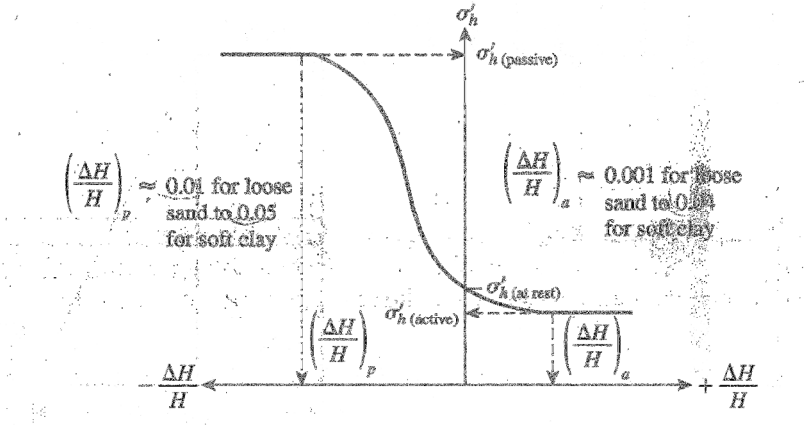

Figure 3.6 Nature of variation of lateral earth pressure [Das B.M. , 2007]

Similar values are indicated by EC7 1997 and 2003.

A different approach from the one discussed so far was proposed in 1776 by Coulomb [1776] for calculating the lateral earth pressure on an earth retaining wall with granular soil backfill. Later the method was extended to more general configurations by Mueller-Breslau [1924]. Coulomb methods does not assume neither vertical nor smooth wall but still assumes that the failure surface of the soil is plane.

The solution method is based on *global limit equilibrium method* and is based on the following steps:

1) finding by trial and error the inclination of a plane failure surface which maximises earth pressure on the wall.

2) assuming a stress distribution along such surface and its resulting force.

3) solution of the problem by mean of *global equilibrium* of the soil wedge (considered as a rigid body) inside the failure surface.

For a wall as the one showed in Figure 3.7 a) the force triangle is shown in Figure 3.7 b).

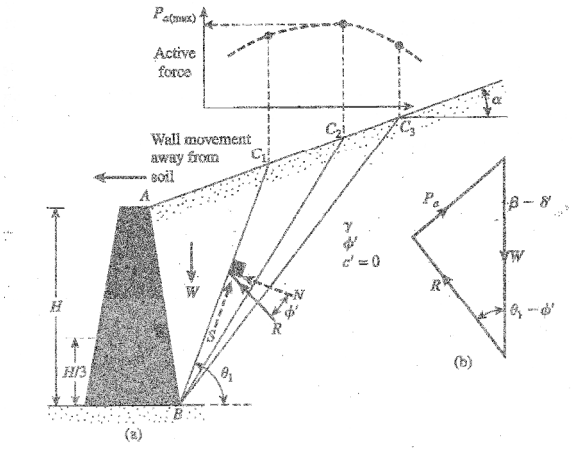

Figure 3.7 Coulomb's active pressure [Das B.M. , 2007]

The active state corresponds to the failure surface designated by a value of the angle Θ_1 for which the active pressure P_a is maximum. The value of active pressure found by Coulomb is the following:

$$P_a = 0.5 \cdot \gamma \cdot H^2 \cdot K_a \tag{3.3}$$

Where the coefficient of active pressure K_a is

$$K_a = \frac{sin^2(\beta + \phi')}{sin^2\beta \cdot sin(\beta - \delta') \cdot \left[1 + \sqrt{\frac{sin^2(\phi'+\delta') \cdot sin(\phi'-\alpha)}{sin(\beta - \delta') \cdot sin(\alpha + \beta)}}\right]^2} \tag{3.4}$$

and reduces to the value found by Rankine theory based on local stress considerations, for the case of vertical frictionless wall and horizontal backfill. Analogous considerations in the case of passive pressure (see Figure 3.8) lead to the following results

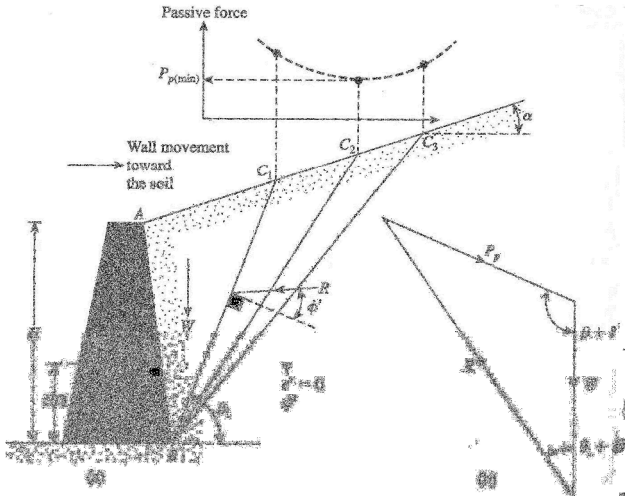

Figure 3.8 Coulomb's passive pressure [Das B.M. , 2007]

$$P_p = 0.5 \cdot \gamma \cdot H^2 \cdot K_p \tag{3.5}$$

Where the coefficient of passive pressure K_p is

$$K_p = \frac{sin^2(\beta - \phi')}{sin^2\beta \cdot sin(\beta + \delta') \cdot \left[1 - \sqrt{\frac{sin(\phi'+\delta') \cdot sin(\phi'+\alpha)}{sin(\beta + \delta') \cdot sin(\beta + \alpha)}}\right]^2} \tag{3.6}$$

The method is not exact for several reasons such as that none of the continuum generalized equations is satisfied inside or outside the failure surface where rigid body assumption is assumed. Moreover a fundamental assumption in Coulomb's approach is the acceptance of *plane failure surface*. The nature of actual failure surface in the soil mass for active and passive pressure for non smooth wall is shown in Figure 3.9 for a vertical wall with horizontal fill. In both active (a) and passive (b) case following a curved part (CD) a plane part (BC) is present.

Although the differences between Coulomb plane surface and the actual surface, for the active case are not so important, in the case of passive pressure Terzaghi [1943] has shown that for smooth walls, the rupture surface is planar and for values of the wall friction angle $\delta_p > \phi/3$, where ϕ is the soil friction angle, only curved rupture surfaces should be assumed in the analysis for the passive case under static condition. As the value of δ_p increases, Coulomb's method gives increasingly erroneous values of P_p and lead to an unsafe condition.

In the static case the passive earth pressure problem has been solved by a number of researchers using different techniques such as limit equilibrium with the choice of either planar [Coulomb, 1776] or curved surfaces [Terzaghi, 1943; Caquot and Kerisel, 1948], limit analysis [Chen, 1990] and the method of characteristics [Sokolowski, 1960].

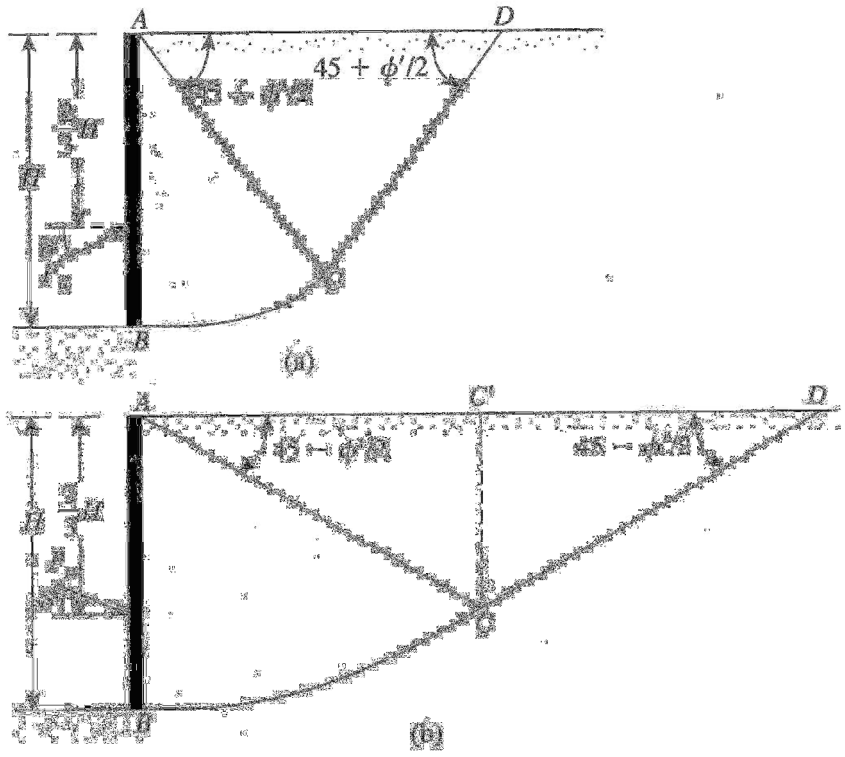

Figure 3.9 Nature of failure surface in soil with wall friction (a) active pressure (b) passive pressure [Das, 2007]

3.1.2 Active Lateral Earth Pressure: dynamic case

Coulomb's theory has been modified by Mononobe-Okabe [Mononobe and Matsuo, 1929] by considering the contribution of the inertia force to the soil wedge equilibrium in the determination of total earth pressure.
In Figure 3.10 a retaining wall of height H and inclined vertically at an angle α retains dry soil with unit weight γ, an angle of shearing resistance φ and a wall friction δ. For a trial failure surface bc_1, the inertia force may act on the assumed failure wedge abc_1 both horizontally and vertically. Given vertical (a_v) and horizontal (a_h) accelerations of the wedge of soil, the corresponding inertial forces ($W_1 \cdot a_h/g$ and $W_1 \cdot a_h/g$) can be assumed, in the worst condition, acting horizontally toward the wall and vertically in both directions.
Assuming the following definition for the *horizontal and vertical seismic coefficient k_h and kv*

$$\frac{a_h}{g} = k_h \qquad (3.7) \qquad\qquad \frac{a_v}{g} = k_v \qquad (3.8)$$

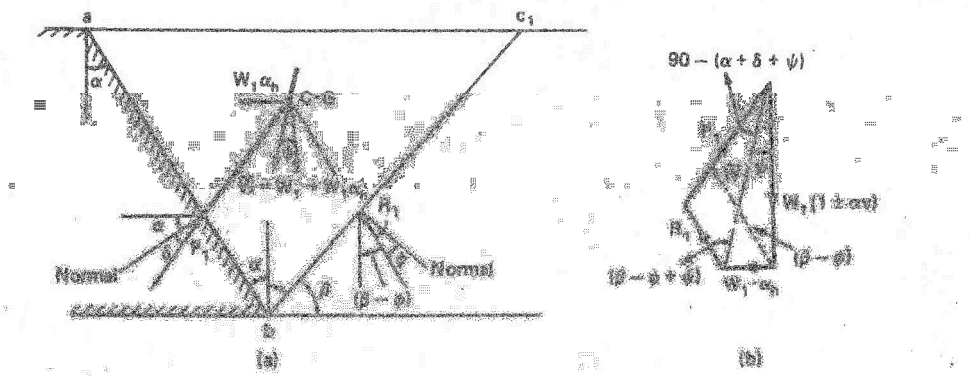

Figure 3.10 Active earth pressure under earthquake load (a) force on failure wedge (b) forces polygon [Prakash, S., 1981]

The forces acting on the wedge abc_1 (Figure 3.10) maybe listed as follows:
1- W_1: weight of the wedge abc_1 acting at its centre of gravity
2- P_1: earth pressure inclined at an angle δ with respect to the normal of the wall
3- R_1 soil reaction, inclined at an angle φ with respect to the normal to the face bc_1
4- $W_1 \cdot \alpha_h$, acting at the centre of gravity of the wedge abc_1
5- $\pm W_1 \cdot \alpha_v$, vertical inertia force

The angle between the resultant $\overline{W}_1 = W_1 \cdot ((1 \pm k_v)^2 + k_h{}^2)^{0.5}$ is vertically inclined at an angle Θ such that

$$\psi = \tan^{-1}\left(\frac{k_h}{1 \pm k_v}\right) \qquad (3.9)$$

From the triangle of forces that is drawn in Figure 3.10 c, the value of the total earth pressure can be determined for each value of the inclination β of the tentative failure surface. The solution is found when the pressure is maximum.
In analogous way as for the static case the numerical value of the total active pressure can be found as

$$P_{ae} = 0.5 \cdot \gamma \cdot H^2 \cdot K_{ae} \cdot (1 \pm K_v) \qquad \textbf{(3.10)}$$

Where

$$K_{ae} = \frac{\cos^2(\phi' - \psi - \alpha) \cdot (1 \pm k_v)}{\cos^2 \alpha \cdot \cos \psi \cdot \cos(\delta + \alpha + \psi) \cdot \left[1 + \sqrt{\frac{\sin(\phi' + \delta') \cdot \sin(\phi' - i - \psi)}{\sin(\alpha - i) \cdot \sin(\delta + \alpha + \psi)}}\right]^2} \qquad (3.11)$$

The incremental dynamic force $\Delta P_{ae} = P_{ae} - P_a$.

3.1.3 Dynamic active earth pressure point of application.

The total pressure P_{ae} can be thought as the sum of the static pressure P_a plus the increment due to dynamic effects ΔP_{ae}. Such a distinction is specially important because the point of application of $P_a = P_{ae} - \Delta P_{ae}$ can be found by Rankine Theory to be H/3 whereas that of ΔP_{ae} is recommended at 2/3H above the base of the wall [Jacobsen, 1951] or at 1/2H.
In effect within a complex soil-structure interaction problem as the one of retaining structures, it is a difficult task to identify exactly the point of application for the resultant dynamic pressure.
The interdependence between wall deformation and the forces acting on the wall has been extended to problems involving dynamic earth pressures in tests on model retaining walls conduced by several authors.
The test conducted at the University f Washington involved a series of static and dynamic tests using an instrumented model retaining wall mounted on a shaking table as described by Sherif, Ishibashi and Lee [1982], Sherif and Fang [1984] and Ishibashi and Fang [1987]. The shaking table used in this testing program is capable of applying a harmonic motion of constant amplitude to the base of the wall and the backfill. In each of the tests the wall was constrained either to translate or to rotate around either the top or the base of the wall, or some combination of translation and rotation. During the course of the dynamic earth pressure test, the wall moved away form the backfill in a prescribed manner while the base was vibrated. Movement of the wall continued until active dynamic earth pressure acted along the back of the wall. Static tests were also carried for comparison.
One the important results that were found is that the active state during the dynamic tests occurred at almost the same wall displacement as in the static tests, at a value of wall rotation equal to 0.001 for the static and dynamic test results that are shown in Figure 3.11 on dense Ottawa sand.

The magnitude of these wall movements are in general agreement with those suggested by Clough and Duncan [1991].
Regarding the point of application of the resultant thrust Ishibashi and Fang [1987] observe that for rotation about the base (RB) there is a high residual stress region near the base of the wall and that the point of application of the total active thrust is lower than one third of the wall height. For rotation about the top (RT) dynamic active distribution is also non linear. There is a high stress region near the top of the wall due to soil arching. The point of application of the total dynamic active thrust becomes very high. For lower horizontal acceleration level, dynamic stress distribution at the active stage is controlled mainly by wall displacement geometry. For high acceleration level, on the other hand, the effect of dynamic inertial force becomes dominant and thus the effect of the wall displacement geometry becomes negligible. Dynamic active thrust converges to nearly the value of h/H=0.5 at k_h<0.5 as visible Figure 3.12. Incremental dynamic active thrust is nearly equal to that obtained by Mononobe Okabe for RT and T (translational) modes but, on average, 26% higher than M-O values fir RB mode.

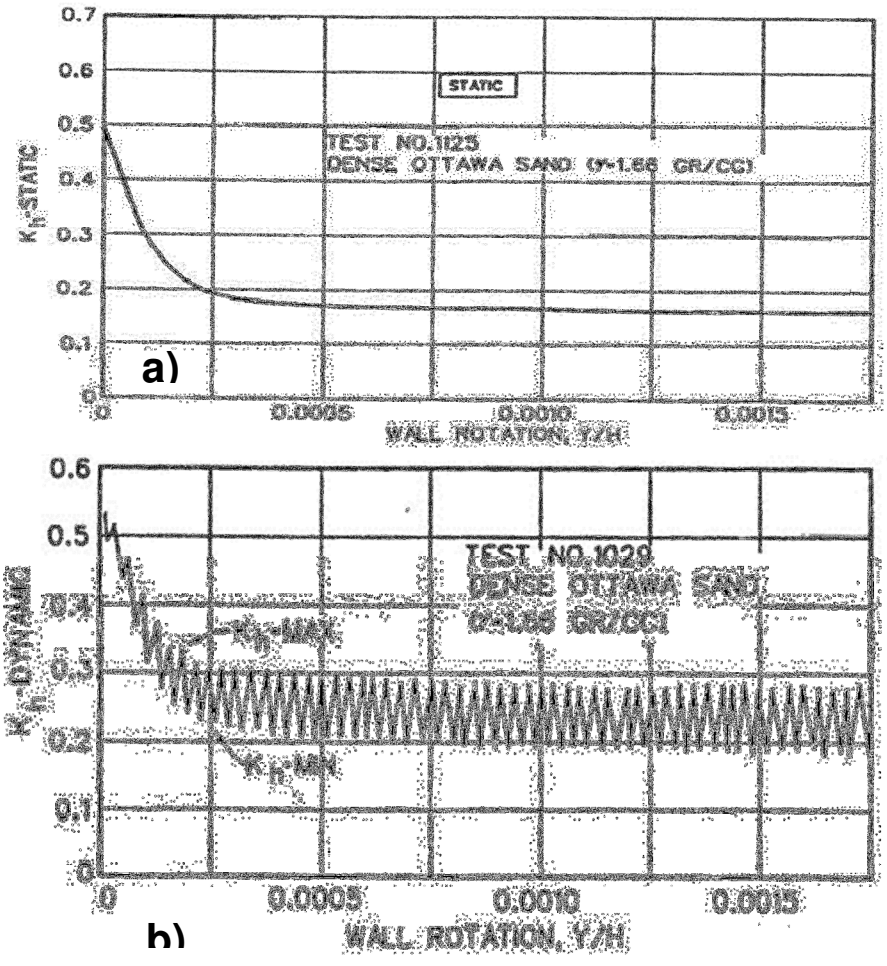

Figure 3.11 (a) Static horizontal earth pressure (b) Dynamic horizontal earth pressure (Sherif and Fang [1983]).

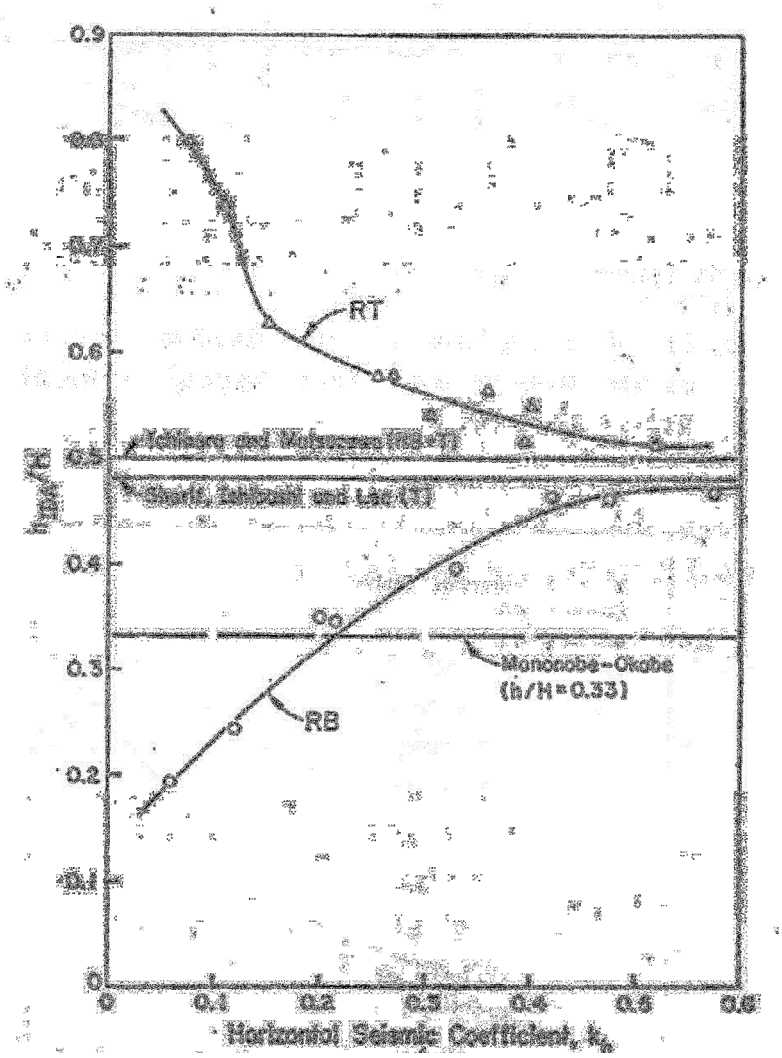

Figure 3.12 Point of application of incremental dynamic active thrust versus horizontal acceleration coefficient [Ishibashi and Fang, 1987].

Tests were also performed on two small walls (1-m high flexible, 1-m high rigid) by Nandkumaran [1973] and reported by Prakash and Nandkumaran [1979]. Using a shake table, earth pressure, under both static and dynamic conditions were measured in both of the walls. Earth pressures, under both conditions, were monitored by nine diaphragm-type earth pressure cells. Poorly graded sands, SP type, with little or no fines was used. Relative density 56% and friction angle at this relative density 40º. Uniformity coefficient C_u=2.1, effective size D_{10}=0.13mm, specific gravity S_s=2.66.
Typical data from four testes on a 1-m flexible and 1-m high rigid wall are reported respectively in Table 3.1 and Table 3.2.
In Figure 3.13 the recorded static and dynamic pressures are plotted along with the K_0 and K_a lines.

Movements during backfilling were not permitted in the rigid wall. Active conditions were then generated by allowing subsequent rotation of the wall. The test bin was then excited and the dynamic increment of pressure with height was recorded. Two types of tests were performed. In one series (test 1, 2, and 3, Table 3.2), the top of the wall was not allowed to move, while in another, (test 4, 5 and 6) the wall was free to move during the dynamic loading. The point of application, for a given table acceleration, was slightly increased in this case.

From these results it is possible to observe that the point of application of the dynamic increment in earth pressure was between 0.483 *H* and 0.5465 *H* in the flexible wall and between 0.364 *H* and 0.433 *H* from the base in the rigid wall, where *H* is the height of the wall.

Table 3.1 Particulars of test data on 1-m flexible wall [Nandkumaran, 1973]

Test no.	Total static pressure, g/cm, of wall	Static EP coefficient	Point of application above base, cm	Acceleration in test (peak), g	Total dynamic increment, g/cm, of wall	Point of application above base, cm	Dynamic increment static pressure
1	[illegible]	[illegible]	[illegible]	[illegible]	[illegible]	[illegible]	[illegible]
2	[illegible]	[illegible]	[illegible]	[illegible]	[illegible]	[illegible]	[illegible]
3	2641.3	0.3322	34.25	3.34	1680.0	50.05	0.646
4	2697.0	0.3392	36.00	4.55	2177.0	48.30	0.807

Table 3.2 Particular of test data on 1-m high rigid wall [Nandkumaran, 1973]

Test no.	Table acceleration, g	Dynamic pressure, g/cm	Point of application above base, cm	Remarks
1	2	3	4	5
1	4.21	2647.0	41.5	No wall movement
2	3.71	2469.5	36.4	No wall movement
3	3.31	1732.5	40.6	No wall movement
4	4.21	2394.0	44.3	Wall moves during shocks
5	[illegible]	[illegible]	[illegible]	[illegible]
6	[illegible]	[illegible]	[illegible]	[illegible]

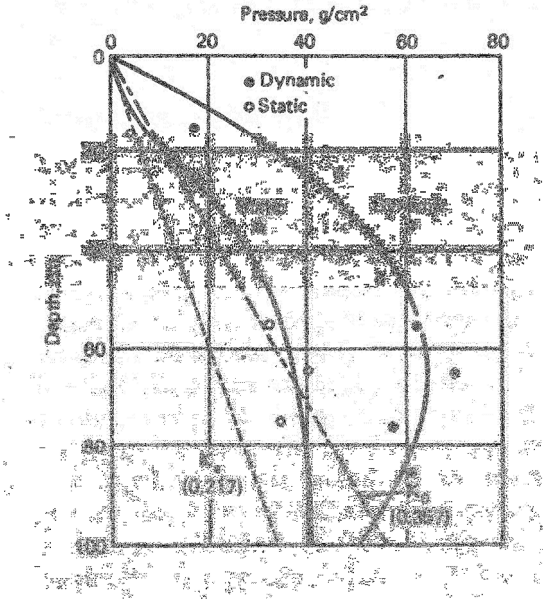

Figure 3.13 Static and Dynamic earth pressure distribution behind 1-m high flexible wall test no. 4 [Nandkumaran, 1973]

A plot of peak ground (or table) velocity with the coefficient of dynamic earth pressure c_p, was found to essentially agree with the theoretical solution, if the ground motion is assumed to have a period of 0.3s (Figure 3.14). For a given velocity, flexibility of the wall leads to a reduction in the coefficient of dynamic earth pressure.

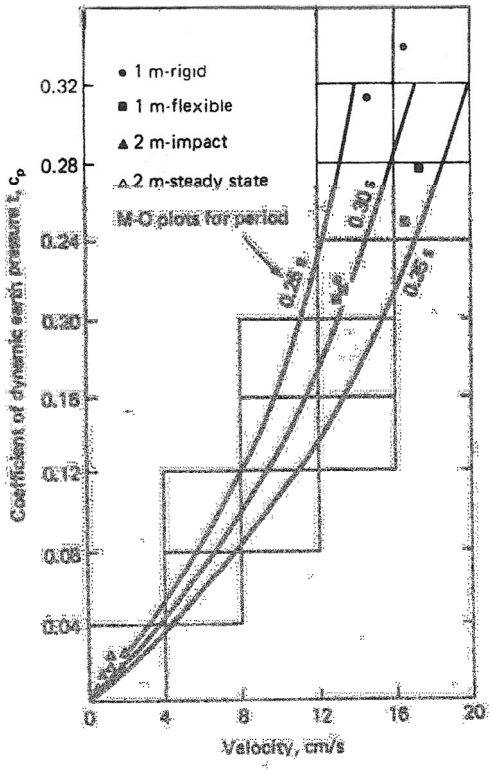

Figure 3.14 Peak ground or table velocity versus dynamic increment of earth pressure for flexible and rigid wall [Prakash and Nandkumaran, 1979]

3.1.4 Simplified procedure for Dynamic Active Earth Pressure and limiting horizontal acceleration.

Seed and Whitman [1970] presented a simplified procedure for computing the dynamic earth pressure on a vertical yielding walls retaining dry backfill. They considered the group of structures consisting of a vertical wall retaining a granular horizontal backfill with friction angle equal 35º, static active pressure force and the dynamic active pressure increment $P_{ae}=P_a+\Delta P_{ae}$ where $\Delta P_{ae}= \Delta K_{ae}\cdot 0.5\cdot\gamma_t\cdot H^2\cdot(1\pm K_v)$. The dynamic earth pressure coefficient is equal to

$$K_{ae}=K_a+\Delta K_{ae} \tag{3.12}$$

$$\Delta K_{ae}=(3/4)\cdot k_h \tag{3.13}$$

All forces act at an angle δ from the normal to the back of the wall (Figure 3.10). P_a acts at an height $H/3$ above the heel of the wall and ΔP_{ae} acts at a height equal to $0.6\cdot$H. P_{ae} acts at a height Y which ranges form $H/3$ to $0.6\cdot H$ depending on the value of k_h. As stated in 3.1.3, the results of instrumented shake table confirm this range of values, the actual value depending upon the model of wall movement.
Seed and Whitman [1970] approximate the value of β (Figure 3.10) as equal to ϕ where ϕ equals 35º. Thus, for a wall retaining a dry granular backfill of height H, the theoretical active failure wedge would intersect the top of the backfill at a distance equal to 1.5 times H, as measured from the top of the wall (tan 35º~1/1.5).

Richard and Elms [1979] show that equation (3.11) is limited to the case where $(\phi-i)$ (where i is the slope of the backfill) is greater or equal to ψ. Substituting $(\phi-i)$ in equation (3.11) results in β equal to the slope of the backfill (i), which is the stability problem for an infinite slope. Zarrabi [1973] shows that this limiting value for ψ corresponds to a limiting value for k_h which is equal to

$$k_h^*=(1-k_v)\cdot\tan(\varphi-i) \tag{3.14}$$

When k_h is equal to k_h^* the shear strength is fully mobilised, and the backfill wedge verges on instability. Values of k_h^* are also shown in Figure 3.15.

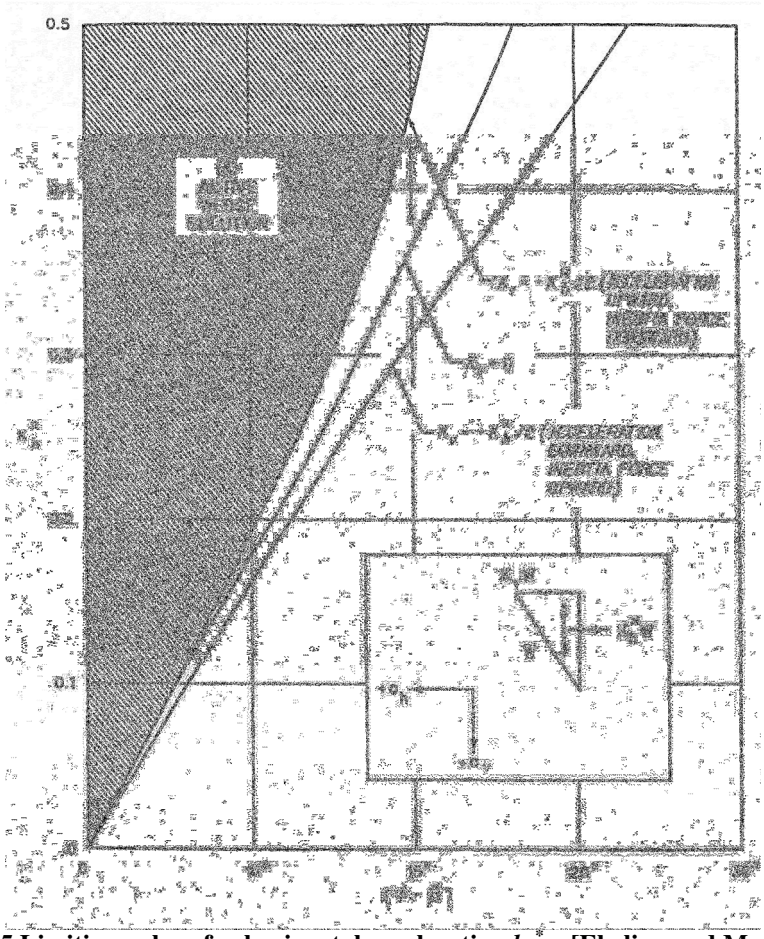

Figure 3.15 Limiting values for horizontal acceleration $k_h^* \cdot g$ [Ebeling and Morrison, 1992]

3.1.5 Analytical Solution for Total Active Earth Pressure for C-φ soil [Prakash, 1968]

The Monobe-Okabe pseudostatic method is formulated under the hypothesis of cohesionless soil only. A general solution for determination of total (static plus dynamic) earth pressures for a c- φ soil has been developed by Prakash and Saran [1966] and Prakash [1968].

Figure 3.16 shows a wall with face *ab* in contact with soil and vertically inclined at surcharge *q* per unit area. The assumed failure surface is a vertical inclined at angle Θ through *b*. If the depth of tension crack is H_c, let

$$H_c=n\cdot(H_1- H_c)=n\cdot H \tag{3.15}$$

In which H_1=height of the retaining wall and H=height of the retaining wall free from cracks. In this analysis only the horizontal inertia force has been considered and sol-wall adhesion is assumed equal to soil cohesion (c=c'). By simple equilibrium considerations the dynamic pressure can be written in the form

$$P_{dyn}=\gamma\cdot H^2\cdot(N_{a\gamma})_{dyn} +q\cdot H\cdot(N_{aq})_{dyn} -c\cdot H\cdot(N_{ac})_{dyn} \tag{3.16}$$

In which $(N_{a\gamma})_{dyn}$, $(N_{aq})_{dyn}$ and $(N_{ac})_{dyn}$ are the *pressure coefficients* and depend on α, n, φ, and Θ. The values of the pressure coefficients has been optimised so that (3.16) gives the upper bound of active earth pressure.

$$(N_{ac})_{dyn} = \frac{\cos\beta\cdot\sec\alpha+\cos\phi\cdot\sec\theta}{\sin(\beta+\delta)} \tag{3.17}$$

$$(N_{aq})_{dyn} = \frac{\left[(n+1)\cdot\tan\alpha+\tan\theta\right]\cdot\left[\cos(\theta+\phi)+\alpha_h\sin(\theta+\phi)\right]}{\sin(\beta+\delta)} \tag{3.18}$$

$$(N_{a\gamma})_{dyn} = \frac{\left[(n+0.5)\cdot(\tan\alpha+\tan\theta)+n^2\cdot\tan\alpha\right]\cdot\left[\cos(\theta+\phi)+\alpha_h\sin(\theta+\phi)\right]}{\sin(\beta+\delta)} \tag{3.19}$$

Maximum values for earth pressure coefficients were also obtained for the static case (in which α_h=0) and it is seen that N_{ac} has the same value in the static as well as in the dynamic case. The ratio of the coefficients from the dynamic to the static case may then be defined as

$$\lambda_1 = \frac{(N_{aqm})_{dyn}}{(N_{aqm})_{stat}} \tag{3.20}$$

$$\lambda_2 = \frac{(N_{a\gamma m})_{dyn}}{(N_{a\gamma m})_{stat}} \tag{3.21}$$

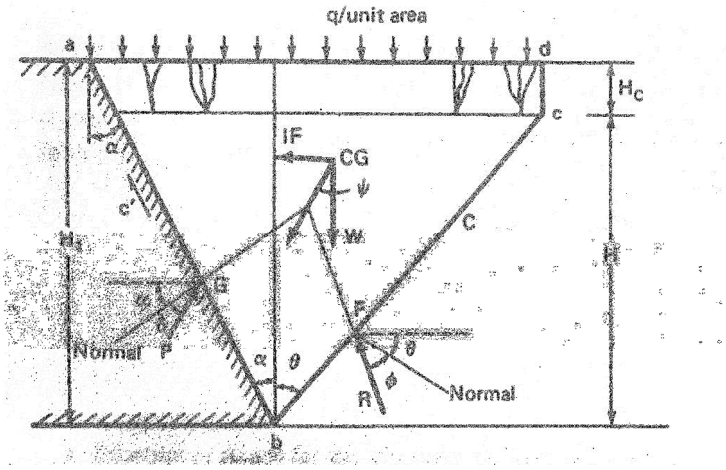

Figure 3.16 Force acting on a wall retaining c-φ soil and subjected to an earthquake type load [Prakash, 1968]

In Figure 3.17, N_{ac} has been plotted against ϕ. This plot is independent of n and the inclination of the wall α has been considered from 0 to ±20º.

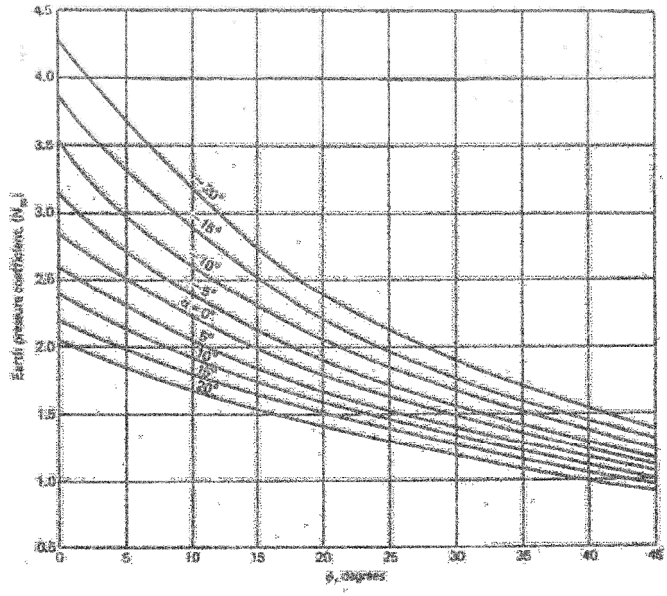

Figure 3.17 $(N_{ac})_{stat}$ versus ϕ for all n [Prakash, 1968]

Figure 3.18 and Figure 3.19 shows the plot of $(N_{aq})_{stat}$ versus φ for n=0 and n=0.2, respectively. Figure 3.20 and Figure 3.21 show $(N_{a\gamma})_{stat}$ versus φ for n=0 and n=0.2 respectively. It was found that the value of λ_1 and λ_2 are nearly equal. Hence only one value of λ ($=\lambda_1=\lambda_2$) has been plotted in Figure 3.22. The value of λ represents the ratio of earth pressure coefficients in the dynamic to the static case and both the coefficients decrease with ϕ. It is possible to observe that the dynamic coefficient is always higher than the static one and that tends to one for lower acceleration. Naturally λ increases with increasing α_h. Moreover while for lower acceleration the dynamic pressure coefficients are always increasing faster for increasing friction angle, the same cannot be said for higher accelerations

for which the rate of increase of the dynamic pressure coefficients has a minimum for friction angles equal to α. For this reason the curves in Figure 3.22 present a minimum for $\phi=\alpha$.

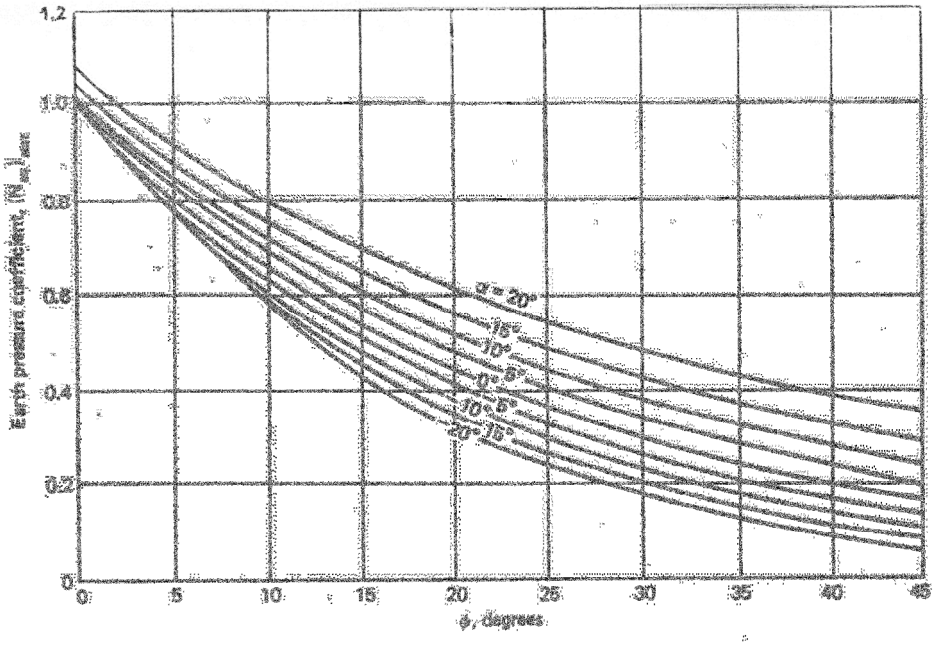

Figure 3.18 $(N_{aq})_{stat}$ versus ϕ for *n=0* [Prakash, 1968]

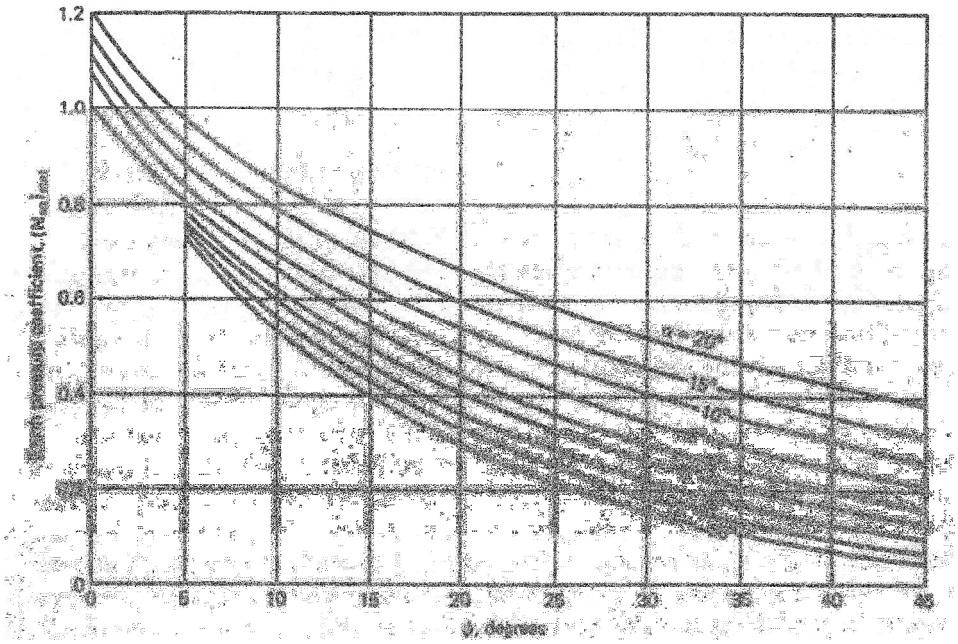

Figure 3.19 $(N_{aq})_{stat}$ versus ϕ for *n=0.2* [Prakash, 1968]

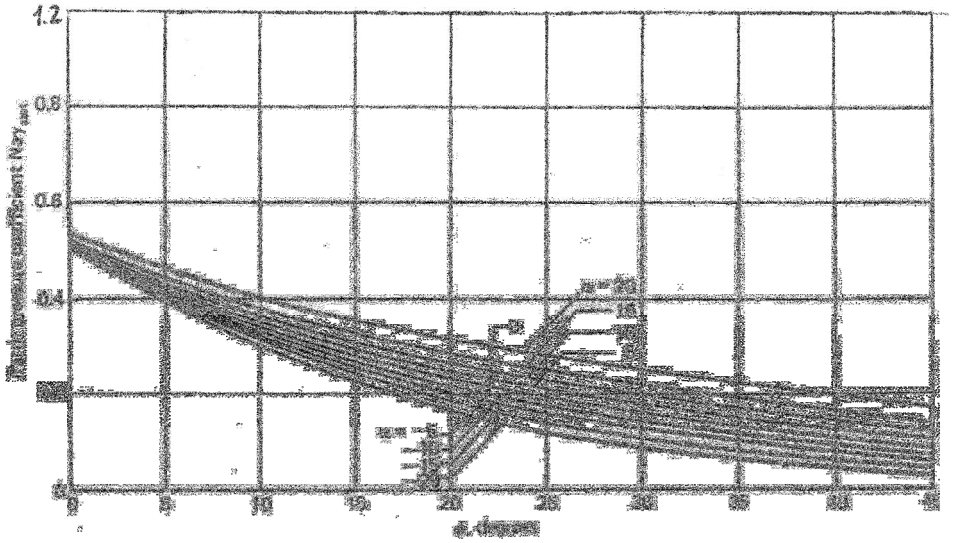

Figure 3.20 $(N_a\gamma)_{stat}$ versus ϕ for *n=0* [Prakash, 1968]

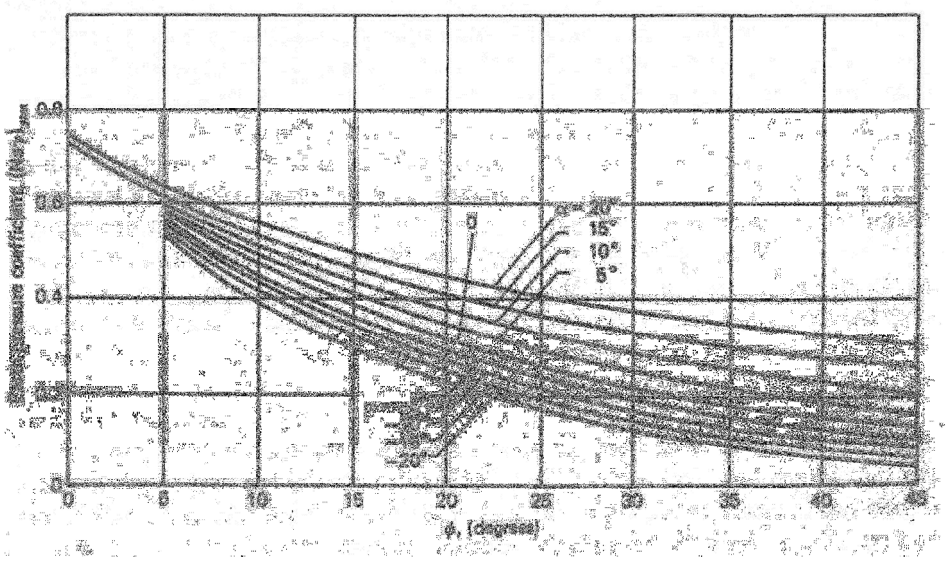

Figure 3.21 $(N_a\gamma)_{stat}$ versus ϕ for *n=0.2* [Prakash, 1968]

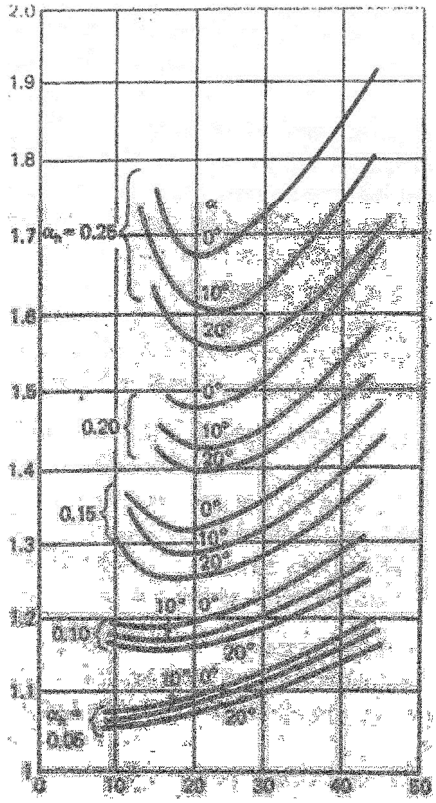

Figure 3.22 λ versus ϕ [Prakash, 1968]

3.1.6 Passive Lateral Earth Pressure: dynamic case

As already stated in 3.1.1, for values of the wall friction angle $\delta > \phi/3$ [Terzaghi ,1943], where ϕ is the soil friction angle, only curved rupture surfaces should be assumed in the analysis for the passive case. For this reason the solution proposed by Mononobe and Okabe is not described in the following review.

Under static condition and several solutions have been proposed based on several available methods of solution [Caquot and Kerisel, 1948; Chen, 1990; Sokolowski, 1960]. More recently several solutions have been proposed also for the seismic passive earth pressure problem as well either by mean of limit equilibrium method with log-spiral failure surface [Morrison and Ebeling, 1995; Rao and Choudhury, 2005] or by limit analysis [Chen and Liu, 1990; Soubra, 2000; Kumar, 2001 ;Lancellotta, 2007] along with a curved surface. In the following a description of the two solutions by Rao and Choudhury [2005] and Lancellotta [2007] will be given.

- Solution using limit equilibrium [Rao and Choudhury,2005].

In the solution proposed by Rao and Choudhury [2005] limit equilibrium method is adopted for determining individually the seismic passive earth pressure coefficients corresponding to own weight, surcharge and cohesion components. In the determination of each of these components, composite (logarithmic spiral and planar) failure surfaces were considered. Effects of a wide range of parameters such as wall batter angle, ground slope, wall friction angle, angle of internal friction of the soil, wall adhesion to soil cohesion ratio, and the horizontal and vertical seismic accelerations on the seismic passive earth pressure coefficients were studied. It was considered that the occurrence of an earthquake does not affect the basic soil parameters: unit cohesion c, friction angle ϕ, and unit weight g. Uniform seismic accelerations are assumed in the domain under consideration.

A retaining wall AB of a vertical height H, wall batter angle α, ground slope β, wall friction angle δ, soil friction angle ϕ, coefficient of seismic horizontal acceleration k_h, and a coefficient of seismic vertical acceleration k_v, as shown in Figure 3. 23. The seismic passive force P_{pd} could be divided into three components

$$P_{pd} = P_{p\gamma d} + P_{pqd} + P_{pcd} \tag{3.22}$$

The principle of superposition is assumed to be valid and the minimum of each component is added to get the minimum seismic passive force. The magnitude of error between the method of superposition considering minimum of each component and finding the minimum of total earth force is seen to be very small, or less than 3%. In Fig. 1, the failure surface includes portion BD, which is a logarithmic spiral and a planar portion DE, which is similar to the Rankine passive planar failure surface including the pseudostatic the seismic forces are shown in Fig. 1. Seismic forces. F is the focus of logarithmic spiral and is located at a distance L from A. The initial radius r_0 and the final radius r_f of the logarithmic spiral are given by distances FB and FD, respectively.

The exit angle ξ at point E on the ground surface is found $\xi = \xi$ (□β, φ, k_h□□, k_v)□ by imposing equilibrium and Mohr Coulomb failure criterion. For k_h=k_v=0, the value of ξ found is the same value as given by Rankine and the same value as given by Kumar (2001) for k_v=0.

For P_{pgd} the point application was assumed at H/3 from the base of the wall as in Chen and Liu [1990], whereas for $P_{pqd} + P_{pcd}$ are assumed to act at H/2 from the base of the wall).

Cohesive force C is assumed to act on the failure surface BD along with normal force N and frictional force N tan ϕ. Adhesive force C_a is acting on the retaining wall–soil interface AB. Rankine passive forces P_{pcR}, P_{pqR}, and P_{pgR} are assumed to act on the surface DG.

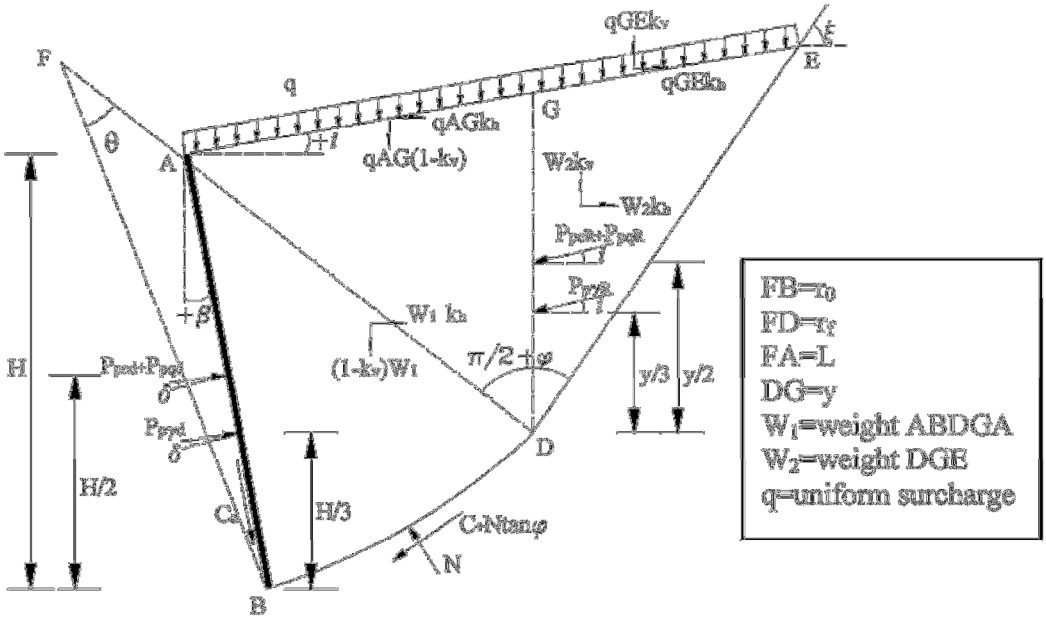

Figure 3. 23 Composite failure surface and forces considered

Pseudostatic forces due to seismic weight components for zone *DGE* are $W2k_h$ and $W2k_v$ in the horizontal and vertical directions, respectively. Pseudostatic forces due to seismic weight component for zone *ABDGA* are $W1k_h$ and $W1k_v$ in the horizontal and vertical directions, respectively.

Pseudostatic forces due to $q.AG.k_h$ and $q.AG.k_v$ in the horizontal and vertical directions, respectively, are assumed to act on *AG*. Similarly pseudostatic forces $q.GE.k_h$ and $q.GE.k_v$ in the horizontal and vertical directions, respectively, are assumed to act on *GE*.

Determination of the seismic passive earth pressure coefficient for the unit weight component $K_{p\gamma d}$, for the surcharge component K_{pqd},, for the cohesion component K_{pcd}, correspond respectivelly to the minimum value of $P_{p\gamma d}$, P_{pqd} and P_{pcd}.

Considering the moment equilibrium of all forces about the focus *F* the minimum value of *Ppgd* is obtained by considering different logspirals by varying the distance *L*. The minimum values of $P_{p\gamma d}$, P_{pqd} and P_{pcd} are found considering different logspirals by changing the value of the distance L. The total seismic passive force P_{pd} acting at an angle δ on the retaining wall of height *H* becomes

$$P_{pd} = (2 \cdot c \cdot H \cdot K_{pcd} + q \cdot H \cdot K_{pqd} + \frac{1}{2} \cdot \gamma \cdot H^2 \cdot K_{p\gamma d}) \cdot \frac{1}{\cos \delta} \tag{3.23}$$

Where:

$$K_{p\gamma d} = \frac{2 \cdot P_{p\gamma d} \cdot \cos\delta}{\gamma \cdot H^2} \tag{3.24}$$

$$K_{pqd} = \frac{P_{pqd} \cdot \cos\delta}{q \cdot H} \tag{3.25}$$

$$K_{pqd} = \frac{P_{pcd} \cdot \cos\delta}{2 \cdot c \cdot H} \tag{3.26}$$

Table 3.3 shows a comparison of $K_{p\gamma d}$ values obtained from different analyses. For δ/ϕ=0.5, it is seen that the present method results in the least values of the coefficients. However for δ/ϕ =1.0, it is not necessarily the least in cases for higher k_h values, but the difference is very marginal.

Table 3.3 Computation of seismic earth pressure by various methods

δ/ϕ	kh	Kv	Mononbe Okabe	Morrison Ebeling	Chen Liu	Soubra	Kumar	Choudhury
	0	0	4.807	4.463	4.71	4.53	-	4.458
	0.1	0	4.406	4.24	4.37	4.202	-	4.24
	0.1	0.1	4.35	4.16	-	-	-	3.89
	0.2	0	3.988	3.87	4	3.9	-	3.86
	0.2	0.2	3.77	3.6	-	-	-	3.02
	0.5							
0.5	0.3	0	3.545	3.46	3.59	3.47	-	3.45
	0	0	8.743	6.15	7.1	5.941	5.785	5.783
	0.1	0	7.812	5.733	6.55	5.5	5.361	5.4
	0.2	0	6.86	5.28	5.95	5.02	4.902	5.1
	0.3	0	5.875	4.94	5.3	4.5	4.4	4.75
	0.4	0	4.83	4.3	-	-	3.9	4.1
	1							
1	0.5	0	3.645	3.4	-	-	3.2	3.3

- Solution using limit analysis [Lancellotta, 2007].

Standard codes when dealing with earth pressure problems suggest solutions provided by limit equilibrium methods. Even if curved surface solutions are considered [e.g. Caquot and Kerisel, 1948], as already mentioned these solutions are based on several approximations and are essentially kineamtic in nature so they are not conservative. In fact, should the assumed mechanism be admissible in kinematic terms, these solutions represent an upper bound to the exact solution.

In literature [e.g. Soubra, 2000] it is possible to find solution to the passive seismic earth pressure coefficient base on the strict application of the kinematic approach of limit analysis, but also in this case an upper bound of the real solution is found. For this reason, it is still of interest to have available a solution based on a statically admissible stress field, this approach providing a conservative answer or the exact one.

Lancellotta [2007] contributes to this problem by deriving an analytical solution for passive earth resistance coefficients in the presence of seismic actions, based on the lower-bound theorem of plasticity. Considering the problem shown in Figure 3. 24 : a soil surface, sloping at an angle i with respect to the horizontal axis x is subjected to the vertical body force γ', due to gravity, and to the horizontal body force $k_h \cdot \gamma$', which represents the seismic action, the coefficient kh being the horizontal seismic coefficient (positive assumed if the inertia force is towards the backfill). In order to compute the passive resistance on a vertical wall of roughness δ (i.e.$\sigma'_{xz} = \sigma'_{xx} \cdot \tan\delta$), imagine transforming the problem geometry through a rigid rotation ψ, given by

$$\psi = \tan^{-1}\left(\frac{k_h}{1 \pm k_v}\right) \tag{3.27}$$

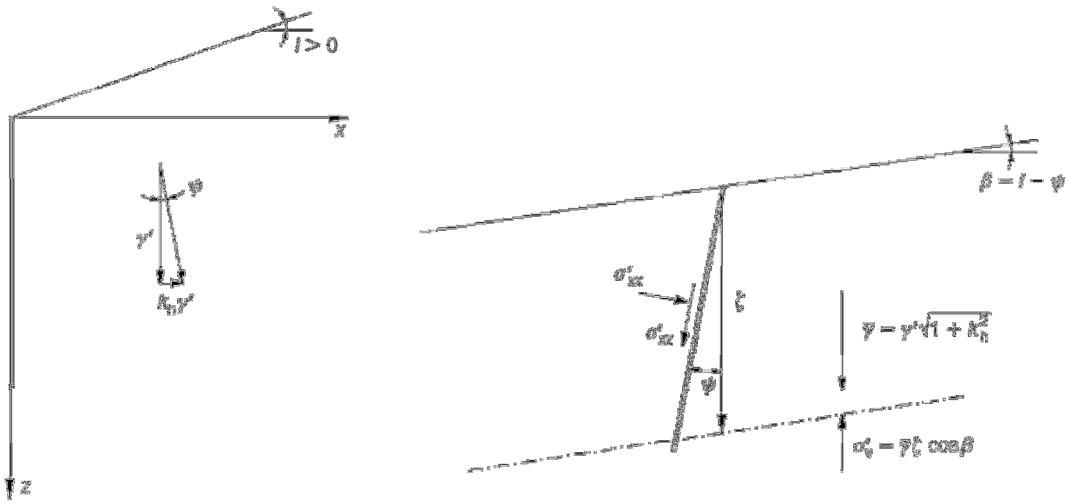

Figure 3. 24 Initial and transformed geometry [Lancellotta, 2007]

Where k_h is the coefficient of vertical acceleration. Considering a rough wall, tilted from the vertical by the angle ψ, and interacting with a backfill of slope $\beta=i-\varphi$, the resulting vertical body force is represented by the vector

$$\bar{\gamma} = \gamma' \cdot \sqrt{(1 \pm k_v)^2 + k_h^{\,2}} \tag{3.28}$$

With reference to Figure 3. 25(a), zone 2 is the conventional passive zone in which the stress state is known, as represented by the small Mohr circle in Figure 3. 25(b). If the segment OM represents the resultant stress

$$\sigma'_v = \bar{\gamma} \cdot \xi \cdot \cos \beta \tag{3.29}$$

acting at depth ξ on the plane parallel to the ground surface, it can be observed that the following relations hold OM =OH_2 + H_2M where substituting OH_2 and H_2M it is found

$$OM = \sigma'_v = \gamma' \cdot \sqrt{(1 \pm k_v)^2 + k_h^{\,2}} = s'_2 \cdot \left(\cos\beta - \sqrt{\sin^2\phi' - \sin^2\beta}\right) \tag{3.30}$$

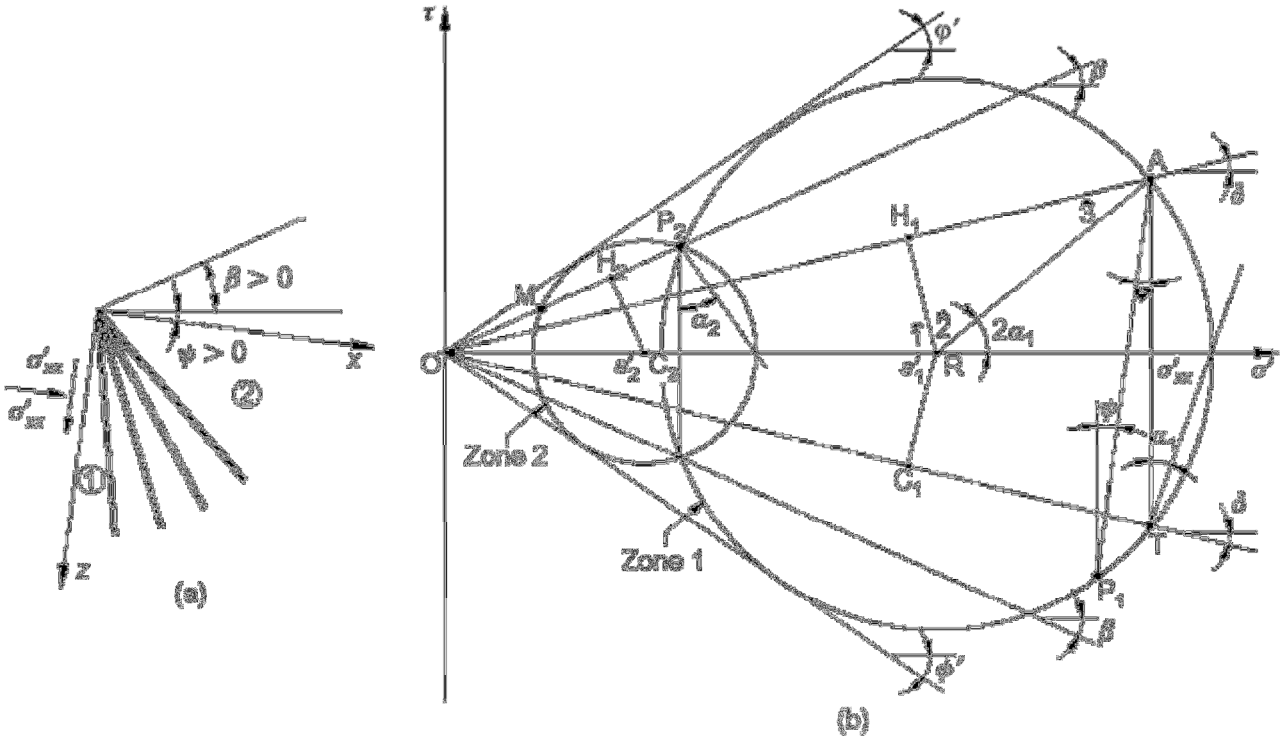

Figure 3. 25 Stress discontinuity analysis: a) fan of stress discontinuities; b) Mohr circles relative to zone 1 and zone 2; c) Mohr circle relative to conventional passive zone [Lancellotta, 2007]

Moving through a fan of stress discontinuities to zone 1 adjacent to the wall, the normal component σ_{xx} of the passive earth resistance is obtained from the large Mohr circle in Fig. 2(b) by observing that

$$\sigma'_{xx} = \gamma' \cdot \bar{OT} \cdot \cos\delta = s'_1 \cdot \cos\delta \cdot (\cos\delta + \sqrt{\sin^2\phi' - \sin^2\delta}) \tag{3.31}$$

If equation (3.31) and (**3.30**) are combined it is found

$$\sigma'_{xx} = \frac{s'_1}{s'_2} \cdot \frac{\cos\delta \cdot \left(\cos\delta + \sqrt{\sin^2\phi' - \sin^2\delta}\right)}{\cos\beta - \sqrt{\sin^2\phi' - \sin^2\beta}} \cdot \bar{\gamma} \cdot \xi \cdot \cos\beta \tag{3.32}$$

if a fan of stress discontinuities is considered (Figure 3. 25(a)), across which the rotation of the principal direction assumes the finite value Θ, then the shift between the two extreme Mohr circles is defined by [Lancellotta, 2002]

$$\frac{s'_1}{s'_2} = e^{2\theta\tan\phi'} \tag{3.33}$$

so that by inserting (**3.33**) in (3.32) the solution is found

$$\sigma'_{xx} = K_{pe} \cdot \bar{\gamma} \cdot \xi \cdot \cos(i - \psi) \tag{3.34}$$

$$K_{pe} = \left(\frac{\cos(\delta)}{\cos(i-\psi) - \sqrt{\sin^2\phi' - \sin^2(i-\psi)}}\right) \cdot \left(\cos(\delta) + \sqrt{\sin^2\phi' - \sin^2\delta}\right) \cdot e^{2\theta\tan\phi'} \tag{3.35}$$

$$\theta = 0.5 \cdot \left(\sin^{-1}\left(\frac{\sin\delta}{\sin\phi'}\right) + \sin^{-1}\left(\frac{\sin(i-\psi)}{\sin\phi'}\right) + \delta + (i-\psi) + 2\cdot\psi\right) \tag{3.36}$$

The value of K_{pe} obtained is compared to the one of Chang [1981] based on composite failure surface in Figure 3.26 which shows that Chang's method may overestimate passive resistance for higher shear angle comparing to Lancellotta's method.

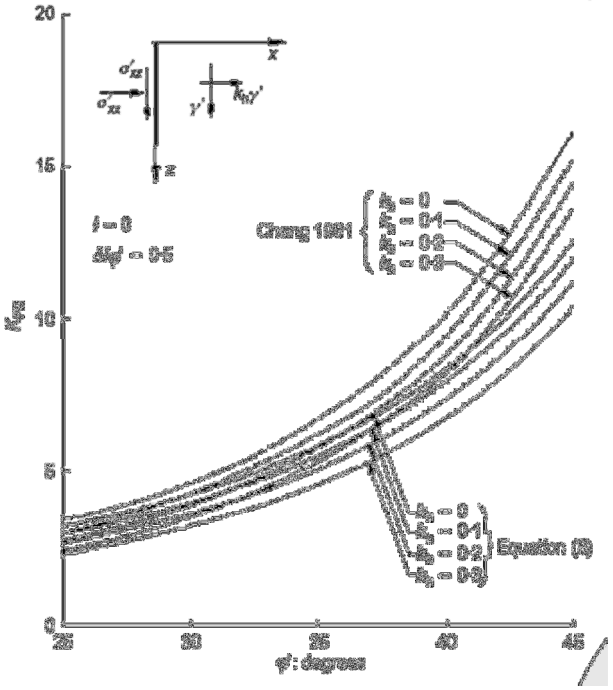

Figure 3.26 Comparison of coefficient of passive resistance [Lancellotta, 2007]

Moreover, for static case, ψ=0 and the equation **(3.35**) reduces to the static value for K_p obtained by Lancellotta [2002] and in accordance to the solution obtained by the *method of characteristics* by Sokolowskii [1965]. Such solution for the static case is used instead of the Coulomb's solution.

3.2 Pseudodynamic approach.

As already stated pseudo-dynamic methods for flexible retaining structures can be grouped in two: either based on rigid block method [Newmark, 1965] as maybe the case of Towata and Islam [1987] where emphasis is put on displacement analysis or subgrade reaction method as the case of Richards et al. [1999]. In both cases the effect of the input accelerogram is considered in a simplified way.

3.2.1 Rigid block methods.

The original work by Newmark [1965] was concerned with the effect of earthquakes on slopes, which he treated with the analogy of the block resisting on an inclined plane (rigid block). Based on this analogy Newmark developed a model for prediction of permanent displacements of a slope subjected to any ground motion.

Later on Richard and Elms [1979], in manner analogous to the Newmark sliding block procedure, proposed a method for seismic deign of gravity walls based on allowable permanent wall displacements. The level of acceleration that is just large enough to cause the wall to slide on its base is the *yield acceleration*. By combining horizontal and vertical equilibrium of a gravity wall the yield acceleration can be computed as

$$a_y = \left[\tan\phi_b - \frac{P_{AE}\cos(\delta+\theta) - P_{AE}\cdot\sin(\delta+\theta)}{W} \right] \cdot g \qquad (3.37)$$

δ soil-wall friction; Θ wall inclination

Richard and Elms recommended that P_{AE} be calculated by M-O method which requires the knowledge of the yield acceleration and therefore an iterative procedure should be followed.

The permanent block displacement is given by

$$d_{perm} = 0.087 \cdot \frac{V^2{}_{\max} \cdot a^3{}_{\max}}{a^4{}_y} \qquad (3.38)$$

The procedure proposed by Towhata and Islam [1987] applies the rigid block methodology to the case of liquefying anchored bulkheads (Figure 3. 27)

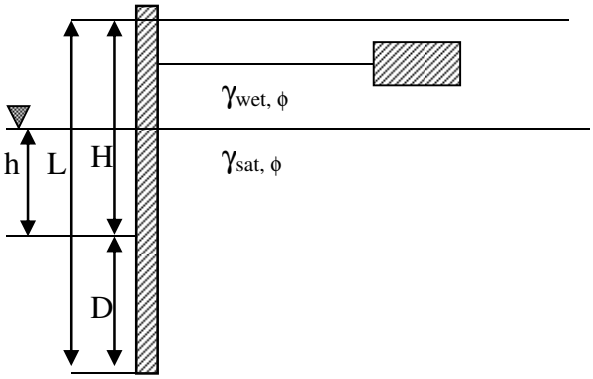

Figure 3. 27 Anchored bulkheads extending below water level [Towhata and Islam, 1987]

With the system of forces (shown in Figure 3. 28) including:
- W weight of the soil wedge
- Inertia $k_h \cdot W$
- Hydrostatic water pressure on the slip surface U_1
- Inertial increment of U_1 that is ΔU_{i1}
- Excess pore pressure due to shear ΔU_{s1}
- Normal force in the slip surface N whose effective component id N'
- Shear strength S
- Anchor resistance mT_e
- Passive earth pressure P_{pr}
- Hydrostatic water pressure on the river side U_2
- Inertial increment of U_2 that is ΔU_{i2}
- Excess pore pressure due to shear ΔU_{s2}

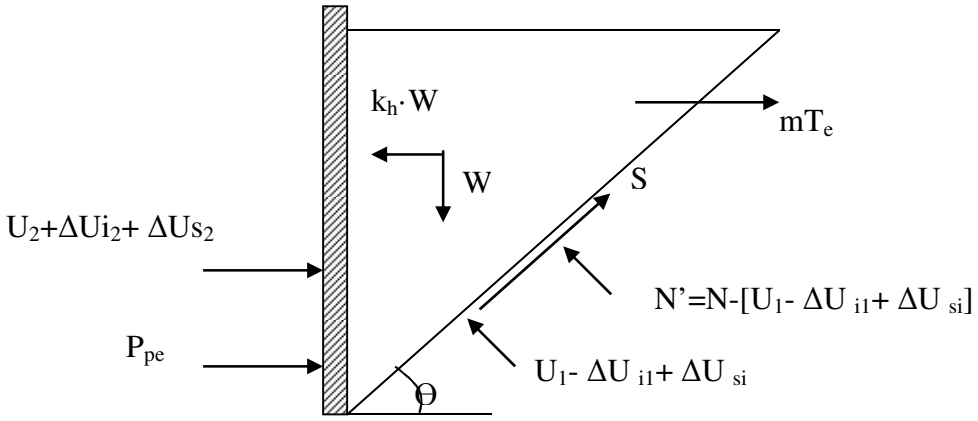

Figure 3. 28 Soil wedge and acting forces/pressures [Towhata and Islam, 1987]

They assume a translation type of mechanism and taking the equilibrium of forces in vertical and horizontal direction the following value is found for the critical acceleration

$$k_h = \frac{a \cdot \tan\theta - b + \cdot \tan(\phi - \theta) \cdot (1 + b \cdot \tan\theta)}{1 + c \cdot \tan\theta} \tag{3.39}$$

$$W = \frac{W_m}{\tan\theta} \tag{3.40}$$

$$a = \frac{m \cdot T_e + P_p + \cdot 0.5 \cdot \gamma_w \cdot (h_w + D)^2 - \nabla U_{s2}}{W_m} \tag{3.41}$$

$$b = \frac{0.5 \cdot \gamma_w \cdot (h_w + D^2) \cdot \tan\phi + \nabla U_{s2}^{*}}{W_m} \tag{3.42}$$

$$\nabla U_{s2}^{*} = \nabla U_{s2} \cdot \sin\theta \tag{3.43}$$

$$c = \frac{1}{W_m} \cdot \left\{ \frac{23mn \cdot T_e}{8 \cdot (K_p - K_0)} + \frac{17 \cdot P_p \cdot \gamma_{sat}}{8 \cdot K_p \cdot (\gamma_{sat} - \gamma_w)} + \frac{7}{12} \cdot \gamma_w \cdot h_w^{\,2} \right\} \tag{3.44}$$

From the application of this methods to a practical example the following points were shown:
a)Critical acceleration and is directly proportional and wall displacement inversely proportional to friction angle of the backfill.
b)Anchor capacity does not prevent the displacement and after liquefaction is lost.
c)Reasonable static factor of safety prevents from high displacements except when liquefaction occurs
d)Wall embedment can reduce displacement if soil does not liquefy.
e)Negative critical accelerations leads to very high displacement showing total failure.

3.2.2 Subgrade reaction methods.

Rigid block method originally applied to retaining structures for the case of gravity walls [Richard and Elms, 1979] is best suited for rigid structures which move with syncronicity with respect to the wall and for flexible retaining structures this assumption maybe not adequate. If rigid block method is used for flexible retaining structures it is advisable that more than one hypothesis be done regarding the type of mechanism of failure (e.g. rotation around the top or translation as assumed by Towata and Islam [1987]). Moreover it is necessary to evaluate what are the forces acting in anchoring systems when these are used and as shown by Vecchietti *et al.*[2006] the rigid block method provides values which are strongly dependent on type of mechanism considered. For these reasons according to Callisto [2005] rigid bock method is best suited for a displacement based global stability analysis for the flexible walls and its anchoring system.

Subgrade reaction method is an extension of the Winkler approach for modelling soil-structure interaction. The application of subgrade reaction method is based an uncoupled

approach as it requires first the calculations of free field response and secondly the application of such motion to the retaining walls using spring elements in parallel connected on one side to the free field and on the other side to the retaining structure.

Based on such approach Richard *et al* [1999] study a semi infinite layer of cohesionless soil as shown in Figure 3. 29 of unit weight *g* that is free at its upper surface, is bonded to a rigid base, and is retained on its vertical boundary by a rigid wall. The soil is simplified as an elastic, perfectly plastic material with a Mohr-Coulomb yield criterion. The height of the wall and the stratum is considered to be the same and is denoted by *H*. The wall may be either fixed or moveable. For simplicity only a horizontal seismic acceleration, a_x , is applied. The dynamic response of the soil-wall system can be analyzed using superposition. As shown in Figure 3. 30(a) for the particular case of rotation about the base, soil in the free field has the horizontal displacement u_f and the wall has the horizontal displacement u_w. The response of this soil-wall system is the sum of two cases: (1) the wall (boundary AB) has the same deformation as the free field under the inertia body force Figure 3. 30 2(b) and (2) the wall (boundary AB) is pushed back with some horizontal displacement Δu equal to the difference between the horizontal displacement of the free field u_f and the horizontal displacement of the wall u_w Figure 3. 30 (c).

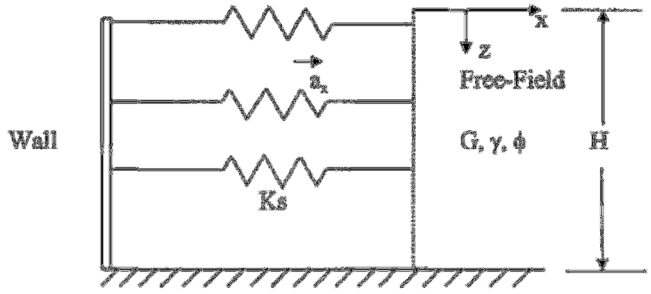

Figure 3. 29 Model for dynamic pressure increment [Richard *et al*, 1999]

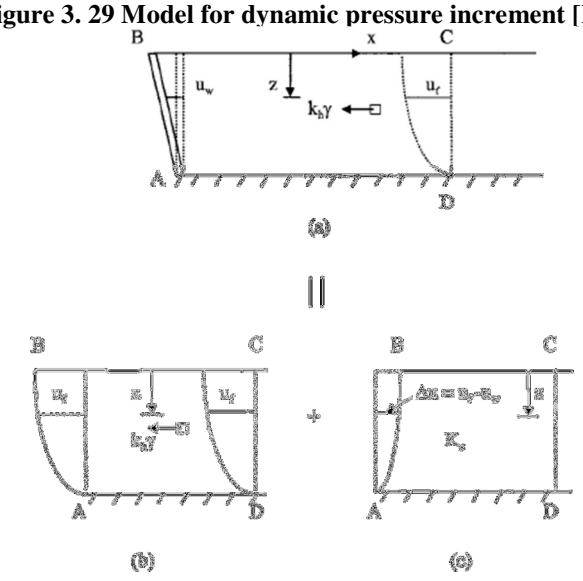

Figure 3. 30 Response of Soil-Wall system by Superposition [Richard *et al,* 1999]

Hence the total horizontal stress σ_{xw} acting on the wall is the sum of horizontal stress σ_{xf} in the free field and the stress increment $\Delta\sigma_x$ due to the relative displacement between the wall and the soil in the free field

$$\sigma_{xy}= \sigma_{xf}+\Delta\sigma_x \tag{3.45}$$

The horizontal normal stress increment, $\Delta\sigma_x$ can be expressed as

$$\Delta\sigma_x=K_s\cdot(u_f- u_w) \tag{3.46}$$

Since the springs in Figure 3. 30 can be thought of as bars with length proportional to the height of the wall [Scott 1973], their stiffness, defined as the subgrade modulus in (2), can be expressed as

$$K_s=C_2\cdot G/H \tag{3.47}$$

Where C_2 lumps all the geometric variables modifying the scale factor H into one average coefficient; and G is the shear modulus of soil behind the retaining structure. In most cases, a value of C_2 = 1.35 seems appropriate based on finite-element analysis [Huang 1996]. Considering only the effect of confining pressure, the shear modulus G of soil behind the wall may be expressed in terms of the shear modulus of the free field, G_f , the average stress, σ_{fc}, in the free field, and the average stress, σ_{wc}, behind the wall as

$$G = G_f \cdot \sqrt{\frac{\sigma_{wc}}{\sigma_{fc}}} \tag{3.48}$$

Where

$$G_f = G_{fi} \cdot \sqrt{\frac{z}{H}} \tag{3.49}$$

G_{fi} is the elastic shear modulus at depth H.

By using the Mohr-Coulomb yield criterion, the horizontal acceleration coefficient, k_i , to cause this initial yield is [Richard *et al.*, 1990]. The soil in the free field is in the elastic range when the horizontal acceleration k_hg is lower than the acceleration $k_{ih}g$ corresponding to the initial yield

$$k_h^i = \frac{1}{2}\cdot\sqrt{(K_0+1)^2\cdot\sin^2\phi-(K_0-1)^2} \tag{3.50}$$

In the plastic nonlinear range free field stress contribute to increase as the acceleration coefficient increases until a state of general fluidization, horizontal failure plane develops and relative motion occurs at the base of the soil layer. The corresponding maximum lateral pressure coefficient is

$$K = K_{EF} = \frac{1+\sin^2\phi}{\cos^2\phi} \tag{3.51}$$

It is found that independently of the free field deformations (if simply elastic analysis or elasto-plastic analysis), the magnitude of the of the active thrust on the wall is simply determined by the free field stress solution or the M-O equation. Regarding the thrust point of application since the horizontal elastic and plastic deformations have the same distribution with depth, the closed-form elastic horizontal displacement solution can be directly used to determine the distribution of the active seismic pressure even after the soil has yielded.

A closed form solution for the free field uniform acceleration for the case of Coulomb material with cohesion including the effect of surface loading based on kinematic method as represented in Figure 3.31, was developed by Richard and Shi [1994]. Similarly to pseudostatic models transient wave effects are not considered nor is the dynamic densification and volume change.

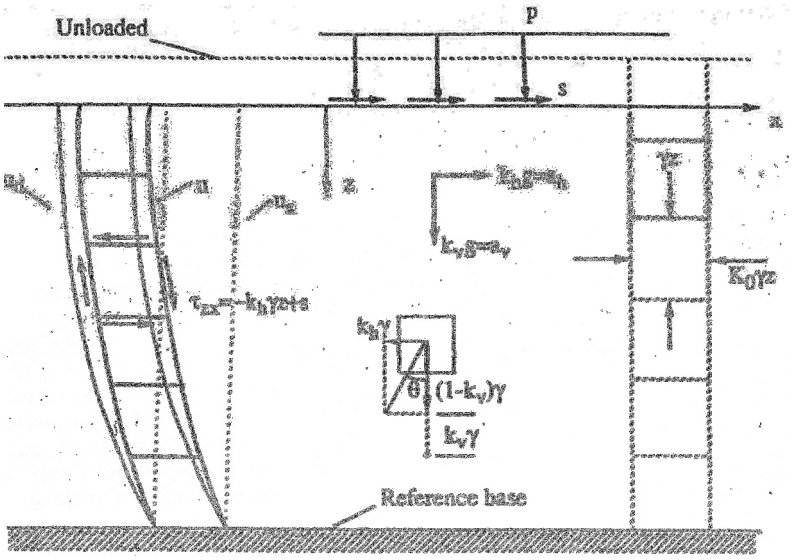

Figure 3.31 Seismic free field (Richard and Shi [1994])

At initial yield, potential slip surfaces form. At higher accelerations, the coefficient of lateral pressure K that in the elastic range is assumed constant and equal to K_0, becomes KE, which now depends on the acceleration ratio, tan $\Theta = k_h/(1- k_v)$. From the Mohr's circle shown in Figure 3.32 , the counterclockwise orientation of the potential slip surface develop at angles ρ_z

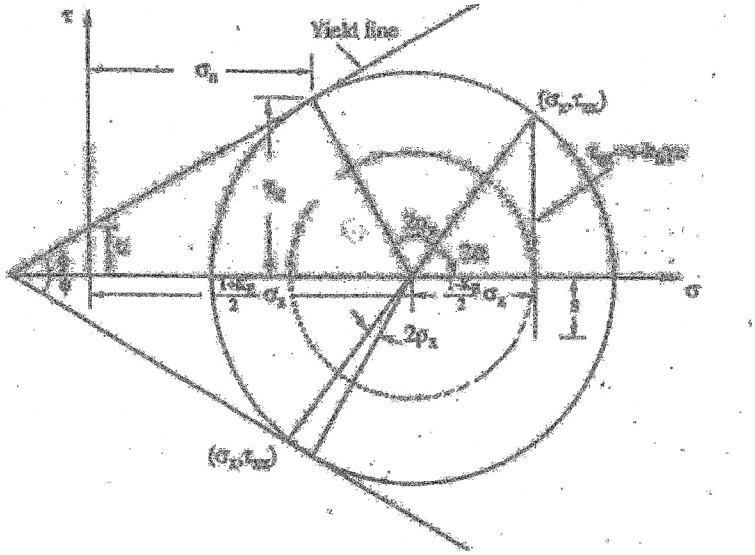

Figure 3.32 Shear stress effect due to *s* and k_h (Richard and Shi [1994])

A closed form solution for the dynamic coefficient of earth pressure for the active and passive state is formulated including cohesion is formulated. Moreover it is observed that while cohesionless soil results are very similar to M-O equation for the active case, in case of passive soil pressure M-O provides much less conservative results unless a soil wall friction angle $\delta=0$ is assumed. For the active case with cohesion, based on the solution for the case of cohesive soil, plots are provided to determine the allowable height of cracked or uncracked (if tension is allowed) height of unbraced cuts. In the case of passive pressure for cohesive soil, since no tension need to occur for passive failure to develop, the solution proposed can be used directly. The disadvantage of this method is that being a kinematic solution is an upper bound of the real solution which does not provide a safe value for the case of passive resistance.

3.3 Full dynamic approach

As already stated, complete dynamic analysis is one of the possible approach for the seismic analysis and design of flexible retaining walls and is based on the integration of the equations of motion considering the seismic excitation. In case of analytical solution such an approach is also usually based on the hypothesys of linear elastic or visco-elastic soil material and perfect wall-soil adhesion. The more general case on numerical approach being more flexible allows for material non linear behaviour both for soil and wall-soil interfaces. In the following section a brief overview of few of the most recent solutions based on fully dynamic approach available in literature will be given.

3.3.1 Analytical Solution for flexible cantilever walls elastically constrained against rotation [Veletsos and Younan, 1997, 2000]

While the M-O method was developed for yielding walls, Wood (1973) developed an equivalent static elastic solution for seismic soil pressure for non-yielding walls. The solution is based on finite element analysis of a soil-wall system for a wall resting on a rigid base and a uniform soil layer behind the wall. In general, Wood's solution amounts to a lateral force that acts about 0.63 times the height of the wall above the base of the wall which corresponds approximately to a parabolic distribution of soil pressure unlike M-O's inverted triangular distribution. Wood's solution predicts seismic soil pressure larger (by a factor of 2 to 3) than the pressure predicted by the M-O method. The elastic solution proposed by Wood has been adopted by ASCE Standards for Nuclear Structures [1986] and has been used in many applications. Wood's solution requires knowledge of the maximum ground acceleration along with the density and Poisson's ratio of the soil to obtain the seismic soil pressure behind the wall.

More recently, Veletsos and Younan [1994a] developed an analytical model to compute seismic soil pressure for rigid vertical walls resting on a rigid base. The proposed model is based on the series of elastically supported semiinfinte horizontal bars with distributed mass to model the soil medium behind the wall. The model was developed for vertically propagating shear waves with the assumption that horizontal variation of vertical displacements in the soil medium is negligible. In this model, contrary to Wood's equivalent static solution, amplification of motion in the soil medium behind the wall is considered. The model highlights the effects of several parameters including the frequency of vibration on the seismic soil pressure magnitude and distribution. Also in this model the wall pressures and associated forces are higher than those determined by Mononobe Okabe approach.

The same authors Veletesos and Younan, [1994b] have shown that for rigid walls if foundation rotational flexibility is considered both the magnitude and distribution of the dynamic wall pressures and forces are quite sensitive to flexibility of the base constraint.

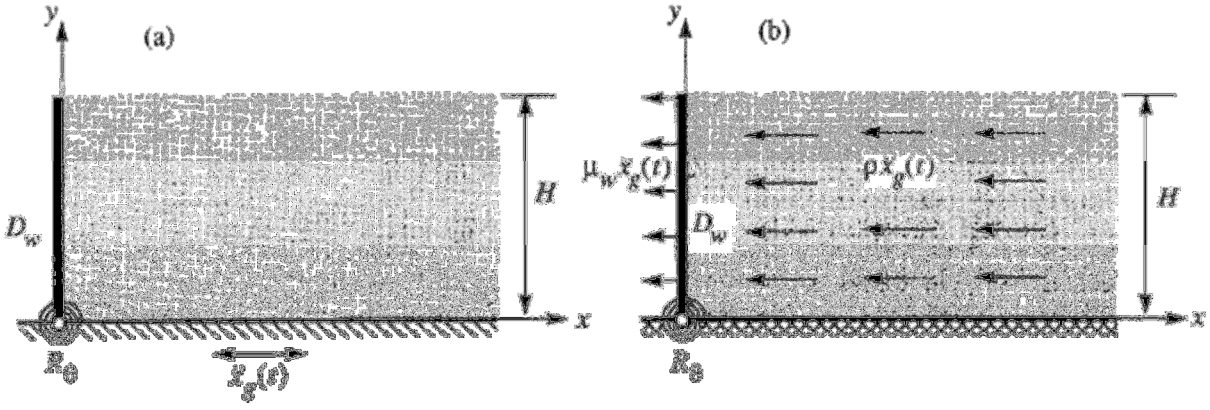

Figure 3. 33 Soil wall system investigated: a) Base-excited system b) Force-excited system [Veletsos and Younan, 1997]

In a subsequent paper by Veletesos and Younan [1997] a critical evaluation of the response for retaining walls both flexible and with elastic rotational constraint at the base is made. The system considered is shown in Figure 3. 33.

It consists of a semi infinite uniform layer of viscoelastic material of height *H* that is free at its upper surface, is bonded to a rigid base and is retained along one of it vertical boundaries by a uniform, flexible cantilever wall that is elastically constrained against rotation at its base. The bases of both the walls and the soil stratum are presumed to experience a space invariant horizontal motion with acceleration $\ddot{x}_g(t)$ with maximum value $\ddot{X}_g$. Material damping for the medium is considered to be of the constant hysteretic type. The properties of the soil stratum are defined by its mass density ρ, shear modulus of elasticity *G*, Poisson's ratio υ and the material damping factor $\delta=2\cdot\beta$ where β is the damping ratio. The properties of the wall are defined by its thickness t_w, mass per unit of surface area μ_w, Young's modulus f elasticity E_w, Poisson's ratio ν_w, and material damping factor $\delta_w=2\cdot\beta_w$, which is considered to be the same for both the wall in flexure and the rotational base constraint. The stiffness of the rotation base constraint is denoted by R_Θ.

Fundamental to the analysis used is the assumption that, under the horizontal excitation considered, no vertical normal stresses σ_y develop anywhere in the medium i.e. $\sigma_y=0$. It is further assumed that there is complete bonding between the wall and the retained medium, and that the horizontal variations of the vertical displacements of the medium are negligible so that the horizontal shearing stresses τ_{xy} can be expressed as $\tau_{xy}=G^*\cdot(\partial u/\partial y)$ where *u* is the horizontal displacement of an arbitrary point of the medium relative to the moving base and $G^*= G\cdot(1+i\cdot\delta)$. The reliability of these assumptions has been confirmed for the limiting case of fixed-base rigid wall by comparing the results obtained and Wood's [1973] "exact" solution.

The instantaneous value of the displacement relative to the moving base of an arbitrary point of the wall $w(\eta,t)$ is expressed as:

$$w(\eta,t)=\eta\cdot H\cdot\theta(t)+\sum_{J=1}^{J}\phi_J(\eta)\cdot q_j(t) \qquad (3.52)$$

Where

η=y/H dimensionless vertical position coordinate

$\Theta(t)$ instantaneous values of base rotation

$\phi_j(\eta)$ *j*th natural mode of vibration of the cantilever beam

$q_j(t)$ generalised coordinate defining the dgree of participation of $\phi_j(\eta)$ at any time

J total number of modes considered

The equation of motion for the system are obtained by repeated application of the Lagrange's equation [Clough and Penzien, 1994]. For the evaluation of the generalised forces, the natural modes of vibration of the cantilever beam $\phi_j(\eta)$ are expressed as linear combinations of the corresponding modes of the retained medium when the latter is considered to act as an unconstrained cantilever shear beam as

$$\phi_J(\eta) = \sum_{n=1}^{N} c_n \cdot \psi_n(\eta) = \sum_{n=1}^{N} c_n \cdot \sin\left[\frac{(2n-1)\cdot\pi}{2}\cdot\eta\right] \tag{3.53}$$

Where

c_n is a dimensionless participation factor defined by appropriate integrals of ϕ_j and ψ_n

n is the order of the shear beam mode under consideration

N is a sufficiently large number

The primary parameters governing the response of the system are the relative flexibility of the wall and the retained medium, defined by the relative flexibility of the wall and the retained medium

$$d_w = \frac{G\cdot H^3}{D_w} \tag{3.54}$$

And the relative flexibility of the rotational base constraint and retained medium, defined by

$$d_\theta = \frac{G\cdot H^2}{R_\theta} \tag{3.55}$$

The symbol D_w represents the flexural rigidity per unit length of the wall

$$D_w = \frac{E_w \cdot t_w^{\,3}}{12\cdot(1-\nu_w^2)} \tag{3.56}$$

Also affecting the response are the characteristics of the base motion. The response of the system is evaluated first for excitations the dominant frequencies of which are extremely small compared to the fundamental frequency of the soil-wall system (i.e. for values $\omega/\omega_1 \rightarrow 0$); such excitations and the resulting effects are referred to as "static". In terms of forces the static excitation is represented by a horizontal body forces of intensity $-\rho \ddot{X}_g$ for the retained medium and of $-\mu_w \ddot{X}_g$ for the wall. An amplification factor is then used to indicate the amplification of the dynamic response with respect to the static case.

A first observation is that increasing the flexibility of the wall or its base reduces the horizontal extensional stiffness of the medium relative to its shearing stiffness, and this reduction increases the proportion of the inertia forces transmitted by horizontal shearing action to the base and decreases the proportion transmitted to the wall. For this reason increasing flexibility factors d_w or d_Θ leads to lower wall pressures. Regarding the distribution of the pressure while for $d_w=0$ and $d_\Theta=0$ the distribution reveals that for the fixed-based and rigid wall the contribution of the fundamental mode of vibration of the soil is dominant

whereas the distribution for flexible walls reveals that vibration of the soil is affected significantly by higher modes.

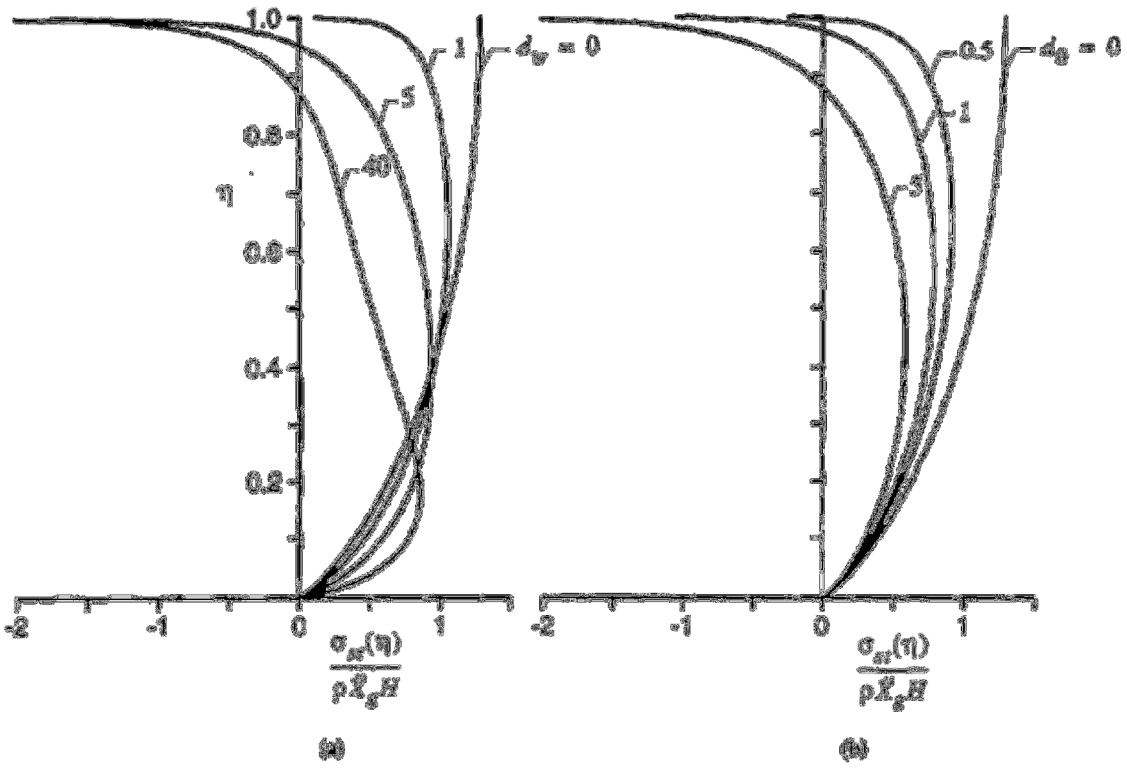

Figure 3.34 Distributions of wall pressure for statically excited systems with different wall and base flexibilities (v = 1/3, μ_w= 0):(a)for d_Θ= 0;(b)for d_w=0) [Veletsos and Younan, 1997, 2000]

For rigid wall on rigid base the base shear is equal to the inertia force acting on a rectangular body of soil of width *0.94H* and height *H* and the base moment is equal to the base shear multiplied *0.6H* (effective height). Increasing wall flexibility decreases strongly also base shear and moments: for d_w=5 and d_Θ=1 the base shear is 53% of that for a fixed base rigid wall and 32% higher than the value calculated with M-O approach. For higher and still realistic flexibility values agreement is even better. The values of effective height are also strongly effected by flexibility (see Figure 3.35) and can be close to M-O value *H*/3 (e.g. for d_w=5 and d_Θ=1) or even lower for larger flexibility as it could be the case of rocking walls. As the M-O approach also the static approach neglects dynamic amplification

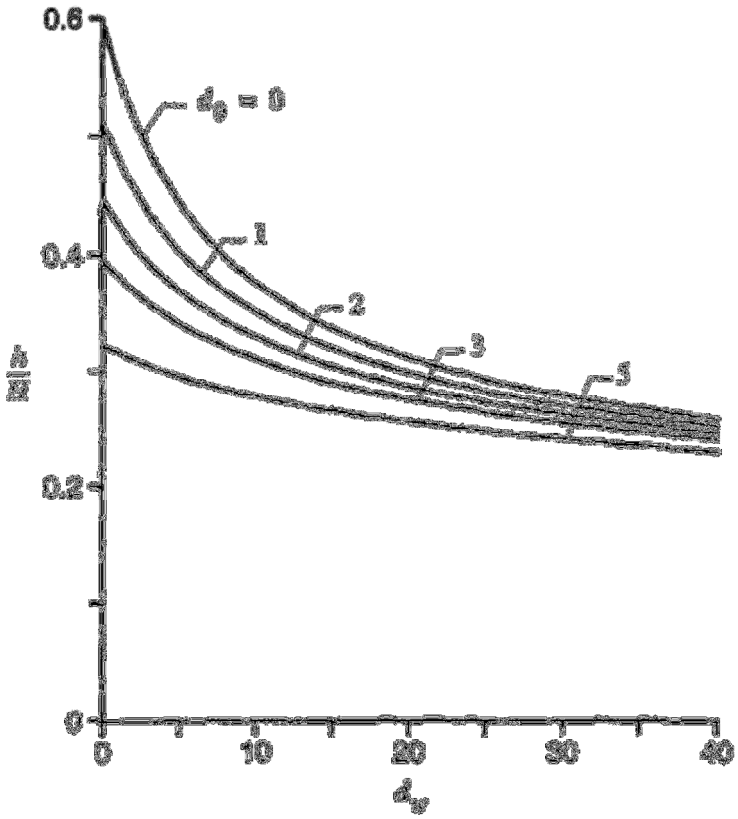

Figure 3.35 Normalised effective heights for statically excited systems with different wall and base flexibilities (v = 1/3, μ_w= 0) [Veletsos and Younan, 1997]

Assessing the response in terms of displacement distribution shows a linear displacement distribution for low value of flexibilities and tending, for increasing flexibility values, to the distribution of a shear beam for both high d_w or d_Θ values. Top displacement for a moderately high value of wall flexibility d_w, tipical concrete wall E_w Young modulus and V_s=150m/s, and H=5m, d_w=0.5m considering a PGA of 0.3g are lower than the threshold values 0.1-0.4% for which development of a failure surface and a limit state occurs. In the case of harmonic excitation the response is controlled by the ratio between the steady state response frequency ω and the natural frequency of the stratum ω_1 when it is considered to act as unconstrained. Amplification of base shear for harmonic response shows the peak or resonant values of the amplification factors occur at exciting frequencies equal to the natural frequencies of the stratum, i.e., for ω/ω_1 = 1, 3, 5 (see Figure 3.36) and a strong dependency on relative flexibility. While for fixed base rigid wall the maximum amplification factor is $1/\sqrt{\delta}$ (equal 3.16 for δ=0.1), for flexible walls that do not reflect and dissipate by radiations well, this factor reaches higher values. At the limit, for infinite relative flexibility the stratum behaves as a cantilever and the ratio tends to $1/\delta$ (equal 10 for δ=0.1). Being the base shear amplification factor more influenced by higher modes than the top displacement amplification

factor, the former amplification ratio will be higher.(see Figure 3.36)For an arbitrary transient excitation, the relevant stratum property is its fundamental cyclic frequency f $=\omega_1/2\pi$, or its corresponding period when it is considered to respond as an unconstrained cantilever shear beam $T = 1/\phi = 2\pi/\omega_1 = 4H/Vs$.

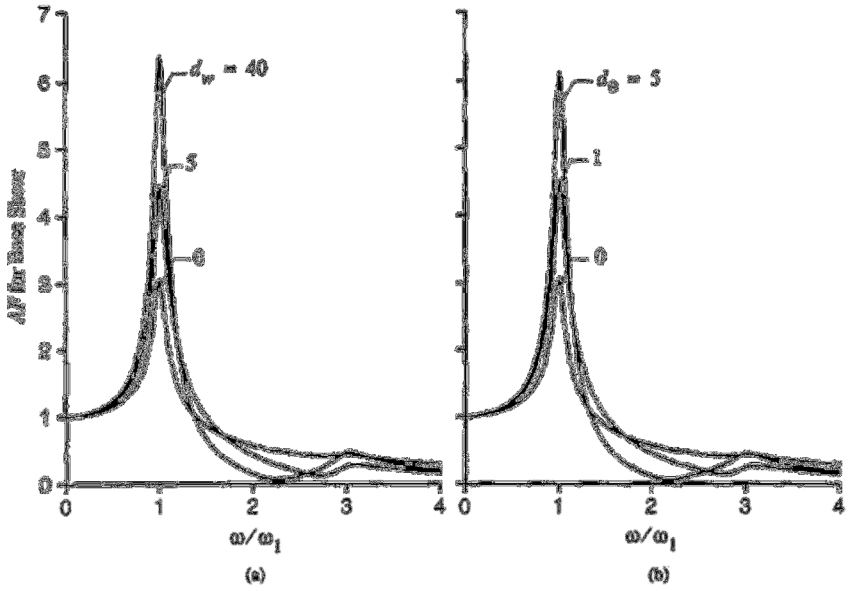

Figure 3.36 Amplification Factors for Base Shear in Wall of Harmonically Excited Systems with Different Wall and Base flexibilities (v = 1/3,δ = 0.1,μ_w=0, and δ_w = 0.04): (a)for d_Θ = 0; (b)for d_w = 0 [Veletsos and Younan, 1997]

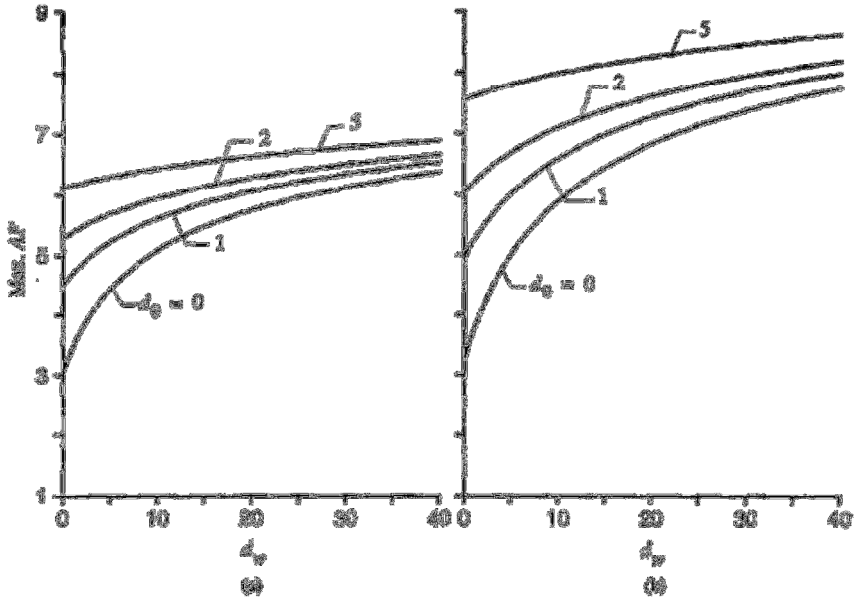

Figure 3. 37 Maximum Amplification Factors for Base Shear and Top Displacement Relative to Base of Harmonically Excited Systems with Different Wall and Base Flexibilities (v = 1/3,δ = 0.1, μ_w = 0, and δ_w = 0.04): (a) Base Shear; (b) Top Relative Displacement [Veletsos and Younan, 1997]

Similarly to the harmonic case it is seen that the higher the flexibility the higher the amplification factor.

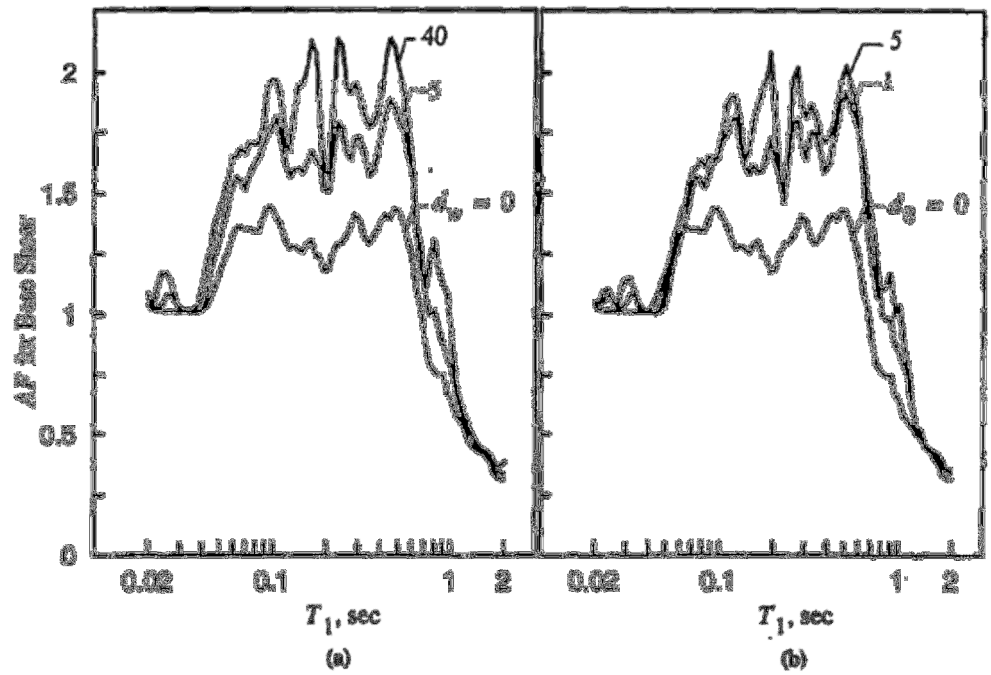

Figure 3. 38 Amplification Factors for Base Shea in Wall of Systems with Diferent Wall and Base Flexibilities Subjected to El Centro Earthquake Record (v = 1/3,δ = 0.1, μ_ω. = 0, and δ_w=0.04): (a) for d_Θ = 0; (b) for d_w, = 0 [Veletsos and Younan, 1997]

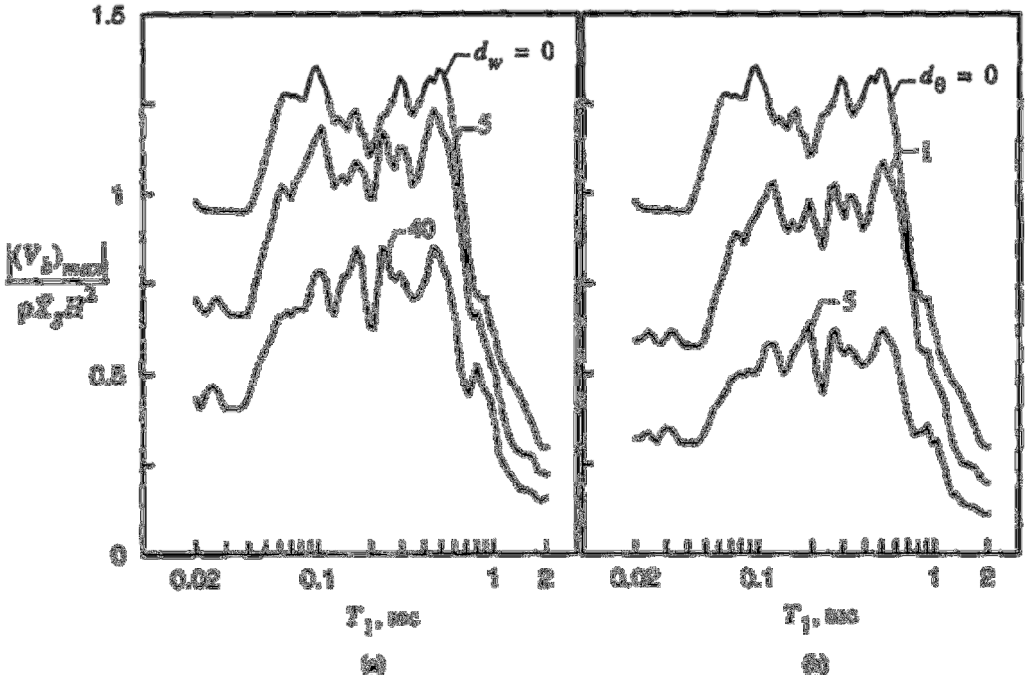

Figure 3. 39 Normalized Values of Maximum Base Shear In Wail of Syst.ms with Different Wail and Base Flexibilities Subjected to El Centro Earthquake Record (v = 113, 8 = 0.1, p.,,. = 0, and 5,, = 0.04): (a) for d, = 0; (b) for d.,. = 0 [Veletsos and Younan, 1997]

Limitations of the solution proposed are that perfect bonding between soil and wall is considered. In reality when tensile pressure induced by soil-wall movement exceeds the gravitational one the soil separates from the wall and wall shear and moment will increase. On the other hand assuming parabolic stiffness distribution in the soil would lead to a decrease in wall pressure and forces.

The most important conclusions are summarised in the followings:

a) wall pressures and associated forces reduce when increasing soil-wall flexibility (base shear may reduce of one half and base moment even more). The reason is that increasing either flexibility reduces the horizontal extensional stiffness of the retained medium relative to its shearing stiffness, and this reduction decreases the proportion of the soil inertia forces that gets transferred to the wall and, hence, the forces developed in it.

b) in "statically" excited systems, excluding dynamic amplification and including flexibility leads to values comparable to those given by M-O method for both wall force values and point of application of pressure.

c) for systems excited by earthquake motion amplification ratio may vary between 1.3 for fixed base to 1.9 for flexible. Point of application of the resultant instead is unchanged from the one found in statically excited system.

d) the effect of soil non-uniformity and soil interface debonding during dynamic loading needs further study

3.3.2 Numerical Solutions for flexible cantilever walls under Earthquake loading

- Solutions by Psarropoulos *et al*., 2005 and Gazetas *et al*.., 2004

The solution by Veletsos and Younan was extended using the finite element method to treat also the cases of inhomogeneity of the retained soil and translational flexibility of the wall foundation. The results show that the inhomogeneity of the soil leads to reduced earth pressures near the top of the wall, especially in the case of very flexible walls, while the compliance of the foundation may not easily be modeled by a single rotational spring (Figure 3. 40), due to wave propagation phenomena. Presuming plane-strain conditions, the numerical analysis was two-dimensional, and was performed using the commercial finite-element package ABAQUS. Soil is presumed to act as a visco-elastic material. As the efficiency of the viscous dashpots depends strongly on the angle of incidence of the impinging wave the dashpots were placed 10H away from the wall to improve the accuracy of the simulation (see Figure 3. 40). The wall pressures predicted by the analytical formulation and the numerical model seem to be in agreement, but the same is not observed for the base shear and the overturning moment, as shown in (Figure 3. 41).

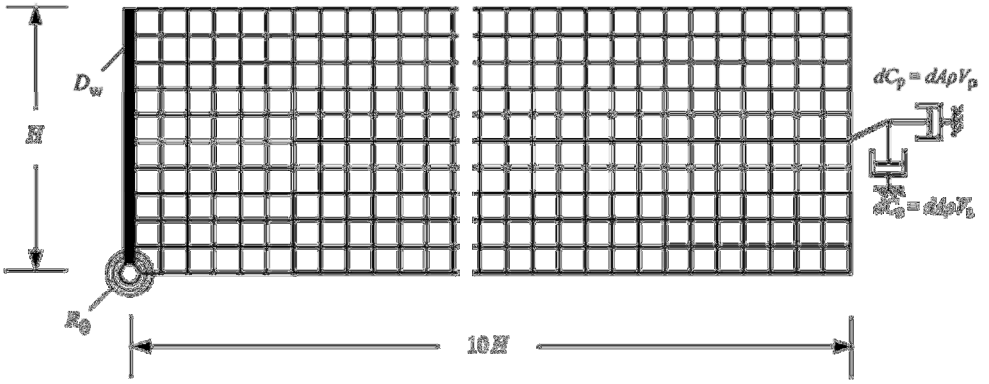

Figure 3. 40 The finite-element discretization of the examined single-layer systems. The base of the model is fixed, while absorbing boundaries have been placed on the right-hand artificial boundary [Psarropoulos *et al*, 2005]

The reason is that in the post-processing of the numerical results, tensile stresses have been regarded as unrealistic, and therefore, ignored leading to an increase in base shear and bending moment. This fact seems quite logical considering the double effect of the tensile stresses: (a) the reduction of the base shear, and (b) the reduction of the corresponding effective heig

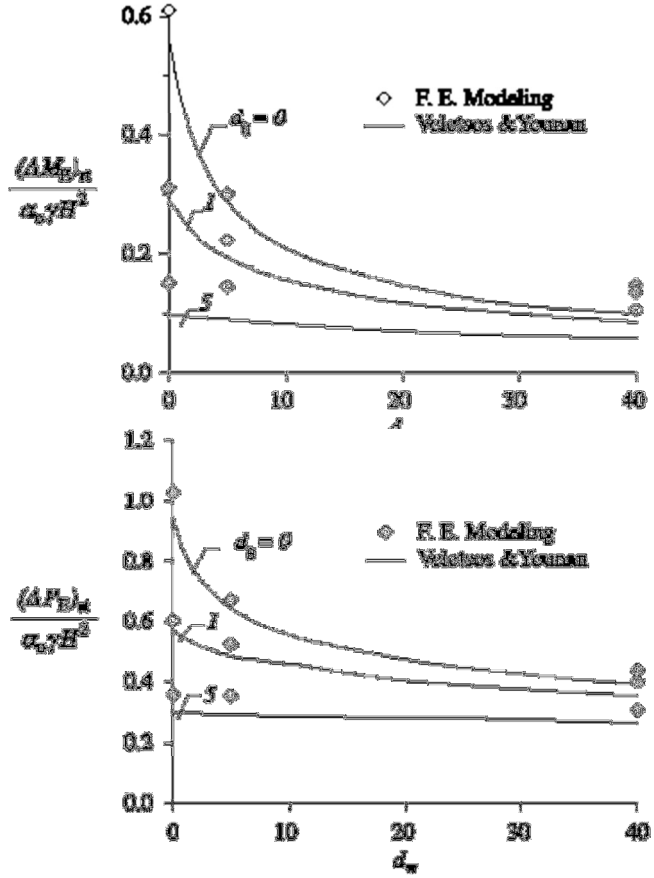

Figure 3. 41 Comparison between the normalized values of base shear $(\Delta P_E)_{St}$ and overturning moment $(\Delta M_E)_{St}$ from the analytical formulation (continuous line) of Veletsos and Younan [1997] and those of the numerical simulation (dots). Quasi-statically excited systems with different wall and base flexibilities (d_w and d_O) [Psarropoulos *et al*, 2005].

In reality soil modulus is likely to increase with depth. Such a unhomogeneity reflects the unavoidably-reduced stiffness under the small confining pressures prevailing near the top and leads to two strong- shaking effects: the softening of the soil due to large shearing deformations, and the non-linear wall—soil interface behavior, including separation and slippage. Even if the second effect is too complicated to incorporate in the analysis it is possible to observe that due to the nullification of shear modulus at the surface the pressures developed near the top converge to the same value for every combination of d_w and d_Θ. Therefore, no tensile stresses are present, making the assumption of complete bonding more realistic. In (Figure 3. 42), a comparison between the homogeneous and the inhomogeneous soil is shown for the case of a rigid fixed-base wall and a very flexible fixed-base wall.

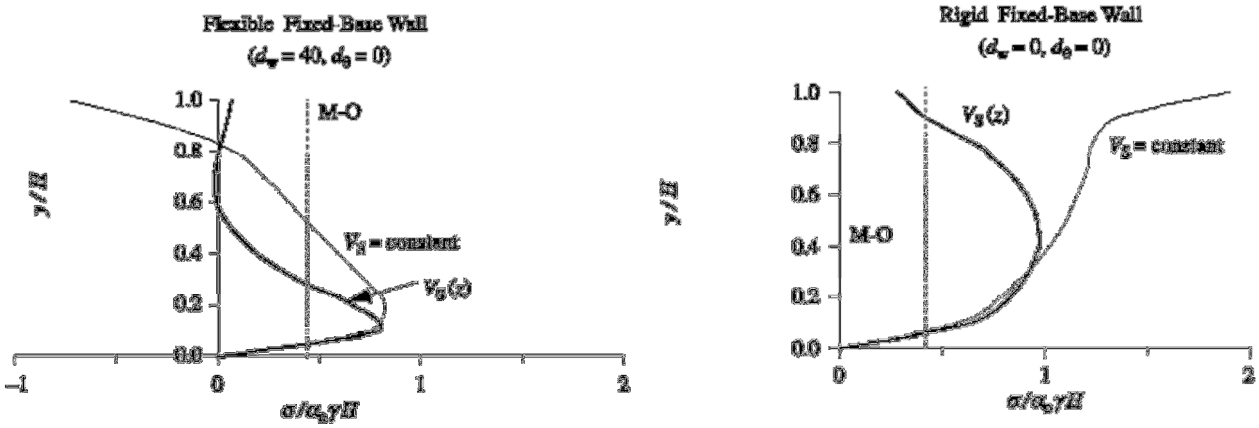

Figure 3. 42 Effect of soil inhomogeneity on the elastic dynamic earth-pressure distribution for a rigid fixed-base wall (d_wZ0, d_qZ0) and for a flexible fixed-base wall (d_wZ40, d_qZ0). Comparison with the corresponding curves for the homogeneous soil from Fig. 4 [Psarropoulos *et al*, 2005].

Regarding the second innovative aspect f this study, that is the way rotational flexibility is modeled, a soil layer of equivalent rotational stiffness was considered such that

$$R_\theta = K_r = \frac{\pi \cdot G_f \cdot B^2}{8 \cdot (1-\upsilon_f)} \cdot \left(1 + \frac{1}{10} \cdot \frac{B}{H_f}\right) \tag{3.57}$$

Valid for a strip footing of width B, resting on a soil layer which has thickness H_f, shear modulus G_f and Poisson's ratio ν_f. Furthermore by this replacement the stiffness of the horizontal translation is taken into account being

$$K_h \approx \frac{2.1 \cdot G_f}{(2-\upsilon_f)} \cdot \left(1 + \frac{B}{H_f}\right) \tag{3.58}$$

For a fixed value of rotational relative flexibility d_Θ two different values of B were considered leading to a lower K_h for the higher B and to lower pressure values. For both quasi static and harmonic loading tension in the upper part of the wall was found for higher d_Θ values. The dynamic effects for the case of harmonic excitation at resonance amplify these effects even more clearly (Figure 3. 43).

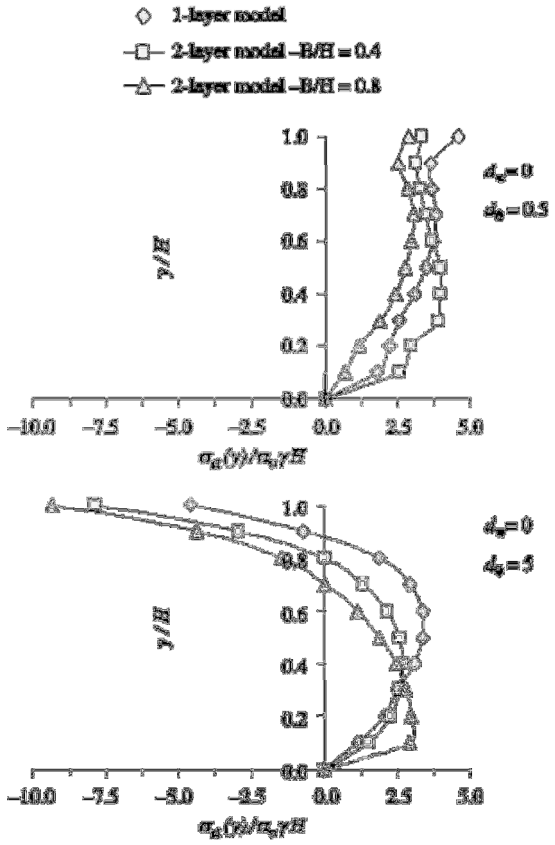

Figure 3. 43. Distribution of the wall pressures in the case of resonance ($\omega=\omega_1$): (a) d_O=0.5 (b) d_O=5 [Psarropoulos *et al*, 2005]

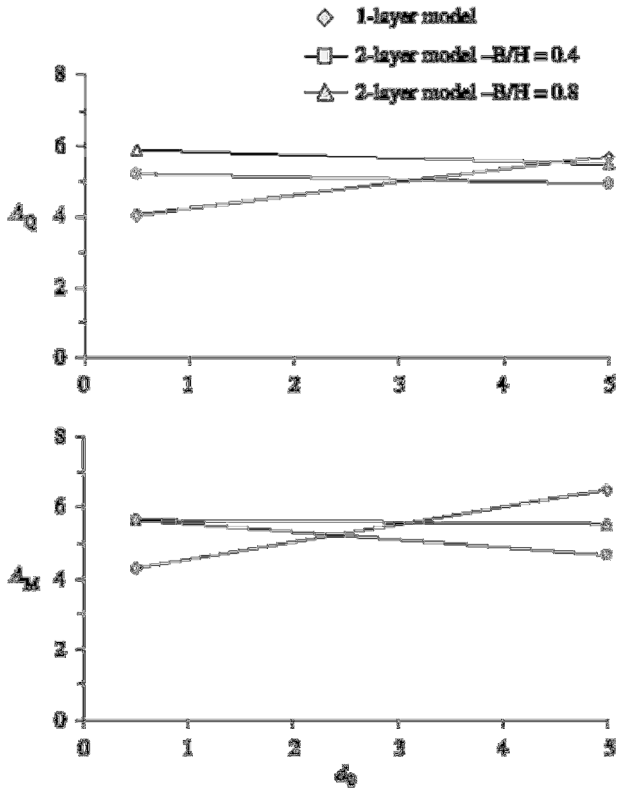

Figure 3. 44 Maximum dynamic amplification factors A_Q and A_M for the resultant overturning moment, respectively, in the case of resonance ($\omega=\omega_1$) [Psarropoulos *et al*, 2005]

Moreover for increasing d_Θ amplification ratio for base shear and overturning moments were not found increasing (Figure 3. 44), this is different from the analytical model in which rotational flexibility was modeled by a spring and damping and wave propagation effects due to impedance contrast could not be accounted for. Also in an extension of the analytical model of Veletsos and Younan proposed by Li [1999] the same results were found.

- Solutions by Madabhushi and Zeng, [2006, 2007]

In the context of fully dynamic approach it is worthwhile to mention the numerical solutions recently proposed by Madabhushiand Zeng for the cases of cantilever retaining wall and comparison with experimental results from the Cambridge Geotechnical Centrifuge Centre for both dry [Madabhushiand Zeng, 2006] and saturated [Madabhushiand Zeng, 2007] sand soil. The finite element code used was SWANDYNE developed by Chan [1988] and for the dry soil case a modified elasto plastic Mohr-Coulomb model while for the saturated case the P-Z Mark III bounding surface model [Pastor *et al*, 1985] was used. A schematic diagram showing the FE discretization zones is shown in Figure 3. 45.

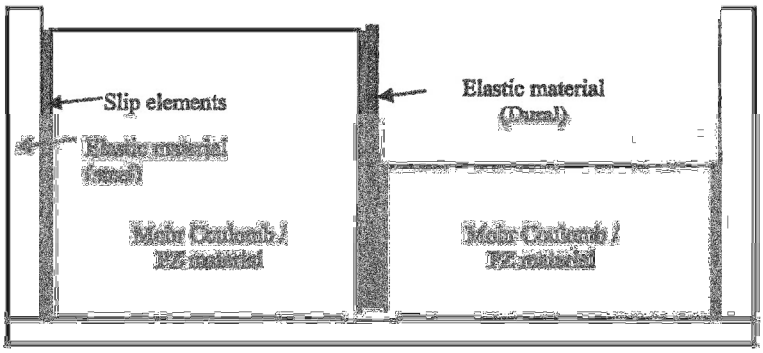

Figure 3. 45 Schematic diagram showing the FE discretization zones [Madabhushi and Zeng, 2007]

The experimental results of bending moment at 80g of vertical acceleration prior to earthquake are contained in Figure 3.46 and show a very good distribution of bending moments on the wall. For the case of saturated soil and dry soil, the peak dynamic bending moment distributions on the wall recorded during the three earthquakes together wilth the results of numerical simulation are shown in respectively in Figure 3.47 a) and b).

For the saturated case the three earthquakes had peak acceleration (expressed as a percentage of centrifugal acceleration) equal to 10% (EQ1) 17% (EQ1) and 30% (EQ3) respectively. It is clear that numerical simulation matched fearly well, with the difference in maximum bending moment between the two between 10% of each other. This overprediction of numerical simulation semmed to increase with increasing peak acceleration .

For the case of dry soil model, results of the numerical simulation the three earthquakes had peak acceleration (expressed as a percentage of centrifugal acceleration) equal to 12% (EQ1) 22% (EQ1) and 23% (EQ3) respectively and also in this case the matching is good even if a simplified model was used however as in the static case the maximum bending moment

occurred at locations slightly lower in the numerical simulation than that recorded in the centrifuge test.

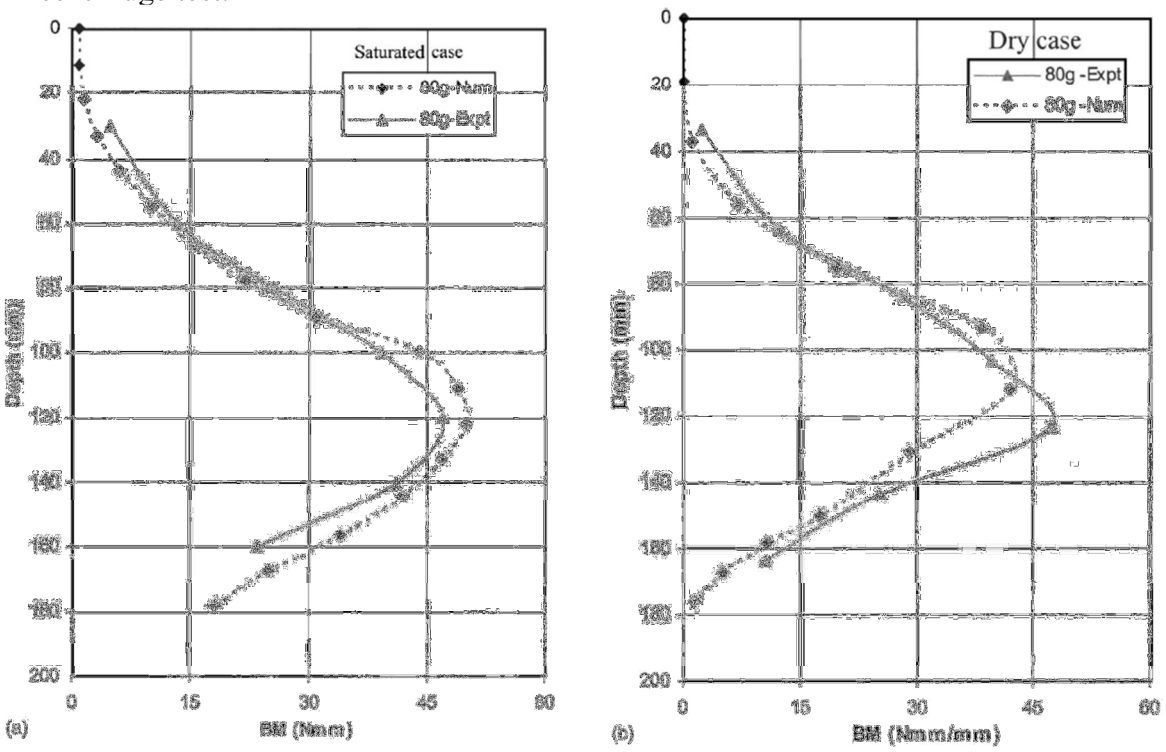

Figure 3.46 Variation of bending moment at 80g in a) saturated case and b) dry case [Madabhushi and Zeng, 2007]

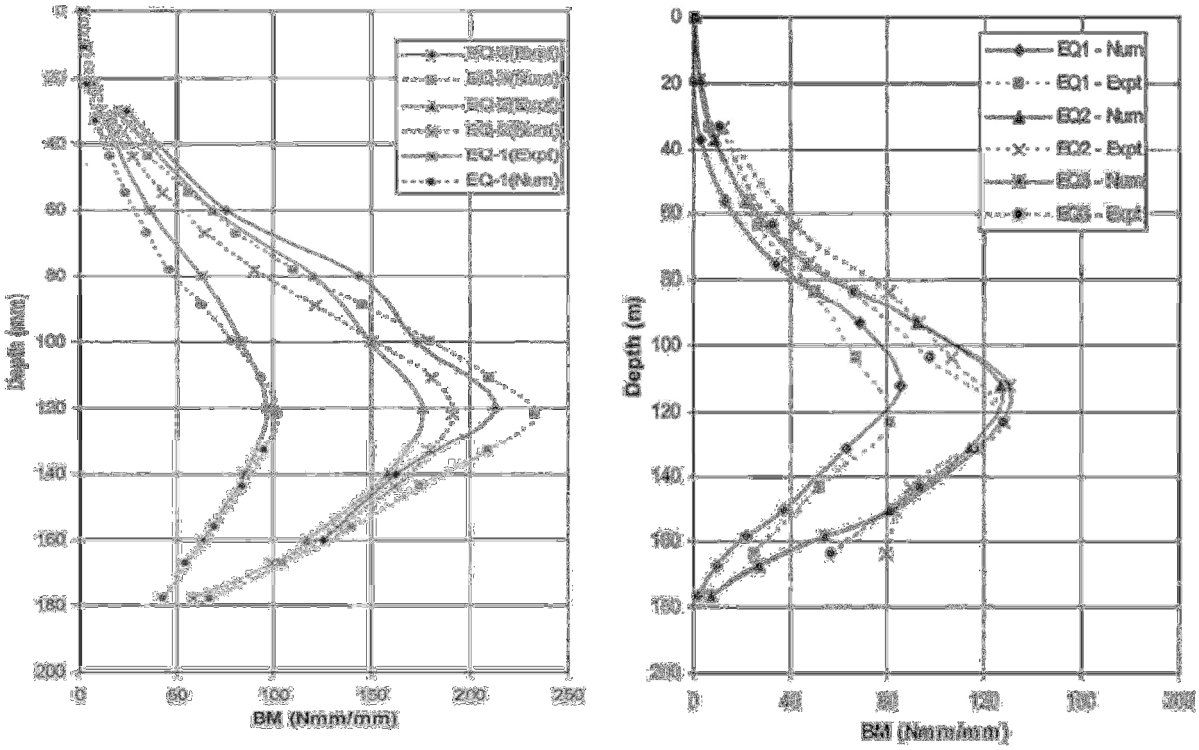

Figure 3.47 Bending moment distribution along the wall for the saturated (a) and unsaturated (b) case during three earthquakes [Madabhushi and Zeng, 2007]

Comparing for the dry case and for the case (EQ2) having 0.22g PGA the peak dynamic bending moment on the cantilever wall with the static bending moment, an increase of 180% is seen. For the saturated case and for the case (EQ2) having 0.17g PGA the same comparison shows an increase of 240%. This observation shows that the effect of an earthquake is more severe on a cantilever retaining with saturated backfill than that with dry backfill.

Also deformations were much larger in the saturated case than in the dry case. For the case of (EQ3) with PGA of 0.3g considerable settlements ranging from 30cm (4mm at model scale) to 1m near the wall (11.5mm at model scale) were found within an area of 12 m (15 cm at model scale) beside the backfill. A sketch of the settlement profile and top wall deformation is shown in Figure 3. 48.

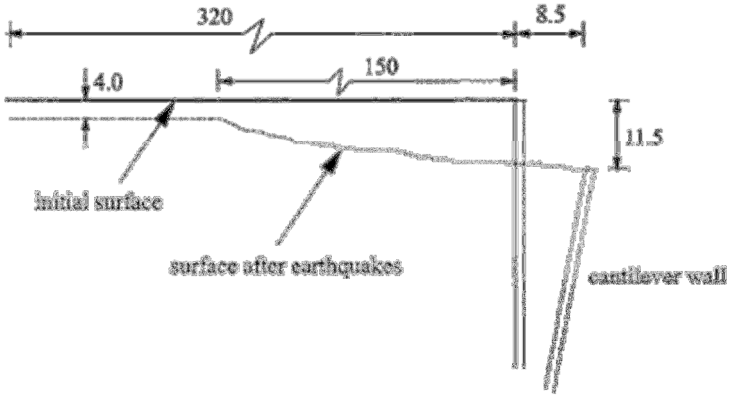

Figure 3. 48 Profile of the centrifuge model XZ3 for (EQ3) at 0.3g PGA before and after earthquake [Madabhushi and Zeng, 2007].

3.4 Conclusions.

In this Chapter it was outlined that also under static conditions [Rowe, 1957], soil-structure interaction for flexible retaining structures is complex and further complexity is added for the seismic case [Faccioli, 1996]. For this reason some degree of idealization and approximation is required in the solution and for this reason methods considered in this chapter were grouped based on the type of modelling assumption they are based on. In order to highlight the limiting assumptions of each type of approach, a schematic summary of the main requirements either satisfied (S) or not satisfied (NS) by each of the proposed approaches for seismic analysis and design of earth retaining structures is shown in Table 3.4.

On the base of such considerations the choice of the solution approach can be related to the fact if forces or displacements or both are of primary concern and the balance between degree of precision required and simplicity of application.

Pseudo-static approaches and pseudo-dynamic approaches based on subgrade reaction methods based on forces maybe preferred for a simplified analysis of yielding walls in terms of forces. That could be the case of ultimate limit design. On the other hand pseudo-dynamic methods based on rigid block assumption maybe preferred for a simplified displacement analysis of yielding walls as in the case of serviceability limit state design.

It is important to notice that for the passive resistance pseudostatic methods based on limit analysis should be preferred as they provide a lower bound to the solution and therefore are a safe estimate. For active case on the other hand, solutions based on kinematic approach maybe preferred.

For more comprehensive results including both displacements and forces a fully dynamic approach maybe required. Independently on the type of method this approach presents the additional task of choosing an adequate set of input accelerograms based on the selection criteria which will be outlined in Chapter 6.

If simplified assumptions regarding wall-soil interfaces and linear material behaviour are met then closed form solutions are to be preferred for their simplicity and reliability, on the contrary, a numerical approach is preferred.

Finally it should be said that fully dynamic numerical approach for non linear problems presents the disadvantage of being very time consuming and requiring an experienced user. Many issues relating this aspect are described in detail in the following Chapter.

Table 3.4 Basic solution requirements satisfied (S) or not satisfied (NS) by the various methods of analysis [Pott and Zdravkovic, 1999]

Method of analysis		Solution requirements				
		Equilibrium	Compatibility	Constitutive behavior	Boundary conditions	
					Force	Disp
Limit Equilibrium		S	S	Rigid with a failure criterion	S	NS
Limit Analysis	Lower bound	S	NS	Ideal plasticity with associated flow rule	S	NS
	Upper bound	NS	S		NS	S
Beam-spring approaches		S	S	Soil modelled by springs or elastic interaction factors	S	S
Full numerical analysis		S	S	Any	S	S

4 NUMERICAL MODELLING ISSUES.

This Chapter introduces the numerical codes used in the analysis (DYNAFLOW and FLAC), giving an overview of some general topics and techniques such as Finite Elements and Finite Difference methods.

At the same time this Chapter describes several topics related to numerical modelling for earthquake geotechnical engineering and for the specific topic of seismic analysis of flexible retaining structures and explains how such topics are dealt with in each one of the numerical codes used.

These points are summarized as follow:

a) Discretization method: Finite Element Method and Finite Difference Method.

b) Non linear Hysteretic Soil Behavior

c) Radiation of dynamic energy, element size and choice of control point

d) Soil-wall interaction and possible separation

e) Possibility of Liquefaction in saturated Soil

4.1 Discretization methods: Finite Element and Finite Difference Method.

The analysis process by computer methods can be characterized by the stages diagrammed in Figure 4.1. The stages are: idealization, discretization and solution. These steps allow to pass from the physical system to the mathematical model, from the mathematical to the discrete model and from the discrete model to the discrete solution.

A classification of computational solid mechanics (CSM) maybe done on the base of the discretization methods distinguishing among Finite Element (FEM), Boundary Element (BEM), Finite Difference (FDM), Spectral elements and Meshfree. In this study only FEM and FDM will be considered.

The mathematical model can be formulated in three forms:

Strong form (SF): when a system of *ordinary or partial differential equations* in space and/or time, complemented by appropriate boundary conditions. Occasionally this form may be presented in integraodifferentialform, or reduce to algebraic equations

Weak Form (WF): presented as a *weighted integral equation* that "relaxes" the strong form into a domain-averaging statement. These are integral equations, obtained by premoltiplication by weighting functions and by integration over the domain of both the balance equation (BE) -as in elasticity are the stress equilibrium equations- and of the flux boundary conditions (FBC) such as in elasticity are the force boundary conditions. The solution which minimize the residuals can be found by several techniques namely Galerking method (the most used in finite elements applications), least square method, collocation method or subdomain method [Bathe, 1982].

Variational Form (VF). presented as a *functional* whose stationary conditions generate the weak and strong forms. Moreover if and only if u^* is the solution for the independent (*master*) variable, for any small variation δu around u^* the functional must be equal to zero. An example of such functional is the total potential energy for the case of elasticity problem but more recent such as Hellinger Reissner or the Hu–Washizu are well known. Since functionals are scalars, and scalars are invariant with respect to coordinate transformations, the VF provides automatically for transformations between different coordinate frames. VFs, and to less extent WFs, directly characterizes "overall" quantities of interest to scientists and engineers such as mass, momentum ,energy and VFs clarify and systematize the treatment of boundary and interface conditions.

The essence of all approximation methods is *discretization*. Continuum mathematical models stated in SF, WF or VF have an infinite number of degrees of freedom. Through a discretization method this is reduced to a finite number, yielding *algebraic* equations than can be solved in a reasonable time. Each form: SF, WF and VF have a *natural* class of discretization methods than can be constructed from it.

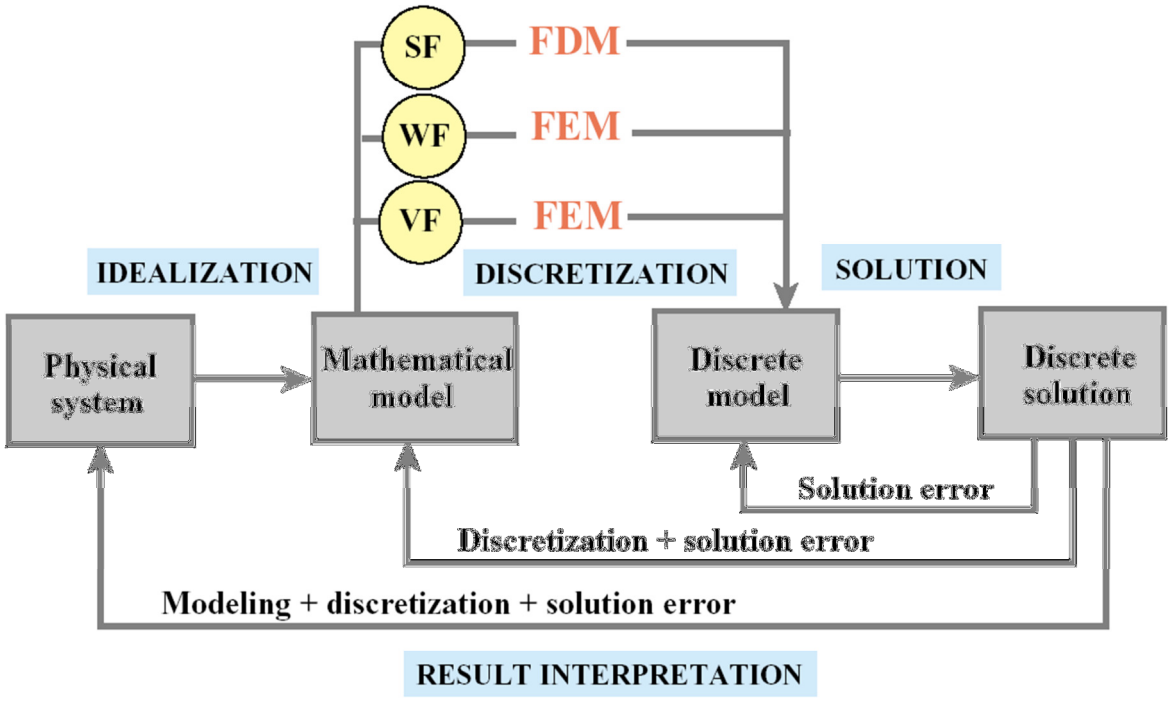

Figure 4.1 The main stages of computer-based simulation: idealization, discretization and solution [notes from Advanced Finite Element course of Prof. Carlos Felippa at University of Colorado Boulder]

Finite difference method:

The natural discretization class for SFs is the *finite difference method* (FDM). These are constructed by replacing derivatives by differences. This class is easy to generate and program for regular domains and boundary conditions, but runs into difficulties when geometry or boundary conditions become arbitrary. The other problem with conventional FDM is that the approximate solution is only obtained at the grid points, and extension to other points is not always obvious or even possible. Nevertheless the FDM class is theoretically *general* in that any problem stated in WF or VF can be put into SF.

Finite element method:

The natural discretization class for WFs is the *weighted residual method* (WRM). There are well known WRM subclasses: Galerkin, Petrov-Galerkin, collocation, subdomain, finite-volume, leasts quares. Sometimes these subclasses, excluding collocation, are collectively called *trial function methods*, an alternative name that accurately reflects the discretization technique. Unlike the FDM, trial-function methods yield approximate solutions defined *everywhere*. Before computers such analytical solutions were obtained by hand, a restriction that limited considerably the scope and accuracy of the approximations. That barrier was overcome with the development of the Finite Element Method (FEM) on high speed computers.

The natural discretization class for VFs is the *Rayleigh-Ritz method* (RRM). Although historically this was the first trial-function method, it is in fact a special subclass of the Galerkin weighted residual method. The Finite Element Method was originally developed along these lines, and remains the most powerful computer based RRM.

Note that FEM, like FDM, can be viewed as a *universal* approximation method, because any problem can be placed in WF. This statement is no longer true, however, if one restricts FEM to the subclass of Rayleigh-Ritz method, which relies on the VF.

4.1.1 DYNAFLOW

The following is a brief overview of DYNAFLOW capabilities and is largely based on information provided in the DYNAFLOW manuals [Prévost, 2006]. The reader is referred to these manuals for additional details.

DYNAFLOW is a finite element analysis program for the static and transient response of linear and nonlinear two- and three-dimensional systems. In particular, it offers transient (time dependent) analysis capabilities for both parabolic -open time domain- boundary value problems such as conduction or consolidation and hyperbolic –closed domain solution - boundary initial value problems in solid, structural and fluid mechanics.

Regarding solution schemes in both static and transient (dynamic) analyses, an implicit-and explicit (see 4.1.2) predictor-corrector scheme is used. The nonlinear implicit solution algorithms available include several approaches: Newton-Raphson method in which a tangent stiffness matrix is used at each iteration, a modified Newton in which the stiffness matrix is kept constant during the iteration and quasi-Newton iterations (which reduces to secant stiffness in one dimensional case).

Features include multi-field/physics analysis capabilities via selective specification of multiple solution staggers, multi-staggered solution analysis options. The term *staggered solution* procedure maybe intuitive explained as a zig zag two way iterative process occurring between two fields due to the alternation between *prediction* and *substitution* process. [Felippa and Park, 1980].

In order to speed up calculation for large size models DYNAFLOW includes vectorized coding designed to fully exploit the architecture of parallel machines. Moreover it is possible to carry out coupled field analysis for treatment of saturated porous media and multi-phase flows. Arbitrary Euler-Lagrange description options (see 4.1.2) for fluid and/or fluid-structure(-soil) interaction problems are available.

Generalized boundary conditions for convective, radiative analysis for heat transfer analysis as well as prescribed nodal and/or surface forces options, prescribed nodal displacement, velocity or acceleration options and arbitrary load-time functions are available.

Regarding earthquake engineering DYNAFLOW has earthquake acceleration time history generation capability, for generating earthquake motions compatible with prescribed acceleration response spectra. As explained later consistent free-field motion can be obtained by running simple one dimensional analysis and local wave transmitting boundaries are available to avoid un wanted wave reflection.

In order to calibrate numerical model to soil test results, tools are available for simulation of constitutive experiments along prescribed stress and/or strain paths on selected material elements within the finite element mesh.

Regarding pre processing in order to make model generation easier data generation schemes (Cartesian, Cylindrical/Polar and Spherical) are included and a fully integrated interface with the graphical pre- and post-processing program FEMGVis available. Data blocks can be processed by means of corresponding macro commands to speed up model generation and post processing.

The element library contains a one-dimensional, two-dimensional (

Figure 4. 2), and three-dimensional continuum element with axisymmetric options. An interface element with Coulomb friction, a contact element, a slide-line element with either perfect friction or frictionless conditions, a slide-line element with Coulomb friction, a truss element, a beam element, a plate/shell element, a membrane element and a link element are also available for two- and three-dimensional analysis.

The elements used in the analysis of this work were 4 node quadrilaterals for solid equation

$$\Delta\cdot\sigma+\rho\cdot\mathbf{b}=\rho\cdot\mathbf{a} \qquad (4.1)$$

b: body force; **a**: solid acceleration

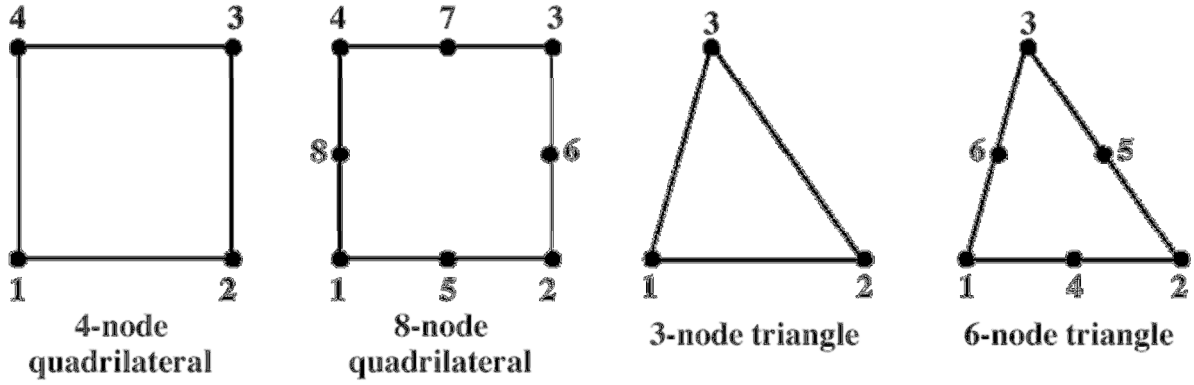

Figure 4. 2 2D continuum elements [DYNAFLOW user manual, 2006]

Mean dilatational formulation was selected. This formulation is useful for eliminating element locking which occurs when modelling nearly incompressible materials. The standard displacement interpolation functions are used, but the strain-displacement matrix is split into dilatational and deviatoric parts. The dilatational part is replaced with the mean dilatational strain-displacement matrix for the element. This technique is called the strain projection or B technique [Hughes, 1987]. A single value for the mean stress or pressure is obtained across the whole element.
The material library of DYNAFLOW contains the following models:

- Linear/ non linear isotropic/orthotropic elastic model;
- Nonlinear hyperelastic model;
- A nonlinear Von Mises viscoelastic model;
- A diffusive transport model;
- Linear/nonlinear thermal, heat conduction and piezoelectric models;
- A Newtonian fluid model;
- Elasto(-visco)-plastic model of type Von Mises, Drucker-Prager, Mohr-Coulomb (Matsuoka's);
- An elasto-plastic Cap model;
- A multi-mechanism (Ishihara's) elasto-plastic model;
- A family of multi-yield elasto(-visco)-plastic models.

4.1.2 FLAC

The following is a brief overview of FLAC and is largely based on information provided in the FLAC manuals (Itasca Consulting Group, Inc., 2000). The reader is referred to these manuals for additional details.

FLAC is a commercially available, twodimensional, explicit finite difference program, which was written primarily for geotechnical engineering applications. The basic formulation of FLAC is planestrain,. FLAC 3D version is commercialized separately as a different package.

As already mentioned in 4.1 Finite Difference is the natural discretization method for SF and it is based on replacing differential equations in with finite differences in time domain. In fact being a SF no weighted integral equation is taken and no global matrices are formed.

The general explicit time marching calculation sequence embodied in *FLAC* is illustrated in Figure 4. 3. This procedure first invokes the equations of motion to derive new velocities and displacements from stresses and forces. Then, strain rates are derived from velocities, and new stresses from strain rates.

One timestep is taken for every cycle around the loop. Each box in Figure 4. 3 updates all of its grid variables from *known* values that remain fixed (implicit solution) while control is within the box. For example, the lower box takes the set of velocities already calculated and, for each element, computes new stresses. The velocities are assumed to be *frozen* for the operation of the box—i.e., the newly calculated stresses do not affect the velocities.

This may seem unreasonable because if a stress changes somewhere, it will influence its neighbors and change their velocities. However, we choose a timestep so small that information cannot physically pass from one element to another in that interval. (All materials have some maximum speed at which information can propagate.) Since one loop of the cycle occupies one timestep, our assumption of "frozen" velocities is justified—neighboring elements really cannot affect one another during the period of calculation.

Of course, after several cycles of the loop, disturbances can propagate across several elements, just as they would propagate physically.

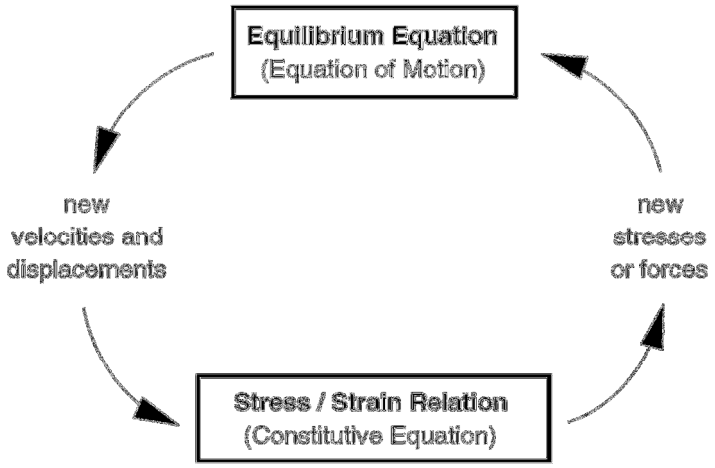

Figure 4. 3 Basic explicit calculation cycle [FLAC 5.0 user manual, 2005]

Explicit solution scheme does not require iterative return algorithm for integration of non linear problems. Considering that such algorithms are also material dependent, it is possible to remark that implementation and good convergence for such non linear material models is easier to achieve.

On the other hand being implicit integration conditionally stable, a small time step is required which leads to longer calculation times.

Generally speaking explicit solution schemes maybe superior only for strongly non linear, very large strain and physical instabilities type of problems.

Regarding the term Lagrangian it can be said that in this formulation as opposed to Eulerian formulation, incremental displacements are added to the coordinates so that the grid moves and deforms with the material it represents.

Either stress or displacement may be applied at the boundary of a solid body in *FLAC*. Displacements are specified in terms of prescribed velocities at given gridpoints. At a stress boundary, forces are derived considering the force perpendicular to the boundary segment and adding it into the force sum of the appropriate grid point.

Dynamic analyses can be performed with FLAC using the optional dynamic calculation module, wherein user-specified acceleration, velocity, or stress time histories can be input as an exterior boundary condition or as an interior excitation. FLAC allows energy-absorbing boundary conditions to be specified, which limits the numerical reflection of seismic waves at the model perimeter.

In principle FLAC does not require any additional pre-post processing tool as it includes a built in *menu-driven* tool for curves and contours plottings. The command-driven structure allows to develop pre- and post-processing programs to manipulate *FLAC* input/output as desired.

In FLAC the solid body is divided by the user into a finite difference mesh composed of quadrilateral elements. Internally, FLAC subdivides each element into two overlaid sets of constant-strain triangular elements, as shown in

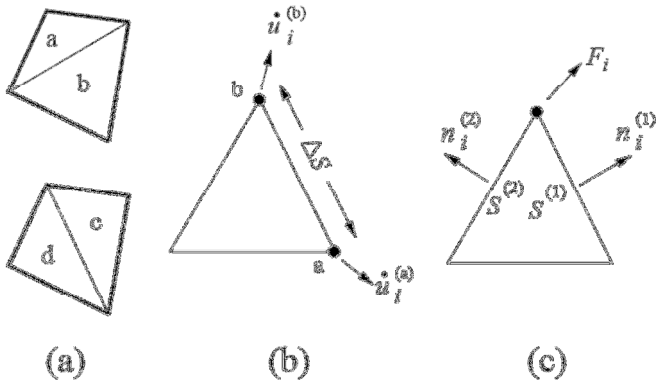

: a) Overlaid quadrilateral elements used in FLAC; b) Typical triangular elements with velocity vectors; c) Nodal force vector [FLAC 5.0 user manual, 2005]

All constitutive models are intended mainly for use in quasi static loading or dynamic situations where the response is mainly monotonic (e.g. extensive plastic flow caused by seismic excitation). The ten FLAC constitutive models are listed in the following:

- Null model;
- Elastic transversely isotropic model;
- Drucker Parger model;
- Mohr Coulomb model;
- Hook and Brown Model;
- Modified Cam Clay model;
- Ubiquitous-joint model, strain hardening/softening model, bilinear strainhardening/softeing model ubiquitous-joint model, double yield model.

The null model is commonly used in simulating excavations or construction, where the finite difference zones are assigned no mechanical properties for a portion of the analysis.

4.1.3 Opensees

OpenSees is a unique finite element tool for earthquake engineering researchers in that it uses an object-oriented, open source code including advanced constitutive models and elements formulation for both geotechnical and structural elements and including parallel multiprocessor applications. Users have the option of participating in the development process, allowing them to adapt the program to meet their modeling needs. As a result, OpenSees is undergoing continuous improvement, adaptation, and debugging from numerous sources. The programming language used is the class based, object oriented language C++.

The overall OpenSees structure consists of four fundamental components Figure 4. 4. The role of the *domain* object is fairly simple, yet critical. It stores objects created by the *model builder* and allows access to the *recorder* and *analysis* objects. The *domain* is the home from which the simulation is executed. The components of the remaining three objects are somewhat more complex and will be described below.

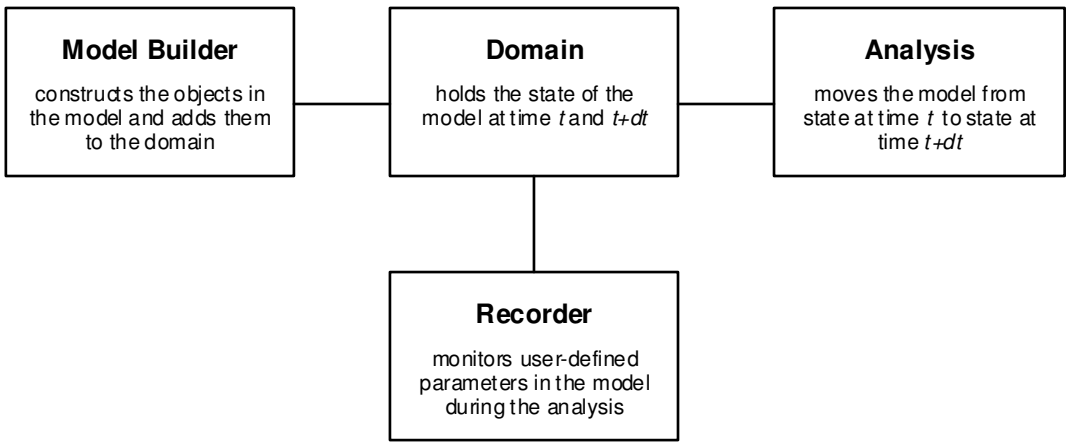

Figure 4. 4: Basic framework of OpenSees (OpenSees and NEESgrid Component User Workshop, 2008).

4.1.3.1 The model builder object

Construction of the model builder object begins by defining the number of dimensions and number of degrees of freedom (which may or may not coincide). This research uses mainly two-dimensional models with two translational degrees of freedom for each nodal point.

Definition of the various analysis materials is the next step. The OpenSees material library consists of uniaxial materials, useful for the modeling of elements ranging from a one-dimensional spring and damper system to concrete or steel structural members. It also includes multi-dimensional materials, which are better suited to the modeling of soils. This study used the PressureDependMultiYield (PDMY) material described in Chapter 2, which allowed modeling of pressure-sensitive soils, and the FluidSolidPorous material material, which was coupled with the PDMY soil to simulate saturated, undrained conditions. FluidSolidPorous material requires definition of the corresponding solid material and the fluid bulk modulus. An excerpt of the OpenSees TCL (the script programming language used for OpenSees) programming script is included to show the definition of the model builder object and of the PDMY and fluid materials (Figure 4.5). For each parameter, a variable is defined using TCL commands. Examination of the PDMY parameters is the basis of the model calibration, and these parameters are described later in this chapter.

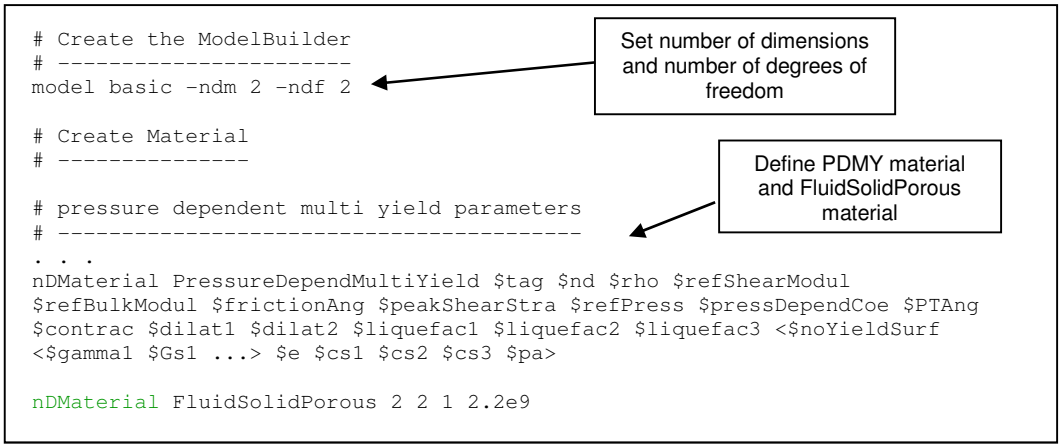


```
# Create the ModelBuilder
# -----------------------
model basic -ndm 2 -ndf 2

# Create Material
# ---------------

# pressure dependent multi yield parameters
# -----------------------------------------
. . .
nDMaterial PressureDependMultiYield $tag $nd $rho $refShearModul
$refBulkModul $frictionAng $peakShearStra $refPress $pressDependCoe $PTAng
$contrac $dilat1 $dilat2 $liquefac1 $liquefac2 $liquefac3 <$noYieldSurf
<$gamma1 $Gs1 ...> $e $cs1 $cs2 $cs3 $pa>

nDMaterial FluidSolidPorous 2 2 1 2.2e9
```

Figure 4.5: Construction of the model builder object and definition of materials in Open Sees.

Once the desired materials have been selected, the finite element mesh is constructed. Nodes can be defined as fixed or free in any dimension or can be made slaves to other nodes (i.e. constrained to have equal displacement) in one or all dimensions. This study used quad elements (four-node quadrilateral elements) for both the single element, free field analyses and retaining structures analyses. The quad element requires definition of node boundary conditions, material type (selected from the materials already defined), the node coordinates, and the body forces (gravitational acceleration for this case) acting on the element (Figure 4.6).

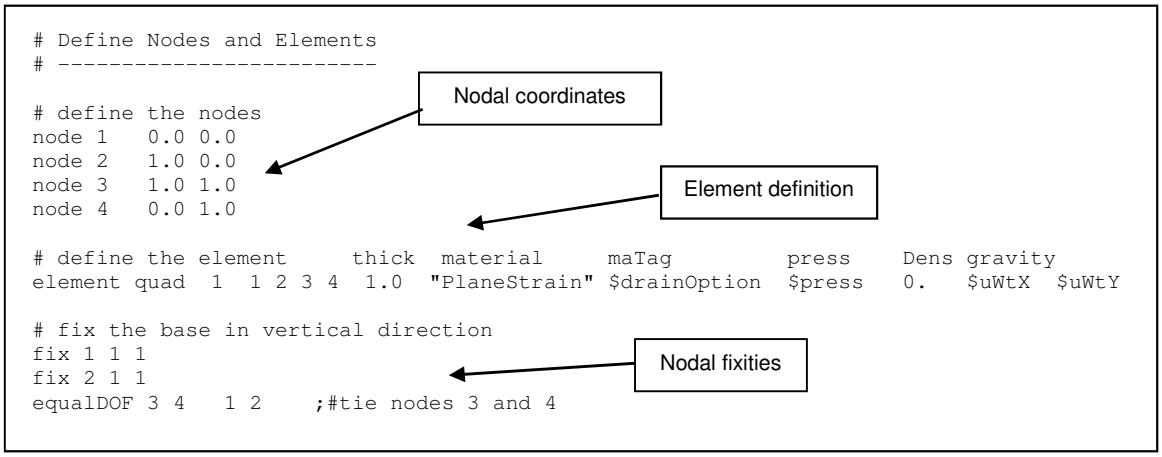


```
# Define Nodes and Elements
# -------------------------

# define the nodes
node 1   0.0 0.0
node 2   1.0 0.0
node 3   1.0 1.0
node 4   0.0 1.0

# define the element     thick  material     maTag          press    Dens gravity
element quad  1  1 2 3 4  1.0  "PlaneStrain" $drainOption  $press   0.   $uWtX  $uWtY

# fix the base in vertical direction
fix 1 1 1
fix 2 1 1
equalDOF 3 4   1 2    ;#tie nodes 3 and 4
```

Figure 4.6: Construction of the finite element mesh

The final component of the model builder object is the pattern command. The pattern command is used to describe the excitation to which the soil or structural unit is subjected. The excitation can be in the form of forces, accelerations, velocities, or displacements. They can be applied in built-in time series formats, to include constant, linear, or sinusoidal fluctuation, or applied as user-defined time series (Figure 4.7). The user-defined time series allows application of selected earthquake time histories

```
pattern Plain 1 {Series -dt 1.00 -filePath inputForce.dat}
                        {load 3 $cFactor 0}
```

Figure 4.7: Definition of loading pattern.

4.1.3.2 Recorder object

The recorder object is unique in that it is not essential to the execution of the program, but is necessary to render the program useful. Recorders record and write data taken from each time step throughout the analysis and can be placed in locations specified by the user to record behaviors of interest. Nodal recorders are used to record nodal displacements, velocities, and accelerations. Element recorders record stress, strain, and pressures at selected gauss points on specified elements (Figure 4. 8). The data is written to user-defined data files from which it can be reduced using the user's program of choice. Matlab was the primary data reduction tool for this research.

```
recorder Node -file $fDir/disp.out  -time  -node 1 2 3 4 -dof 1 2 -dT 1.00 disp
recorder Node -file $fDir/acce.out  -time  -node 1 2 3 4 -dof 1 2 -dT 1.00 accel
recorder Element 1 -time -file $fDir/stress1.out material 1 stress -dT 1.00
recorder Element 1 -time -file $fDir/strain1.out material 1 strain -dT 1.00
recorder Element 1 -time -file $fDir/press1.out material 1 pressure -dT 1.00
```

Figure 4. 8: Construction of the recorded objects to save nodel displacements and accelerations and element stress, strain and pressure data with each time step.

4.1.3.3 Analysis object

As noted in Figure 3.1, the analysis object is used to update the model state from one point in time to the next. Both static and transient analyses are available in OpenSees. Gravity loads are applied using the static analysis, including body forces and the element's self-weight. The transient analysis is used for dynamic loading, representing the state at each point in time by several matrices and using integral operations to advance each time step. Several commands are necessary to formulate each type of analysis and govern the time step solutions. They allow for different ordering strategies, solution methods, and time step advancing solutions (Figure 4. 9).

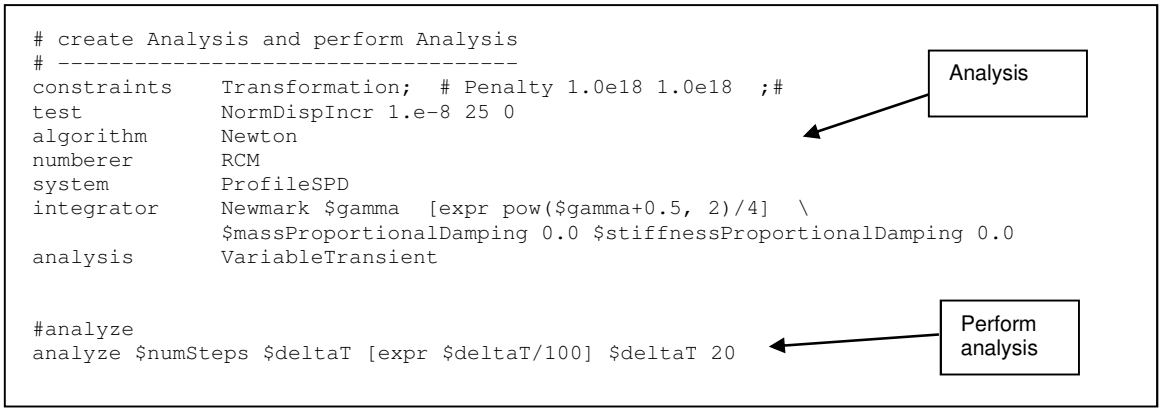


```
# create Analysis and perform Analysis
# -------------------------------------
constraints    Transformation;  # Penalty 1.0e18 1.0e18  ;#
test           NormDispIncr 1.e-8 25 0
algorithm      Newton
numberer       RCM
system         ProfileSPD
integrator     Newmark $gamma  [expr pow($gamma+0.5, 2)/4]  \
               $massProportionalDamping 0.0 $stiffnessProportionalDamping 0.0
analysis       VariableTransient


#analyze
analyze $numSteps $deltaT [expr $deltaT/100] $deltaT 20
```

Figure 4. 9 Construction of analysis objects and execution of analysis.

In the dynamic (transient) case the integration tool is selected by the user to update the velocity and displacement from accelerations. This research used the Newmark integration method for the transient analyses. Once the displacements are determined, the program solves the material nonlinear problem using, in this case, the modified Newton-Rhapson algorithm, which uses the constitutive laws to iterate until convergence upon the current stress and strain.

4.2 Non linear Hysteretic Soil Behavior and cyclic strength degradation

Under a macroscopic phenomenological point of view it is possible to observe that soil under earthquake loading may behave in a very special way: liquefaction and cyclic strength degradation may lead to spectacular foundation (Figure 4. 10) or slope (Figure 4.11) failures. Non linear hysteretic behavior of soil and cyclic strength degradation are some of the reasons which may contribute to cause such events. To illustrate in more detail the fundamental issues related to such behavior a few preliminary concepts are here introduced.

A natural geological deposit usually shows mechanical features (stiffness and mass density) that increase with depth. Seismic waves that propagate upwards through the soil will encounter a discontinuity passing from stronger to weaker strata. The Snell law shows that for a small admittance ratio, as maybe encountered in such conditions, the wave will propagate

Figure 4. 10 Soil liquefaction and tilting during Niigata earthquake 1964
[http://www.ce.washington.edu/~liquefaction/html/quakes/niigata/niigata.html]

to the above stratum in a almost vertical direction. For this reason, the hypothesys tipically accepted in earthquake geotechnics is that vertical movement will be caused only by P (compression) waves propagation and that horizontal movement only by S (shear) waves propagation so the movements are uncoupled.
If soil is horizontally stratified then the problem maybe reconduced to a 1D problem in either vertical or horizontal direction. A sketch is shown in Figure 4.12. showing the schematization of the 1D problem.

Figure 4.11 Slope failure in Colonia Las Colinas earthquake 1964 [Tsatsanifov,2007].

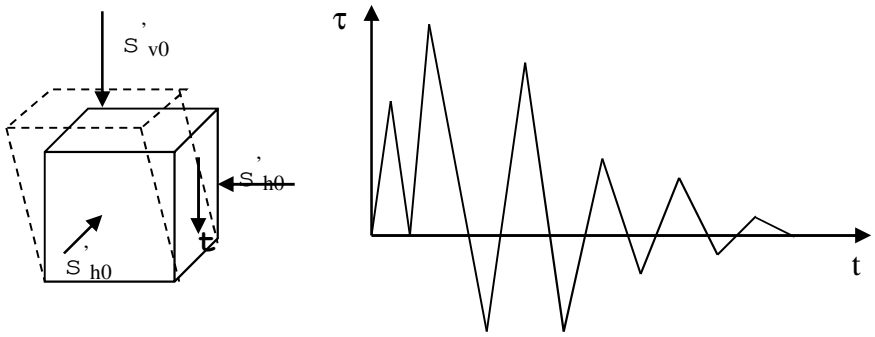

Figure 4.12 Simple shear idealization of soil under earthquake loading

Under this assumption the differential equation for horizontal displacements is:

$$\frac{\partial \tau}{\partial z} = \rho \cdot \frac{\partial^2 u}{\partial t^2} \tag{4.2}$$

The corresponding stress strain relationship between shear stresses and strain is

$$\tau = G \cdot \gamma \tag{4.3}$$

Depending on the problems that are of concerns, and on the expected strain level, different modeling approaches are appropriate as a trade off between simplicity and ability to catch the most significant soil features affecting the problem considered. As shown in Figure 4.14 three main shear strain ranges maybe identified: small deformation with linear elastic behavior, average strain with non linear elastic behavior and large deformation where elasto-plastic modeling is adequate.

For the case of vibrating foundation or geophysical testing, for example, it is reasonable to assume that the level of strain involved are so small below (1E-5 and 1E-6) that soil behaves linearly elastically and G is equal to G_0=G_{max} small strain shear modulus;

The assumption of linear elasticity elasticity is not really correct: experience shows that the small strain G_0 and volumetric modulus K_0 or Poisson ratio (for isotropic material) depends on the first stress invariant [Hardin and Drenvich, 1972; Seed-Idriss, 1970]; it was shown [Loret, 1980] that G_0 and K_0 do not depend only on the actual stress level and an incremental law for constant G_0 and K_0 (i.e. constant Poisson ratio) would be uncorrect and residual deformation would occur. Such a behavior is called hypo-elasticity. It is possible to write the tensorial non linear elastic form of τ=G in incremental way [Loret, 1980], assuming constant Poisson ratio if it is imposed that elastic deformations are deriving from an elastic potential. Experimental studies [Hardin and Drenvich, 1972; Seed-Idriss, 1970] have shown that the main parameters affecting G_0 are the void index (*e)*, the stress state and the stress history

(over consolidation ratio: OCR). Based on the work of Hertz based on micromechanical model [Hertz, 1881], the following law is proposed for granular soils

$$G_{\max} = K \cdot P_a \cdot F(e) \cdot \left[\frac{\sigma_m^{'}}{p_a} \right]^n \tag{4.4}$$

Where K and n depend on the material considered, $\sigma_m^{'}$ is the average stress, p_a the atmospheric pressure and Hardin [1978] proposes

$$F(e)=1/(0.3+0.7 \cdot e^2) \tag{4.5}$$

For clayey soil instead Hardin and Black [1968] propose

$$G_{\max} = K \cdot P_a \cdot OCR^K \cdot F(e) \cdot \left[\frac{\sigma_m^{'}}{p_a} \right]^n \tag{4.6}$$

Where the exponent K increases for increasing plasticity index IP. In order to reproduce cyclic dissipative behavior, linear visco elastic model can also be used for such low strain level. In this case the shear modulus G^* becomes

$$G^*=G+i \cdot \omega \mu' \tag{4.7}$$

Which can be represented by the Kelvin-Voigt model as a spring with stiffness G in parallel with a dashpot with damping equal μ'. Since energy losses in soil are frequency independent also the product $\omega\mu'$ should be frequency independent therefore constant. For an harmonic

$$\eta = \frac{2 \cdot D}{4 \cdot \pi \cdot W} = \frac{\omega \cdot \mu'}{G} = 2 \cdot \beta \tag{4.8}$$

excitation ($\omega=cost$) this can be achieved by assuming for a given material shear modulus G, a constant material *loss coefficient* η (see Figure 4.14). Where D and W (Figure 4.16) are respectively the dissipated work and the elastic energy in a cycle loop for a material with stiffness G and loss coefficient η. According to the approach followed by Jacobsen [1930] then, there is an equivalence between the energy dissipated in a material with stiffness G and loss coefficient η and the energy dissipated at resonance by a simple oscillator with material properties G and $\beta=\eta/2$. Lysmer [1975] proposed a different formulation of the complex shear modulus:

$$G^*=G \cdot e^{i\Theta} \tag{4.9}$$

In this case the equivalence is obtained by minimization of the difference between response of the linear equivalent system and that of the non linear model. The dissipated energy found is

$$D_{\mathrm{mod}\,el} = 4 \cdot \pi \cdot W \cdot \beta \cdot \frac{\sqrt{1-\beta^2}}{1-2 \cdot \beta^2} \tag{4.10}$$

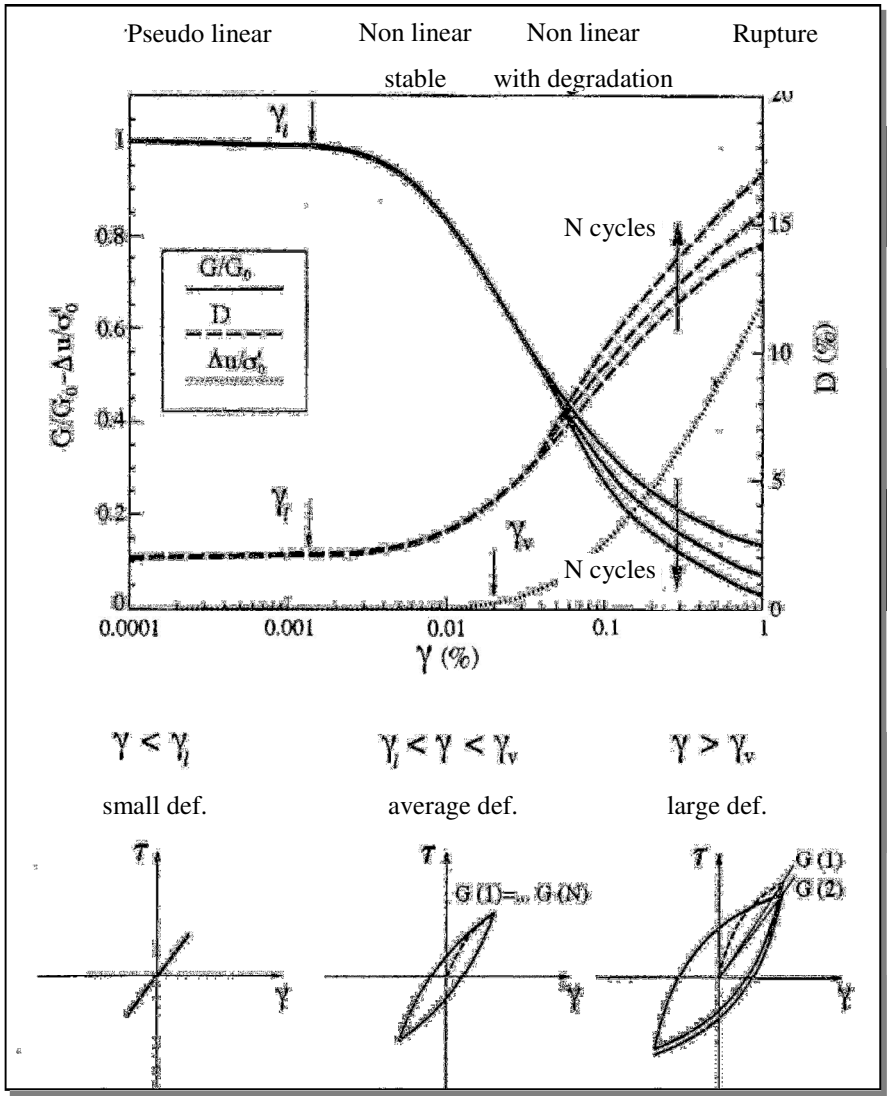

Figure 4.13 Strain level and types of soil mechanical behaviour in simple cyclic shear [Silvestri, 2005]

and for usual values of damping ratio (<20%) differs maximum of 6% from the dissipation of the simple model.

On the other hand in order to simulate energy dissipative behavior for linear material model in the general multidimensional loading Rayleigh damping can be used. *Rayleigh damping* is commonly used to provide damping that is approximately frequency independent. In its original formulation in matrix form for implicit formulation of dynamic equation of motion, Rayleigh damping consists of a mass proportional and stiffness proportional term preserving decoupling of equation of motion for linear problems and allowing modal superposition solution (*modal analysis*).

Simulation of free field seismic response under earthquake of moderate intensity is one of the cases where shear strain predominantly below the order of magnitude 1E-4 and 1E-3 maybe

expected. In this strain range it is necessary to account for decrease in shear stiffness as well and visco linear equivalent model maybe used according to the backbone curves $G/G_{max}(\gamma)$ and $\beta/\beta_{max}(\gamma)$ laws given by Seed Idriss [1970], Hardin-Drnevich [1972b] (Figure 4. 15), Vucetic and Dobry [1991] as shown in Figure 4.16 and Ishibashi and Zhang [1993].

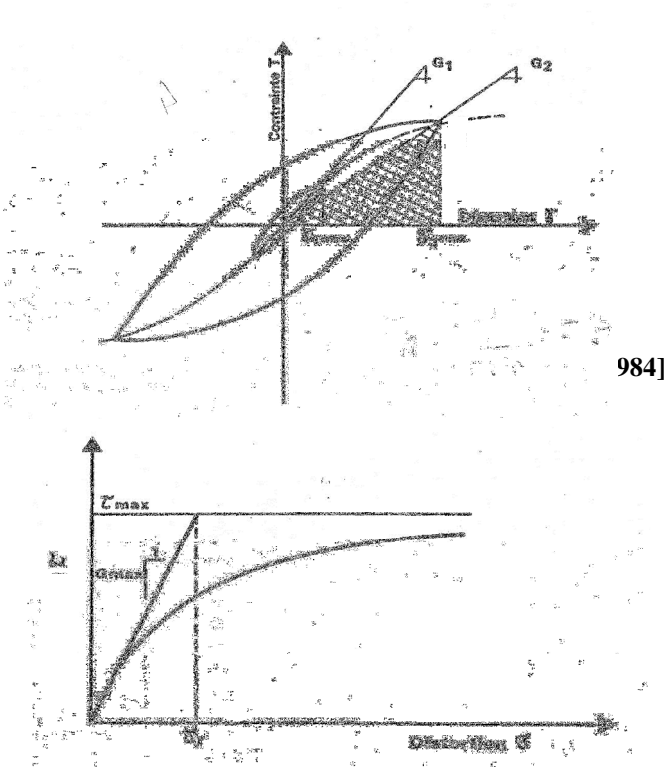

Figure 4. 15 Model parameters for Hardin-Drevnich method [Pecker, 1984]

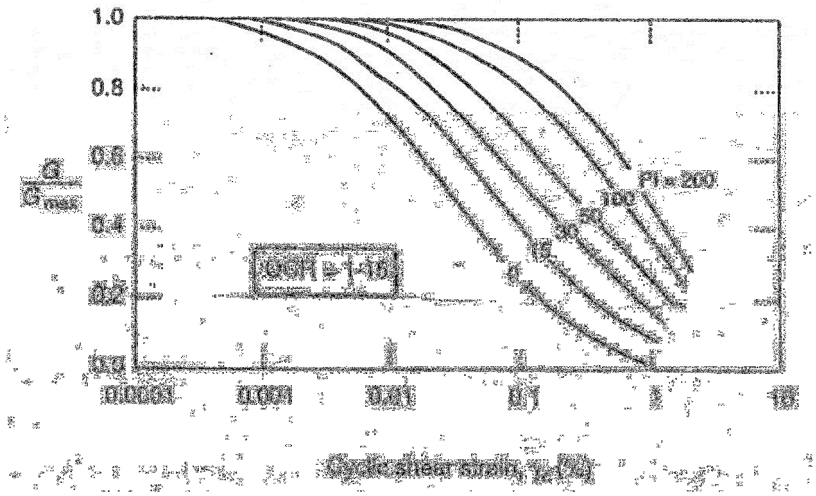

Figure 4.16 Modulus reduction curves for fine-grained soils of different plasticity (Vucetic and Dobry[1991])

For strain of the order of magnitude 1E-3, 1E-2 or larger, non linear material models should be adopted. As mentioned above cyclic strength degradation may become an essential feature governing soil behavior for larger strains in undrained conditions and can eventually lead to soil liquefaction. Mainly this occurs in loose, saturated sands that have a tendency to contract upon deformation. Dynamic excitation causes loose, saturated soil grains to try to contract, but the rapid nature of the loading does not allow the pore water to escape. An increase in pore pressure and a decrease in the effective stresses between the grains results in a loss of soil strength. Essentially, liquefaction can occur in any soil with poor drainage, no cohesion, and a tendency to contract upon loading. It is most common in sands, but can also occur in coarse, non-plastic silts or in gravel confined by impermeable layers. Vibration of rounded particles may lead to liquefaction more rapidly, as they have less inter-granular friction. In terms of geological history fluvial, colluvial, and aeolian soils are susceptible because these natural processes sort the soil into uniform grain size distributions and deposit them loosely, as does the once popular hydraulic fill method.

There are two types of liquefaction. Flow liquefaction is the most severe form, and occurs when a soil mass's static shear stress exceeds its post-liquefaction shear strength, leading to sudden flow failures such as bearing capacity failures (Figure 4. 10) and landslides (Figure 4.11). Cyclic mobility can cause lateral spreading and differential deformation of a building foundation or pipeline, or can be quite severe in one direction if the ground is even slightly sloped (Kramer, 1996). Lateral spreading of bridge abutments led to the collapse of a bridge in the 1964 Niigata Earthquake (Figure 4. 17).

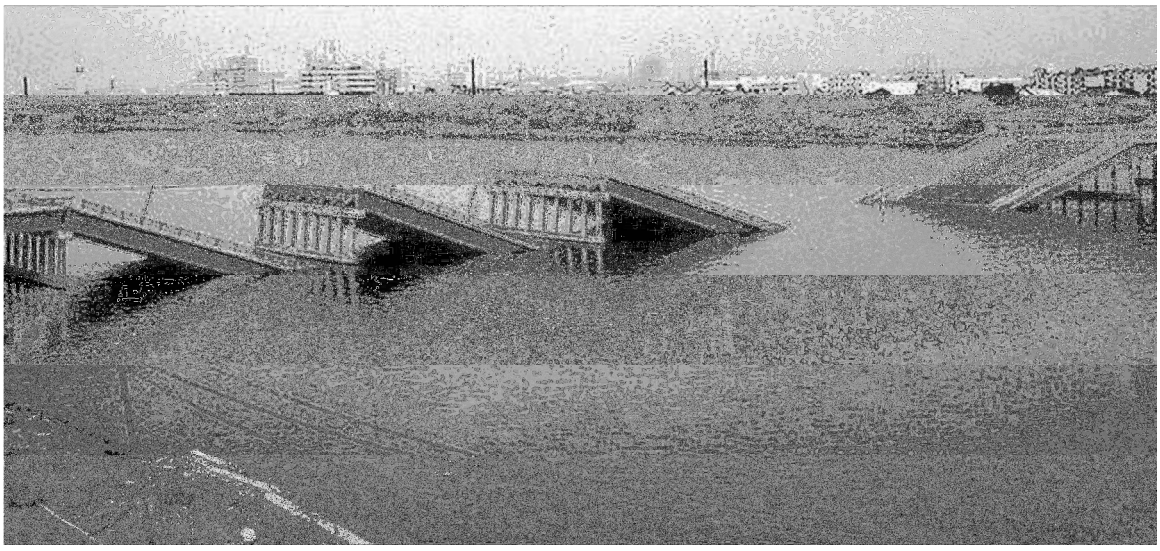

Figure 4. 17 Collapsed bridge after 1964 Niigata Earthquake (University of Washington Web Site).

Cyclic mobility, the other form of liquefaction, occurs when the static shear stress is below the soil's shear strength after liquefaction but is characterized by incursions of contraction and dilation induced by cyclic loading at very low effective stresses. This does not result in

sudden flow failure, but incremental deformations with each cycle in the motion which can be unacceptably high. This study concentrates on modeling only cyclic mobility.

Under a phenomenological point of view with decrease in stiffness of a liquefiable layer, the propagation of high frequency waves to the surface can be significantly reduced. Often, when looking at a surface acceleration time history, the time of liquefaction initiation can be identified as the point when the predominant frequency and the acceleration amplitudes decrease. This does not necessarily reduce damage to structures at the surface. Instead increased velocity and displacement amplitudes can cause the motion to become more destructive to taller structures with longer natural periods (Kramer, 1996).

Sand settlement is another result of earthquake shaking. In saturated sands, settlement follows liquefaction, but can also occur even if the pore pressure increases are not high enough to induce liquefaction. The amount of settlement of liquefied sand can be predicted based on soil density, maximum shear strain during shaking, and amount of excess pore pressure generated. For loose deposits of dry sand, the settlement occurs very quickly, but for the saturated deposits, the rate of settlement depends on the permeability of the sand and confining layers (Kramer, 1996).

Before describing the threedimensional models, unidirectional non linear models are described first. These are traditionally more related to experimental or empirical approach than those developed in multidirectional loading. Masing postulates are assumed [Masing, 1936] regarding the scaling of vertical/horizontal ($\Delta\tau/\Delta\gamma$) proportion in the cyclic stress-strain curves at first and subsequent loading/reloading branches.

Mathematical formulations for the stress-strain curves incorporates Masing rules and adopt a scaling parameter n which equals 1 or 2 depending whether first of subsequent loading is assumed and a functional describing the shape of the first loading curve as, for example, the functional H proposed by Ramberg Osgood [1943]

$$H(\tau) = \alpha \cdot \left[\frac{\tau}{\tau_y} \right]^{R-1} \tag{4. 11}$$

$$\gamma = \gamma_c + \left[\frac{\tau - \tau_c}{G_{\max}} \right] \cdot \left[1 + H \cdot \left[\frac{\tau - \tau_c|}{n} \right] \right] \tag{4. 12}$$

Where τ_c and γ_c are the maximum/minimum stress and strain values reached in the previous loading/unloading branch. Within the group of one dimensional stress-strain laws, Iwan [1967], propose to model non linear soil behavior considering a model composed by groups of springs and sliders. He shows that in this way it is possible to reproduce more complex cyclic loadings conditions including the effects of softening – hardening related to plastic volumetric strains (dilatancy). For closed loop this model reduces to Masing's model and for multidirectional loading there is an equivalence to kinematic hardening as in the framework of elastoplasticity theory.

The simple idealized analysis of a regular array of spheres [Dobry *et al*, 1982] allows to calculate the value of volumetric threshold shear strain corresponding to the initiation of gross sliding and volumetric strain as a function of the elastic grain properties (E and ν). Experimental evidence for drained and undrained sand [Pyke, 1973; Dobry *et al*., 1972] shows that there is a good correspondence with the calculated value and that such value γ_{tv} is around ten times as high as the linear cyclic threshold shear strain γ_{tl}.

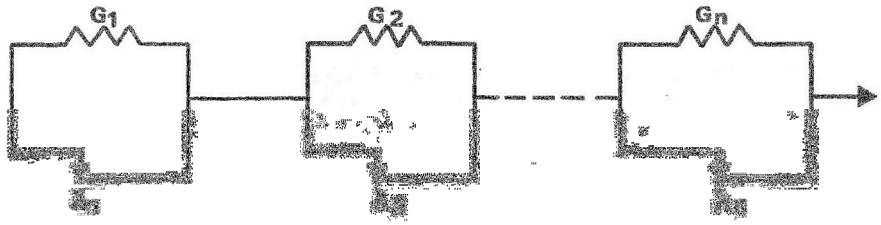

Figure 4. 18 Iwan model [1967]

General three dimensional non linear material models for cyclic soil modeling are mostly based on the incremental elastoplasticity theory [Jennings, 1964; Finn et all. 1977; Martin, 1975; Prevost, 1980; Elgamal, 2003] or on Hypoplasticity [Osinov, 2003] .

For a 3D, tensorial elastoplastic model strain tensor will be the sum of an elastic and a plastic part.

The following fundamental equations are required:

- Yield criterion: that tells when plastic strain occur.
- Flow rule: indicating the direction and magnitude of plastic strains. For a material which follows the principle of maximum work [Hill, 1950] it can be shown that the incremental plastic strain can be written as:

$$\dot{\varepsilon}^{p} = \dot{\lambda} \cdot \frac{\partial \cdot g}{\partial \cdot \underline{\sigma}} \qquad (4.\ 13)$$

  Where the scalar plastic multiplier λ is different from zero when stress state lay on the yield surface and the stress increment is directed outward. The flow rule is called associated when the plastic potential function g equal to the yield surface f

- Hardening rule: tells how the yield surface evolves. Kinematic hardening involves translation of the yield surface whereas isotropic hardening involves change in size of the yield surface (Figure 4. 19).

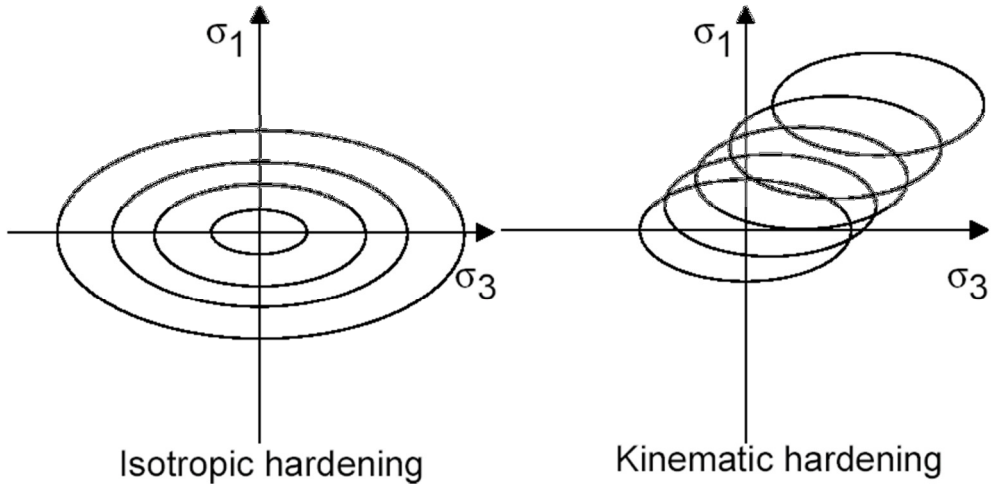

Figure 4. 19 Schematis representation of two hardening types [Elgamal *et al*, 2003]

Even though in principle hysteretic model can represent energy dissipation of soil, for very small strains (less than 1e-4/1e-2) viscous damping is incorporated because is not adequately captured by non linear models. Thso occurs because the backbone curve il nearly linear at these strains, which produces nearly zero hysteretic damping when the backbone curve is used with the extende Masing rules. Th addition of viscous damping term in the analysis avoids unrealistic responses for problems involving small strains (Vucetic and Doubry, 1986).

4.2.1 Implementation in FLAC: Mohr Coulomb model, Hysteretic Damping and Finn model.

As already mentioned in 4.1.2, all constitutive models implemented in FLAC are intended mainly for use in quasi static loading or dynamic situations where the response is mainly monotonic. Nevertheless, as it will be said, there is the possibility in FLAC to reproduce an equivalent linear type of behavior (see 4.2); in this case non linearity is allowed inside the Coulomb failure surface. In the seismic analysis of flexible retaining structures that will be shown in the following Chapters, soil material was first modeled by an elastic perfectly plastic Mohr-Coulomb model and secondly with a linear equivalent type of model. The representation of the Mohr-Coulomb model in 3D stress space is shown and compared to the Tresca one in Figure 4. 20.

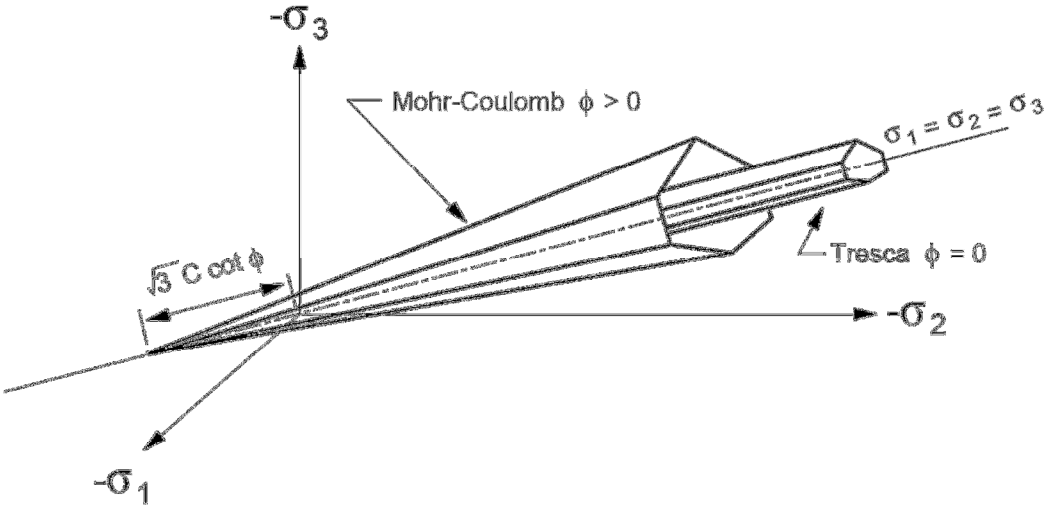

Figure 4. 20 Mohr Coulomb and Tresca Yield surfaces in principal stress space [FLAC 5.0 user manual, 2005]

In the shear yield formulation of the yield surface depends only on the maximum and minimum stresses are active. In the plane σ_1, σ_2 the failure criterion maybe represented as follow:

$$Y = \sigma_1 - \sigma_3 \cdot N_\phi + 2 \cdot C \cdot \sqrt{N_\phi} \tag{4. 14}$$

where

$$N_\phi = \frac{1+\sin\phi}{1-\sin\phi} \tag{4. 15}$$

and $\sigma_1 \le \sigma_2 \le \sigma_3$

The plastic potential is

$$g = \sigma_1 - \sigma_3 \cdot N_\psi \tag{4. 16}$$

where

$$N_\psi = \frac{1+\sin\psi}{1-\sin\psi} \tag{4. 17}$$

and ψ is the dilation angle. If the initial elastic trial shows yielding (Y<0) then

$$\Delta\sigma_1 = \sigma_1 - \sigma_1^0 = \alpha \cdot \Delta\varepsilon_1^e + \beta \cdot (\Delta\varepsilon_2^e + \Delta\varepsilon_3^e) \tag{4. 18}$$

$$\Delta\sigma_2 = \sigma_2 - \sigma_2^0 = \alpha \cdot \Delta\varepsilon_2^e + \beta \cdot (\Delta\varepsilon_1^e + \Delta\varepsilon_3^e) \tag{4. 19}$$

$$\Delta\sigma 3 = \sigma_3 - \sigma_3^0 = \alpha \cdot \Delta\varepsilon_3^e + \beta \cdot (\Delta\varepsilon_1^e + \Delta\varepsilon_2^e) \tag{4. 20}$$

Where

$$\alpha = K + (4/3)\cdot G \tag{4. 21}$$

$$\beta = K - (2/3)\cdot G \tag{4. 22}$$

Differentiating the plastic potential, the plastic strain increments are

$$\Delta\varepsilon_1^p = \lambda \cdot \frac{\partial g}{\partial \sigma_1} = \lambda \tag{4. 23}$$

$$\Delta\varepsilon_2^p = \lambda \cdot \frac{\partial g}{\partial \sigma_2} = 0$$

$$\Delta\varepsilon_3^p = \lambda \cdot \frac{\partial g}{\partial \sigma_3} = -N_\psi \cdot \lambda \tag{4. 24}$$

Recalling the partition of strains $\Delta\varepsilon^e_\iota = \Delta\varepsilon_\iota - \Delta\varepsilon^p_\iota$ and substituting in the previous equations

$$\begin{aligned}
\sigma_1 &= \sigma_1^0 + \alpha \cdot (\Delta\varepsilon_1 - \lambda) + \beta \cdot \lambda(\Delta\varepsilon_2 + \Delta\varepsilon_3 + \lambda N_\psi) \\
\sigma_2 &= \sigma_2^0 + \alpha \cdot \Delta\varepsilon_2 + \beta \cdot (\Delta\varepsilon_1 - \lambda + \Delta\varepsilon_3 + \lambda \cdot N_\psi) \\
\sigma_3 &= \sigma_3^0 + \alpha \cdot (\Delta\varepsilon_3 + N_\psi \cdot \lambda) + \beta \cdot (\Delta\varepsilon_2 + \Delta\varepsilon_1 - \lambda)
\end{aligned} \tag{4. 25}$$

λ can be determined imposing Y=0 and substituting in Y=0 the new stresses to give

$$\lambda = \frac{\alpha \cdot \Delta\varepsilon_1 + \beta \cdot (\Delta\varepsilon_2 + \Delta\varepsilon_3) - (\alpha \cdot \Delta\varepsilon_3 + \beta \cdot (\Delta\varepsilon_1 + \Delta\varepsilon_2) \cdot N_\phi + 2c \cdot \sqrt{N_\phi}))}{(\alpha - \beta \cdot N_\psi) \cdot (\beta - \alpha \cdot N_\psi) \cdot N_\psi} \tag{4. 26}$$

The exact solution for the stresses is obtained by substituting λ. This example is to show that, on the base of the considerations done in 4.1, differently from FEM no iterative return mapping algorithms are needed for this type of non linear soil model. There are many steps as the time step is small but convergence is faster than for implicit FEM.

In order to prevent inadmissible tension, a tension yield formulation of the yield surface is added as well in the form $f^t = \sigma^t - \sigma_3$. The flow rule in this case is associated and the maximum admissible tension is:

$$\sigma^t_{\max} = \frac{c}{\tan\phi} \tag{4. 27}$$

Mohr Coulomb model in FLAC assumes linearly elastic behavior inside the yield surface and no hardening (perfectly plastic model).

Since the perfectly plastic material model adopted cannot implicitly incorporate hysteretical soil behavior in the elastic range, a Rayleigh damping was applied to the model to account for dissipative behaviour of soils at small to moderate level of cyclic strains. In the following numerical analysis the *hysteretic damping* model was used as well. Likewise the *equivalent linear method* [Seed and Idriss 1969], the hysteretic damping allows modelling the cyclic

shearing of the soil due to earthquake; this determines progressive decay in shear stiffness (initially equal to small strain shear modulus G_0) and progressive increase in hysteretic, frequency independent , material damping, usually expressed as percentage ratio to the critical one ($\zeta(\%)$).

Differently from the equivalent linear model though, since the elasto-plastic Mohr Coulomb model is applied as well, the hysteretic damping allows under all aspect a non linear behavior with possibility of material yield, plastic straining and residual displacements.

The so called *Hysteretic model* available in FLAC allows to represent modulus reduction curves. Only built-in continuous functions are used in FLAC and fitting of available experimental degradation curves requires calibration of numerical coefficients included in such build-in functions. In the following application the *default* built-in function was used; for such type of function the following apply

$$G_{secant}=s^2\cdot(3-2\cdot s) \tag{4. 28}$$

$$s=\frac{L_1-L}{L_2-L_1} \tag{4. 29}$$

Where L is the logarithmic strain

$$L=\log10(\gamma) \tag{4. 30}$$

(e.g. L_1=-3 $\gamma=10^{-3}$=0.001%) and L_1 and L_2 are the extreme values of L at which the derivative of the backbone G/G_0 curve is zero and are also the coefficients that have to be determined for the fitting process (see 5.2).

In order to take into account the pore pressure build up which occurs in saturated soils during earthquake shaking not only a non linear cyclic soil model is needed but also the soil must be modelled as a porous material . FLAC offers the possibility of modelling the relationship between the volumetric plastic strain ($\Delta\varepsilon_{vd}$) related to cyclic shear stress in the so called *Finn model* and the Byrne formula (*Byrne*, 1991)

$$\frac{\Delta\varepsilon_{vd}}{\gamma}=C_1\exp(-C_2(\frac{\Delta\varepsilon_{vd}}{\gamma})) \tag{4. 31}$$

where $C_1=7600(D_r)^{-2.5}$ and $D_r=15\cdot(N_1)_{60}{}^{0.5}$ so it is possible to write the costant C_1 as a function of the corrected SPT value. The suggested value for C_2=0.4/ C_1 and C_3=0.

4.2.2 Implementation in DYNAFLOW

The yield criterion used in DYNAFLOW in the following application is the Matsuoka mode. Elastic perfectly plastic behaviour is assumed therefore as input it is not required the knowledge of any hardening properties but is required knowledge of elastic properties, plastic flow and yield parameters. Relation between 3D extension of Mohr Coulomb criterion and Matsuoka on deviatoric plane is shown in .

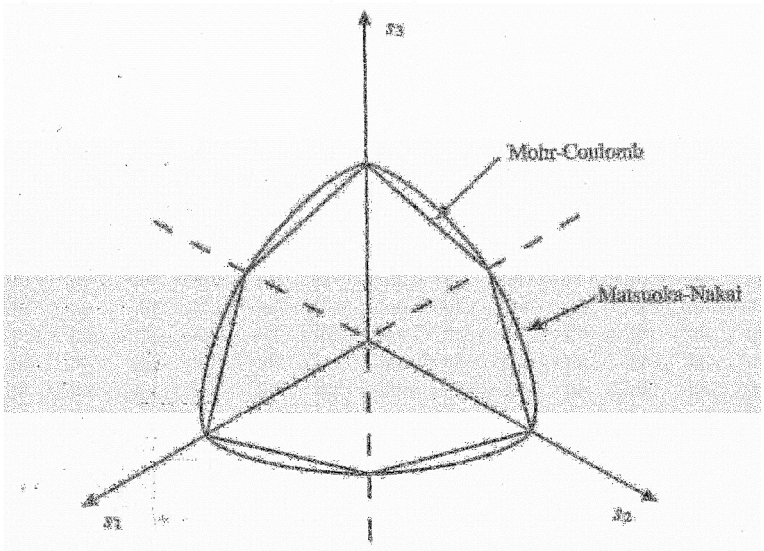

Figure 4.21 Comparison between Coulomb-Matsuoka criteria on deviatoric plane [Matsuoka,1985]

In the case of granular material the criterion assumes that soil fails when the ratio of the shear to the normal stress in any of the three mobilized planes (τ_{mob}/σ_{mob}) [Matsuoka, 1985] reaches a limiting value. In terms of deviatoric invariant this criterion can be written as

$$J_1 \cdot J_2 / J_3 = const \qquad (4.\ 32)$$

The shape of the yield surface is set by specifying the effective shear angle, additionally allowable traction is set to zero. Dilantancy ψ is set to zero (no plastic volumetric strain at yield) meaning non associative flow rule since yield surfaces considered are I_1 (trace of stress tensor) dependent and not parallel to hydrostatic axis. The reason for setting dilatancy to zero [Potts and Zdravkovic, 1999] is to avoid excessive plastic volumetric strain.
Dynaflow also incorporates a multy yield constitutive model developed by Prevost [1985]. Input parameters for the model can be obtained through compression-extension triaxial tests and cyclic shear tests. Tested under stress paths different from those of these tests, the model shows also a good agreement to experimental data [Prevost, 1985]. This model is therefore a complete and good model.

4.2.3 Implementation in Opensees

In general, during a shear loading process near liquefaction (low confinement levels), a saturated undrained cohesionless soil exhibits the following pattern of behavior (Lambe and Whitman, 1969; Ishihara, 1985):

1. At low shear strains, the soil skeleton experiences a tendency for contraction (phase 0–1 in Figure 4.23), leading to development of excess pore-pressure and reduction in effective confinement.

2. As the shear stress approaches the failure envelope, or more precisely the so called Phase Transformation (PT) envelope (Ishihara, 1985; Iai, 1991; Vaid and Thomas, 1995; Vaid and Sivathayalan, 1999), significant shear strain may develop without appreciable change in shear stress (essentially, the perfectly plastic phase 1–2 in Figure 4.23). Numerical versatility is achieved by defining this highly yielded segment of stress-strain response as a distinct phase (as shown in Figure 4.23, where $\gamma = \sqrt{\frac{2}{3} e : e}$ refers to octahedral shear strain, and e=deviatoric strain tensor). This feature allows for direct control over the extent of shear strain accumulation.

3. Thereafter (above the PT envelope), a dilative tendency (phase 2–3 in Figure 4.23) increases effective confinement (and consequently shear stiffness and strength), allowing the soil to resist increased levels of shear stress (by moving along the failure envelope).

For the purpose of liquefaction-induced shear deformations, medium-dense clean granular soils are found to exhibit the above-described response. A survey of experimental research (triaxial and shear tests) compiled by Seed (1979) suggested that such clean sands, with a relative density Dr of about 45% or more, appeared to exhibit the mechanism of limited strain cyclic mobility during liquefaction.

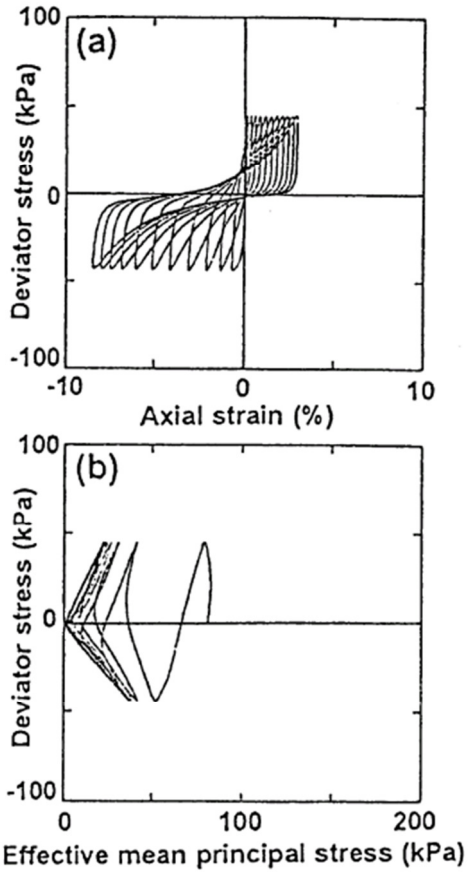

Figure 4.22 Stress–strain relationship and stress path for undrained cyclic triaxial test on reclaimed gravely Masado soil (Hatanaka et al., 1997), which developed major liquefaction-induced deformations during the 1995 Kobe, Japan earthquake.

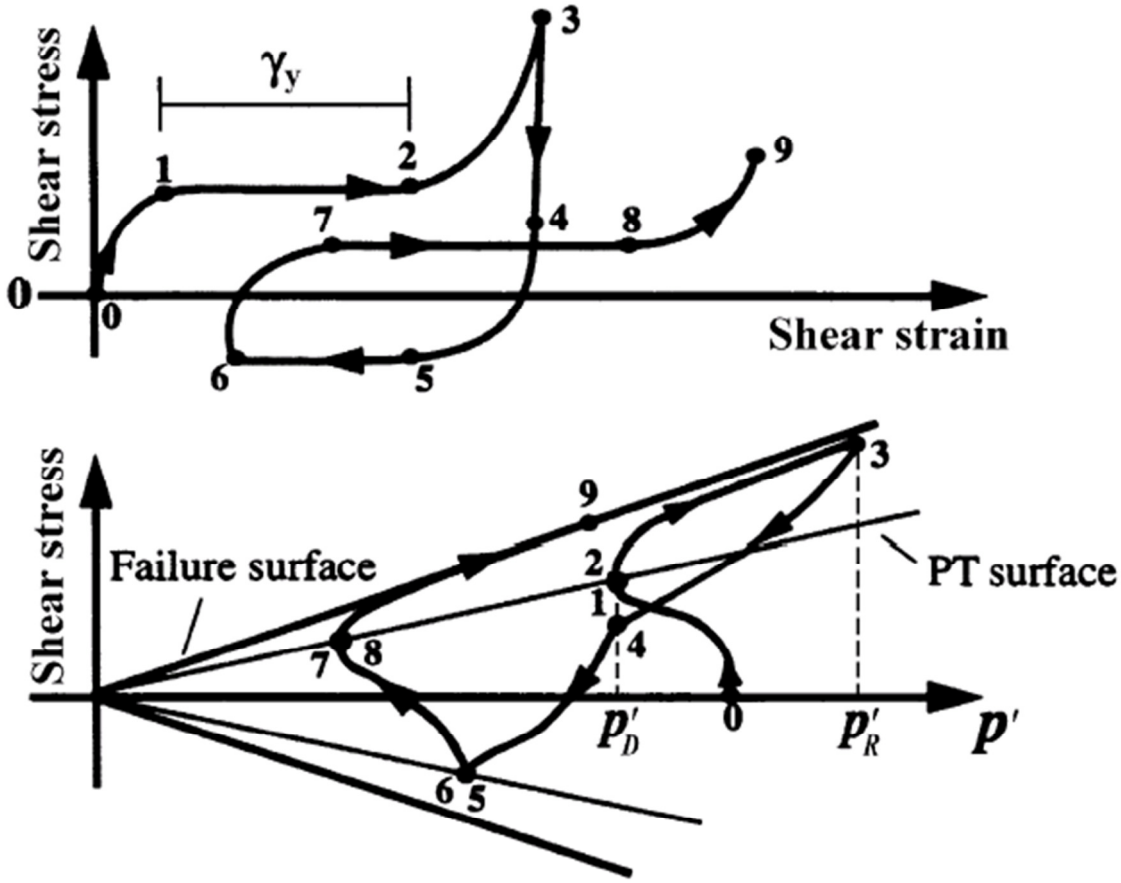

Figure 4.23 Schematic of constitutive model response showing shear stress, effective confinement, and shear strain relationship [Elgamal *et al*., 2003].

The plasticity model used from Opensees (Parra, 1996;Yang, 2000) is based on the original framework of Prevost (1985), in which a multi-surface approach is adopted for cyclic hysteretic response (Iwan, 1967; Mroz, 1967). The contractive, perfectly plastic, and dilative phases of Figure 4.23 are incorporated using a new appropriate flow rule (Elgamal *et al.* 2003). The incorporated new flow rule significantly changes the characteristics of model response, in order to reproduce the salient cyclic mobility mechanisms (Figure 4.22 and Figure 4.23), and exercise more direct control over shear strain accumulation (in accordance with experimental observations). In addition, a new hardening rule was developed for more robust and efficient numerical performance.

(a) Yield function

The yield function (Figure 4.24) is selected of the following form (Prevost, 1985):

$$f = \frac{3}{2}(\mathbf{s} - (p' - p'_o)\boldsymbol{\alpha}) : (\mathbf{s} - (p' + p'_o)\boldsymbol{\alpha}) - M^2(p' + p'_o)^2 = 0 \qquad (4.\ 33)$$

in the domain of $p' \geq 0$, where $\boldsymbol{s}=\boldsymbol{\sigma}'-p'\,\boldsymbol{\delta}$ is the deviatoric stress tensor ($\boldsymbol{\sigma}'$=effective Cauchy stress tensor, $\boldsymbol{\delta}$=second-order identity tensor), p' is the mean effective stress, p'_0 is a small positive constant (2.0 kPa in this study) such that the yield surface size remains finite at $p'=0$ (for numerical convenience and to avoid ambiguity in defining the yield surface normal at the yield surface apex,Figure 4.24), $\boldsymbol{\alpha}$ is second-order kinematic deviatoric tensor defining the yield surface coordinates, M dictates the yield surface size (defined by friction angle for the outmost surface), and ":" denotes doubly contracted scalar product of two tensors. In the context of multi-surface plasticity, a number of similar yield surfaces with a common apex and different sizes form the hardening zone (Figure 4.24). Each surface is associated with a constant plastic modulus. The outmost surface is designated as the failure surface. As usually postulated (Prevost, 1985), the low-strain (elastic) moduli and plastic yield surface moduli increase in proportion to the square root of effective confinement.

It is realized that the employed yield surface is open in the positive direction of hydrostatic axis (Figure 4.24). One may introduce a cap yield function (e.g., DiMaggio and Sandler, 1971; Lacy, 1986; Wang et al., 1990) to close the open end. As indicated by Manzari and Dafalias (1997), under normal confining pressures of interest in geotechnical engineering, a stress path along the positive branch of the hydrostatic axis induces relatively small strains. Thus, for shear-dominated load paths (such as earthquake excitation), many researchers have opted to maintain a level of simplicity, and do without a cap function (e.g., Prevost, 1985; Manzari and Dafalias, 1997; Li and Dafalias, 2000).

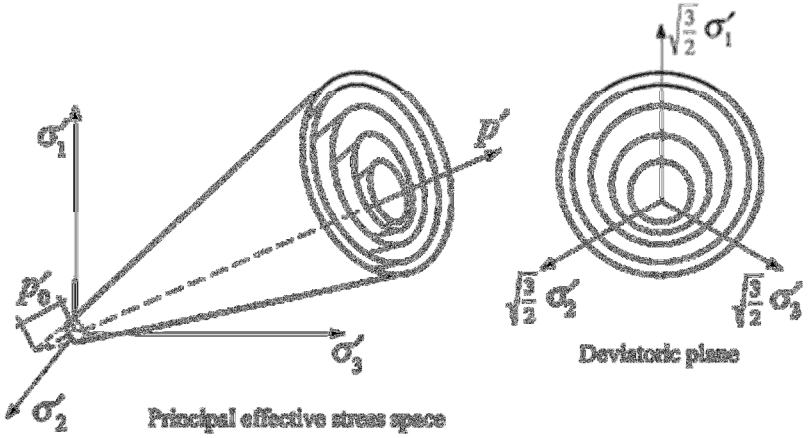

Figure 4.24 Conical yield surface in principal stress space and deviatoric plane [after Prevost, 1985; Parra, 1996; Yang, 2000].

(b) Flow Rule

Within the theory of plasticity framework, the phenomenological interaction between shear and volume change (contraction or dilation) is typically handled by specifying an appropriate non-associative flow rule (e.g., Prevost, 1985; Dafalias, 1986; Bousshine et al., 2001; Nemat-Nasser and Zhang, 2002; Radi et al., 2002). In the current model, the deviatoric component of the flow rule is associative, and nonassociativity is restricted to the volumetric component only (similar to earlier formulations).

Denoting ***P*** as the direction of plastic flow, its volumetric component P'' defines the desired level of dilation or contraction in accordance with experimental observation. Consequently, P'' is defined by (Prevost, 1985; Parra, 1996):

$$3P'' = \frac{1-(\eta/\bar{\eta})^2}{1+(\eta/\bar{\eta})}\Psi \qquad (4.\ 34)$$

$$\eta = \frac{\sqrt{(3/2)\mathbf{s}:\mathbf{s}}}{(p'+p'_o)} \qquad (4.\ 35)$$

Where η is effective stress ratio, $\bar{\eta}$ a material parameter defining the stress ratio of the Phase Trasformation (PT) surface, and Ψ a newly introduced scalar-valued function (Parra, 1996; Yang, 2000) for controlling the magnitudes of dilation and contraction, as described below (a scalar material parameter was used in Popescu and Prevost (1993) in place of the function Ψ). Note that if $(1-(\eta/\bar{\eta})^2)$ is positive, the stress state lies within the PT surface, and if negative, the stress state lies above the PT surface. In addition, loading corresponds to an increasing η, and unloading corresponds to a decreasing η.

-Within phase transformation surface (phase 0-1, Figure 4.23)

Within the PT surface, contraction always takes place irrespective of loading/unloading condition. The contraction scaling function in (4. 34) is chosen to be (Parra, 1996):

$$\Psi = c_1 \exp(c_2 p'/P_a) \qquad (4.\ 36)$$

Where c_1 and c_2 are two material constants dictating the rate of contraction (or equivalently, the rate of excess pore-pressure buildup under undrained condition), and P_a is atmospheric pressure (101 kPa, used as a normalization constant). The parameter c_1 depends on the particular soil type and relative density (larger c_1 values correspond to stronger contraction), and c_2 allows for a form of confinement dependence if deemed necessary.

-Above phase transformation surface (phase 2-3, Figure 4.23)

Upon the accumulation of γ_y, a sharp dilation tendency is activated (compared to earlier formulations, Prevost, 1985; Popescu and Prevost, 1993). The dilation scaling function in (4. 36) is defined by (Parra, 1996)

$$\Psi = d_1 \exp(d_2 \gamma_d) \qquad (4.\ 37)$$

Where d_1 and d_2 are material constants, and γ_d is cumulative octahedral plastic strain during the current dilative phase. Larger d_1 and d_2 values result in increasingly stronger dilation, eventually limited by the conical yield surface gradient (associated flow). Equation (4. **37**)

allows the dilation tendency to increase progressively, and significantly reduces further straining (Figure 4.25). The increase in shear stress and effective confinement due to dilation may be limited by (Casagrande, 1975): (a) reaching the critical void-ratio (or constant-volume) state at large shear strain (Li and Dafalias, 2000), or (b) fluid cavitation (i.e., pore water pressure reduced to −1 atmospheric pressure)

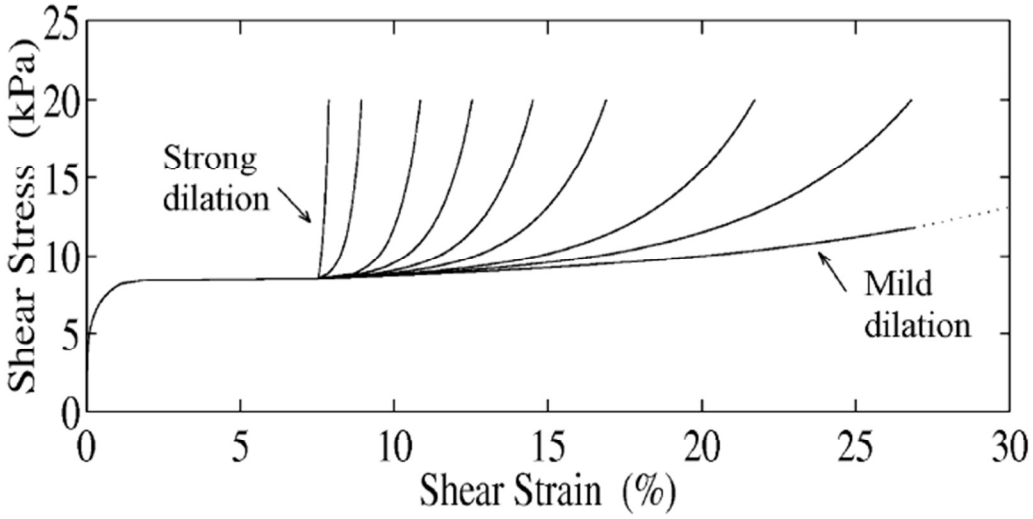

Figure 4.25 Dilation function performance for a given γ_y and different user defined rates of dilation [Elgamal *et al*., 2003].

-Above phase transformation surface (phase 3-4, Figure 4.23)

A different definition of P'' is needed (Parra, 1996) to allow for a swift return to the confinement level p'_D upon unloading (phase 3-4, Figure 4.23). For that purpose, the following relationship resulted in satisfactory performance:

$$\frac{\sqrt{3/2\,\mathbf{P}':\mathbf{P}'}}{P''} = \frac{p'_D}{p'_R}\eta_f \qquad (4.\ 38)$$

in which $\boldsymbol{P'}$ is deviatoric component of the tensor $\mathbf{P}$, η_f is stress ratio along the failure surface, and p'_R is effective confinement at the load reversal point R (Figure 4.23). This rule relates the rate of contraction to the extent of accumulated confinement (distance between p'_R and p'_D, Figure 4.23). Representative performance of unloading behavior is shown in Figure 4. 26. Once confinement decreases to the level of point D, p'_D is no longer a memory parameter, and the contraction logic within the PT surface takes over. Dependence of contraction on earlier dilation conforms with experimental observations (), as also represented in the models of Dafalias and Manzari (1999) and Nemat and Radi.

It is noted that the above newly developed non-associative rules obey the requirement of positive plastic dissipation (Lubliner and Brannon 2002). In addition, the Kuhn–Tucker conditions are satisfied ().

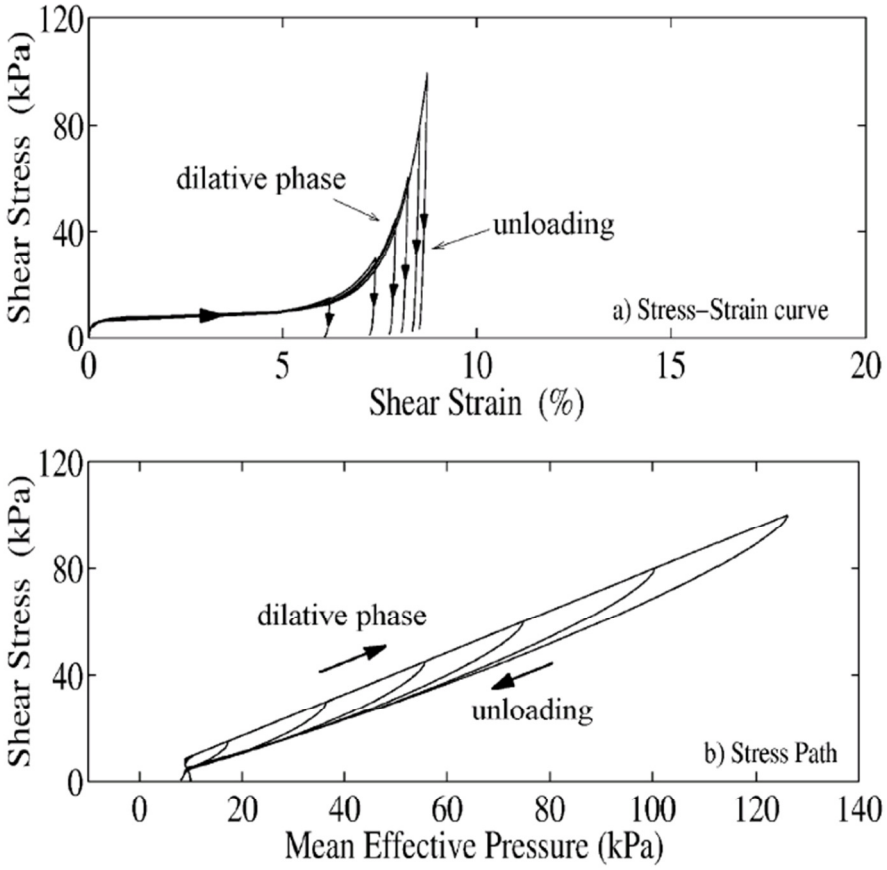

Figure 4. 26 Dilation function performance for a given γ_y and different user defined rates of dilation [Elgamal *et al*., 2003].

(c) Configuration of yield domain

The shear strain γ_d accumulated during dilation (phase 2-3 Figure 4.23, Figure 4. 26 (a)) may enlarge the yield domain (Figure 4. 27 (c)). Specifically, enlargement occurs when shear strain accumulated in the current dilation phase exceeds the maximum γ_d the material has ever experienced before (since phase 2-3 is the first time the material experiences dilation, the domain enlarges throughout). This logic preserves the symmetric pattern of cyclic shear deformation observed in Figure 4.22, and may be physically interpreted as a form of a damage effect.

The presence of superimposed static shear stress results in biased accumulation of shear deformations is very important for the case of inclined strata of infinite slope, below and around embankments or foundations and other lateral spreading situations. This biased accumulation is achieved through translation of the yield domain in the deviatoric strain space (strain induced anisotropy; Bazant and Kim, 1979) allowing yield increment γ_r to develop before subsequent dilation (phase 5-6, Figure 4. 26). According to experimentally documented accumulation patterns (Arulmoli et al. 1992; Ibsen 1994), strain increment γ_r

is proportional to the level of previous unloading strain (phase 3-4,), limited to a maximum of $R \cdot \gamma_s$ where $R=y_3$ is a user defined constant (γ_s is the yield domain size at the current level of effective confinement). Note that the enlargement of the yield domain continues until the strain accumulated during dilation reaches the maximum γ_d recorded previously (i.e. phase 2-3 Figure 4. 27). After phase 5-6 the domain enlarges again.

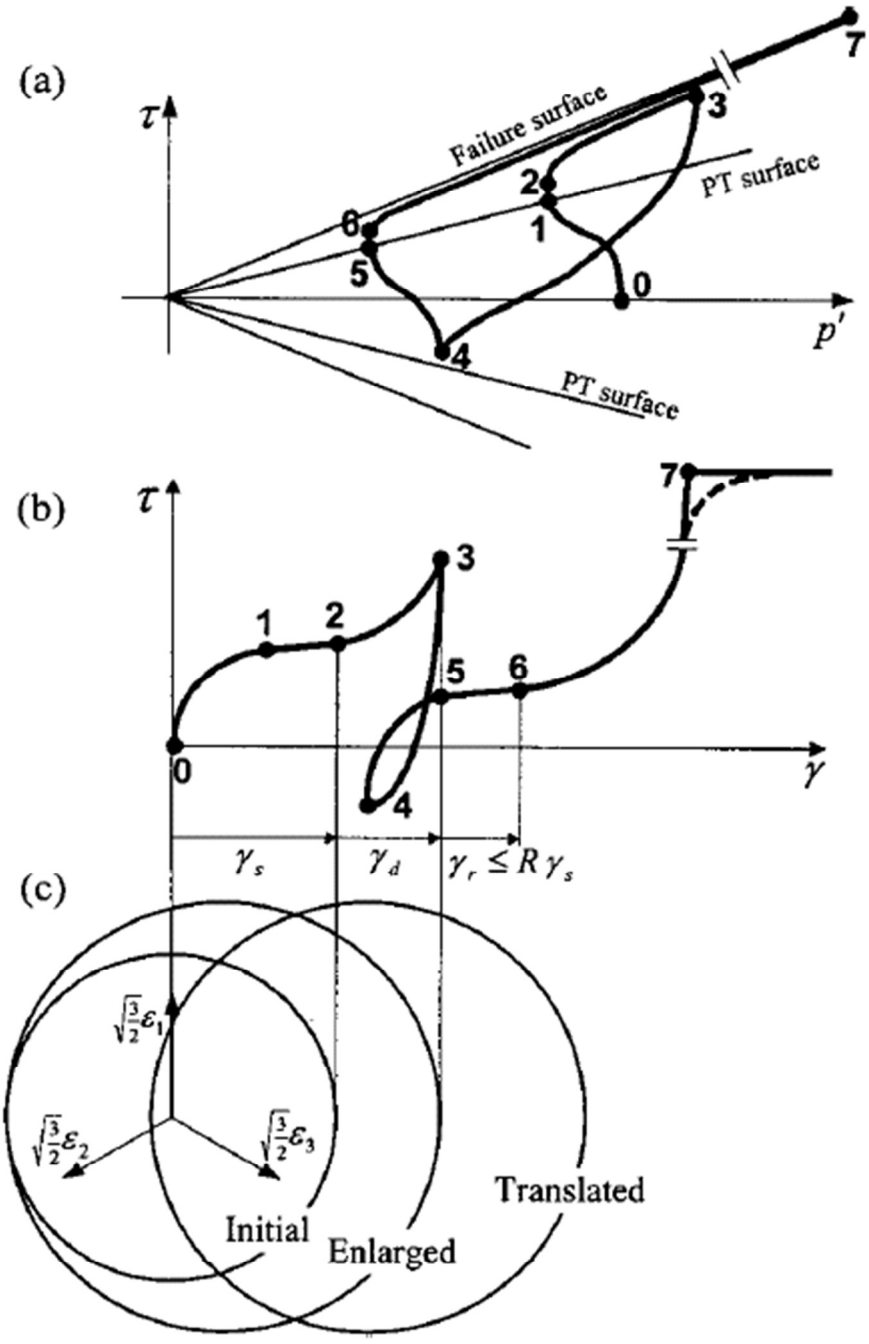

Figure 4. 27 Schematic of constitutive model response showing (a) octahedral stress τ, effective confinement p' response, (b) octahedral stress τ, octahedral strain γ response, and (c) configuration of yield domain [Elgamal *et al*., 2003].

The initial yield domain size γ_s depends on effective confinement *p'*. In the model used by Yang (Yang *et al*. 2003) this dependence is defined by the following simple linear relationship

$$\gamma_s = \gamma_{s\max} \cdot \left\langle \frac{p'_y - p'}{p'_y} \right\rangle \qquad (4.\ 39)$$

Where p'_y and γ_{smax} are model constants that may be easily derived from data such as monotonic simple shear tests. Effective confining pressure below which this mechanism is active is defined by the user defined constant $y_1=p'_y$. The maximum amount of perfectly plastic shear strain developed at zero effective confinement, is set through the user defined constant $y_{2=}\ \gamma_{smax}$.

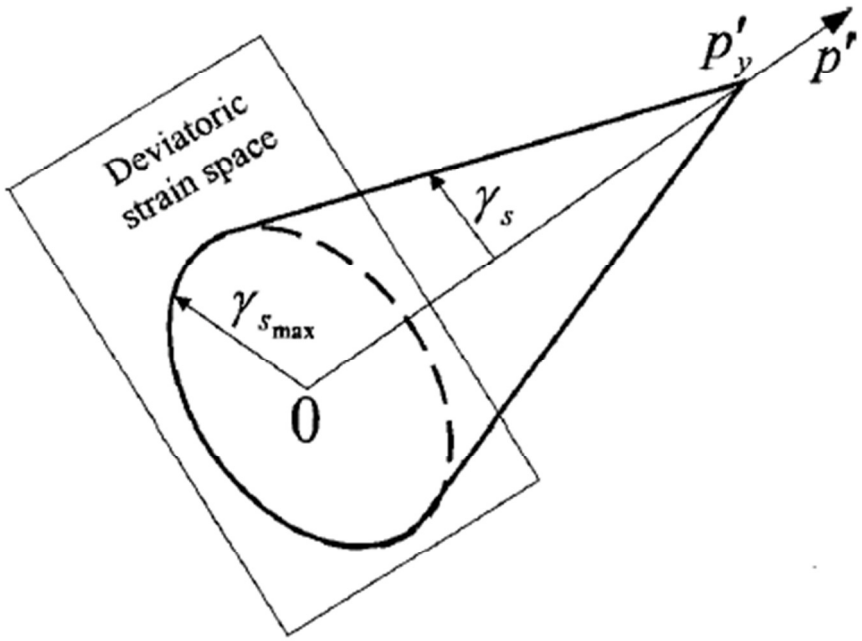

Figure 4. 28 Initial yield domain at low levels of effective confinement [Elgamal *et al*., 2003].

(d) Hardening rule

A purely deviatoric kinematic hardening rule is employed (Prevost, 1985), to conveniently generate hysteretic cyclic response. In the context of multi-surface plasticity, translation of the yield surface is generally governed by the consideration that no overlapping is allowed between yield surfaces (Mroz, 1967). Thus, contact between consecutive similar surfaces f_m and f_{m+1} (Figure 4. 29) must occur only at conjugate points with the same direction of outward normal. In this regard, Mroz (1967) proposed using the current (deviatoric) stress state **s** on the active surface f_m (Figure 4. 29) and its conjugate point *R* on the next outer surface f_{m+1}, to define the translation direction **μ** as follows (Figure 4. 29)

$$\boldsymbol{\mu} = \frac{M_m}{M_{m+1}}\left[\mathbf{s} - (p' - p'_o)\boldsymbol{\alpha}_m\right] - \left[\mathbf{s} - (p' + p'_o)\boldsymbol{\alpha}_{m+1}\right] - \quad (4.\ 40)$$

Where $(p+p'_0)\ \boldsymbol{\alpha}_m$ and $(p+p'_0)\ \boldsymbol{\alpha}_{m+1}$ are the centers of f_m and f_{m+1} respectively in the deviatoric plane. The trajectory of translation is shown as the shadowed zone in Figure 4. 29. With the direction of translation defined, the amount of translation dμ may then be obtained by satisfying the consistency condition f=0 (Mroz, 1967). After updating the active surface f_m, all inner surfaces are translated to be tangential at the updated stress state ($\boldsymbol{s}$+d$\boldsymbol{s}$) on f_m. The translation rule of (4. 40) was subsequently adopted by Dafalias and Popov (1975) in two-surface models, and by Prevost (1978a, b, 1985) in multi-surface model formulations.

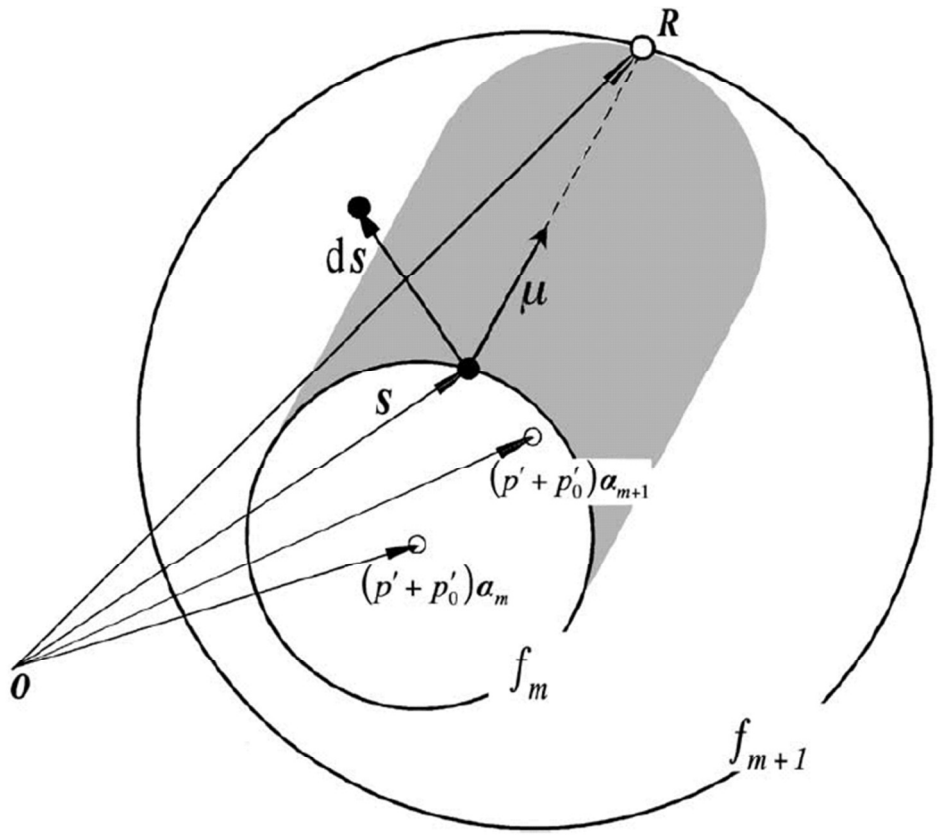

Figure 4. 29 Mroz(1967) deviatoric hardening rule

Elgamal (Elgamal *et al*, 2003) report that in numerical implementation experience, Mroz's rule [Eq. (4. 40)] is found to demand a high level of computational effort under certain loading conditions. This is particularly evident at low confinement levels where yield surfaces are of increasingly small size in the deviatoric plane. In such cases, even with relatively small stress increments, the updated stress state (**s**+d**s**) may still lie outside the trajectory of inner surface translation (Figure 4. 29), and the consistency condition cannot be satisfied. In view of the above, a new translation rule **μ** (Figure 4. 30) was defined (Parra, 1996):

$$\boldsymbol{\mu} = [\mathbf{s}_T - (p' + p'_o)\boldsymbol{\alpha}_m] - \frac{M_m}{M_{m+1}}[\mathbf{s}_T - (p' - p'_o)\boldsymbol{\alpha}_{m+1}] \qquad (4.\ 41)$$

where s_T is the deviatoric stress tensor defining the position of point *T* (Figure 4. 30) as the intersection of f_{m+1} with the vector connecting the inner surface center $(p+p'_0)$ $\boldsymbol{\alpha}_m$ and the updated stress state ($\boldsymbol{s}$+d$\boldsymbol{s}$). This rule [Eq. (4. 41)] is also based on the Mroz (1967) conjugate-points concept, and allows no overlapping of yield surfaces. Use of point *T* to define conjugate points eliminated the numerical challenges mentioned above, as the updated stress state is now always within the inner surface translation trajectory.

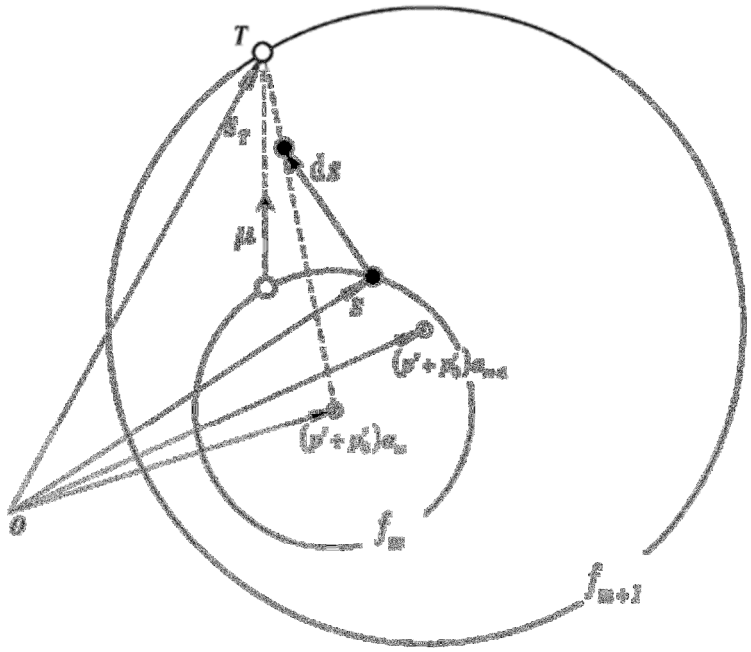

Figure 4. 30 New deviatoric hardening rule (after Parra, 1996).

The concept of using the updated stress state to define a surface translation trajectory was employed earlier by Dafalias and Popov (1977), for an inner surface of vanishing size (vanishing elastic region in a bounding surface formulation).

(e) Summary of input parameters

For OpenSees, four types of soil profile properties are needed:
1. Parameters describing the yield surfaces (for both sand and clay): either defining the modulus reduction at different strain values or a hyperbolic backbone curve (in terms of small-strain shear modulus and reference strain)
2. Parameters controlling contraction and dilatancy response (flow rule).

3. Properties of each layer and visco-elastic halfspace: thickness, saturated (or wet) unit weight, low-strain shear modulus and bulk modulus; unit weight and shear wave velocity of visco-elastic halfspace;
4. Frequencies/modes for the Rayleigh damping formulation.

Table Table 4. 1 lists the six constitutive parameters used in this study

Symbol	Name
c_1	Contraction parameter c (rate of contraction in 0-1 phase dependent on soil type)
d_1	Dilation parameter 1 (rate of dilation above PT line phase 2-3 dependent on soil type)
d_2	Dilation parameter 2 (rate of dilation above PT line phase 2-3 dependent confinement)
y_1	Liquefaction parameter 1 (l_1) (Effective confining pressure below which this mechanism is effective p'_y)
y_2	Liquefaction parameter 2 (l_2) (Maximum amount of perfectly plastic shear strain developed at zero effective confinement γ_{smax}.)
y_3	Liquefaction parameter 3-(l_3) (Extension of the yield phase related to biased loading γ_r)

Table 4. 1 Constitutive input parameters for model Elgamal 2003

Further investigations on the input parameters and their values are given in the following Chapters.

4.3 Radiation of dynamic energy, element size and choice of control point.

Special issues in geometrical modelling are hereby briefly described:

a) The correct transmission of high frequencies with waves propagation requires that the maximum element dimension should not be too coarse comparing to the wave length. According to Kuhlemeyer and Lysmer [1973] the maximum element length should be around

$$h_{\max} \le \frac{1}{5} \div \frac{1}{8} \cdot \left(\frac{V_s}{f_{\max}} \right) = \frac{1}{5} \div \frac{1}{8} \cdot \lambda \qquad (4.\ 42)$$

Where V_s is the shear wave velocity, f_{max} is the maximum frequency to be transmitted and λ the wave length. For FLAC model the coefficient $\lambda/10$ was considered while $\lambda/5$ was considered for DYNAFLOW model.

b) The energy associated with the wave that are reflected form the structure the bottom and the lateral boundaries will be reflected back into the model unless special *absorbing boundaries* or *layers* are used to simulate the wave propagation into the half space.

Generally speaking it is possible to group absorbing boundary or layers into the following groups:

- Elementary boundaries. Elementary boundaries conditions are those in which either displacements (D: Dirichlet condition) are zero or forces (N: Neumann condition) are zero. Usually the conditions imposed is the one corresponding to the free field conditions that is free horizontal movement and zero vertical movement. This type of boundary reflects the the incoming waves and should be used with a wide enough model. Smith [1974] proposed to impose the D and N conditions alternatively to the normal and tangential direction of tangential direction of the boundary but in this is not sufficient to eliminate the problem. Elementary boundaries should be placed far enough from the structure so that reflected waves are damped out.

- Local boundaries. Local boundaries were proposed first by Lysmer-Kuhlemeyer [1969] and they can be represented by dampers connected to the model boundary and with characteristics that are depending on the properties of the local soil. This boundary can perfectly absorb the incoming wave only in the case that it is perpendicular to it; moreover strains must be low so that the soil can be considered in the linear deformation range.

- Consistent boundaries. Consistent boundaries can absorb perfectly all type of waves independently of the inclination. They can be interpreted as the results of condensation of the degrees of freedom of all nodes beyond the boundary on the boundary itself and therefore are not local. Since their definition of frequency dependent they can be implemented effectively only in codes formulated in frequency domain. These boundaries were first formulated by Lysmer-Wass [1972] for plane waves only and were further extended to more general case.

- Absorbing layers: are based on the idea to surround the model by areas where the incoming wave is trapped as once entered is damped. This can happen in several ways, for example by including a compound parabolic collector where the wave undergoes multiple reflections [Madhabhushi, 1993] or as Sochacki *et al*. by including an attenuation term proportional to the first time derivative.

Regarding the lateral boundaries in FLAC, the free field motion as it would be in absence of structure, is automatically calculated and is applied together with viscous dashpots as represented in Figure 4.31.

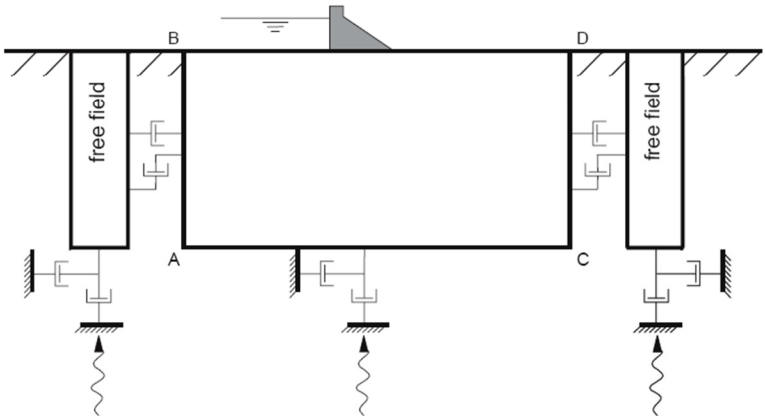

Figure 4.31 Model for seismic analysis of surface structures and free field mesh [FLAC 5.0, User manual]

The lateral boundaries in Dyanflow are similar except for the fact that free field motion must be calculated separately and applied to the lateral nodes by the user. Moreover no dashpot are included so an elementary type of boundary rather than a local boundary type is considered.

Regarding the bottom part of the model both FLAC and DYNAFLOW allow the user to include local boundaries. The formulation and the way these boundaries were used are briefly explained.

More specifically, since the source strong motion database used is not providing specific information regarding local geology for the seismic events considered (Table 6. 2) it was assumed that recorded time histories come from a site where no strong impedance contrast is present that is the case of a homogeneous half space. In this condition incident waves will pass through the model lower boundary without generation of reflected waves.
The implementation of an appropriate boundary condition at the base of the soil column requires detailed knowledge of the nature of the prescribed seismic input, that is whether it corresponds to an incident vertically propagating motion or is the sum of an incident and a reflected motion. For both codes DYNAFLOW [Prévost, 1981] and FLAC [ITASCA,1992], propagating motion, are defined in terms of incident motion only (for codes such as Shake, EERA, NERA also reflected waves are included).
For the purpose of illustrating the features of the boundary formulation, the vertical propagation of shear waves is considered. The equation of motion may be expressed as:

$$u_{,tt} = G \cdot u_{,zz} \tag{3.59}$$

where z is the depth coordinate and u the horizontal displacement.

The fundamental solution of (3.59) can be expressed as

$$u(x,t) = I(t - \frac{x}{V_s}) + R(t + \frac{x}{V_s}) \tag{3.60}$$

Where I and R are two arbitrary functions of their arguments and represent respectively a upward and downward propagating motions named respectively *incident and reflected motion*. The following identities apply

$$I_{,x}+\frac{1}{V_s}\cdot I_{,t}=0 \tag{3.61}$$

$$R_{,x}-\frac{1}{V_s}\cdot R_{,t}=0 \tag{3.62}$$

After differentiating (3.60) with respect to t and x, the shear stress $\tau(x,t)=Gu_{,x}$ upon elimination of $u_{,x}$ and $R_{,t}$ can be expressed as:

$$\tau(x,t)=\rho\cdot V_s(u_{,t}-2\cdot I_{,t}) \tag{3.63}$$

If the incident wave encounters a *free boundary* at $x=0$ then imposing $\tau(0, t)=Gu_{,x}=0$ at that boundary it is possible to find

$$u(x,t)=I(t-\frac{x}{V_s})+I(t+\frac{x}{V_s}) \tag{3.64}$$

The reflected wave has the same shape and sign of the incident wave.
When an incident wave I encounters a *silent boundary*, it passes through it without modification and continues propagating. No reflected wave R, which would propagate back in can arise. Mathematically the boundary condition that must be satisfied for u at a boundary placed at $x=h$ is in order to absorb the downward reflected wave from the free boundary is the so called *radiation condition* that is obtained from (3.61) substituting at $x=h$, I with u

$$(u_{,x}+\frac{1}{V_s}\cdot u_{,t})_{x=h}=0 \tag{3.65}$$

Resulting in $R=0$ at $x=h$ and consequently

$$\tau(h,t)=-(\rho\cdot V_s\cdot u_{,t})_{x=h} \tag{3.66}$$

Since downward reflected wave and upward incident will have equal intensity and shape, the shear stress required for having transparent boundary in both directions is doubled.

$$\tau(h,t)=-(2\cdot\rho\cdot V_s\cdot u_{,t})_{x=h} \tag{3.67}$$

Such boundary condition can be used in both FLAC and DYNAFLOW, is frequency independent and is local in space and time. It is exact for linear systems only, and therefore requires that the boundary be placed at a sufficiently large distance such that the response be linear at that distance.
c) Another issue is the choice of the point at which the reference project earthquake is defined. Usually the reference earthquake is defined at the outcrop. This is both because earthquake registrations are usually done on the surface and also because the amplitude and frequency content of the earthquake recoded at different depth is different. Usually design earthquake is specified on stiff outcropping soil.

4.4 Soil-wall interaction and possible separation

Veletsos and Younan [1997], have shown that one of the limitations of the solution the have proposed is the perfect bonding between soil and wall. In reality when tensile pressure induced by soil-wall movement exceed the gravitational one the soil separates from the wall and wall shear and moment will increase. The effect of such increase may have been compensated by shear stiffness non homogeneity. On the other hand Psarropoulos *et al*., 2005, show that neglecting tensile stress as unrealistic, leads to an increase in shear force and even greater in bending moment as also effective length decreases. The importance of the correct modeling for soil-wall interface is therefore of great importance.

Gomez et al [2000] propose a hyperbolic type of constitutive model between shear stresses versus wall-soil relative displacements and Green and Ebeling [2002] show how the FLAC interface behaves similarly to such model. The model formulation of the wall soil interface for FLAC [Cundall and Hart 1992] can be illustrated by Figure 4.32

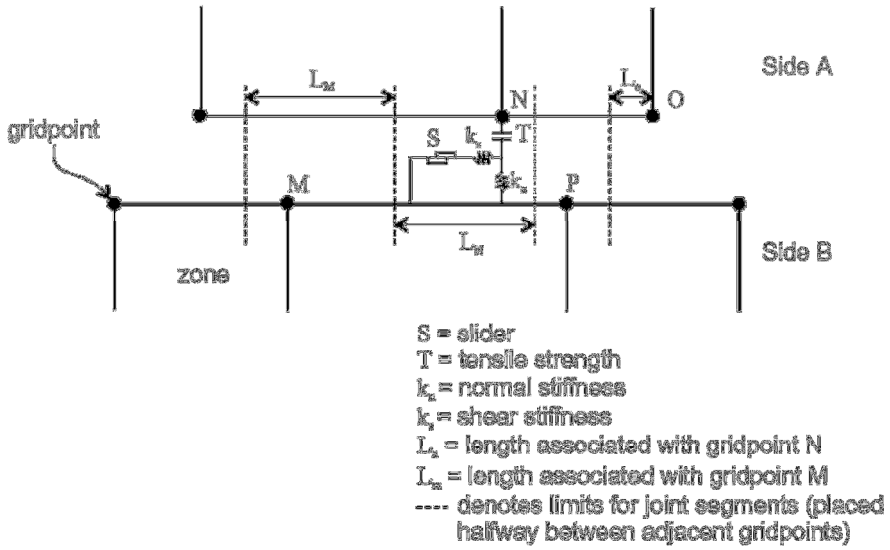

Figure 4.32 An interface represented by sides a and b, connected by shear (k_s) and normal (k_n) stiffness spring [FLAC5.0, User manual]

For a *glued interface* type no slip or opening can take place and elastic displacements occurs according to the given stiffness k_n and k_s. A *bonded interface* on the other hands behaves as a glued interface until in the normal direction, tension exceeds the tensile strength and slippage is allowed. For default the shear bond strength above which slippage occurs is one hundred times the tensile bond strength but it can be changed by the user. Is shear stress exceeds shear bond strength, slippage can occur in shear as well. Finally it is possible to allow shear slippage even if separation has not occurred and shier yield depends on friction and cohesion parameters.

A sketch of one of the interface model available in DYNAFLOW is represented in Figure 4.33. Either perfect friction (i.e., "stick") or frictionless (i.e., "slip") conditions may be achieved. A slide-line element is defined by three nodes and a spring constant or "penalty parameter," *k*. The connection from node A to node B defines the "slide-line" direction, and node C is the contact node.

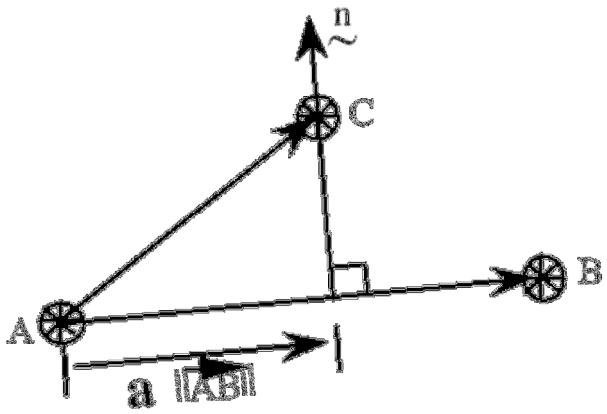

Figure 4.33 Slide line [DYNAFLOW user manual, 2006]

4.5 Possibility of liquefaction in saturated soil

As explained in Gazetas et al, [2004], performance of flexible retaining structures during past earthquakes, has been very strongly dependent on their susceptibility to liquefaction. The plastic volumetric strain induced by shearing (dilatancy) in undrained situation and therefore at constant volume, induces pressure build up, decrease of effective stress and loss of strength which may eventually leads to soil liquefaction. In order to properly capture such behavior, a two phase, effective stress analysis must be performed including a constitutive model which incorporates dilatancy effects. The multiyield material model formulated by Prevost [Prevost, 1978, 1980] based on a anisotropic hardening rule is a generalization of the model proposed by Iwan and is formulated in effective stresses. Flow rule is non associated and several Vom Mises like yield surfaces are nested into each other [Mroz, 1977]. Critical state [Schofield-Doctoral Thesys in Geotechnical Engineering , G. Li Destri Nicosia

Wroth, 1978] is defined as the set of points for which the plastic modulus associated to the outer yield surface is equal to zero. Input parameters for the model can be obtained through compression-extension triaxial tests and cyclic shear tests. Tested under stress paths different from those of these tests, it shows also a good agreement to experimental data [Prevost, 1985]. This model is therefore a complete and good model.

Opensees MYPD model, as explained in 4.2.3, is a development of the Prevost multiyield model.

FLAC *Finn model* and *hysteretic damping* as, as explained in 4.2.1 is a less rigorous model in that it is not based on a rigorous cyclic model formulation but is intended to catch the main behavioural features of soil as porous medium under cyclic loading.

4.6 Conclusions

In this Chapter several types of introductory issues were outlined and several conclusions and observations can be done:

a) It was shown that FEM and FDM are natural discretisations for:

Weak Form/Variational Form for FEM <--------> Strong Form for the FDM

b) Advantages and disadvantages of each of the method were mentioned and are here synthesized:

Table 4. 2 Main differences between FEM and FDM approach

FEM		**FDM**
More difficult to implement and to deal	Material non linearity	Easier to obtain convergence and to implement
Much shorter solution time for implicit formulation	Solution time	Time step restrictions leads to longer solution time
Usually Implicit	Solution scheme	Explicit
Usually Eulerian configuration and small strain	Strain	Lagrangian configuration and large strain easier to formulate

c) The general features of two FEM codes (DYNAFLOW and OpenSees) and one FDM code (FLAC) were described.

d) Several specific issues in numerical modeling for earthquake geotechnical problems were introduced step by step and for each of these topics detailed description of the approach of each of these three codes was done.

e) A synthesys of the main strong/weak points of the three codes examined is hereby introduced:

Table 4. 3 Main differences between DYNAFLOW, Opensees and FLAC

	DYNAFLOW	**OPENSEES**	**FLAC**
Easiness to learn	Requires an experienced user to teach	Extensive material and support in Internet	Well documented and user friendly
Versatility	The 3D formulation and multipurpose program	2D and 3D formulation, specific for earthquake engineering	Only plain strain (and axysimmetric) analysis for geomaterials types of problems
Solution time	Short	Short	Long
Material models specific for cyclic modeling	Yes	Yes	No

5 APPLICATIONS TO BENCHMARK CASE

Flexible retaining walls can be used for temporary or permanent structures: the sheeting or walling selected for a particular project may provide temporary soil support prior to permanent substructure construction, or it may serve as temporary soil support before being incorporated into the works as the permanent means of soil retention. Both anchored and non-anchored flexible retaining structures are usually constructed of steel sheet-piling walls or concrete diaphragms but aluminium or wood are also used. Design procedures, however are similar no matter the material used.
The type of peripheral sheeting will be influenced by the substructure construction method and will vary geographically due to soil and groundwater conditions, proximity to the source of materials and the skill of local contractors. Typical applications of flexible structures include waterfront facilities, excavation retention structures and single-wall cofferdams. Some examples are shown from Figure 5.1 to Figure 5.4 [M. Puller, 1996].

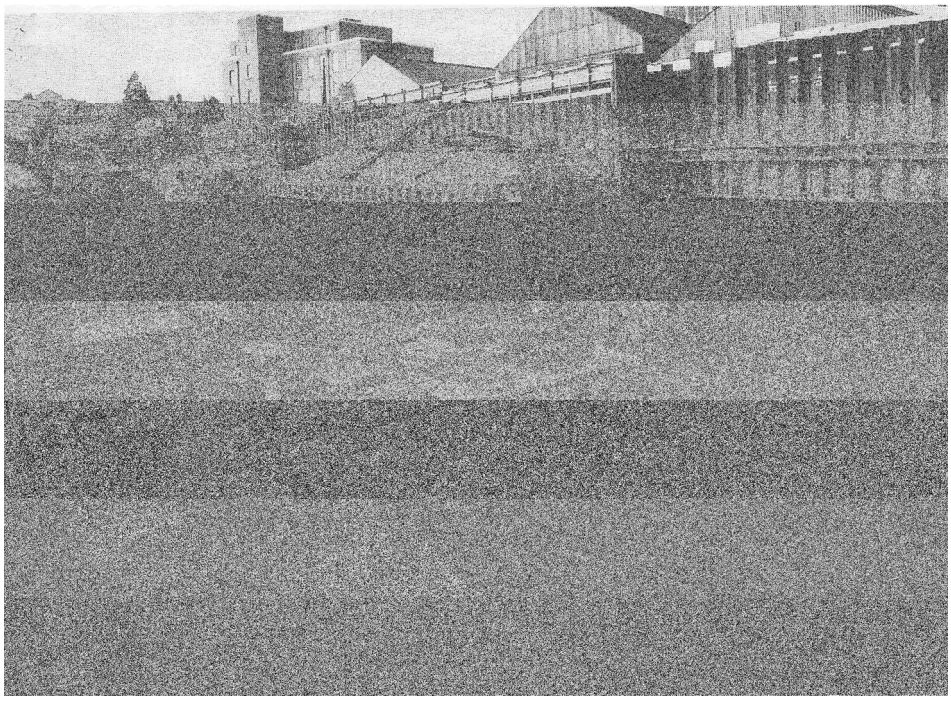

Figure 5.1 Anchored sheet piles in London Clay (telephone switch centre) [M. Puller, 1996].

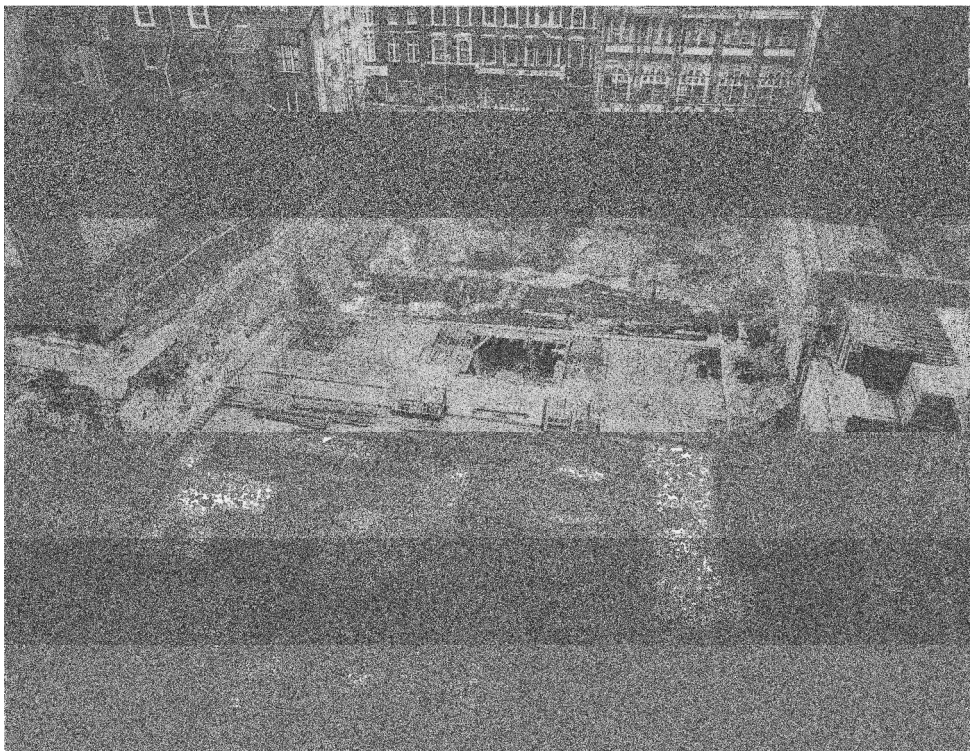

Figure 5.2 Diaphragm wall anchored below existing property and highway (Croydon, UK) [M. Puller, 1996].

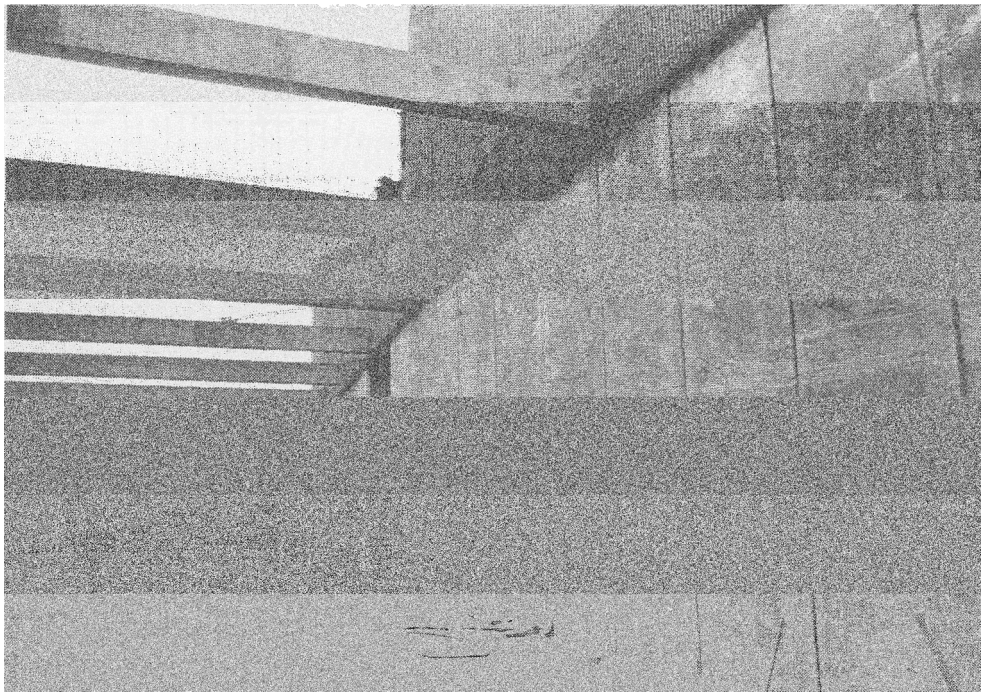

Figure 5.3 Precast diaphragm wall using Prefasil system (Schipol, Nederlands) [M. Puller, 1996].

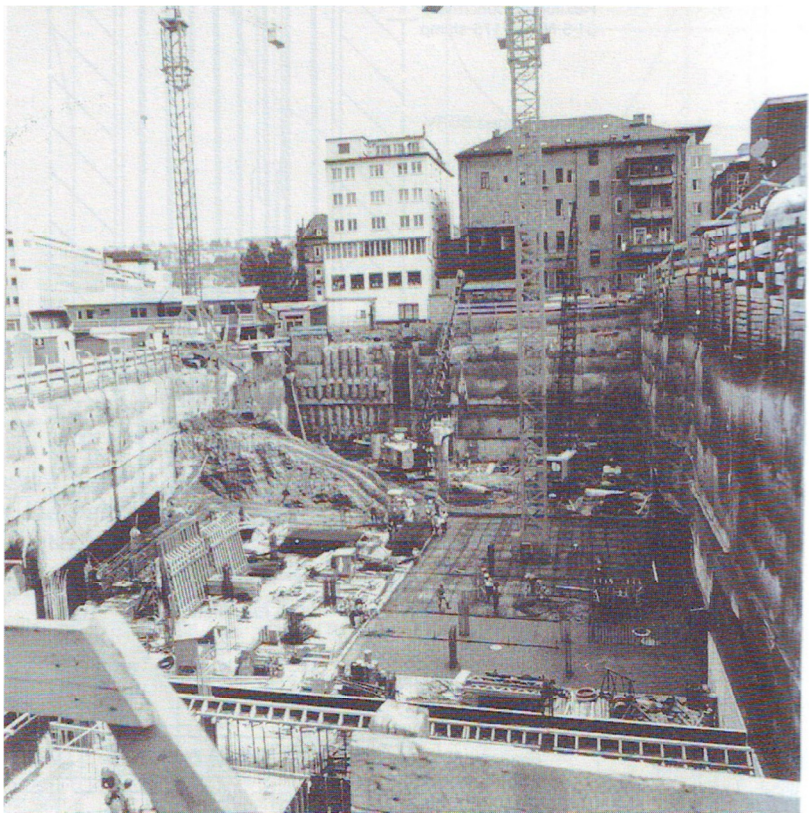

Figure 5.4 Composite use of contiguous bored pile walls and steel soldier beams (Courtesy of Bauer, Stuttgart) [M. Puller, 1996].

The purpose of this chapter is mainly to describe a benchmark case model of dredged cantilever walls in homogeneous granular soil, its geotechnical features including backbone stiffness degradation curves and its structural features including a pre-design largely based on pseudostatic Eurocode 8 methodology.

5.1 Benchmark case study.

The wall considered in a reference example [Fardis, 2005] is originally conceived as made up by contiguous bored pile, similar to those shown in Figure 5.4, having each diameter equal to 1m and 1,5m spacing between pile axis. Thickness of the walls is negligible with respect to its height, shear deformations are negligible and an elastic Bernoully 1D beam element is used to model the diaphragm wall. Corresponding mechanical properties of the wall, assuming characteristic concrete strength f_{ck}=30MPa are summarized in Table 5. 1.

Table 5. 1 Mechanical properties for unit length of diaphragm wall

E (GPa)	I (m^4/m)	A (m^2/m)	ρ (t/m^3)
28.6	0.03272	0.523	2.548

Mechanical properties of soil medium including soil/wall friction angle are summarized in Table 5. 2. The choice of $\delta'_{ak}=0$ has the effect of maximizing active thrust whereas $\delta'_{pk}=\phi$ allows for a higher passive resistance than assuming the conservative value of zero proposed by EC8 part 5 when using M-O solution. This alternative choice will not result in unsafe design because a lower bound solution for the coefficient of passive pressure [Lancellotta, 2007] will be used for pseudostatic design.

Table 5. 2 Soil properties

E_0 (MPa)	ν -	ϕ'_k (°)	ρ_k (t/m^3)	δ'_{ak} (°)	δ'_{pk} (°)
125	0.25	34	2.04	0	34

Regarding design soil strength parameters EC8-5 suggests for cohesive soils to reduce the undrained shear strength (Cu) by a factor γ_{cu}=1,4 and for cohesionless soils to reduce the angle of shear resistance in terms of either total or effective strength respectively by γ_{φ}=1.25 or $\gamma_{\varphi'}$=1.25. These combination of factors are assumed in case of approach 1 combination 2 (A2M2) of D.M. 14/01/08 (corresponding to D.A.1C.2 in EC7) which is indicated as most critical for geotechnical stability.

The homogeneous soil profile has value of Young modulus for small strain E_0 equal to 125 (MPa). This is the reference value for dynamic loading conditions, while for static limit states, larger reference displacement are considered and reference Young modulus E_s equal to 25 (MPa). Mass density ρ=2.04 (t/m^3) and friction angle ϕ'=34(°). Knowing Poisson ratio ν, E_0 and mass density ρ it is possible to calculate the shear modulus and shear wave velocity in soil $Vs=(G_0/\rho)^{0.5}$.

Based on the average value of shear wave velocity Vs=157 (m/s), the soil category can be identified as D type corresponding to a soil amplification factor equal to S=1.35 according to Italian OPCM 3274/2003 and EC8 part 1 (Type 1 spectrum for predominant earthquakes having surface wave magnitude M_s>5.5). The most recent Italian Building code (D.M. 14/01/08), instead, relates the value of such soil factor not only to the soil shear wave velocity but also to the wall height.

A reduction factor for the pseudostatic acceleration accounting for how much displacement can the wall tolerate equal to *0.5* is assumed. According to EC8 part 5 (Annex E-E.1) this coefficient corresponds to the ratio between the design acceleration and the maximum allowable acceleration and the inverse of such ratio is called r coefficient; on the other hand in the recent Italian Building Code (D.M. 14/01/08) this factor is simply plotted as a function of the allowable wall displacement that is admissible without strength reduction.

The resulting pseudostatic acceleration coefficients is respectively K_h=*0.23625*, K_h=*0.1687* and K_h=*0.1012* assuming respectively (see (3.7)) a_h=PGA/g=0.35, a_h=PGA/g=0.25 and a_h=PGA/g=0.15 which correspond to reference PGAs recorded at outcropping horizontal soil of type A (rock) placed respectively in Zone1, Zone2 and Zone3 of O.P.C.M. 3274/2003.

In order to investigate effect of earthquake polarization on retaining structure the model analysed (Figure 5.5) includes two walls placed in front of each others. Distance between the walls is chosen high with respect to wall length this is done in order to minimize reciprocal interaction. Upper boundaries are selected horizontal so as to have reflected waves

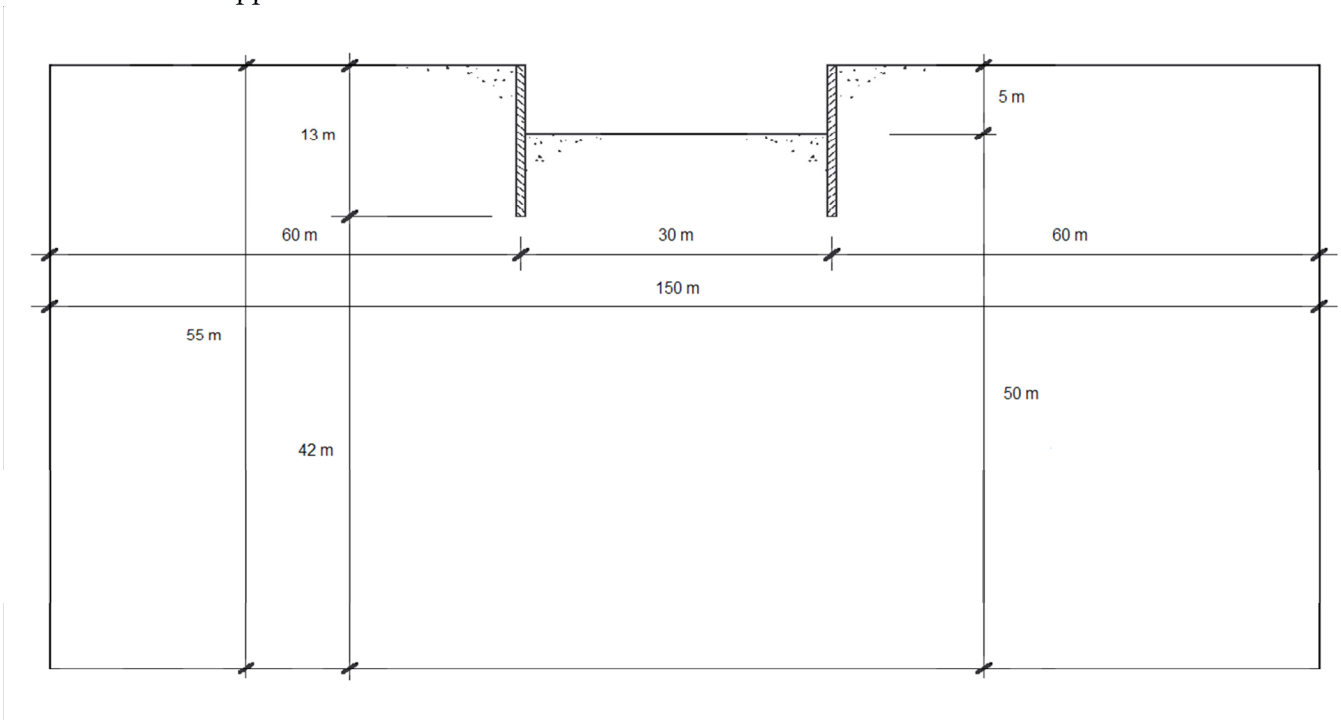

Figure 5.5 Benchmark model geometry

propagating perpendicularly with respect to outcropping soil avoiding topographical effects. Soil medium is homogeneous so there is no impedance contrasts at all along soil stratum. In order to size the walls static and pseudostatic fixed earth support scheme is assumed as explained in the following two paragraphs.

5.2 Soil characterization for cyclic loading

As a rule of thumb linear elastic models can be considered appropriate for shear strain values not exceeding 0.5e-5, visco elastic models for shear strain not exceeding the range between 1e-4 and 1e-3 and fully non linear model for higher values.
For active wedge and above all passive wedge to form, extensive soil yielding is expected in the vicinity of the diaphragm wall. For this reason it is interesting to investigate what is the effect of including fully non linear material model rather than elastic perfectly plastic model. This steps requires modification in both soil stress-strain formulation and in damping definition.
Modulus reduction behaviour, particularly for soil of low plasticity, is influenced by effective confining pressure. The effects of effective confining pressure and plasticity index on modulus reduction behaviour is combined by Ishibashi and Zhang[1993] in the form [Kramer,1996]

$$\frac{G}{G_{\max}} = K(\gamma, PI) \cdot (\sigma_m^{'})^{m(\gamma,PI)-m_0} \tag{5.1}$$

$$K(\gamma, PI) = 0.5 \cdot \left\{1 + \tanh\left[\ln\left(\frac{0.000102 + n(PI)}{\gamma}\right)\right]\right\} \tag{5.2}$$

$$m(\gamma, PI) = 0.272 \cdot \left\{1 - \tanh\left[\ln\left(\frac{0.00056}{\gamma}\right)^{0.4}\right]\right\} \exp(-0.0145 \cdot PI^{1.3}) \tag{5.3}$$

$$n(PI)=0 \text{ for PI=0} \tag{5.4}$$

Experimental data provided by Palmieri [Palmieri, 1995] about Toyoura sand are taken as reference. From such data in fact it can be seen that the value of small shear strain modulus of 50MPa (as in the soil model considered) can be expected for a vertical effective stress of 70 kPa which corresponds to about 4 m depth and can be assumed as average value around the wall.
Comparison between a selected experimental degradation curve [Palmieri, 1995] from resonant column test on Toyoura sand, for a given value of mean stress on one side and the analytical form of the degradation curve in the form given by Ishibashi and Zhang [1993] for the same mean stress value of 100kPa on the other side. Comparison of the experimental curve [Palmieri, 1995] and the analytical one is shown in Figure 5. 6 for 100kPa mean stress

value. Such comparison shows how close the form given by Ishibashi and Zhang [1993] is to experimental results. This backbone curve is used in 7.5 to calibrate the parameters required by the FLAC *hysteretic damping* model.

Figure 5. 6 Comparison between experimental [Palmieri, 1995] and analytical [Ishibashi and Zhang, 1993] degradation curve

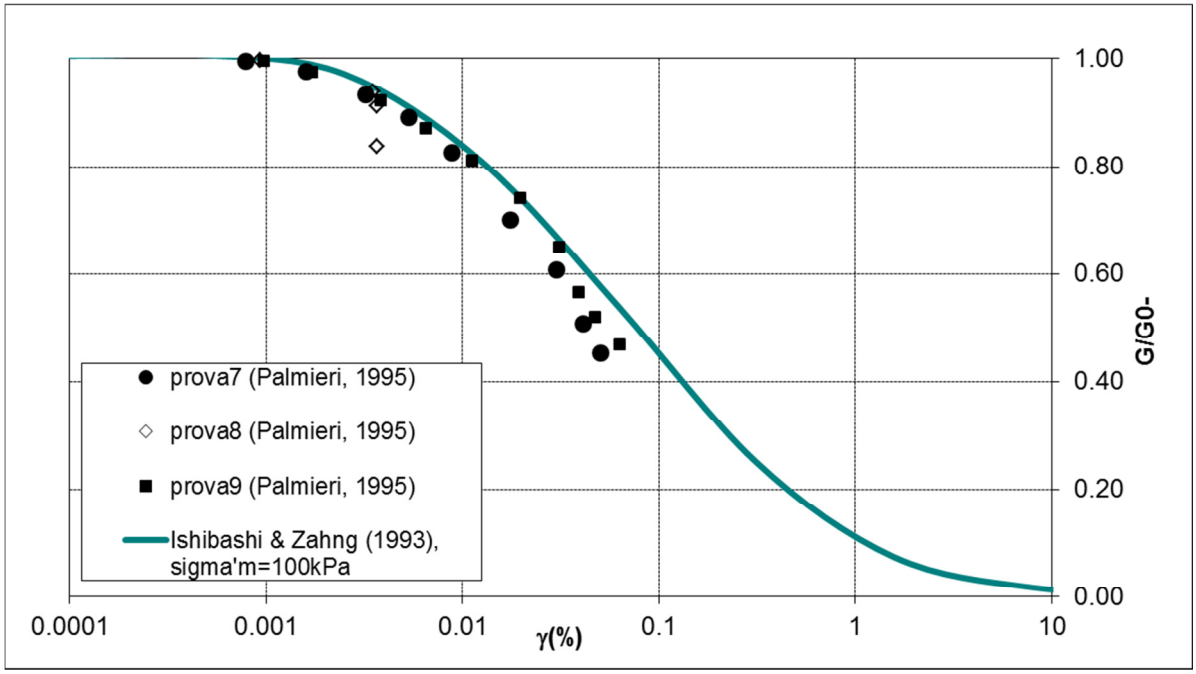

5.3 Limit equilibrium approach: static geotechnical design

Cantilever sheet pile or diaphragm walls are usually recommended for walls of moderate height (about 6m) or less above the dredge line. In such walls the diaphragm acts as a wide cantilever beam. For such type of wall, embedment depth will be high enough to have a fixity conditions for a point placed along the embedded height. Somewhat higher the curvature of the deflected wall is zero and, according to the Bernoulli beam scheme, there the moment is vanishing (a hinge). The basic principles for estimating the static lateral pressure and the bending moment distribution on a cantilever wall can be explained with the aid of Figure 5.7 [CIRIA, 1995]

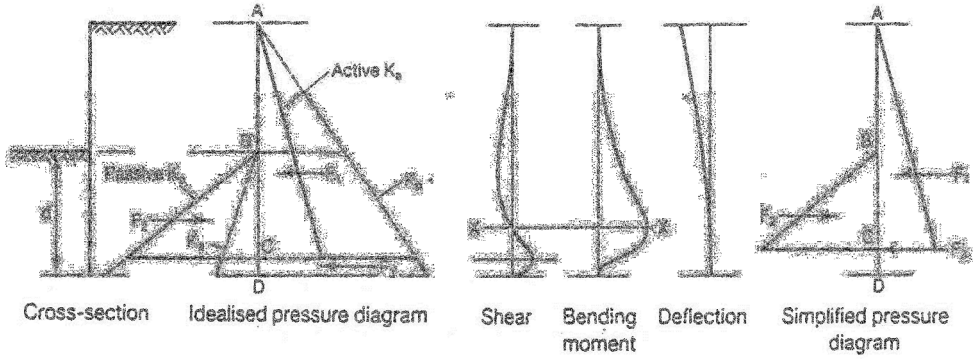

Figure 5.7 Lateral pressure distribution for fixed earth support [CIRIA,1995].

1. Active and passive pressure distributions are found after calculating K_a and K_p in the ways explained in Chapter 2.
2. The pressures at the toe of the wall are replaced by a resultant force F_3 acting at C.
3. Depth BC is found by assuming a level for C and calculating the moments for the forces F_1 and F_2 about level C; repeating until moment balance.
4. Increase the depth BC by 20% to give the design penetration BD.
5. Calculate the maximum moment at the point of zero shear.

For static passive coefficient calculation, as pointed out in 3.1.6, solution based on limit analysis proposed by Lancellotta [Lancellotta, 2002] or [Lancellotta, 2007] but with K_v=K_h=0 in
(3.27), can be used.
The importance of wall flexibility was shown first by Rowe [1952] using model tests. For seismic design the reduction indicated by Rowe is not accounted for.

5.4 Limit equilibrium approach: pseudostatic geotechnical design

For seismic case the same steps described in 5.3 are followed the only difference being the additional dynamic increment in active pressure and reduction in passive resistance. as shown in Figure 5.8.
Active pressure on backfill side is evaluated following codes prescriptions using Mononobe Okabe formula that are indicated both in O.P.C.M. 3274/2003 and EC8-5 (Annex E). The resultant dynamic increment of pressure ΔP_{ae} is evaluated as explained in 3.1.2 and leads for unit wall length, to a force increase ΔF_{ae}.

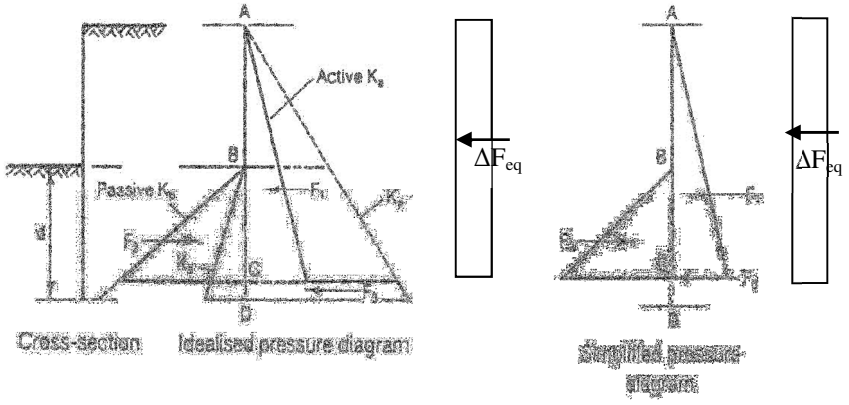

Figure 5.8 Lateral pressure distribution for fixed earth support, seismic case[CIRIA,1995].

For passive pressure calculation, the solution proposed by Lancellotta [Lancellotta, 2007] for passive pressure coefficient K_p described in 3.1.6 is used. The total passive pressure with an assumed triangular distribution is evaluated with the analogous of equation 3.1.4 used for evaluation of total active pressure as follows:

$$P_{tot} = \frac{1}{2} \cdot \gamma \cdot (1 \pm K_v) \cdot K_{pe} \cdot h^2 \qquad (5.5)$$

The results obtained for the bending moment distribution are those shown in Figure 5. 9 assuming values for PGA corresponding to the three seismic zones of O.P.C.M. 3274/2003 and consequently *Kh*. Soil type D is assumed meaning mean shear wave velocity in the upper 30m is lower than 180m/s.

Table 5. 3 shows that required penetration depth (BC) to satisfy the fixed earth support scheme is reported in the first column, and incremented by 20% as in BD. The total height is the sum of h=5m plus BD.

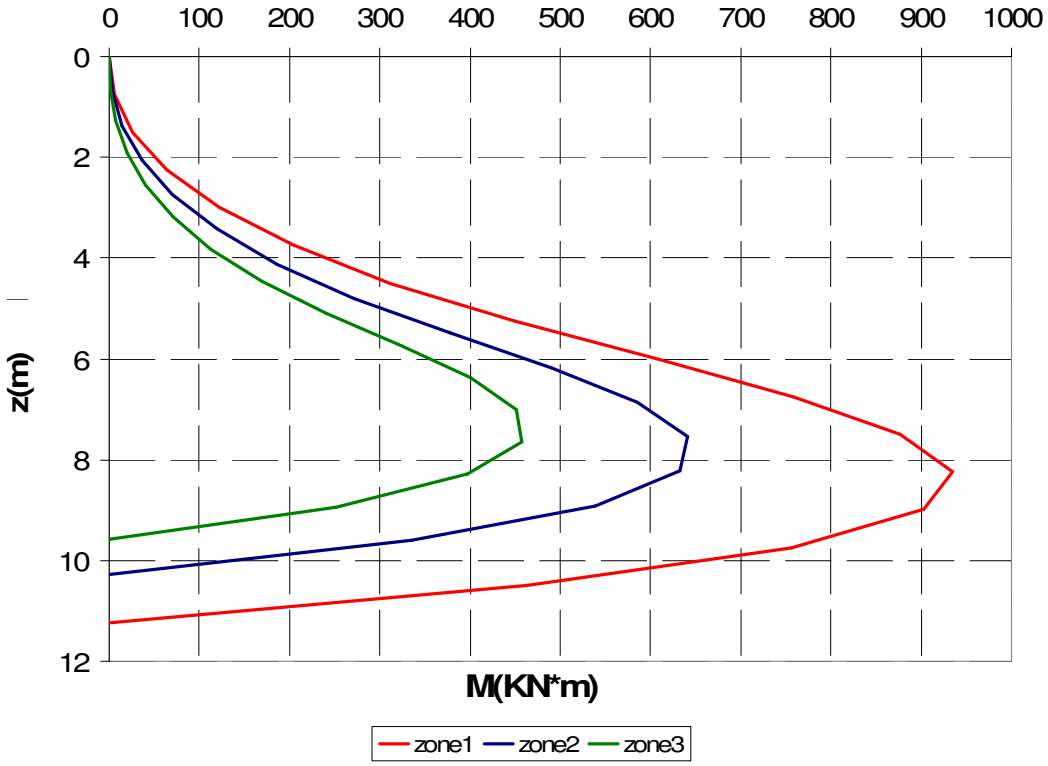

Figure 5. 9 Bending moment distribution for pseudostatic method (Soil D and different PGA equal to 0.35g, 0.25g and 0.15g respectively for zones 1,2 and 3).

Table 5. 3 Calculated embedment depth and total wall height

Zone (n)	BC (m)	BD (m)	H (m)
1	6.2	7.44	12.44
2	5.3	6.36	11.36
3	4.57	5.48	10.48

5.5 Limit equilibrium approach: pseudostatic geotechnical design for saturated case

In the case of a waterfront retaining structure, saturated backfill and water in front of the wall can be expected at the same time. In this case the presence of the water may alter the seismic performance of the retaining structure in different ways: 1) effects on the inertial forces 2) pore water pressure build up 2) hydrodynamic pressure. Under the assumption that the permeability of the soil is low enough to retain the water during earthquake shaking or restrained water conditions ($K \leq 10^{-3}$ cm/s) inertia forces, the active soil thrusts on the wall can ba calculated (Matzuzawa et al, 1985) modifying the expressions used for the dry case using:

$$\gamma = \gamma_b \cdot (1 - r_u) \tag{5. 6}$$

$$\psi = \tan^{-1} \cdot \left[\frac{\gamma_{sat} \cdot k_h}{\gamma_b \cdot (1 - r_u) \cdot (1 - k_v)} \right] \tag{5. 7}$$

where $\gamma_b = \gamma_t - \gamma_w$ is the buoyant soil unit weight and the excess pore pressure ratio r_u is the ratio between the soil pore water pressure and the initial effective confinement pressure. A value or $r_u = 1$ implies liquefaction is occurring. In order to consider the effect of pore water pressure build up on the hydrostatic thrust an equivalent unit weight of water must be considered as follows:

$$\gamma = \gamma_w + r_u \cdot \gamma_b \tag{5. 8}$$

Also the water pressure on the pool side must include in addition to the hydrostatic pressure, the hydrodynamic pressure according to Westergaard's solution (*Westergaard*, 1931). This solution considers a pressure resultant applied at 0.4H from the base of the pool of height H and equal to

$$\Delta P_{dyn} = \frac{7}{12} \cdot \frac{a_h}{g} \gamma_w \cdot H^2 \tag{5. 9}$$

Finally the excess pore pressure water pressure due to earthquake shaking $\Delta u(r_u)$ with excess pore pressure ratio r_u can be calculated considering a gradient equal to $\gamma' r_u$ in the saturated soil and an upper value at depth z_{top} equal to the total vertical stress at the depth z_{top}.
The resulting pressures distributions acting on the wall is shown qualitatively in Figure 2.1.

In order to consider one case for which liquefaction hazard is relevant (*Youd et al.*, 2001), the value of relative density D_r for the upper soil is assumed to be equal to 45%. As explained in more detail in Chapter 0, based on the correlation between *Dr* and the void index *e* and that between *e* and G_o the small strain shear modulus (*Ishihara*, 1993) it is possible to evaluate the shear wave velocity correspondent to D_r 45% at a mean reference pressure for a layer of 23m. The value of shear wave velocity corresponds to a soils category *C*. For this soil type the soil

amplification factor is equal to S=1.15 according to EC8 part 1 (Type 1 spectrum for predominant earthquakes having surface wave magnitude M_s>5.5)

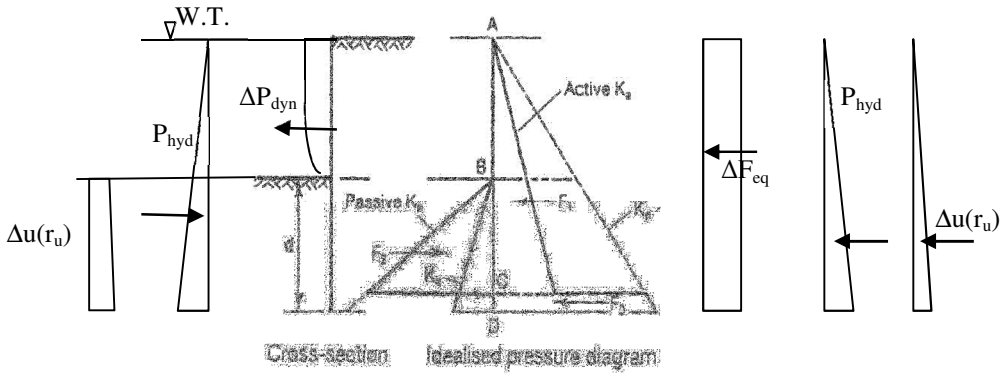

Figure 5.10 Lateral pressure distribution for fixed earth support, seismic case with saturated backfill and pore pressure build up [Ebeling and Morrison, 1992].

The results obtained for wall lengths are those shown respectively in Figure 5. 9 assuming values for PGA corresponding to the seismic zones 2 and 3 of O.P.C.M. 3274/2003 and consequently K_h and the limit value of r_u=30% . Seismic zone 1 cannot be included because for this value of r_u the threshold value of $K_{hlim}=tan\,(\phi-\beta)$ would be exceeded in case of PGA equal 0.35g.

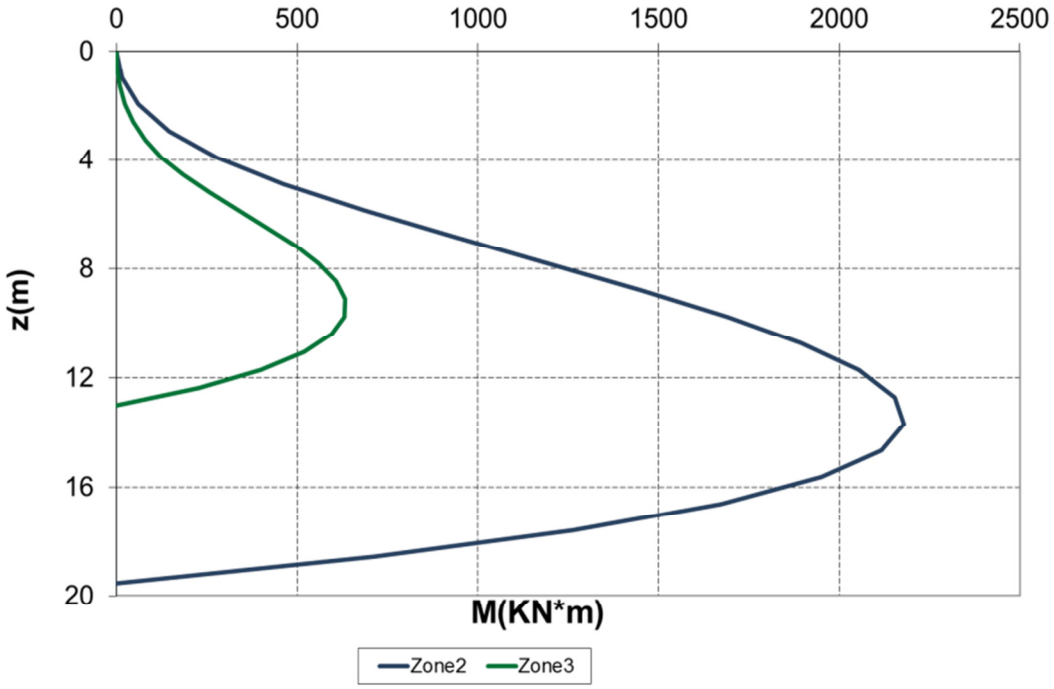

Figure 5.11 Bending moment distribution for pseudostatic method and saturated case (Soil C and different PGA equal to 0.25g and 0.15g respectively zones 2 and 3).

Table 5. 4 Calculated embedment depth and total wall height.

PGA (g)	BC (m)	BD (m)	H (m)
0.15	8.0	9.6	14.6
0.25	14.5	17.5	22.5

Due to the increase in bending moment values the wall thickness for the saturated case is increased to 1.2m for the purpose of the numerical analyses (I_{ela}=0.144m^4) and the envisaged reinforcement for concrete strength f_{ck} 40 MPa and ULS design would be according to EC2 around 1% of the area.

5.6 Summary

In this Chapter the geotechnical and structural features of the benchmark model analysed were described. Degradation curves for linear equivalent soil characterization were introduced based on experimental results on Toyoura sand and an analytical form for shear reduction of shear modulus and increase on damping ration was proposed showing the fitting to experimental results.
Limit equilibrium pseudostatic approach based on the methodology suggested by EC8- part 5 along with the Italian Building Code (D.M. 14/01/2008) were used to design a flexible diaphragm wall according to the fixed earth assumption to substain several levels of reference design accelerations up to 0,35 PGA for both dry and saturated backfill cases.

6 CRITERIA USED FOR SELECTION OF INPUT ACCELEROGRAMS

Parametric analysis were performed to identify value of those parameters used for the selection of sets of accelerogramms depending on the seismic zone and the return period of the design earthquake. To this purpose only zone 1 and zone 2 of the Italian seismic zonation were considered, and return period of 475 and 975 years correspondent to return periods assigned to structures f class 1 and 2 from the Building Codes of 14/09/2005.

6.1 Probablistic seismic hazard analysis

The most rational approach relies in performing seismic hazard analysis at the site by using the probabilistic *Cornell-Mc Guire* method, which results in a Uniform Hazard Spectrum (UHS) for a given return period (see Figure 6. 1 on the left), following a deagregation analysis, that consists in extracting form the hazard study the couples magnitude-distance which give the highest contribution to the probability of exceedance of a prescribed values of spectral acceleration for a given return period (AFOE Annual Frequency of Exceedance). Figure 6. 1 on the right shows an example of the results obtained by a deagregation analysis for the Fivizzano (MS) site placed in Zone II (moderate seismicicty) referred to a spectral period of T=0 (peak ground horizontal acceleration a_{max}) and a given return period (in this case 475 years). Each cell of the three dimensional histograms represents the specific contribution of the single couple of valued magnitude (M) and epicentral distance (R) to the probability of exceedance.

In the case shown in Figure 6. 1, the couple resulting in higher contribution is M = 5.4, R=13 km, and therefore a relatively small magnitude earthquake but a short epicentral distance. Based on the results of the deagregation analysis accelerogramms compatible with the couple M, R will be chosen. The average spectrum of accelerograms satisfying the M, R criterion, is compared with the Uniform Hazard Spectrum for the same return period in order to verify that the discrepancies are acceptable according to code prescriptions. Values of R and M can be

slightly modified with lower tolerances for M as it has a stronger effect than R on spectral shape.

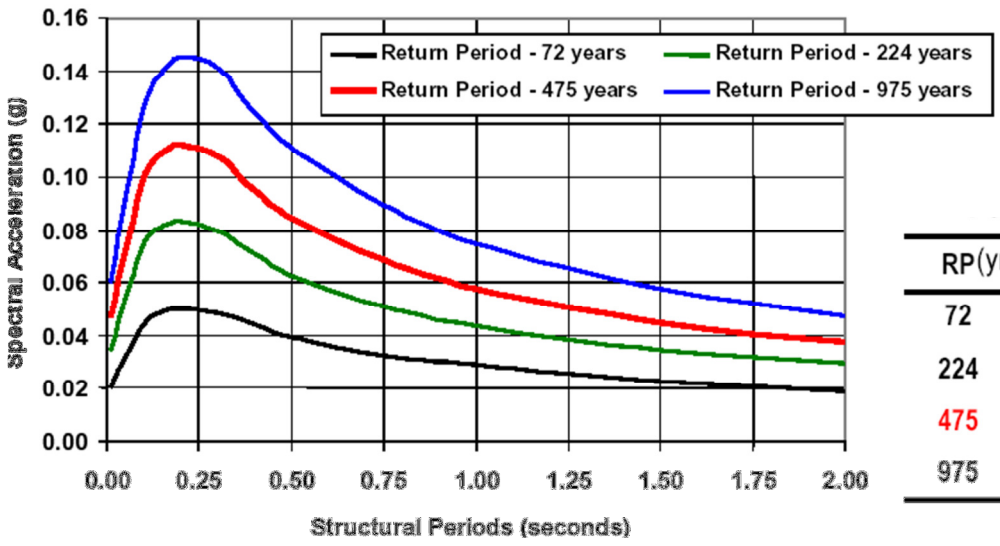

RP(yr)	PHA(g)	PVA(g)
72	0.022	0.013
224	0.032	0.019
475	0.041	0.024
975	0.041	0.024

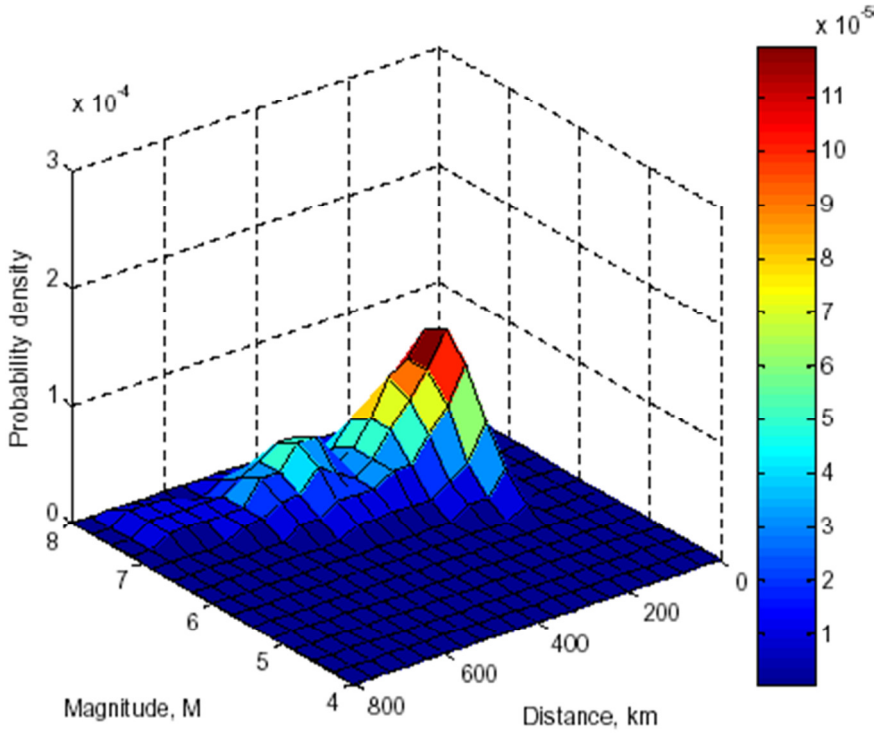

Figure 6. 1 (Up) UHS on stiffsoil for different return periods [Menon *et al.*, 2004] (Down) deagregation for 475 years [Menon *et al.*, 2004]

Stratigraphic conditions of selected accelerograms shall be preferably those of stiff soil type. For a specific site were soil conditions are different from stiff soil, the effect of different

stratigraphic conditions should be investigated performing a site response analysis which, in the case of topographical irregularities or a complex deep geology, should be performed with a bi-dimensional numerical modeling approach.

Only horizontal components are treated as for the case of flexible cantilever walls vertical component is less important and (D.M. 14/01/2008) maybe neglected. If used, vertical acceleration maybe thought unaffected by stratigraphic amplification and correlated through constant coefficients to the horizontal peak ground acceleration on stiff soil (0.3 or 0.5 for EC8-5).

Accelerogramms should be real recordings extracted from accredited *strong-motion databases,* two horizontal components and one vertical component. In fact according to EC8 and other international seismic codes, natural recording are to be preferred when available.

Hybrid accelerograms modified in order to meet the spectro-compatibility requirements maybe used [Silva e Lee, 1987; Abrahamson, 1998] while artificial accelerograms generated through a stochastic approach to meet magnitude-distance compatibility requirements [e.g. Sabetta e Pugliese, 1996; Boore, 2002] maybe used for comparison to the recorded ones while purely stochastic ones [Gasparini e Vanmarcke, 1976] may not be used at all. Also scaling factors for the recording is contained between 0.7 and 1.4. The four groups obtained from the selections of recorded accelerogarsms is shown in Figure 6. 1

Table 6. 1 Example of deaggregation analysis results

Group	Seismic Zone	Return Period (yy)	Site category	amax(g)	M	R(m)	Scale factor
1	I	475	A	0.3-0.4g	6.0-6.5	<30	0.7-4
2		975		0.42-0.56g	6.5-7.0	<30	
3	II	475		0.2-0.3g	5.5-6.0	<30	
4		975		0.28-0.42g	6.0-6.5	<30	

6.2 Selected time histories

Among these accelrograms selected through Probabilistic Seismic Hazard Assessments, three were chosen with features shown in Table 6. 2 with the criterion to be spectrum compatible and with spectral ordinates covering wide range of spectral frequency content.

Table 6. 2 Main features of seismic events considered [PEER, ISESD]

	Chalfant	Erzincan	Tortona
EARTHQUAKE	Chalfant Valley, 1986/07/20	Erzincan, Turkey 1992/03/13	Tortona, 2003/11/04
COUNTRY	U.S.A.	Turkey	Italy
STATION	Zack Brothers Ranch	95 Erzincan	
MAGNITUDE (M)	5.9	6.9	
DISTANCE (km)	11.0 (Hypocentral)	2.0 (closest to fault ruprture)	
PGA X-COMPONENT (g)	0.285	0.496	
PGA Y-COMPONENT (g)	0.207	0.515	
HIGH PASS FILTER (Hz)	0.1	0.2	
LOCAL GEOLOGY	-	-	
REFERENCE	PEER	PEER	

Time histories of the horizontal component used for the analysis are shown in Figure 6. 2 to 6.4
The resulting elastic spectra are plotted and compare to the EC8 Type1 spectrum used as reference for the pseudostatic (and spectral) analysis in Figure 6. **5**. Chalfant and Erzincan time histories spectra show more energy for higher periods than Tortona so different response can be expected depending on what is the predominant frequency of the system that will be analysed. Such feature should become evident for time history numerical analysis but not for pseudostatic analysis. PGA are equal to the spectral accelerations at T~0; as expected EC8 Type1 spectrum is an upper bound, enveloping the three spectra.

Recalling the observation regarding dynamic numerical modelling done in 4.3, any discretised medium has an upper limit to the frequencies that it can transmit, and this limit must be respected if the results are to be meaningful. Numerical distortion of the propagating wave can occur in a dynamic analysis as a function of modelling conditions. Both the frequency content of the input wave and the wave-speed characteristics of the system will affect the numerical accuracy of wave transmission. Kuhlemeyer and Lysmer [1973] show that for accurate representation of wave transmission through a model, the spatial element size, Δl, must be smaller than a fraction of the wavelength associated with the highest frequency component of the input wave.

$$\Delta l \leq \frac{\lambda}{5 \div 10} \tag{6. 1}$$

$$\lambda = \frac{V_s}{f_{\max}} \tag{6. 2}$$

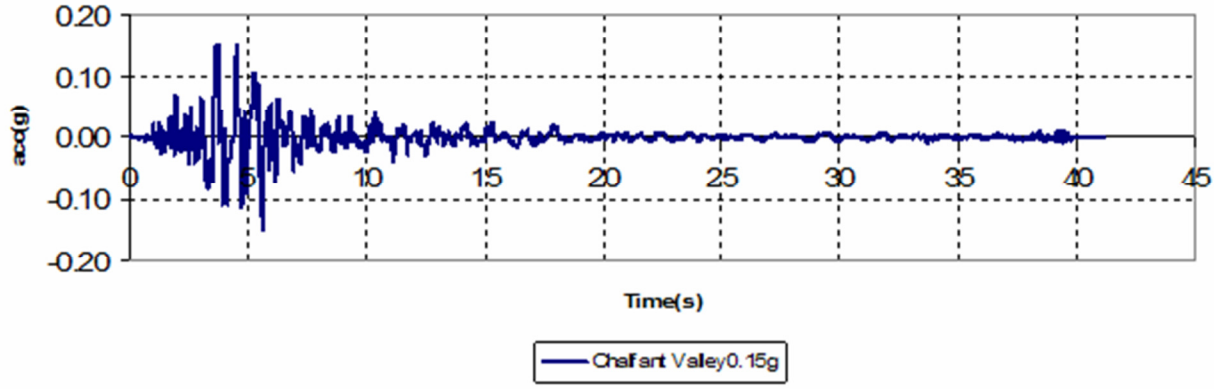

Figure 6. 2 Chalfant Valley accelerogram (scaled 0,15g)

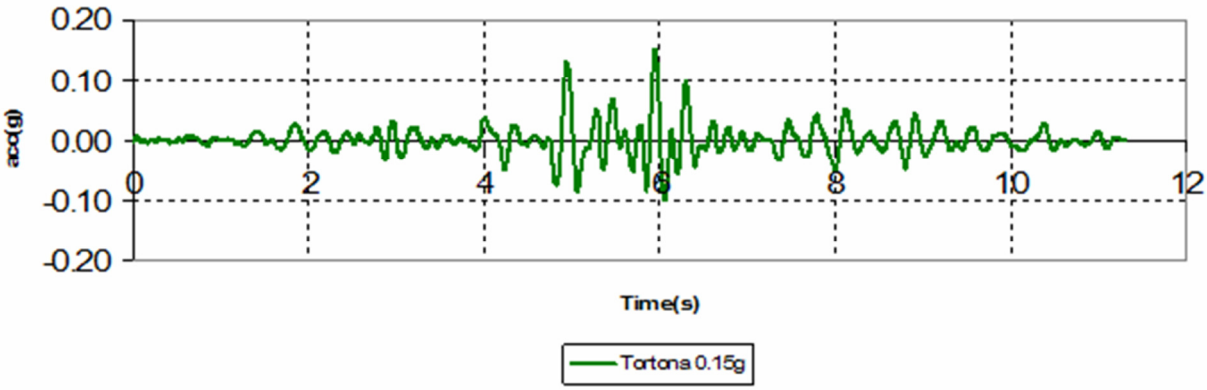

Figure 6. 3 Erzincan accelerogram (scaled 0,15g)

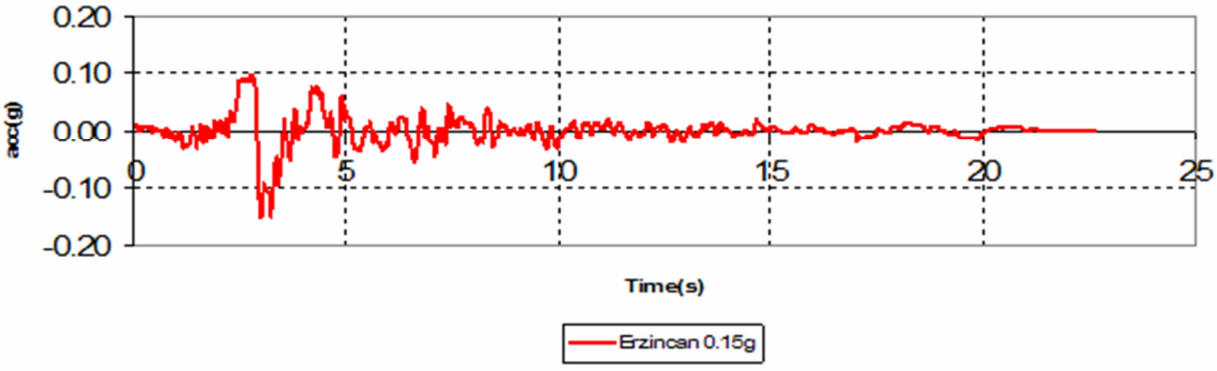

Figure 6. 4 **Tortona accelerogram (scaled 0,15g)**

Observing Figure 6. 7 it is possible to see that all three accelerograms have negligible energy for frequencies higher than 10-15Hz and therefore since V_s=157m/s the resulting maximum element size is Δl_{max}=1,14m and 2,28m for 10 and 5 respectively.

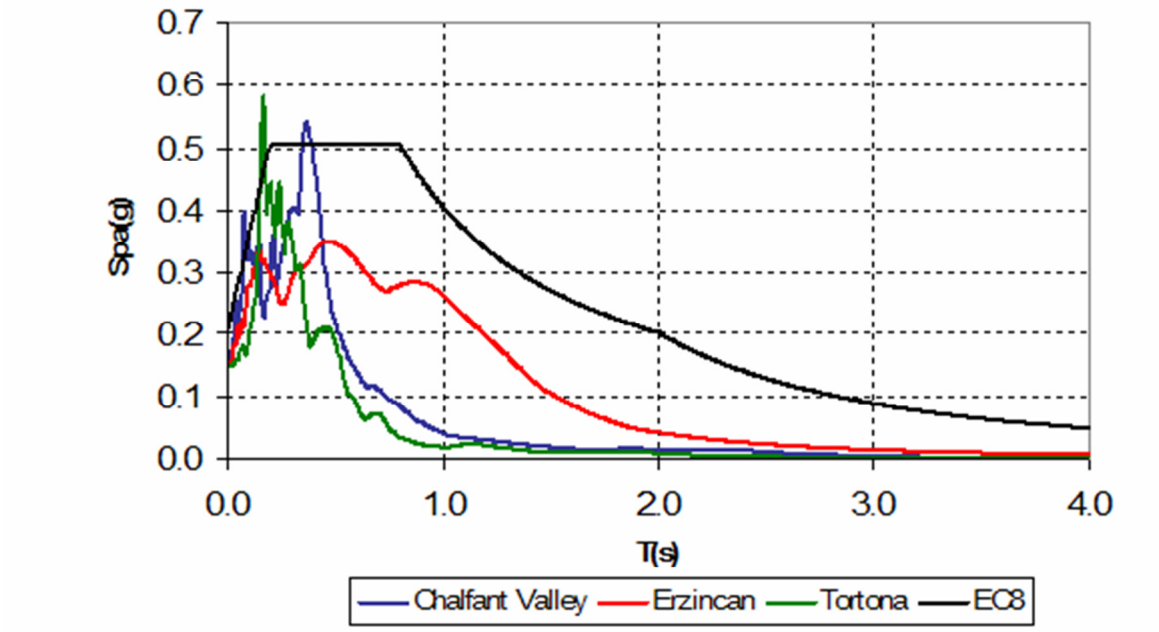

Figure 6. 5 Pseudo acceleration elastic spectra (5% damping) for input accelerograms compared to EC8 Type1 spectrum

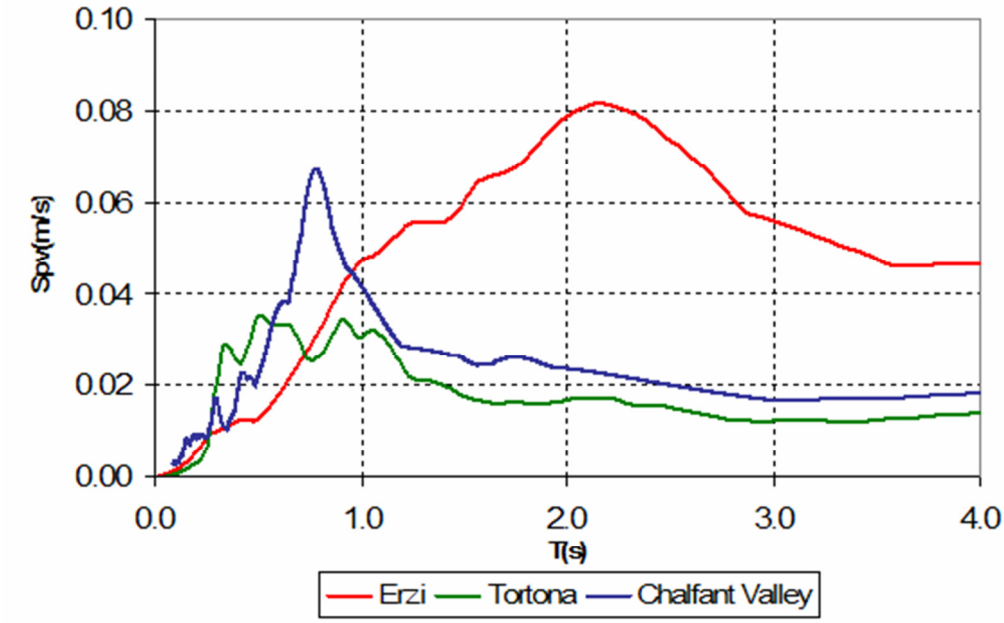

Figure 6.6 Pseudo velocity elastic spectra (5% damping) for input accelerograms compared to EC8 Type1 spectrum

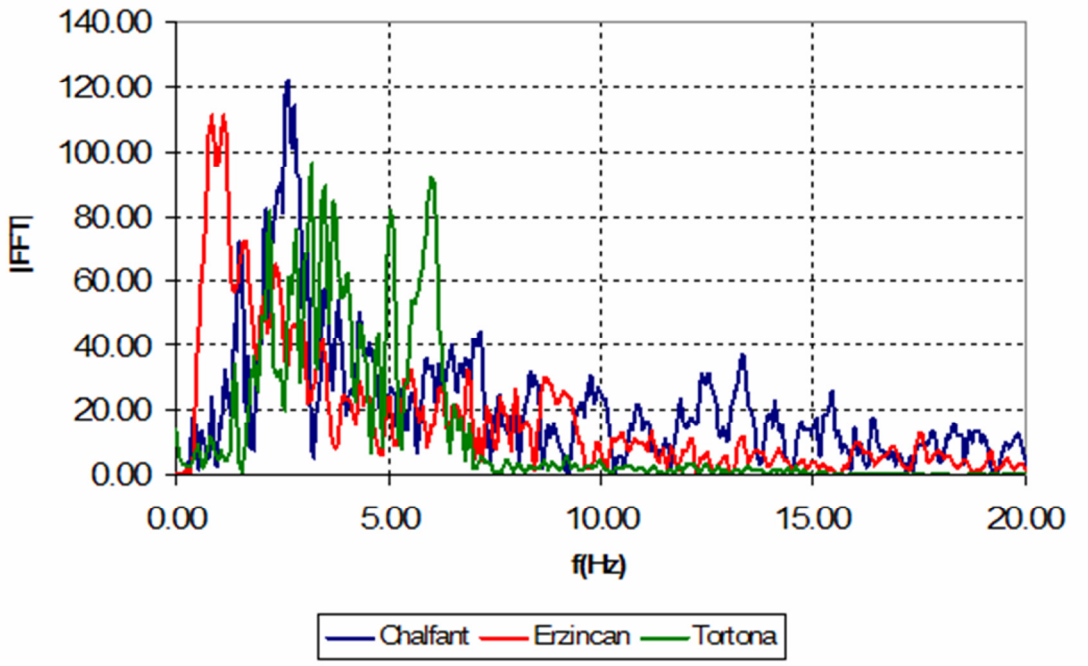

Figure 6. 7 Fourier Transform Amplitude for input accelerograms

6.3 Summary

As already mentioned in 3.2, those analysis and design methods based on the use of accelerograms such as pseudo dynamic and fully dynamic methods, present the additional complexity of choosing the most appropriate input accelerogram or sets of accelerograms. In this Chapter the *Cornell-Mc Guire* method was introduced resulting in a Uniform Hazard Spectrum for a given return period.
General procedures for site specific ground motion selections were explained and following three of the accelerograms were selected and compared in order to evaluate the frequency content of the input motion for the numerical analysis that will be shown later. Such frequency content is particularly important also for determining adequate mesh/grid size and for determining how to specify Rayleigh damping as it will be shown later.

7 RESULTS OF NUMERICAL ANALYSIS IN DRY CONDITIONS

As already mentioned in Chapter 3, among the different approaches for analysis and design of retaining strctures under earthquake loading, fully dynamic non linear analysis represent a more sophisticated but more complex and time consuming option.
At this point it is interesting to focus on the results obtained by using the finite difference code FLAC [Itasca, 2005] and the finite element DYNAFLOW code [Prevost, 1985] for the analysis of the benchmark test described already in 5.
First the static phase including the effect of gravitational forces will be analysed and later dynamic analysis will be observed and commented comparing the results of several types of modeling hypothesys and also those of the pseudo static method.

7.1 FLAC 5.0 model, static and pseudostatic loading

FLAC model with Mohr Coulomb criterion for the benchmark case is shown in Figure 7. 1

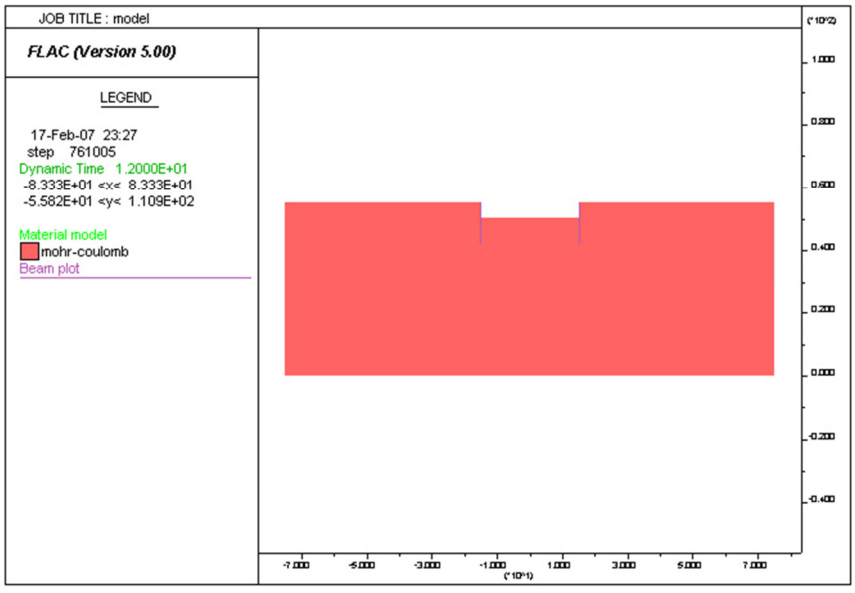

Figure 7. 1 FLAC model for benchmark case

Grid dimension is chosen by progressively reducing size and checking for convergence of the results. The final choice is for a square grid of dimension 1m·1m which satisfies also requirements set in 6.2. Soil wall interfaces (see 4.4) are made by elastic springs in both normal and shear direction with respect to wall axis. This choice does not allow for relative movement, yielding and sliding, along wall-soil interface. Interfaces connect wall nodes to grid nodes and have an *apparent stiffness* value *K* equal

$$K=B+(4/3)\cdot G \qquad (7.\ 1)$$

The first phase consists in applying gravity load, subsequently the so called static phase consisting of 5 steps of 1m excavation each is carried out up to 5m. Results in terms of bending moments and wall displacements are shown respectively in Figure 7. 2 and Figure 7. 3. From the bending moment distribution it is possible to observe a significant inversion in sign passing form the second to the fifth step. Also in displacement profile there is decrease in top displacement despite the increasing trend in the first four excavation steps.

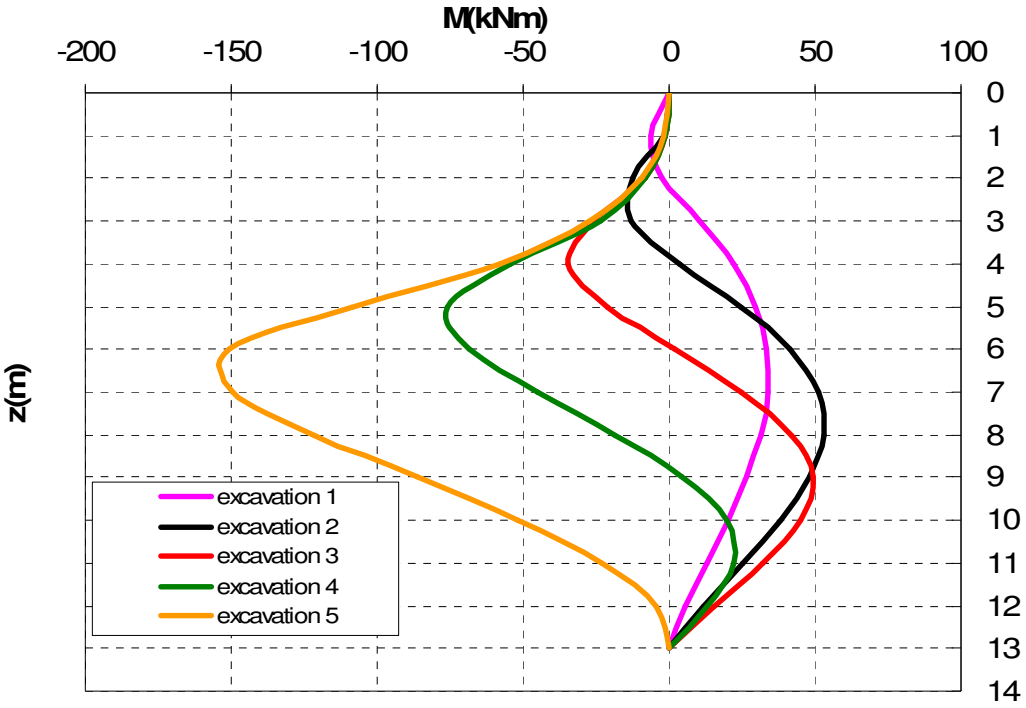

Figure 7. 2 Bending moment versus depth during excavation phases

After excavation phase seismic loading is applied either in the form of a uniform pseudostatic acceleration or in the form of a time history acceleration.

In order to apply a pseudostatic loading phase, acceleration of gravity is progressively rotated and increased in length, as if a horizontal component of acceleration is applied. This loading method will be called FLAC P-S loading The number of steps to rotate acceleration is increased until convergence in the results is reached. The value of such horizontal component

is the one corresponding to Soil D, Zone 1 (PGA=0,35g) and factor $r=2$ resulting in a pseudo static acceleration of $K_h=0.23625$

Comparison of the results in terms of bending moments between FLAC P-S and pseudo static fixed earth support approach for same seismic coefficients are shown in Figure 7.4. Such comparison shows the followings points:

- Fixed earth support assumes that bending moment is zero at point C placed at $z=5m+6.2m=11.2m$ while FLAC simulation gains vanishing moment at wall extreme $z=13m=H$ without moment reversal.
- Maximum bending moment for FLAC P-S (758kNm) is exceeded by pseudostatic prediction (934kNm) of 40%

The main reason for these two discrepancies is the fact that soil-wall flexibility is not taken into account in fixed earth support calculations. The effect of soil-wall flexibility noticed by Rowe [1952] is intentionally neglected for seismic design using the pseudostatic method, while it plays a role in FLAC model.

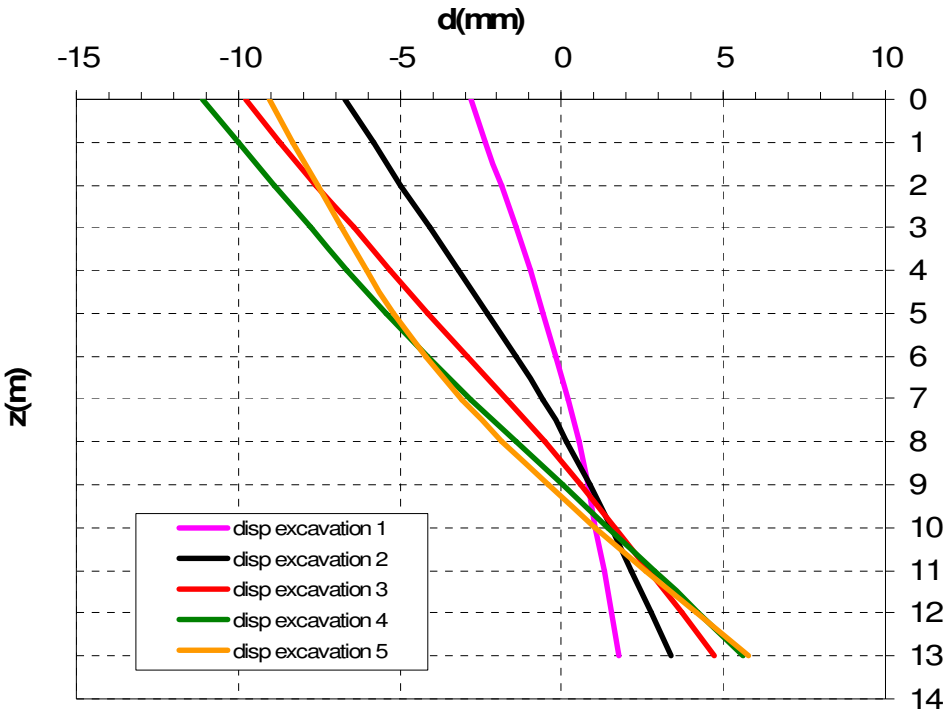

Figure 7. 3 Displacement versus depth during excavation phase

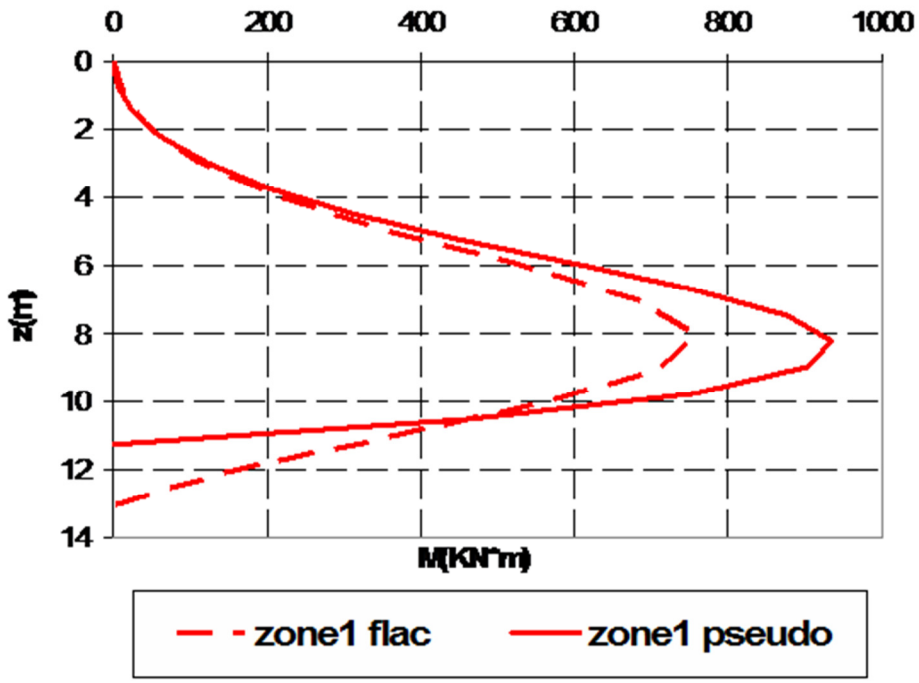

Figure 7.4 Bending moment from FLAC pseudostatic and fixed earth support scheme

7.2 DYNAFLOW model, static and pseudostatic loading

A representation of DYNAFLOW model is given in
Figure 7.5 (element size 1m×2m on the upper part and 2m×2m on the lower part) and satisfies (6.1) as well. Nodes of the wall and of soil are in this case shared without interface. Results in terms of bending moments and displacement during excavation phase are shown in Figure 7. 6 and Figure 7. 7.
Comparison between bending moments during excavation phases calculated by DYNAFLOW and FLAC (Figure 7. 8) shows that while for FLAC bending moment in early excavation phases may have a point of sign reversal, for DYNAFLOW the wall seems to deform as an arch, without change in sign for the curvature. The differences between the bending moments distributions are higher in the early excavation phases and tend to diminish in the last excavation phase. A superposition of the deformed shapes in FLAC and DYNAFLOW at different excavations phases is shown in Figure 7. 9. This shows that wall translational and rotation have both significant differences between the two models but top displacements values (which together with settlements are of concern for nearby structures) at different excavation stages are similar; Figure 2.10 shows the bending moment distribution obtained for a pseudo acceleration coefficient of k_h=0.0937 for both FLAC and DYNAFLOW and the relatively good agreement on the results concerning the peak value of the bending moment.

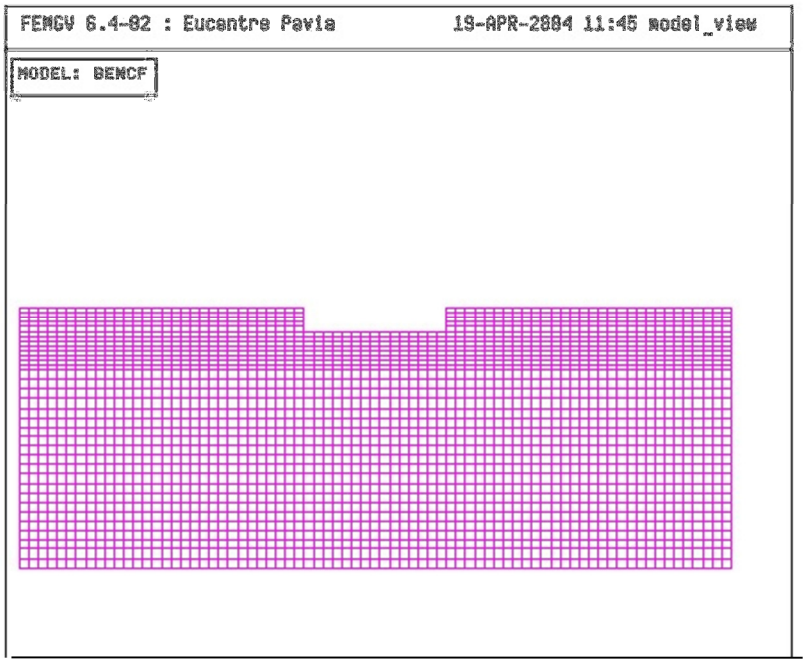

Figure 7.5 DYNAFLOW model

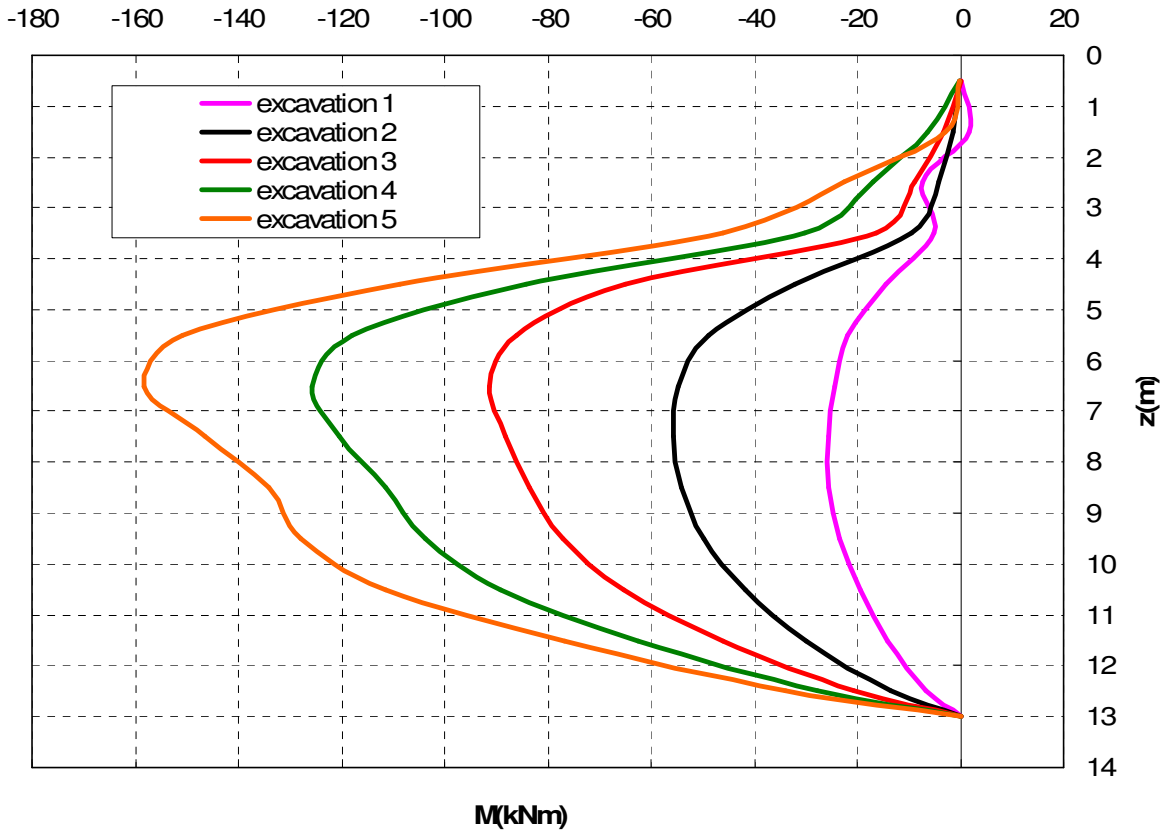

Figure 7. 6 Bending moments from DYNAFLOW model during excavation phases

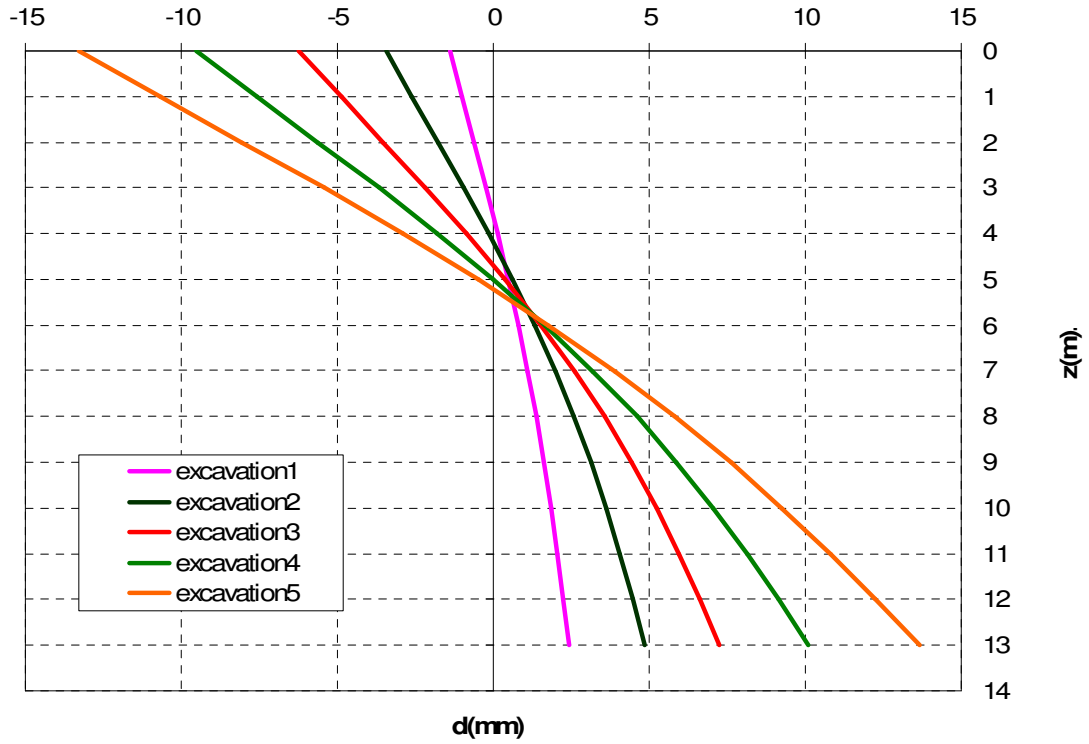

Figure 7. 7 Displacements from DYNAFLOW model during excavation phases

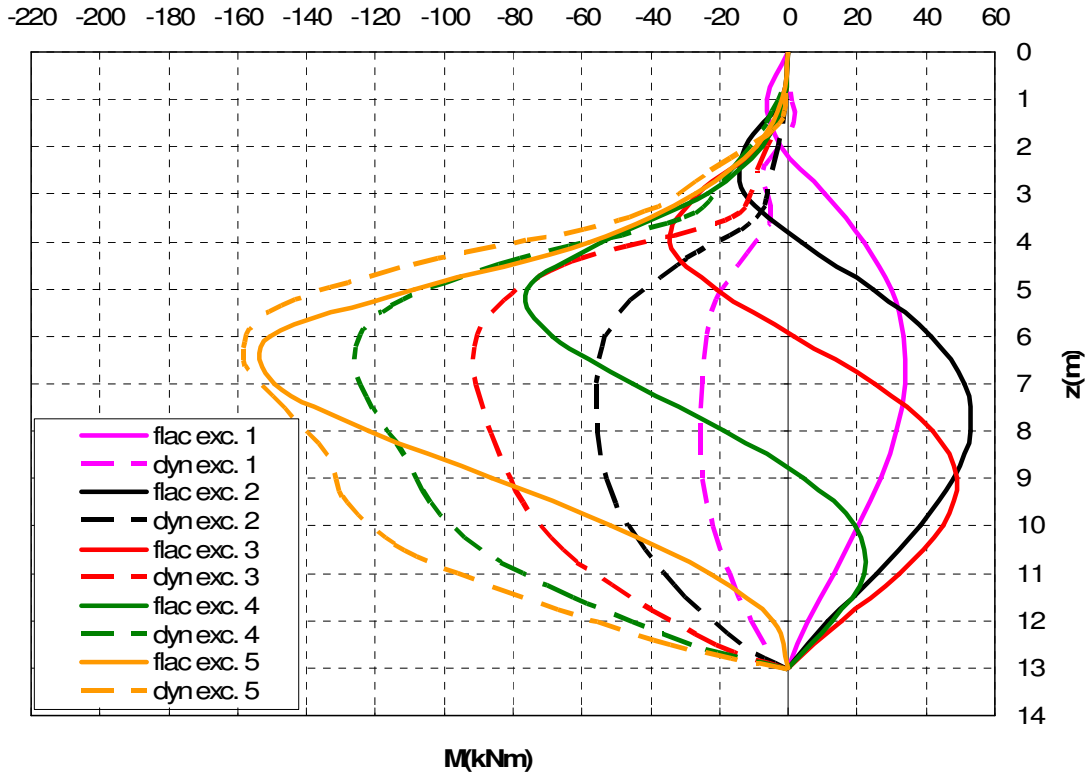

Fi

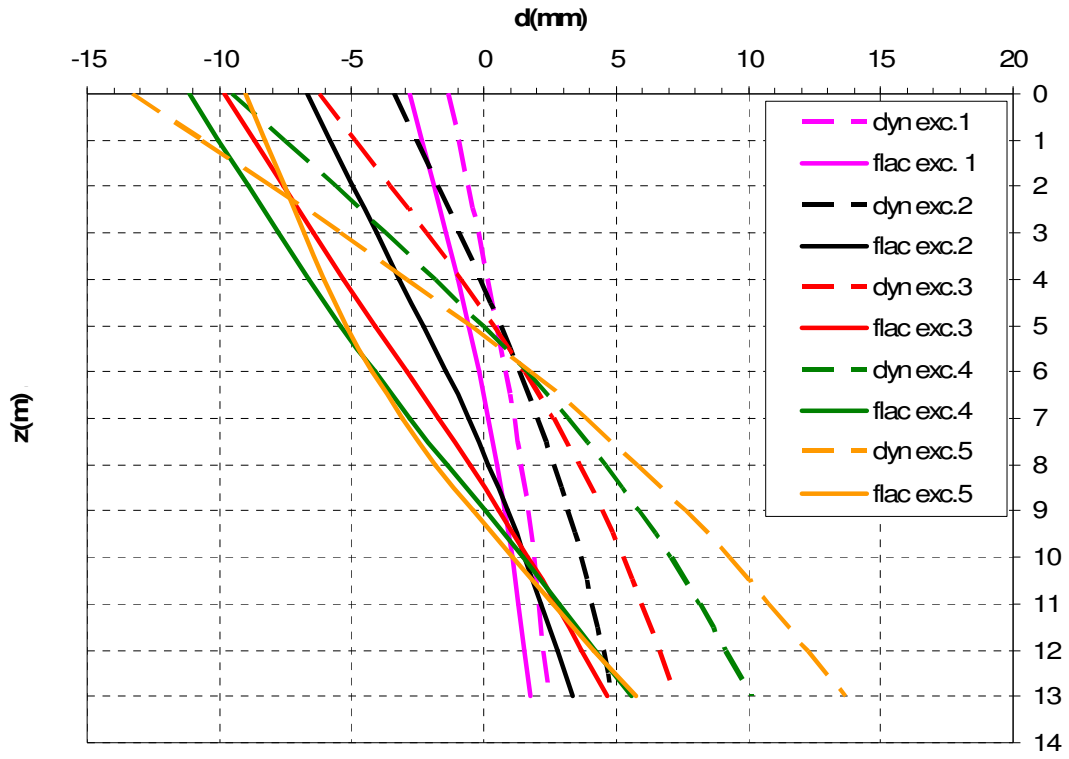

Figure 7. 9 Displacements from DYNAFLOW (dyn) and FLAC (flac) during excavation (exc.) phases.

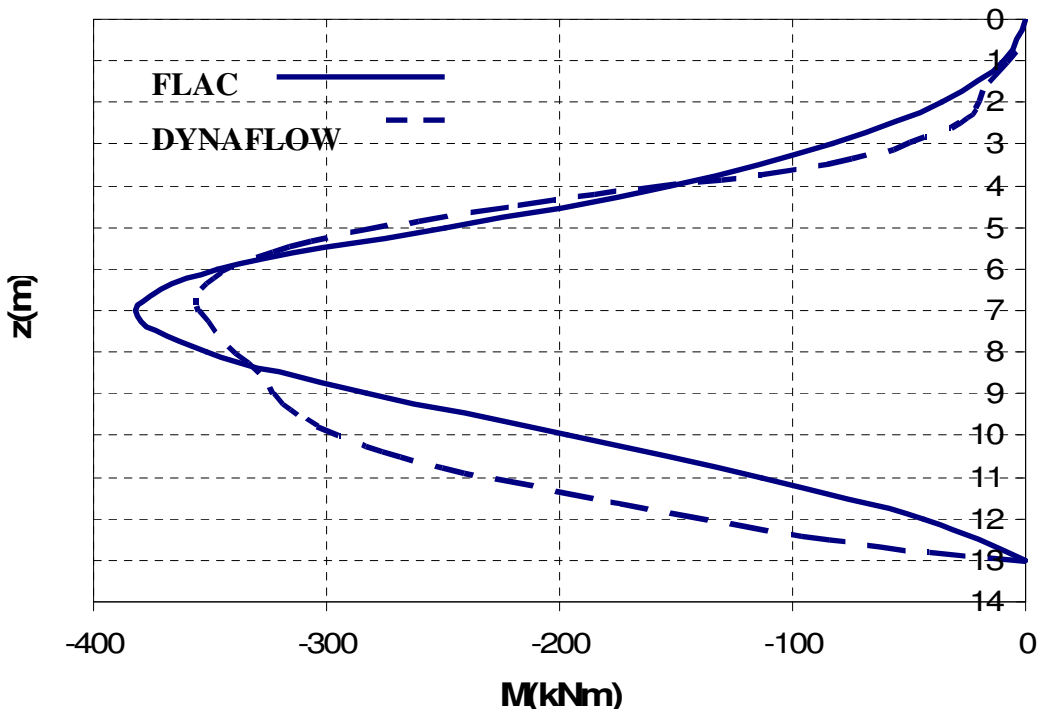

Figure 7. 10 Pseudostatic loading for Kh=0.0937

7.3 Dynamic analysis

As already mentioned in Chapter 4 numerical dynamic time history analysis presents some special issues and in this paragraph it will be explained in more detail how they have been dealt with in both the FLAC and DYNAFLOW models considered.

- Dynamic boundary conditions

As already mentioned in 4.3, geometrical modelling in relation to dynamic energy dispersion is one of the most difficult issues to resolve. Regarding lateral boundaries it was said that in FLAC free field motion is automatically imposed at the lateral boundaries and local absorbing boundaries are included as depicted in Figure 4.31. On the other hands the DYNAFLOW user has to perform a separate one dimensional free field analysis by which it is possible to evaluate horizontal motion of the lateral nodes and then such motion has to be given as input motion to the lateral nodes of the model.
Regarding the bottom boundary instead recalling the formulation of the local boundary and the corresponding shear stress which derives from the *radiation conditions* (3.65)

$$\tau(h,t) = -(2 \cdot \rho \cdot V_s \cdot u_{,t})_{x=h} \qquad (7.\ 2)$$

it is required from both FLAC and DYNAFLOW to be given the value of the constant coefficient
$2 \cdot \rho \cdot V_s$ at the bottom boundary x=*h.*

- Material damping

As already said in 4.2 under cyclic loading soil is subjected to energy losses due to hysteretic behaviour. Such behaviour is frequency independent and is strictly related to the ability of soil constitutive model to reproduce the non linear soil behaviour under cyclic loading. Since the perfectly plastic material model adopted cannot implicitly incorporate hysteretical soil behavior in the elastic range, a Rayleigh damping was applied in FLAC to the model to account for dissipative behaviour of soils at small to moderate level of cyclic strains.
As already mentioned in 4.2, Rayleigh damping has a stiffness and a mass proportional part. It is then understandable that there are two information which must be given to define it : more precisely it is necessary to specify two corner frequencies and their corresponding damping ratio. If a range of vibration frequencies of the systems are identified together with the expected range of damping ratio values within that frequency range, then it is possible to estimate the two corner Rayleigh frequencies and their corresponding damping.
In order to analyse the range of predominant frequencies of the response, for the case of Tortona scaled at 0,35g input motion and Mohr-Coulomb model, the displacement time history for two points of interest one placed at the bottom of the backfill of the wall and one placed at middle height of the backfill (Figure 7. 11) are considered. The displacement response spectrum is plotted in Figure 7. 12.

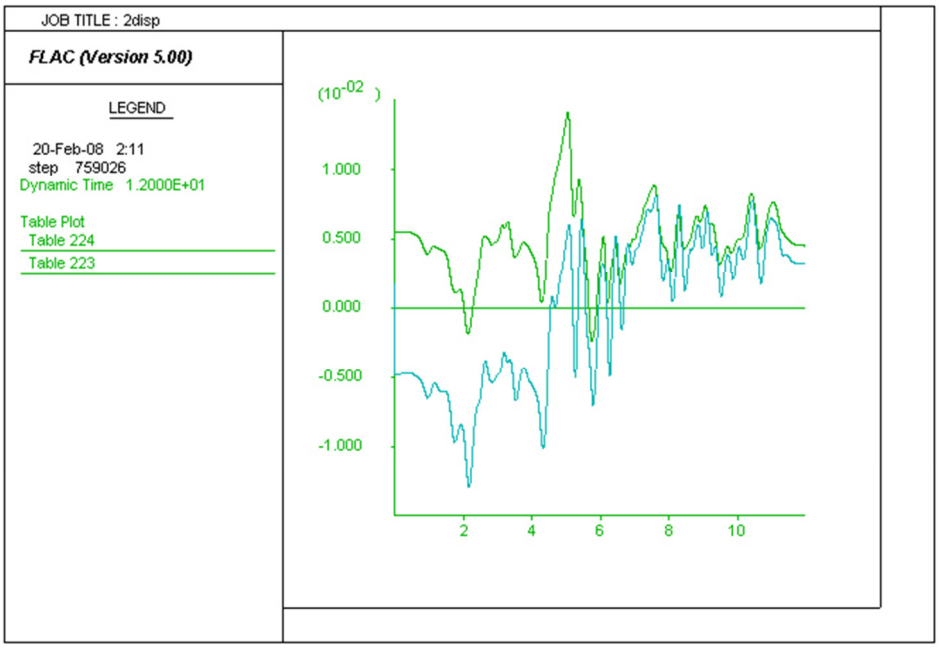

Figure 7. 11 Displacement time histories for points placed at the bottom (224) and mid height (223) of the backfill.

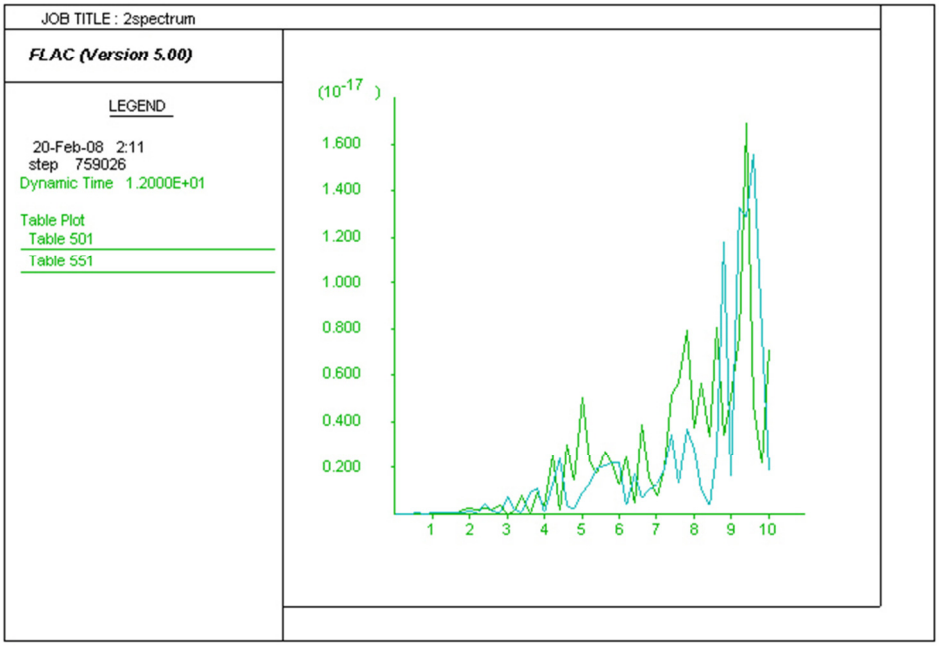

Figure 7. 12 Displacement spectra using as input displacement time histories for points placed at the bottom (224) and mid height (223) of the backfill.

Under the plausible hypothesis that the system dominant frequencies are only slightly dependent on the input ground motion, such spectrum shows that the range of predominant frequencies can be expected to lie between 1sec (1Hz) and 10 sec (0,1Hz).
-This consideration has been used to decide that the corner frequencies for Rayleigh damping ζ=0,5% can be assumed from 0,1 Hz to 1Hz.
-Moreover this observation helps understanding how seismic events with lower frequency content and higher predominant periods such as Chalfant and Erzincan (see Figure 6. 5, Figure 6.**6**) are expected to transfer more energy to the system due to its own low frequency content producing higher increments of dynamic pressure on the wall and higher bending moments than Tortona seismic event, even though they are all scaled at the same PGA. As will be observed this may lead to 80% increase in peak bending moments.
Regarding DYNAFLOW instead, as the Matsuoka Nakai model was not strictly formulated for cyclic-dynamic problem, it does not allow for a viscous or hysteretic damping to be introduced.

- Results for elastic perfectly plastic soil models

For each of the three accelerograms considered (Chalfant, Erzican and Tortona) scaled at 0.15g, results in terms of bending moments distribution are shown in Figure 7. 13 to Figure 7. 14, displacements profiles in Figure 7. 16 to Figure 7. 17 and peak acceleration profiles for one wall in Figure 7.19.

Regarding comparison between FLAC and DYNAFLOW results for dynamic case it should also be mentioned that excavation phases in FLAC can be simulated assuming a value of soil Young modulus equal to E_s different from the one assumed for dynamic phases because FLAC allows for a given entity to change the material properties during the calculation. On the other hand in DYNAFLOW material properties for a given entity cannot be modified. Consequently in FLAC, for the dynamic phase, Young modulus used is five times bigger than static one $E_0=5\cdot E_s=125$MPa. For DYNAFLOW analysis Young modulus is kept equal to E_0 for dynamic analysis and equal to E_s for only static analysis. In order to compensate for such a difference, the difference (with sign) between the static moment distribution assuming Young modulus E_s and that assuming E_0 was added to the residual envelope bending moment.

Regarding moment envelope distribution shown in Figure 7. 13 and Figure 7. 14, results obtained by FLAC and DYNAFLOW are closer on the side of the wall toward the backfill, where highest moment occur and the best comparison is obtained for the average of the three distribution as shown in Figure 7. 15.

Regarding displacements profiles in Figure 7. 16, Figure 7. 17 and Figure 7. 18, in each graph are shown both maximum, minimum and residual displacement for both FLAC and DYNAFLOW (six in total) and it is possible to observe a good agreement between FLAC and DNAFLOW. Morever ther is a significant difference between the displacement profiles obtained for Tortona input accelerogram compared to the others accelerograms. The scatter in displacements due to input accelerogram is more pronounced than that in forces.

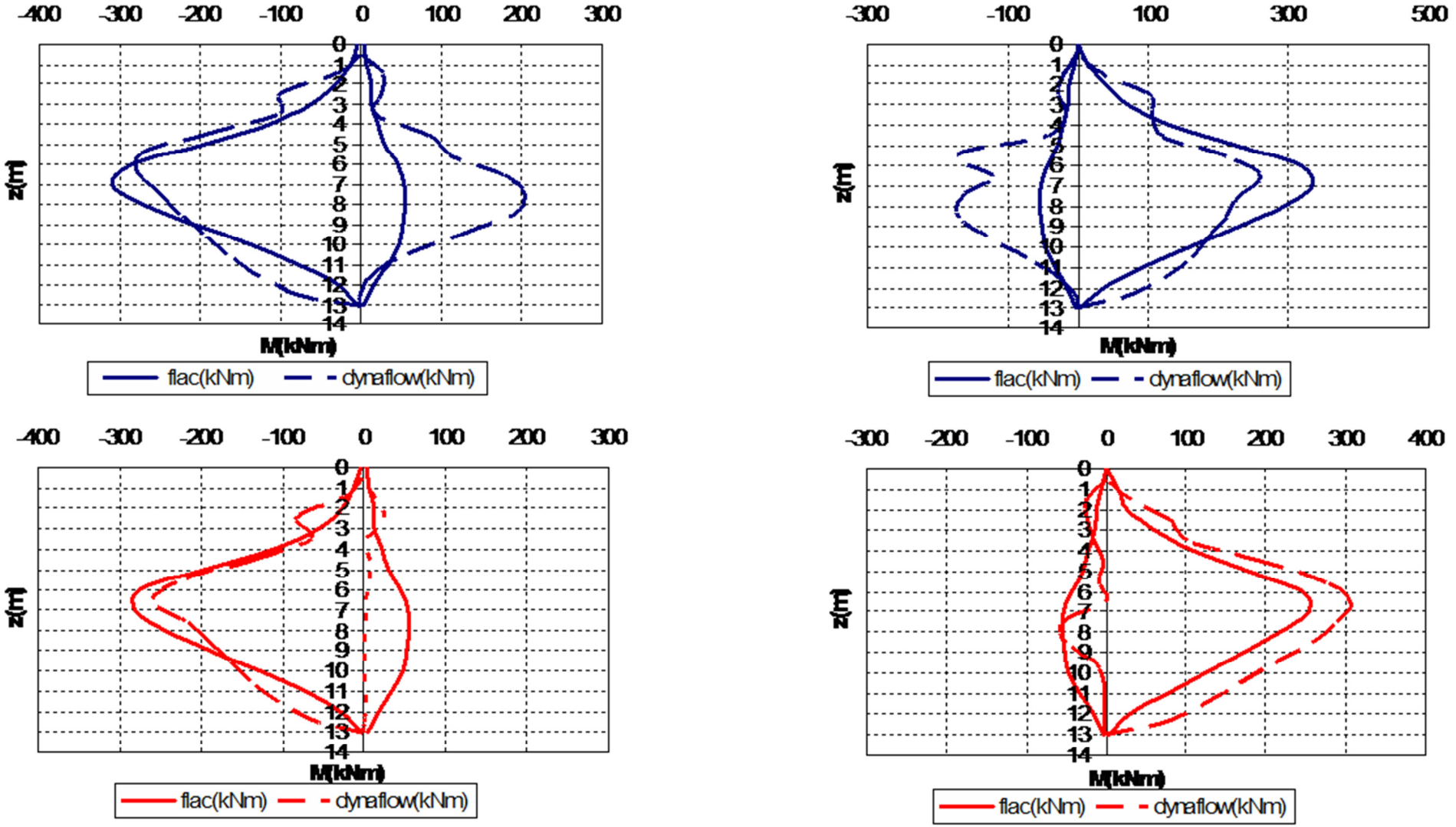

Figure 7. 13 Bending moments for Chalfant Valley 0.15g (left wall a) and right wall b)) and Erzincan 0.15g (left wall c) and right wall d))

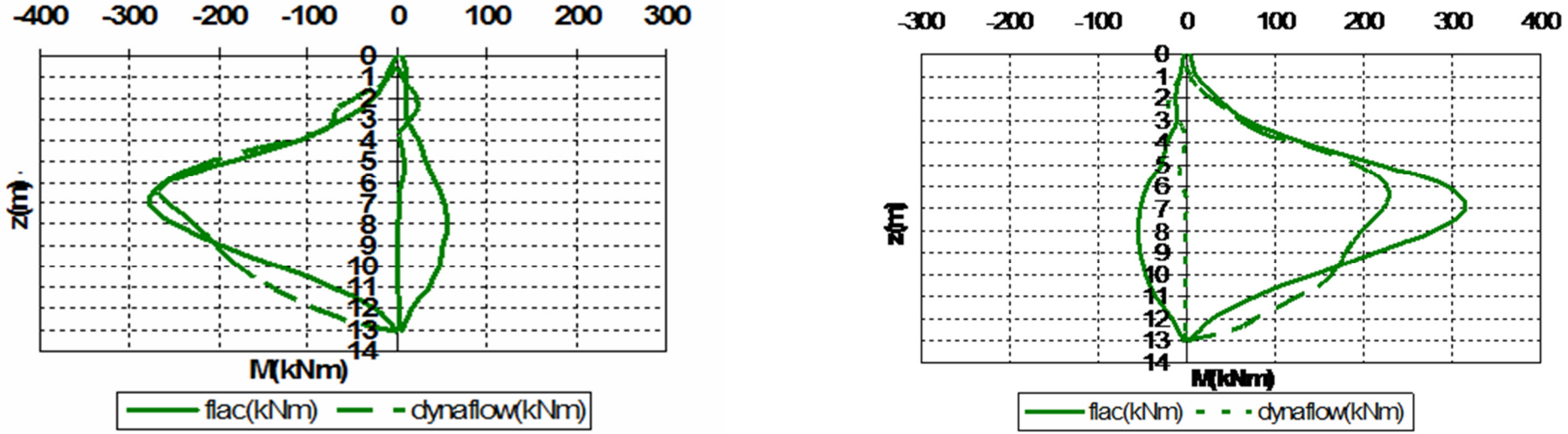

Figure 7. 14 Bending moments for Tortona 0.15g (left wall a) and right wall b))

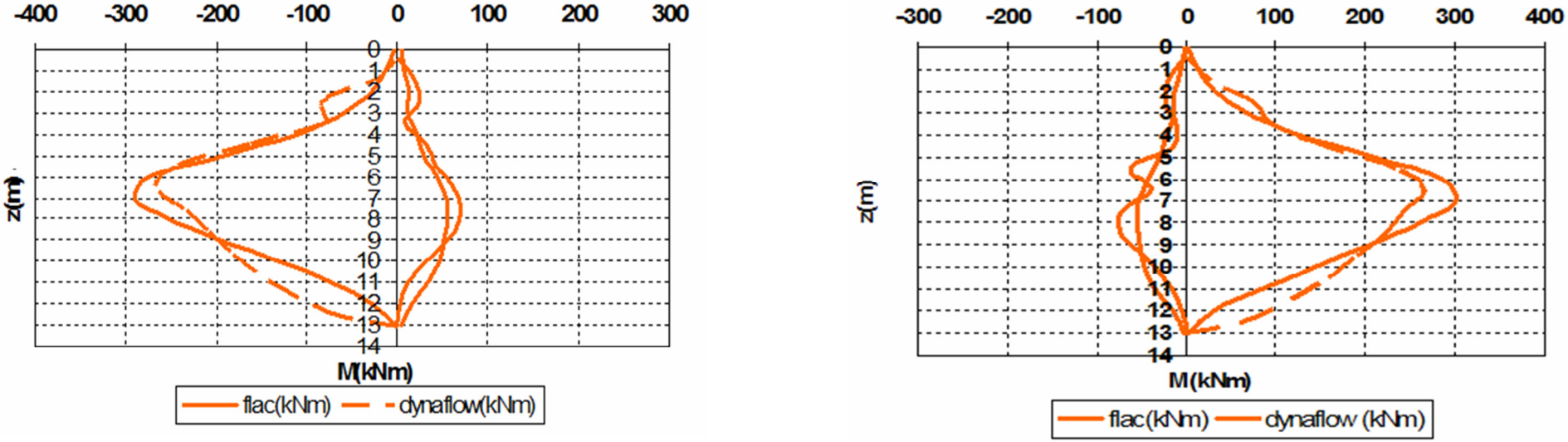

Figure 7. 15 Average of bending moments from all accelerograms (left wall a) and right wall b))

Another observation is that the displacement and moment distribution are not symmetric due to both the non symmetricity of the soil-wall system and the polarization of the accelerograms. This is another aspect wich pseudostatic methods cannot take into account.

In Figure 7.19 instead, it is shown the maximum acceleration distribution along the wall height. It is possible to observe the significant increase in acceleration along the wall height and the fact that in all cases a peak value of 0.2g is reached showing an amplification of 25% if compared to the PGA of 0.15g recorded on stiff outcropping ground and far away from the wall.
It is interesting to note that wave refraction phenomena on the wall causes a steeper increase in wall acceleration in the upper part corresponding to the part of excavated soil. Moreover it is possible to observe that the scatter in the distribution of the acceleration it is not so much dependent on the input accelerogram but rather on the PGA so it seems to confirm that the PGA is a good indicator of the maximum acceleration distribution that can be expected near the wall.
The following observations and conclusions can be drawn regarding the comparison between FLAC-DYNAFLOW for fixed PGA 0,15g and different accelerograms:

- DYNAFLOW and FLAC results show comparable values for bending moments and displacements for both static and dynamic case.
- The deformed wall curvature after static phase shape between DYNAFLOW and FLAC is different (as already pointed out) but minimum, residual and maximum dynamic displacement values are comparable.
- The two main reasons for the above mentioned FLAC-DYNAFLOW results differences are 1) difference in wall soil interface 2) difference in material young modulus values for the static phase.
-

Moreover additional observation can be done regarding the comparison between pseudostatic and dynamic approaches:

- Pseudostatic approach considers as sensible data of the input motion only the PGA while dynamic analysis shows different results for same PGA and for the same accelerogram depending on relative position wall/soil.
- Sensitivity of dynamic analysis with respect to the accelerogram type regards more displacements than bending moments and less than other wall acceleration. This is also reasonable as the former maybe related to the double integral of the latter.
- Bending moments of wall (designed to withstand a 0,35PGA seismic event) under the input of time histories scaled at 0,15g reach values of moment (Figure 7. 13, Figure 7. 14 and Figure 7. 15) that are well below the pseudostatic design moment for 0,15g (around 650 kNm from Figure 5. 9).
- Frequency content (as outlined in 7.3) and PGV may be an additional parameters that can explain the observed differences in the results coming from different input accelerograms. In particular displacements seem directly correlated to PGV (see Figure 6.**6**).

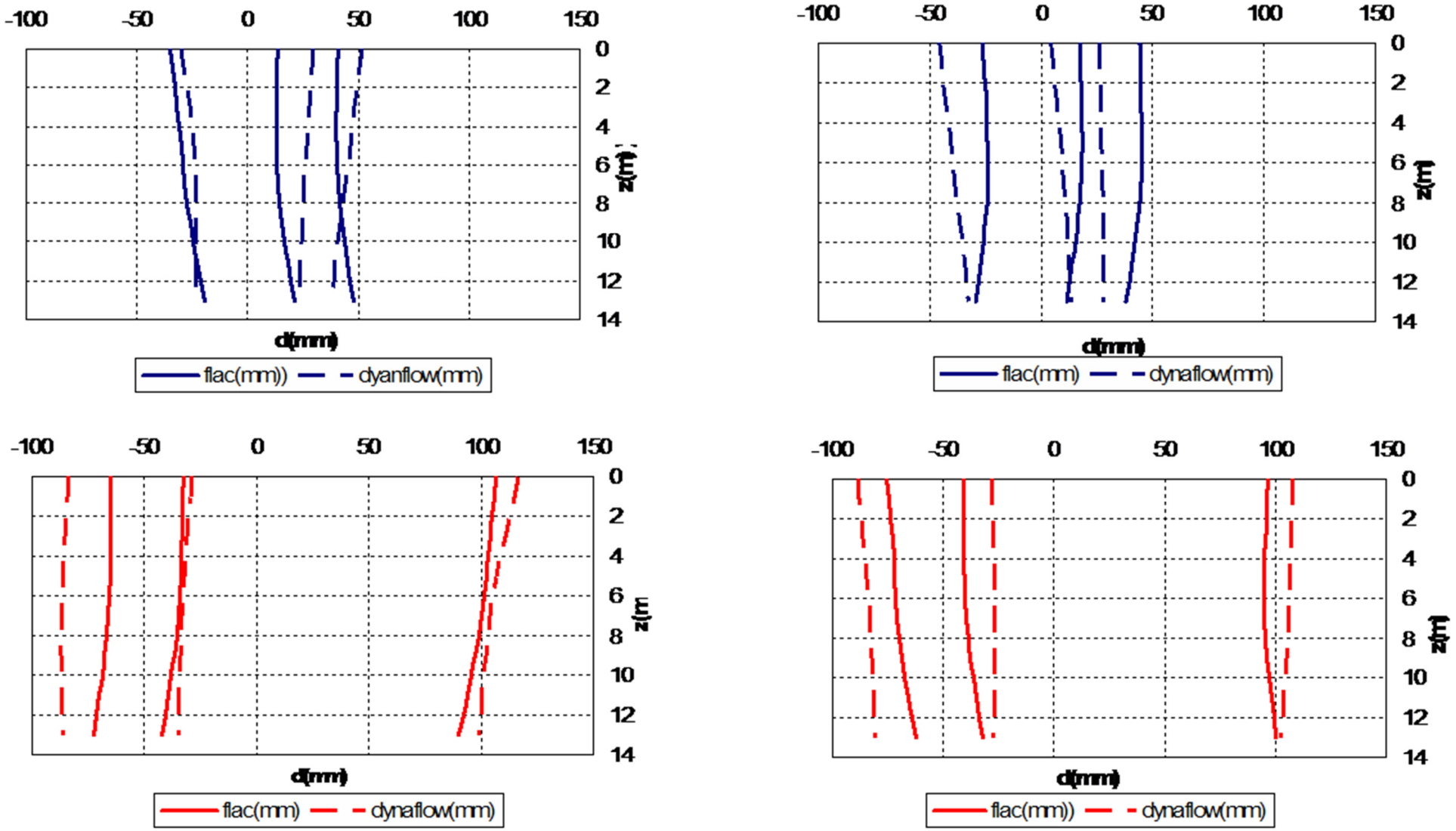

Figure 7. 16 Minimun, residual and maximm displacements for left-right walls for Chalfant Valley, Erzincan scaled 0.15g

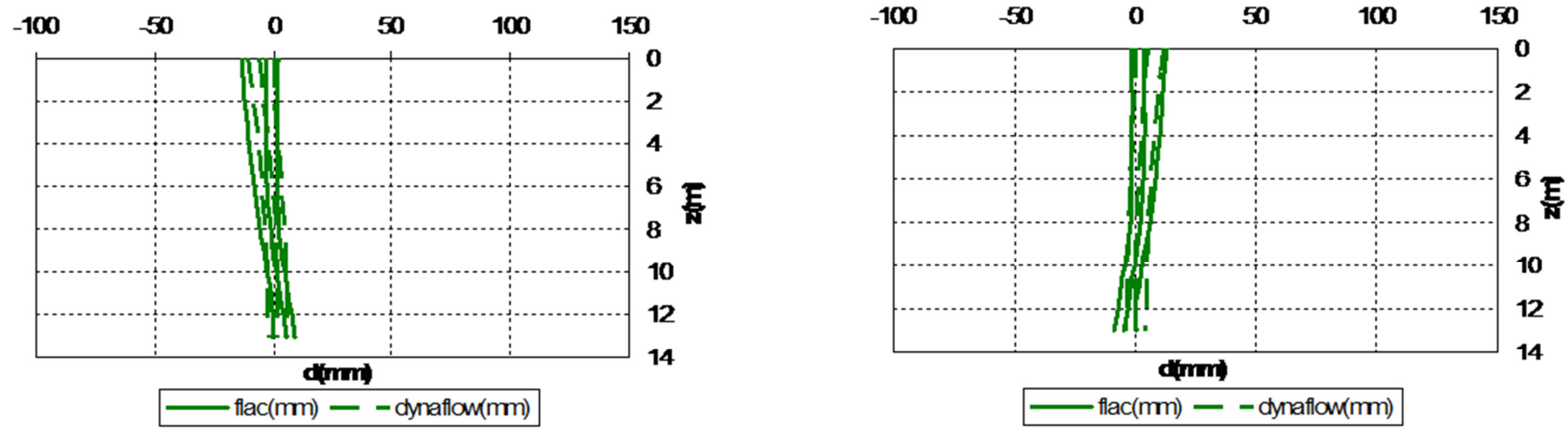

Figure 7. 17 Minimun, residual and maximum displacements for left- right walls for Tortona 0.15g

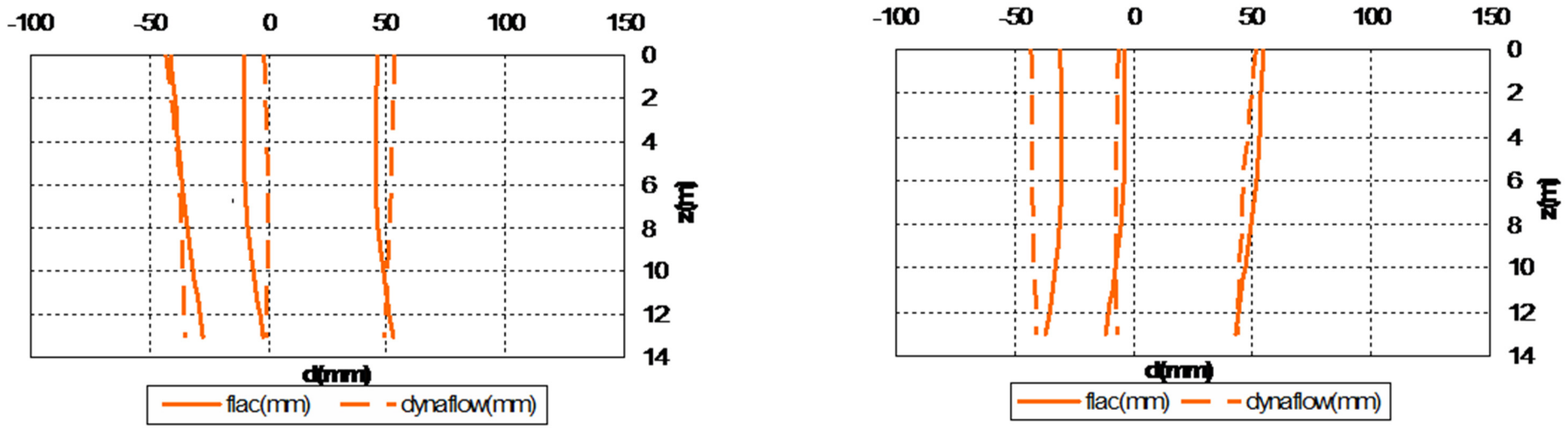

Figure 7. 18 Average of results from three accelerograms for minimun, residual and maximm displacements for left- right walls 0.1

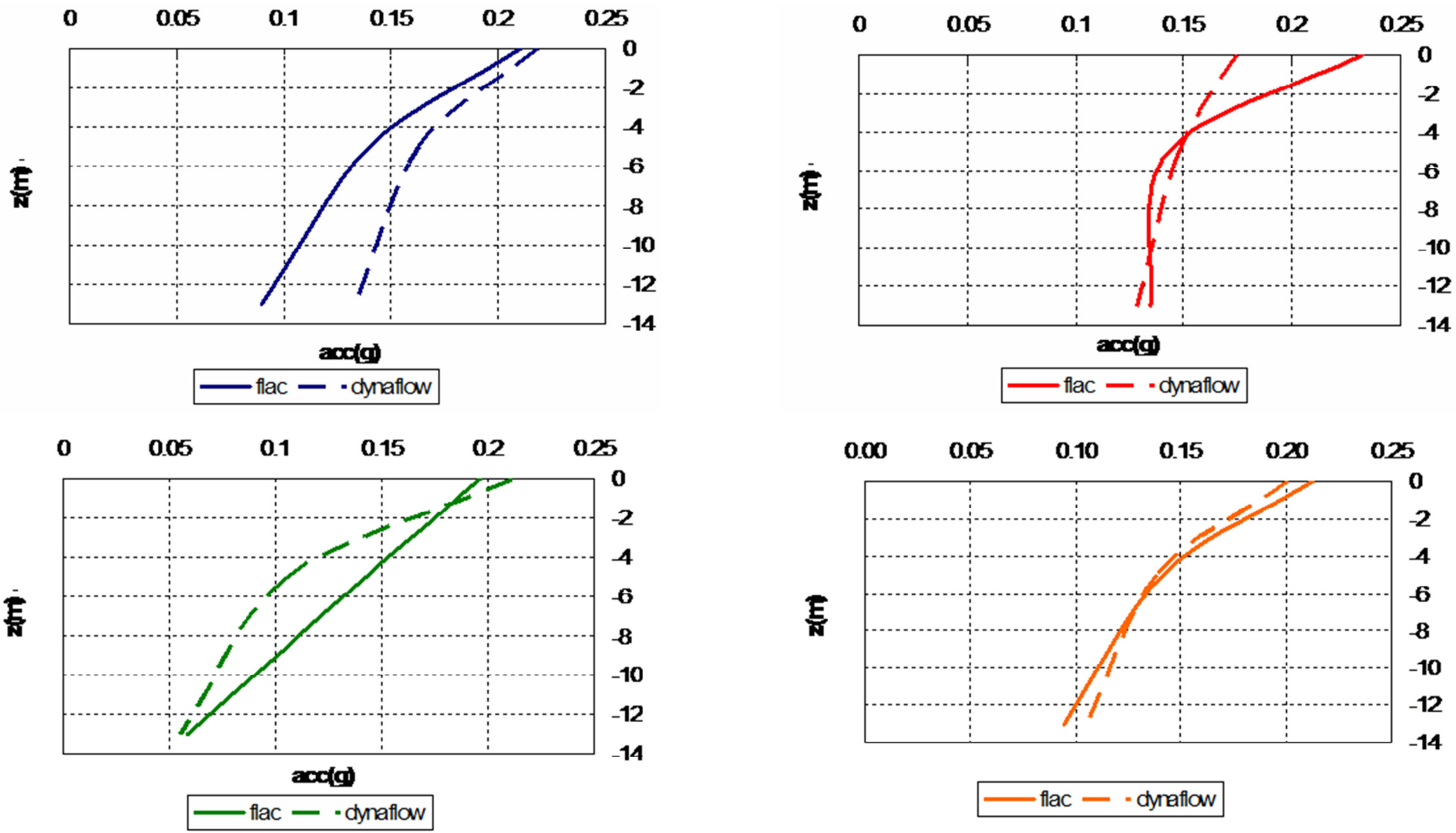

Figure 7.19 Maximum acceleration along the wall for Cahlfany Valley a), Erzincan b) Tortona c) input motion scaled 0.15g PGA and average

7.4 Benchmark case: frequency content of the input motion.

As already stated in pseudostatic approach input time histories are characterized only for what concerns magnitudes (Type I and II spectra) and PGA but they are not characterized regarding actual frequency content.
In the previous section the same PGA but different earthquakes were considered. Sensitivity to different accelerograms was decreaing passing from displacements to bending moments to accelerations. It is of interest to investigate further the difference in the results obtained by pseudostatic design approach and time history dynamic analysis for different input ground motions events using several PGA values. Since the wall considered is designed to withstand PGA_{design}= 0.35g, it is of interest to scale input ground motions not only to values below but also equal and above PGA_{design}.
In this paragraph results obtained for the Mohr-Coulomb model, are compared to each others and with pseudostatic results, for different time histories (Tortona, Erzincan and Chalfant Valley) scaled at several PGA (0.15g, 0.35g and 0.6g).
Results of such calculations are collected in Figure 7. 20, to Figure 7. 25 in terms of horizontal pressures, bending moments and horizontal displacement values. From these plots it is possible to observe that for the same PGA, values of bending moments for the same wall may vary of 80% while displacement may vary as much as 14 times. A synthesis of the peak values for displacements and bending moments is shown in Table 7. 1.

Table 7. 1 Peak values for bending moments and top wall displacements for different PGA and input motions.

		Chalfan	Erzincan	Tortona	PGA (g)	Average (kNm)	standev	coeff corr (%)
	0,15g	310	282	279	0.15	290	13.96	61
moment L (kNm)	0,35g	609	625	482	0.35	572	63.97	29
	0,6g	1131	1270	740	0.6	1047	224.38	76
	0,15g	333	253	315	0.15	300	34.27	61
moment R (kNm)	0,35g	732	558	582	0.35	624	76.99	29
	0,6g	1183	1037	846	0.6	1022	137.99	76
	0,15g	40	97	14	0.15	50	34.66	100
disp. L (mm)	0,35g	120	262	19	0.35	134	99.67	100
	0,6g	227	488	44	0.6	253	182.19	98
	0,15g	44	107	13	0.15	55	39.11	100
disp. R (mm)	0,35g	94	233	22	0.35	116	87.58	100
	0,6g	220	340	61	0.6	207	114.27	98

Standard deviations of the response in terms of moments and displacements included in Table 7. 1 allows also doing some remarks regarding the increase in scatter that both moments and above all displacements have with increasing PGA. The coefficient of variation instead shows

that moment correlations between right/left wall is lower than correlation for displacements and lowest for the design PGA 0,35g.

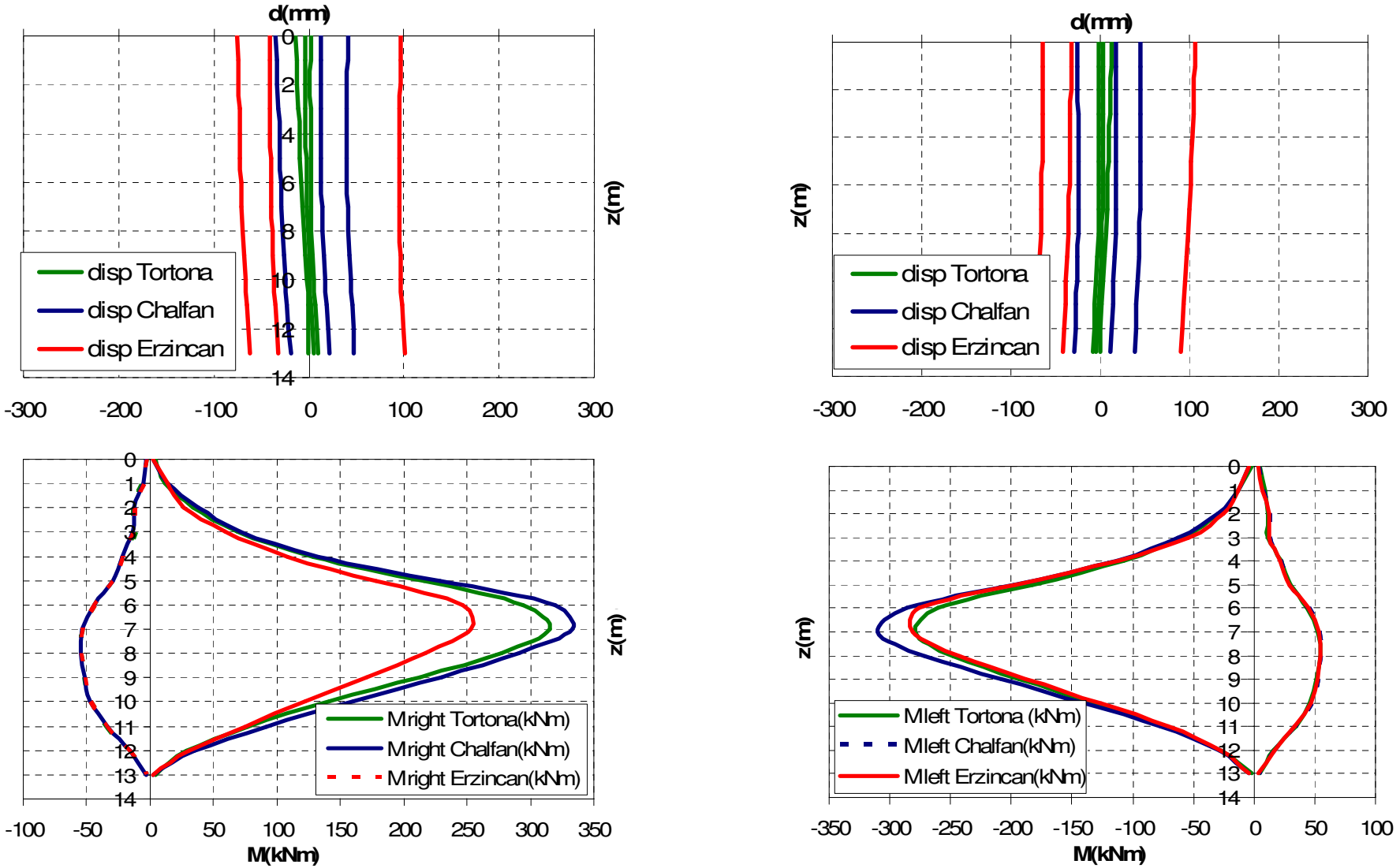

Figure 7. 20 Displacements (maximum, minimum and residual) and bending moments for both walls, for Tortona, Erzincan and Chalfant scaled 0,15g FLAC.

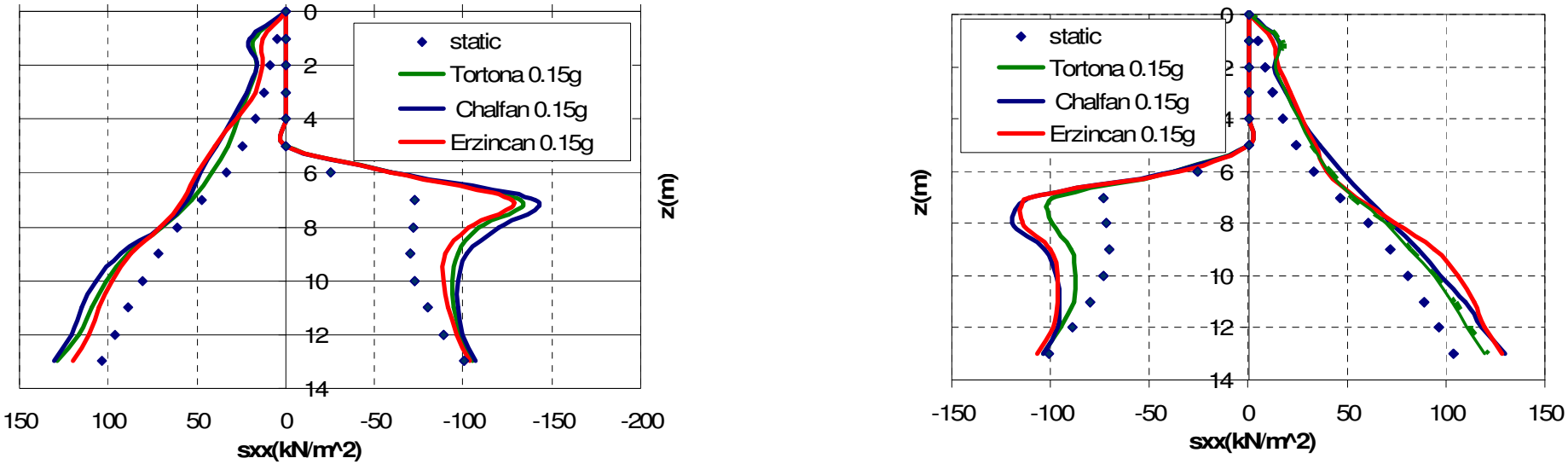

Figure 7. 21 Horizontal pressure distribution for both walls, for Tortona, Erzincan and Chalfant scaled 0,15g FLAC.

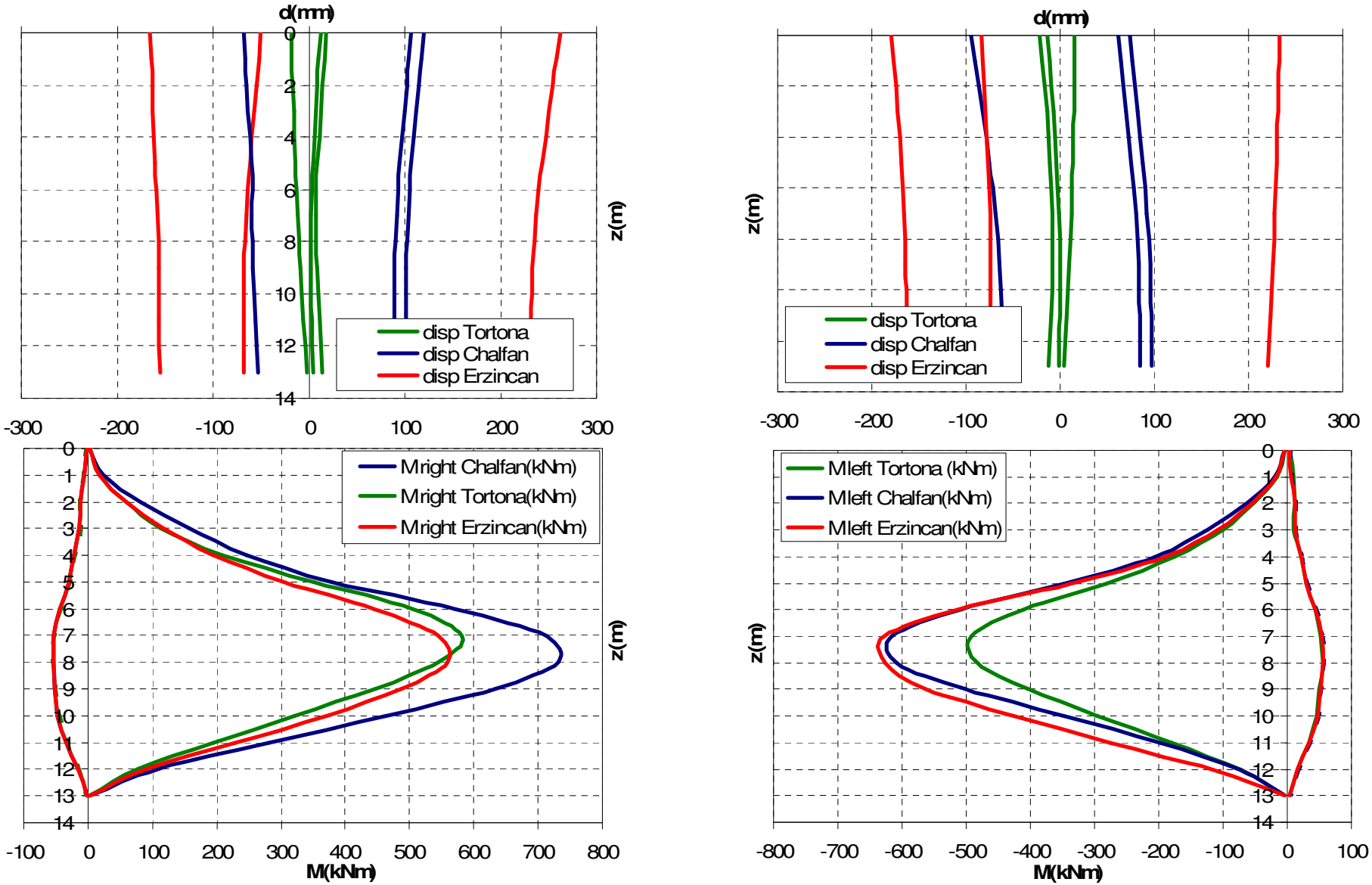

Figure 7. 22 Disp. profiles (maximum, minimum and residual) and bending moments for both walls, for Tortona, Erzincan and Chalfant scaled 0,35g FLAC.

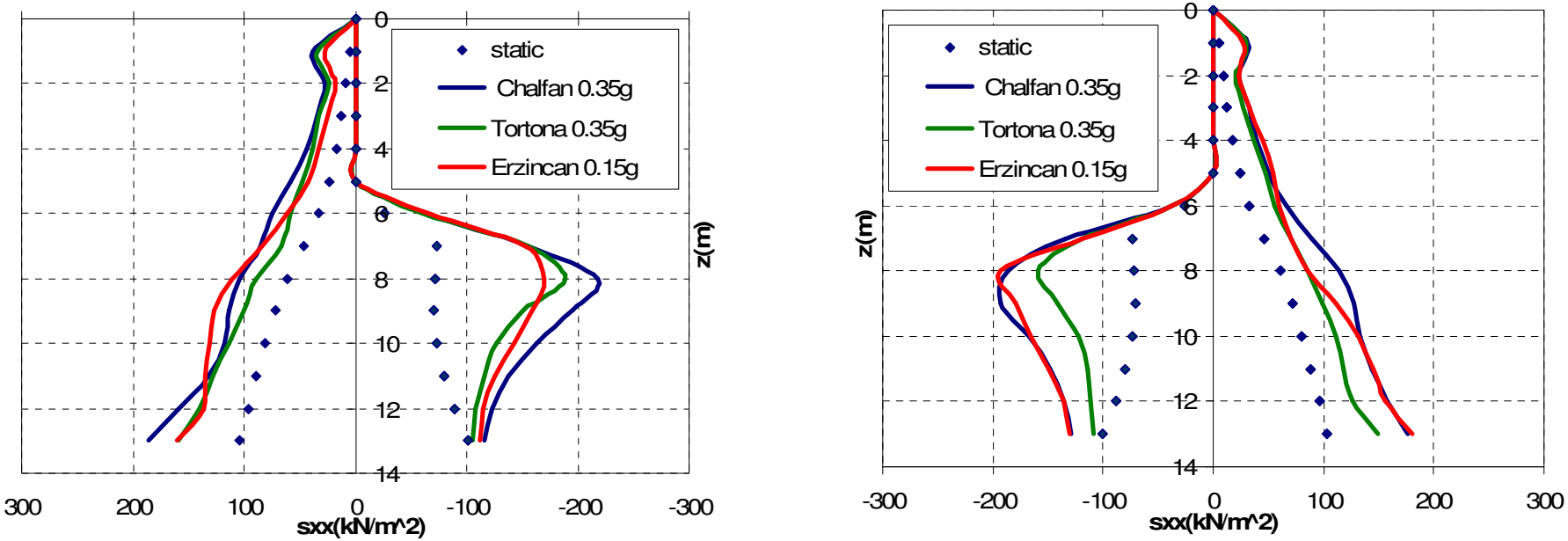

Figure 7. 23 Horizontal pressure distribution for both walls, for Tortona, Erzincan and Chalfant scaled 0,35g FLAC.

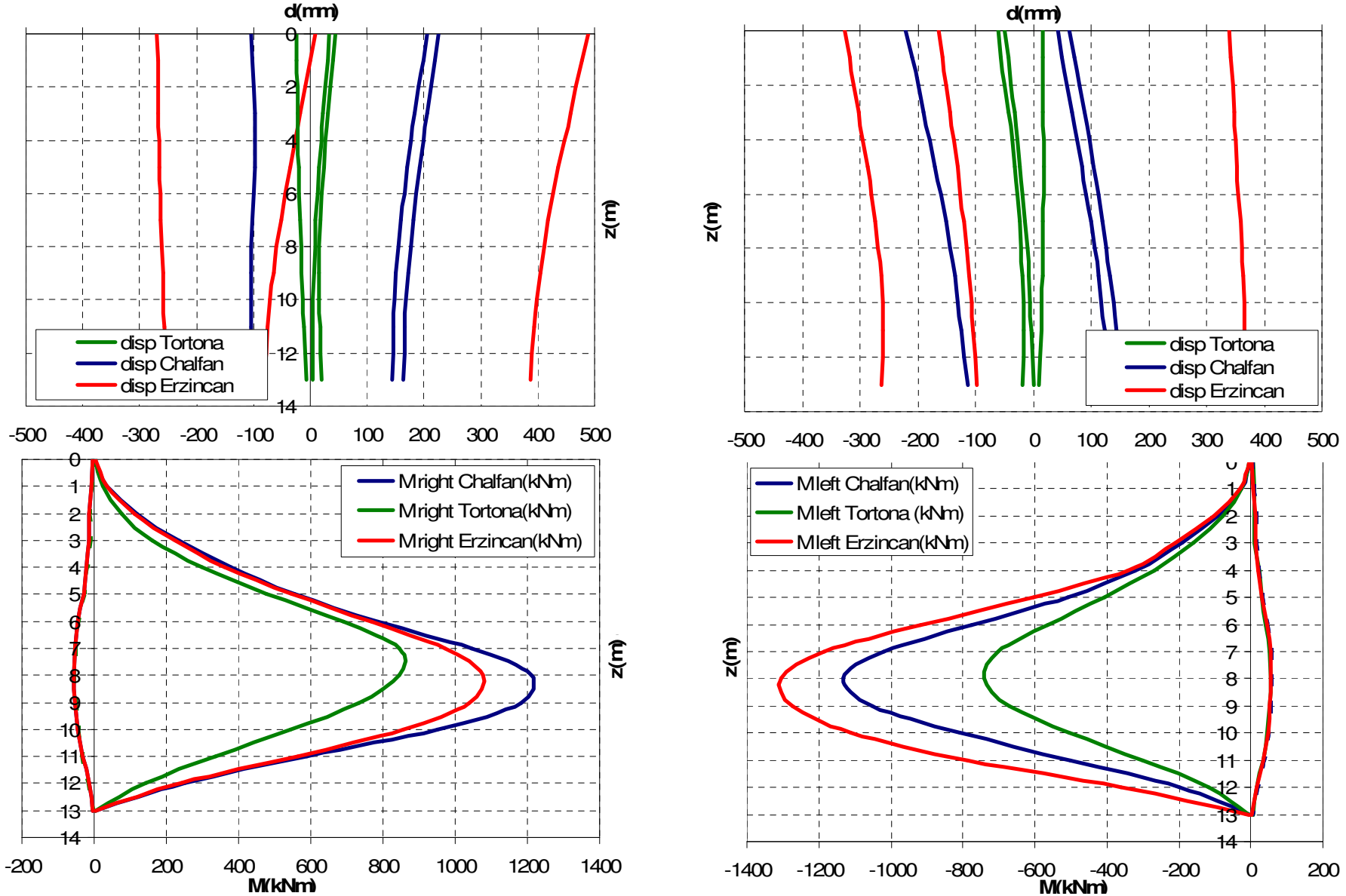

Figure 7. 24 Disp. profiles (maximum, minimum and residual) and bending moments for both walls, for Tortona, Erzincan and Chalfant scaled 0,6g. FLAC

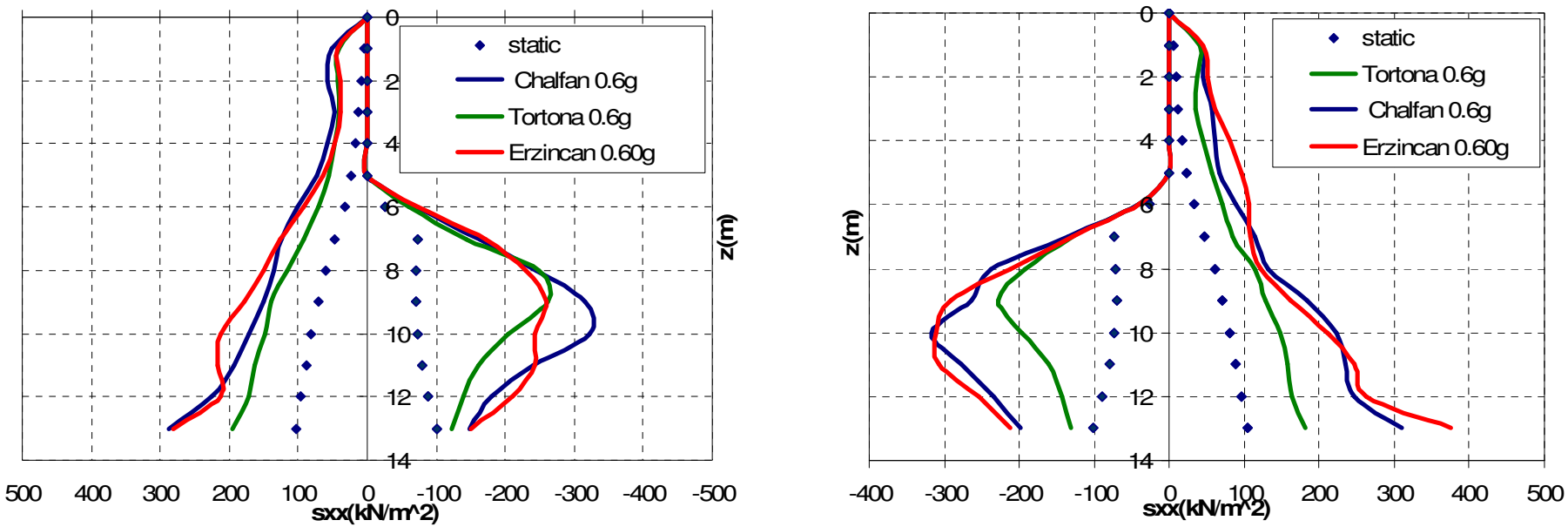

Figure 7. 25 Horizontal pressure distribution for both walls, for Tortona, Erzincan and Chalfant scaled 0,6g FLAC.

Figure 7. 26 and Figure 7. 27 show for both walls the scatter in peak values of bending moments and top wall displacements for varying PGA and input motions by considering the ration in terms of moments and displacement deviding for the smallest value of moment/displacement.
Considering that design PGA is 0,35g one can say that for design PGA increase in bending moment due to change in input excitation may reach about 30% and sensitivity to polarization is not strong (same increase for left and right wall).
As already said for PGA 0,15g, also for the case of different PGA values, the scatter in terms of displacements is much more consistent than that for bending moments.

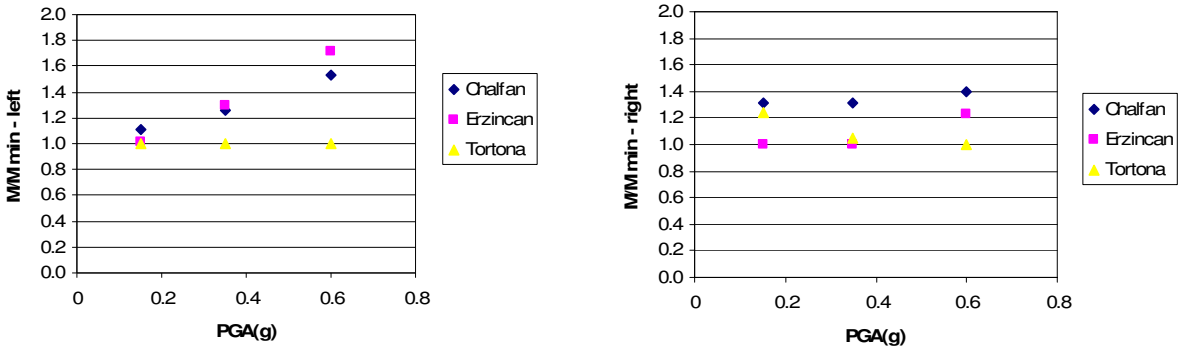

Figure 7. 26 Ratio between peak bending moments of left and right wall for several PGA and input motions.

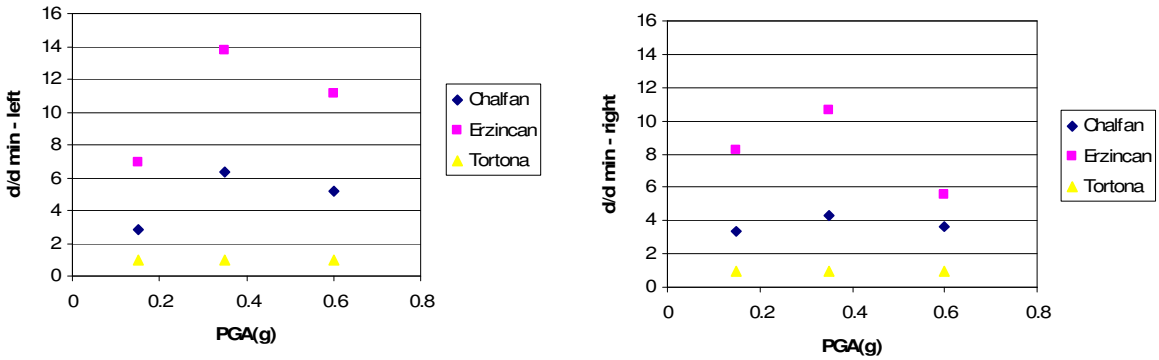

Figure 7. 27 Ratio between peak top wall displacement of left and right wall for several PGA and input motions.

For a given PGA, the Tortona accelerogram, for the effects related to the frequency content already mentioned in 7.3, leads to lower excitation if compared to Erzincan and Chalfan. This is clearly shown in Figure 7. 26, Figure 7. 27.

The following summary can be done:

- For 0,15g PGA the results and the conclusions are already shown in 7.3.
- Investigating time histories with PGA >= 0,35g allows a more significant comparison with pseudostatic design moment because pseudostatic design (see 5.4) assumed PGA=0,35g (zone 1).

- For all time histories investigated at PGA=0,35g maximum bending moment does not go beyond 720kNm which is lower than maximum design bending moment (943 kNm) obtained by pseudostatic approach for the case PGA 0,35g (zone 1), soil D and r=2. A 30% difference is found this means that in terms of forces pseudostatic approach seems conservative if compared to dynamic analysis.
- As expected for PGA equal 0,6g instead, maximum design bending moment obtained by pseudostatic analysis for zone1 is largely exceeded for all seismic events (of around 30%). In a way this means that the degree of conservatism of pseudostatic method is not excessive.
- Comparing the results obtained by numerical application of pseudostatic method (see 5.4) and the results obtained by dynamic time history analysis in terms of maximum bending moments for 0,35g (zone 1), it is possible to observe a good agreement between peak dynamic values (ranging between 609-732 kNm) and pseudostatic value (758 kNm). This indicates a more reasonable degree of conservativism and it may indicate that numerical application of pseudostatic method maybe preferred to classical pseudostatic by hand calculation to determine the design moment for structural design.
- Dependency of both bending moments and above all displacement from the frequency content is clear. If that would be considered in design a consistent saving could be obtained.
- In accordance to what was expected in Figure 7. 3, due to frequency content of the accelerogram and to the natural vibration frequency of the model, the Tortona accelerogram tends to gain lower displacements and moments for the same PGA.

7.5 Benchmark case study: material non linearity.

As already mentioned, as a rule of thumb, for shear strain exceeding the range between 1e-4 and 1e-3 fully non linear soil model maybe necessary.
For active wedge and above all passive wedge to form, extensive soil yielding is expected in the vicinity of the diaphragm wall. For this reason it is interesting to investigate what is the effect of including full non linear material model rather than elastic perfectly plastic model. As already mentioned these steps require modification in both soil stress-strain formulation and in damping definition.

7.5.1 Application of the Hysteretic soil model

As already mentioned in 4.2.1 the so called *hysteretic damping* model in FLAC 5.0 likewise the *equivalent linear method* [Seed and Idriss 1969], assumes that cyclic shearing of the soil due to earthquake excitation, determines progressive decay in shear stiffness (initially equal to small strain shear modulus G_0) and progressive increase in hysteretic, frequency independent , material damping, usually expressed as percentage ratio to the critical one ($\zeta(\%)$).

The expression of the backbone degradation curve G/G_0 in the form given by Ishibashi and Zhang[1993] has been compared to experimental results by Palmieri [Palmieri, 1995] for an average stress of 100kPa in 5.2.
From such data it was noted also that the value of G_0 assumed corresponding to the reference E_0=125MPa maybe expected for a mean pressure that is comparable to the average pressure in the vicinity of the wall.

The average value of effective vertical stress, σ_{ave}=627 kPa, relative to the benchmark model is evaluated considering the relationship $\sigma_{ave}=(2\cdot\sigma_{top}+2\cdot\sigma_{mid}+2\cdot\sigma_{bot})/6$ where σ_{top}, σ_{mid} and σ_{bot} are respectively the vertical stresses at top, middle and bottom height in the model. Such mean pressure was used in the reference curves of Ishibashi and Zhang[1993] which are compared with stiffness degradation curves calculated from FLAC assuming L_1=2 and L_2=0.823 in Figure 7. 28. Damping curves instead are compared in Figure 7. 29

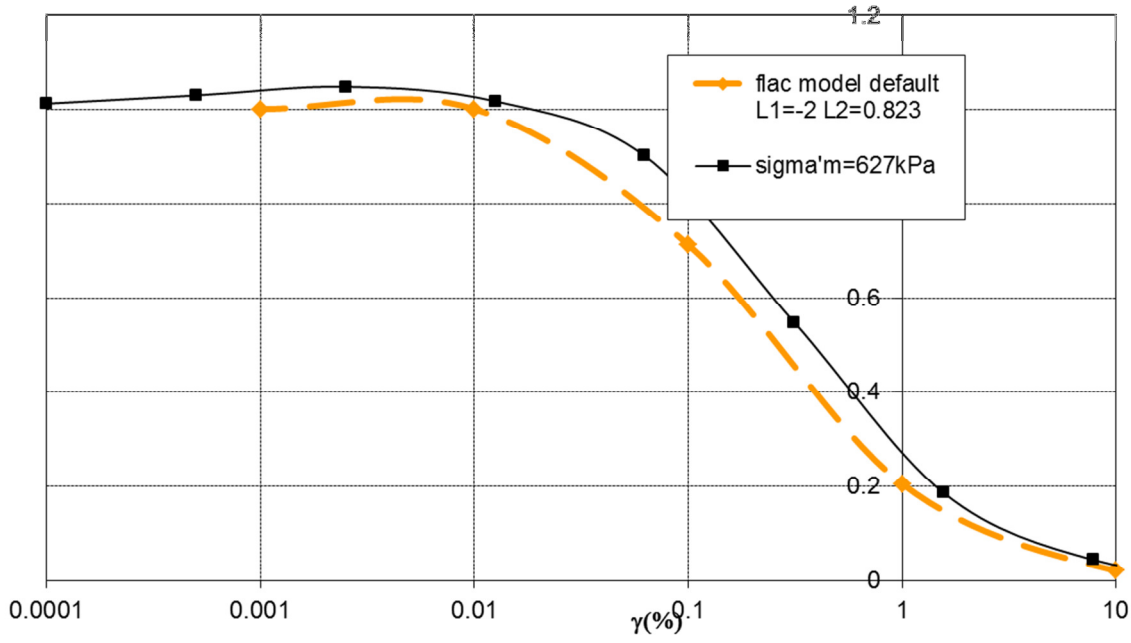

Figure 7. 28 Shear modulus degradation curves for FLAC model versus Ishibashi and Zhang FLAC

Results obtained considering Mohr Coulomb and Hysteretic material models are compared in this paragraph with reference to Tortona input accelerogram scaled at 0.15g, 0.35g and 0.6g. For both left and right wall pressure distribution and resulting bending moments are compared in Figure 7. 30, Figure 7. 32. Displacement profiles are shown in Figure 7. 34 , Figure 7. 35.
As expected differences between results obtained using these two material models are almost negligible for lower acceleration levels as the elastic material behaviour is predominant for and decreases with increasing PGA as strain increases and so does material non linearity.

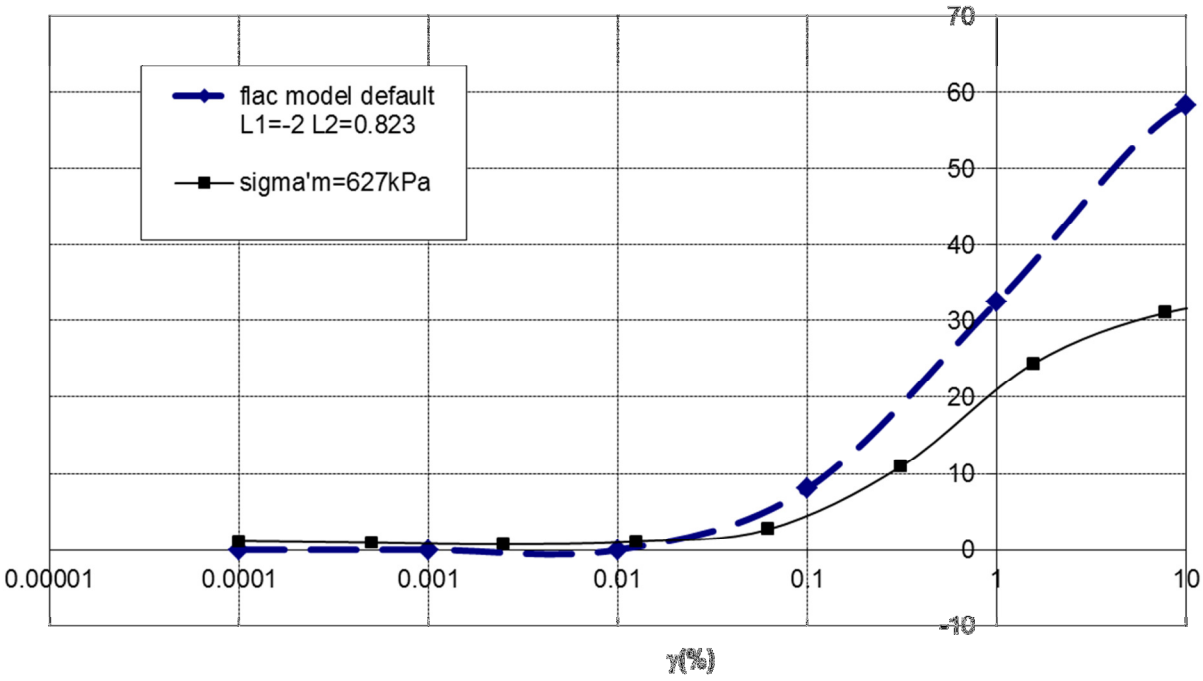

Figure 7. 29 Variation of hysteretic damping for FLAC model versus Ishibashi and Zhang FLAC

Regarding maximum bending moments it is possible to observe that differences between the two models can reach 20% for 0,35g PGA and 25% for 0,6g PGA.
Regarding displacements profiles instead, differences in values of residual and maximum displacement at top reach 5mm (30% of the peak value) and 10 mm (almost 50% of the peak value) for 0,35g and 0,6g respectively. This means that in this case material non linearity seems to have a stronger impact on displacements rather than forces.

A useful summary to compare sensitivity to frequency content with sensitivity to material model, peak response values in terms of bending moments and displacements is done in Table 7. 2

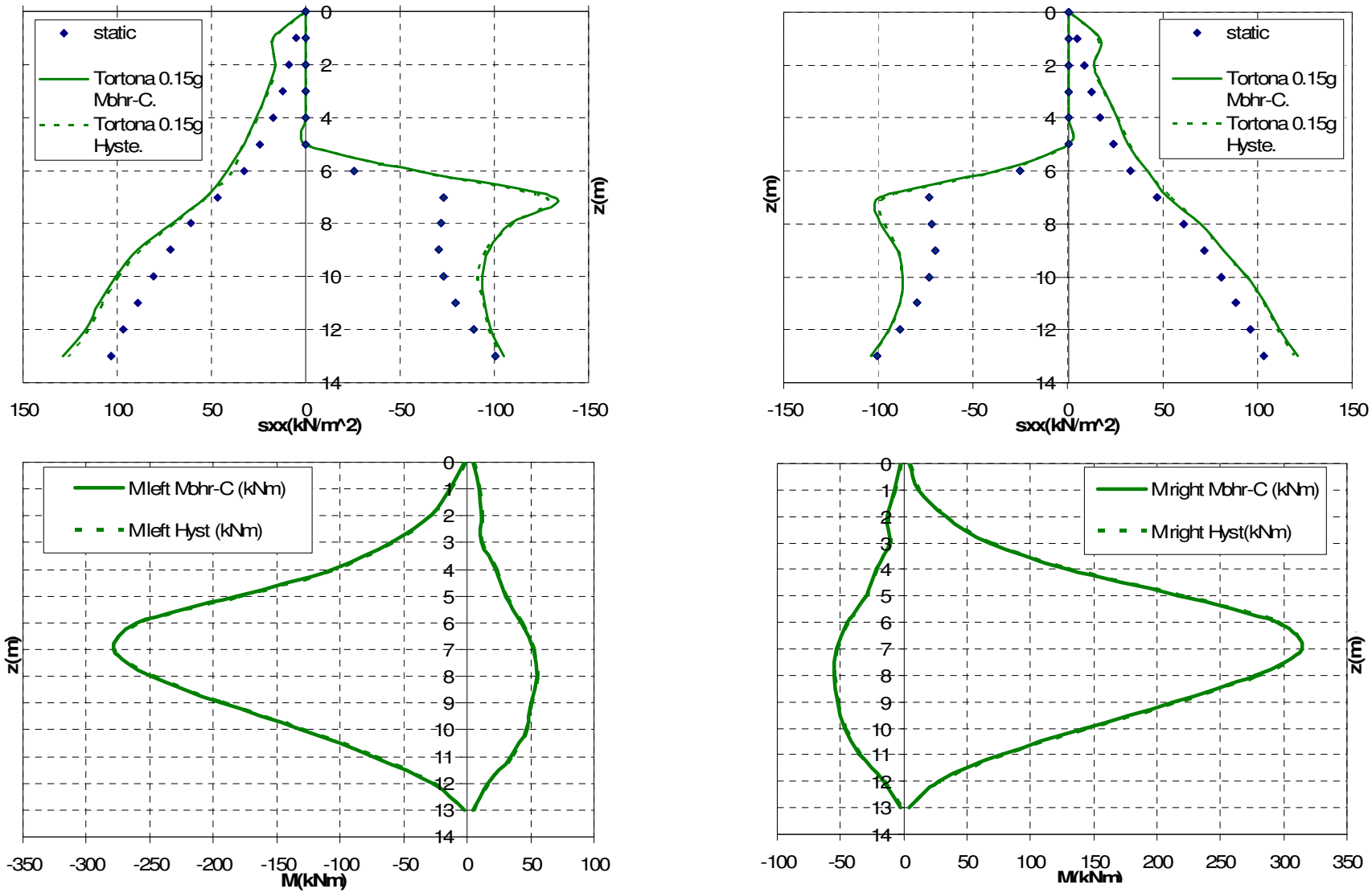

Figure 7. 30 Static and maximum dynamic pressures and bending moments along left and right wall for Tortona 0.15g seismic input FLAC.

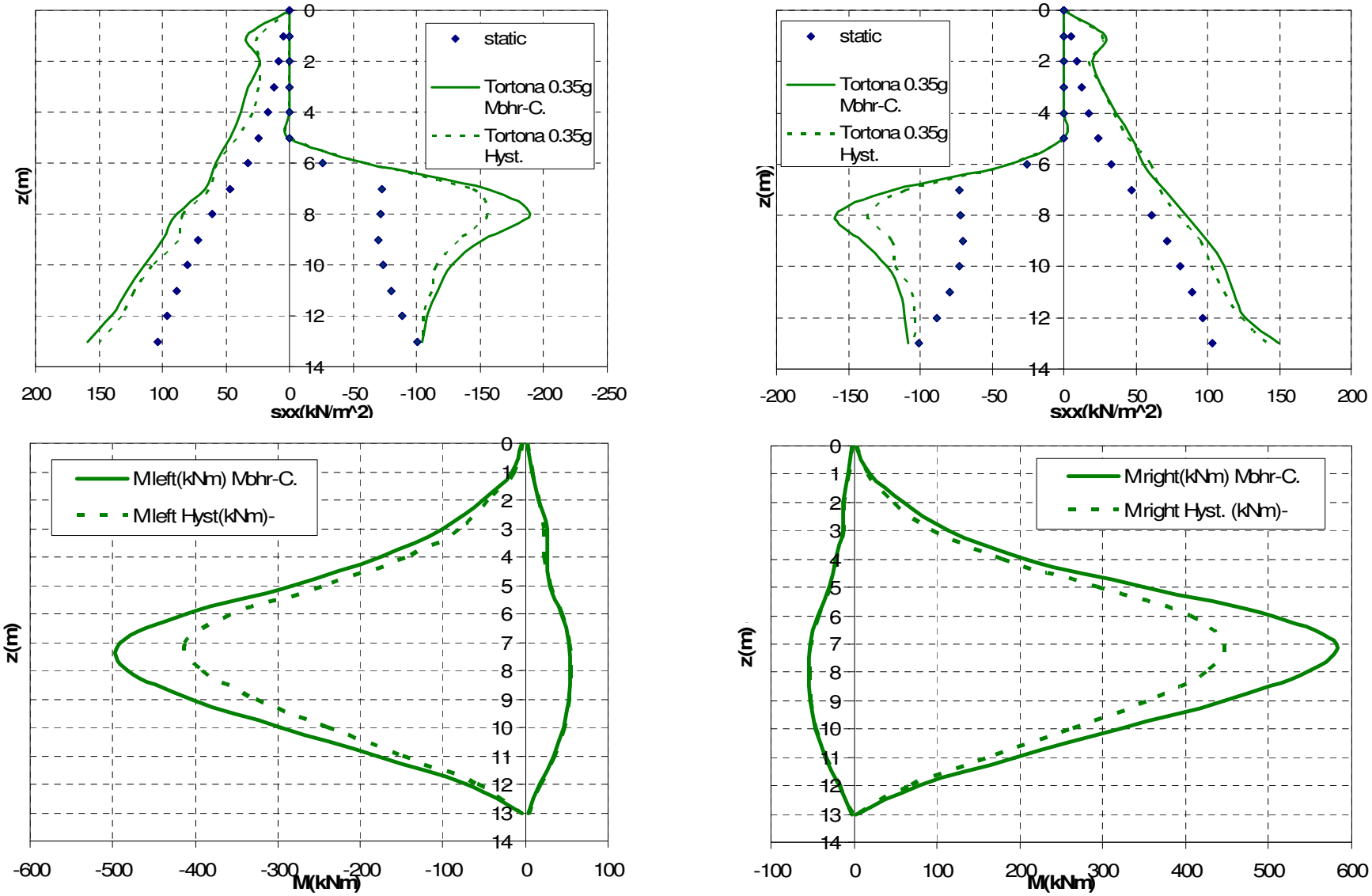

Figure 7. 31 Static and maximum dynamic pressures and bending moments along left and right wall for Tortona 0.35g seismic input FLAC.

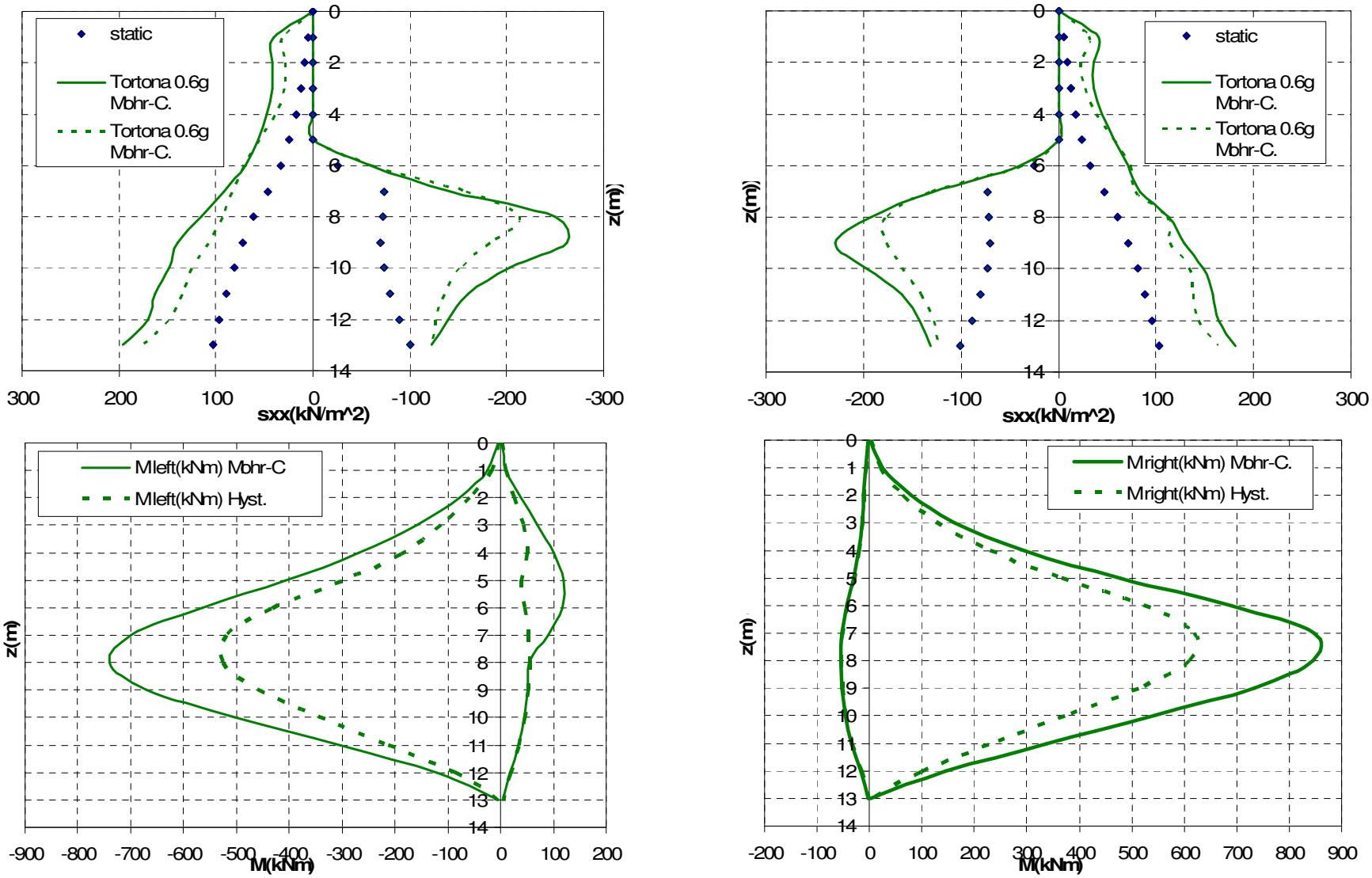

Figure 7. 32 Static and maximum dynamic pressures and bending moments along left and right wall for Tortona 0.6g seismic input FLAC

Table 7. 2 Peak values for bending moments and top wall displacements for different PGA and material models

			Tortona MC	Tortona Hyst	PGA (g)
moment L	(kNm)	0,15g	279	279	0.15
		0,35g	482	413	0.35
		0,6g	740	527	0.6
moment R	(kNm)	0,15g	315	315	0.15
		0,35g	582	425	0.35
		0,6g	846	609	0.6
disp. L	(mm)	0,15g	14	14	0.15
		0,35g	19	19	0.35
		0,6g	44	30	0.6
disp. R	(mm)	0,15g	13	13	0.15
		0,35g	22	16	0.35
		0,6g	61	35	0.6

Figure 7. 33 and Figure 7. 34 show the ratio between peak bending moments and peak displacements with respect to the lowest value found in the case of elastic perfectly plastic model and in the case of fully non linear hysteretic model in way similar to that of Figure 7. 26, Figure 7. 27. The figures scaling is left unchanged on purpose to allow for comparison.

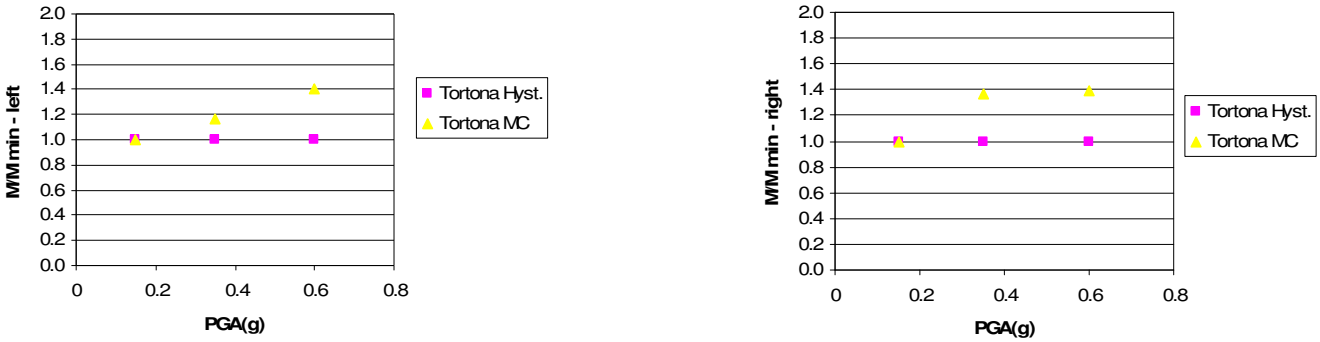

Figure 7. 33 Ratio between peak bending moments of left and right wall for Tortona event scaled at several PGA and elastic perfectly plastic (MC) or fully non linear (Hyst.) model.

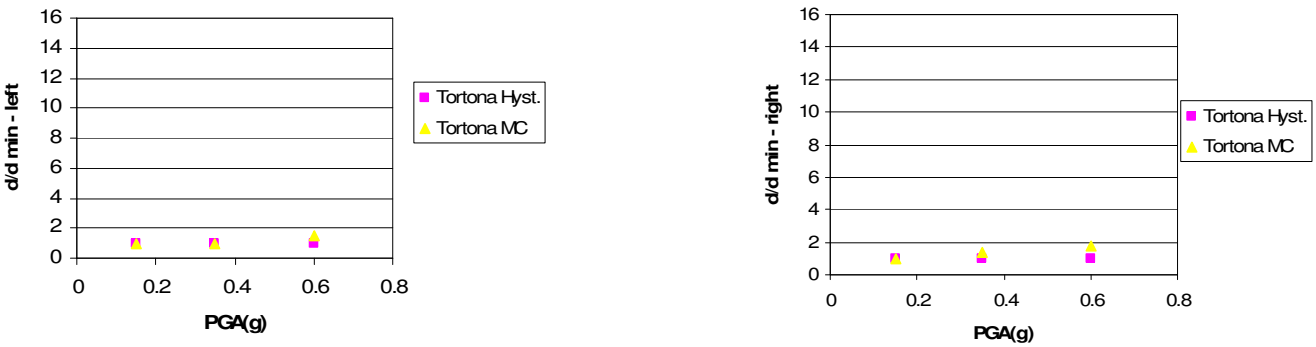

Figure 7. 34 Ratio between peak top wall displacement of left and right wall for Tortona event scaled at several PGA and elastic perfectly plastic (MC) or fully non linear (Hyst.) model

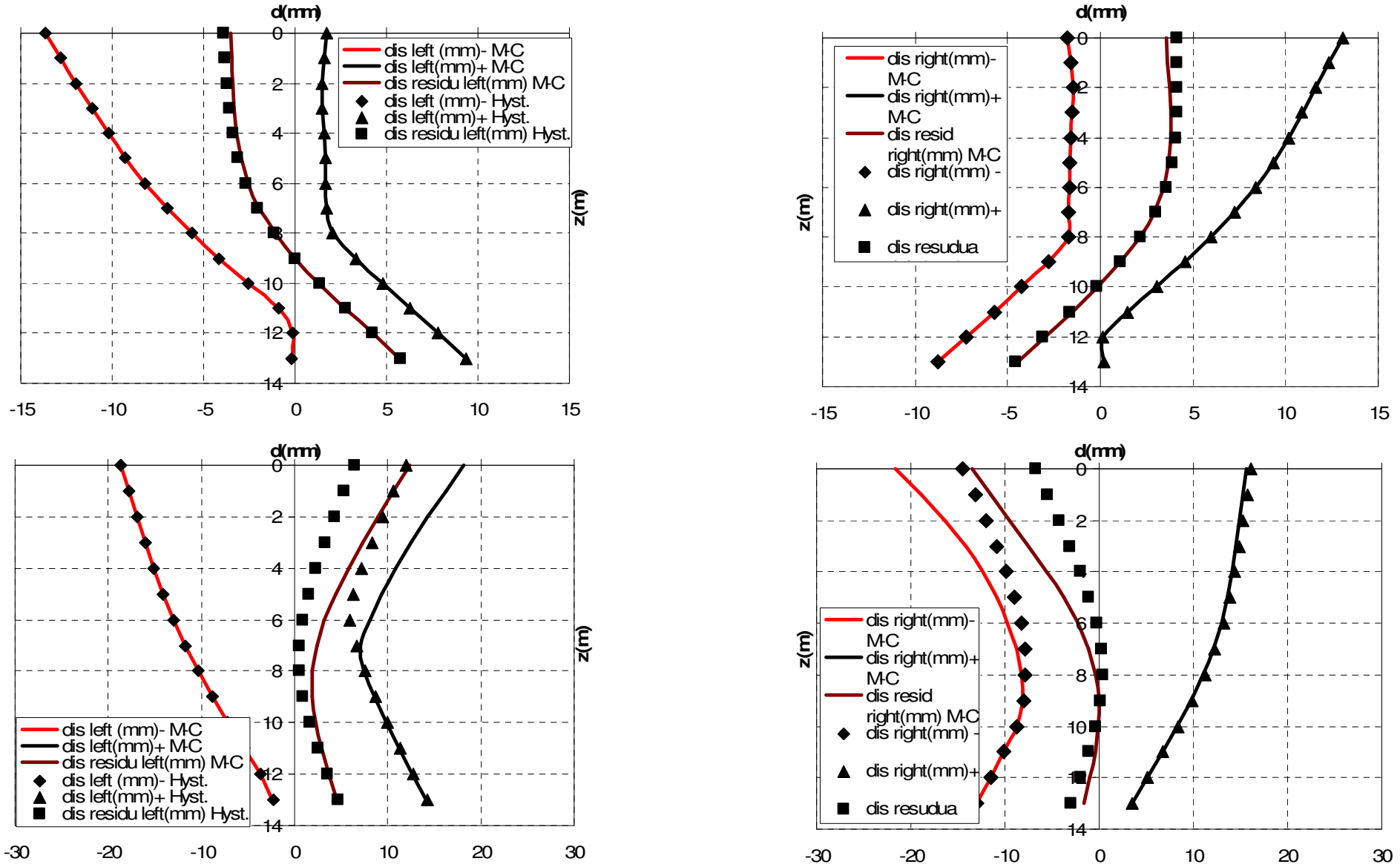

Figure 7. 34 Displacement profiles (maximum, minimum and residual) for left and right wall for Tortona 0.15g (upper) and Tortona 0.35g (lower) FLAC.

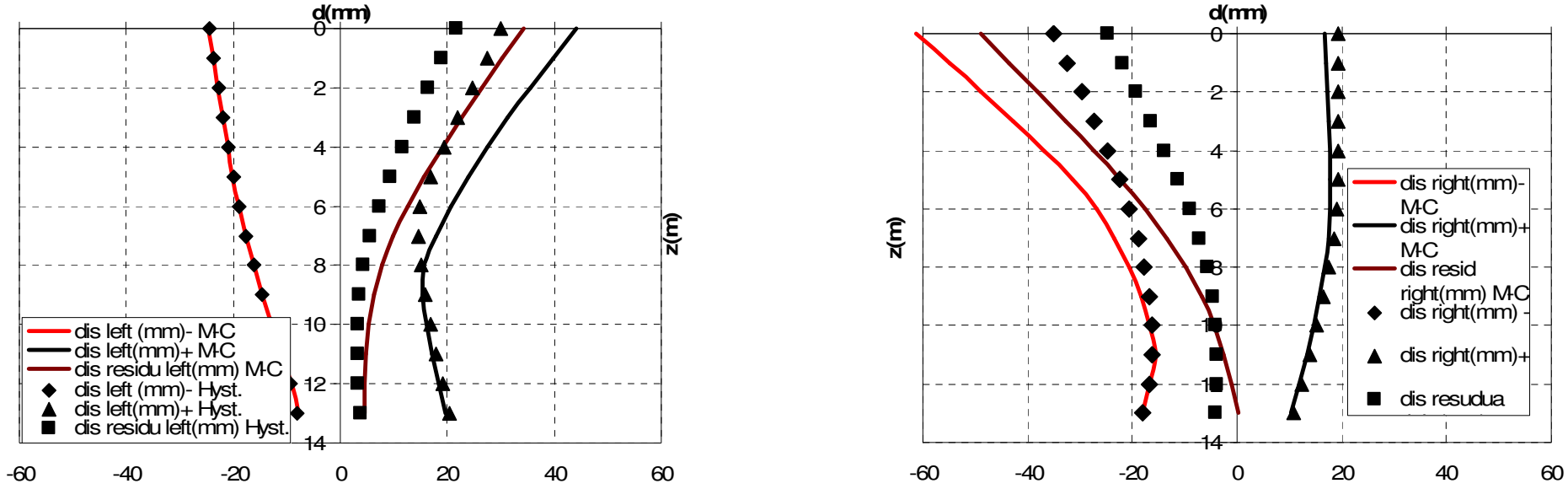

Figure 7. 35 Displacement profiles (maximum, ,minimum and residual) for left and right wall for Tortona FLAC.

As for the case of changing frequency content of the input motion, also in the case of changing material model the scatter increases with increasing PGA.

7.6 Conclusions

The following additional observations can be done:

- Keeping in mind that the design PGA is 0,35g for left wall M/M_{min}=1.2 and for the right wall M/M_{max}=1.4 one can say that sensitivity to material model remains important for bending moment and depending also on polarisation of the accelerogram. In this case considered therefore bending moment sensitivity with respect to material modelling is comparable to the sensitivity with respect to the input accelerograms.
- On the other hand sensitivity of displacement to material model is much lower and almost negligible if compared to sensitivity of displacements to frequency content of the input motion.
- At PGA=0,35g maximum bending moment does not reach above 582kNm which in turn is quite lower than maximum design bending moment (943 kNm) obtained by pseudostatic approach for the case PGA 0,35g (zone 1), soil D and r=2. This means that in terms of forces pseudostatic approach seems quite conservative if compared to fully non linear dynamic analysis.
- Even for PGA equal 0,6g, (846 kNm) maximum design bending moment obtained by pseudostatic analysis for zone1 is not exceeded for the case of Tortona. In case as above, an increase of +/-30% difference for changing input accelerogram is considered, instead, maximum design bending moment obtained by pseudostatic analysis for zone 1 than 943 kNm would be exceeded.
- Comparing the results obtained by numerical application of pseudostatic method (see Figure 5. 9) and the results obtained by dynamic time history analysis with different material type (Table 7. 2) in terms of maximum bending moments for 0,35g (zone 1), it is possible to observe also in this case a good agreement between peak dynamic values (ranging between 413-582 kNm) and pseudostatic value (758 kNm) only if an increase of 30% which account for influence of changing accelerogram is considered. Otherwise, including full non linear material behaviour in the dynamic analysis, also the case of numerical pseudostatic method results in quite conservative results. This in effect maybe due to the fact that numerical pseudostatic analysis are done with Mohr Coulomb soil.

8 MODEL CALIBRATION AND ANALYSIS IN SATURATED BACKFILL CONDITIONS

The preliminary steps before performing a soil structure interaction analysis are to calibrate the soil model parameters in such a way to be able to reproduce in accurate way the reference stress-strain paths of saturated soil undergoing liquefaction under cyclic loading. This is carried out using the FEM code Opensees and the FD code FLAC in order to highlight advantages and disadvantages of both approaches. Secondly simplified methods are used to predict the pore pressure build up for the given accelerogram scaled at different PGA. Finally for the case of saturated deposits a comparison between simplified methods for liquefaction assessment and results obtained by FLAC is carried out.

8.1 Opensees Pressure Dependent Multi Yield Model input parameters.

After describing the main features of the constitutive model used for the saturated case in Chapter 4, the following paragraph describes the steps followed to calibrate the geotechnical parameters which can be normally measured using field measurement and laboratory tests and the model parameters required to replicate the required soil stress-strain behaviour. Table 4. 1 includes reference values for Opensees geotechnical and constitutive parameters to be used with PDMY model.
Table 8.2 includes the geotechnical parameters description and the assumed value and the comparison with reference.
Figure 8.1 to Figure 8.**6** show the comparison between the adopted values for the PDMY material input parameters and those suggested as reference values in the Opensees guidelines.

It is found that there is good agreement for all parameters but the phase transformation angle for which further evidence on the goodness of the adopted relationship is given later.

Parameter	Values			
	Loose sand (15÷35%)	Medium Sand (35÷65%)	Mediumdense sand (65÷85%)	Dense Sand (85÷100%)
Relative Density(%)	25.0%	50.0%	75.0%	92.5%
$(N1)_{60}$	3.2	12.8	28.7	43.7
Mass Density (ton/m^3)	1.7	1.9	2	2.1
Saturated	1.92	2.00	2.10	2.18
Dry	1.46	1.59	1.74	1.87
Shear Modulus (kPa)	5.50E+04	7.50E+04	1.00E+05	1.30E+05
Bulk Modulus (kPa)	1.50E+05	2.00E+05	3.00E+05	3.90E+05
Friction Angle (handbook) (o)	29	33	37	40
Hatanaka and Uchida	27.99	35.98	43.98	49.57
Wolff, 1989	28.05	30.84	35.28	39.18
Peak Shear Strain	0.1	0.1	0.1	0.1
Pressure Dependent Coefficient	0.5	0.5	0.5	0.5
Phase Transformation Angle (o)	27	23	20	16
	19.33	22.00	24.67	26.67
Contraction Constant (c_1)	0.21	0.07	0.05	0.03
Dilation Constant 1 (d_1)	0	0.4	0.6	0.8
Dilation Constant 2 (d_2)	0	2	3	5
Liquefaction Parameter 1 (y_1)	10	10	5	0
Liquefaction Parameter 2 (y_2)	0.02	0.01	0.003	0
Liquefaction Parameter 3	1	1	1	0
Void Ratio	0.85	0.7	0.55	0.45

Table 8.1 Geotechnical and constitutive reference parameters (http://cyclic.ucsd.edu/opensees)

Parameter	Values	Comments	Comparison
Void ratio	$e = e_{\max} - D_r(e_{\max} - e_{\min})$ (8.1)	e_{max}=1 e_{min}=0.4 Holtz and Kovacs (1981) clean, uniform fine or medium dense sand	Opensees reference
Soil mass density	$\rho = \frac{(G_s + Se)\rho_w}{1+e}$ (8.2)	G_s = 2.7 soil specific gravity, ρ_w = 1.0 ton/m^3 S=1 for saturated and 0 for dry condition	Opensees reference
Small strain shear modulus	$G_r = A\frac{(2.17-e)^2}{1+e}p_r^{0.4}$ (8.3)	A = 7900÷14300 depending on fine content Ishihara (1993), p_r exponent 0.4 adequate for strains between 1E-5÷1E-6 (Ishihara 1996)	Opensees reference G_0= $G_0(D_r)$ in accordance with A=10500
Small strain bulk modulus	$B_r = G_r\frac{2(1+\nu)}{3(1-2\nu)}$ (8.4)	ν = 0.5 for perfectly undrained case	Opensees reference ν = 0.35
Friction angle	$\phi = 16.2D_r + 25$ (8.5)	$\phi(\deg) = 27.1 + 0.3N_{60} - 0.00054N_6$ Wolff (1989) $(N_1)_{60}$ corrected for energy ratio, borehole diameter, sampling method and rod length $D_r = \sqrt{\frac{(N_1)_{60}}{C_P C_A C_{OCR}}}$ Kulhawy and Mayne (1990) C_P = 60 + 25 log (D_{50}) (particle size effect) C_A = 1.2 + 0.05 log (t/100) (age of deposit yy) C_{OCR} = OCR $^{0.18}$ Typical values for liquefiable sands are assumed D_{50} = 0.20 mm t = 100 yy OCR = 1	Opensees reference
Phase transformation angle	$\phi_{PT} = -15.7D_r + 31$ (8.6)		Experimental evidence

Table 8.2 Geotechnical parameters

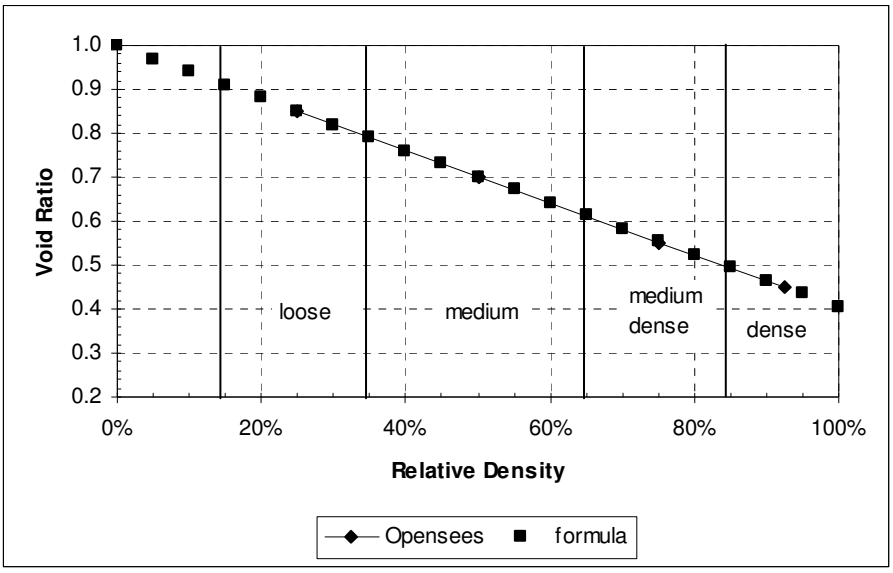

Figure 8.1 Relationship of void ratio to relative density used for PDMY material (values recommended by Opensees and calculated by the formula in Table 8.2).

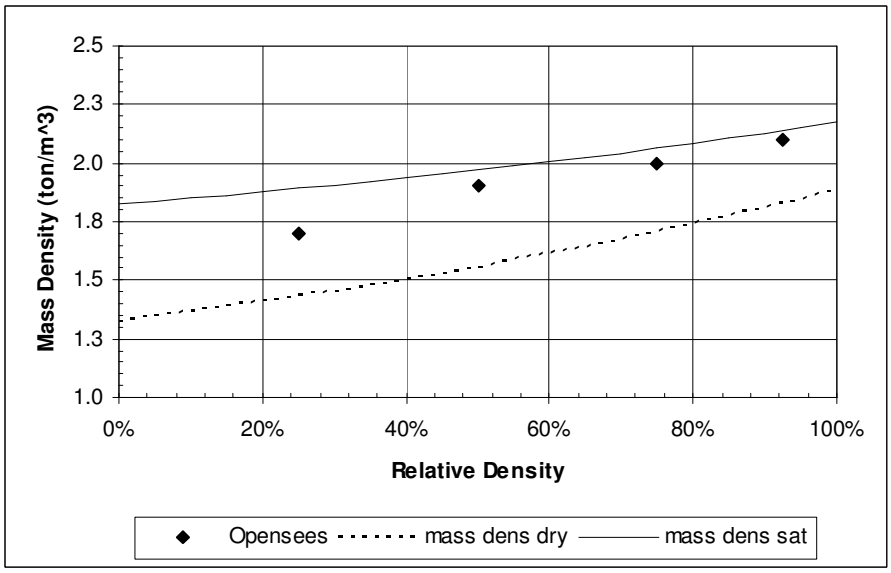

Figure 8.2 Relationship of soil mass density to the relative density used for the PDMY material (values recommended by Opensees and calculated by the formula in Table 8.2).

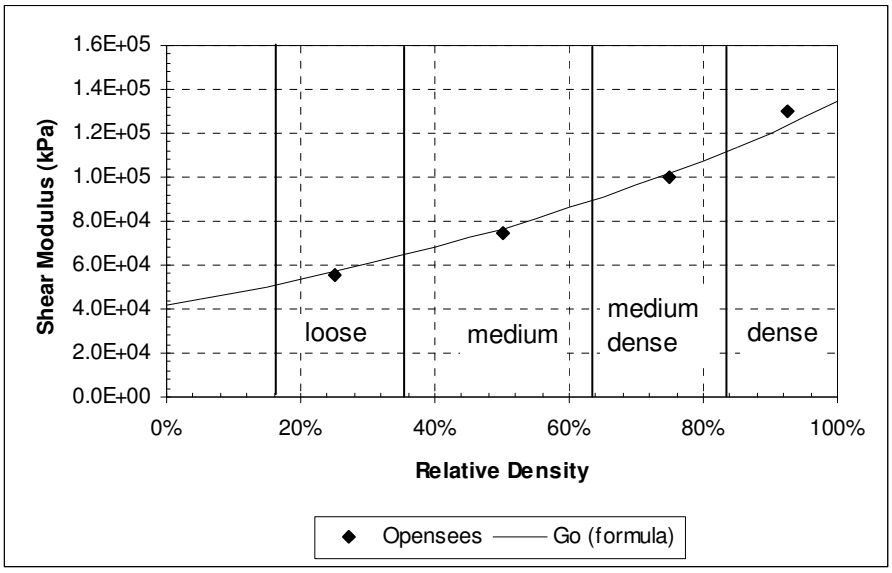

Figure 8.3 Relationship of reference shear modulus to relative density used for the PDMY material (values recommended by Opensees and calculated by the formula in Table 8.2).

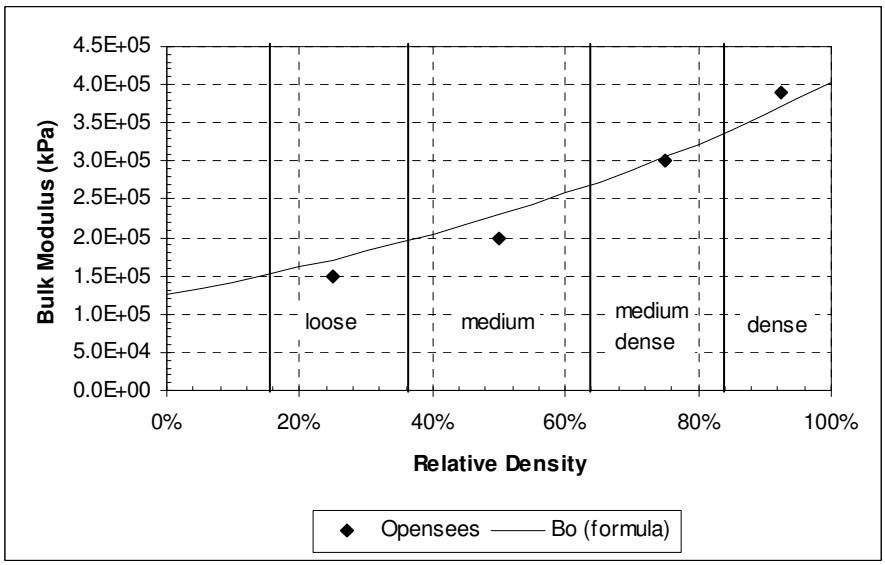

Figure 8.4 Relationship of reference bulk modulus to relative density used for the PDMY material (values recommended by Opensees and calculated by the formula in Table 8.2).

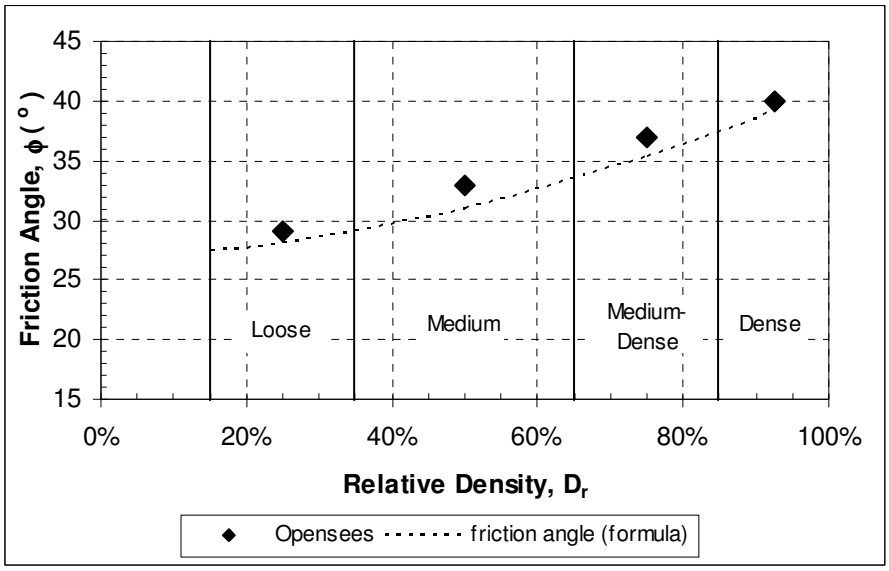

Figure 8.5 Relationship of friction angle to relative density used to define the PDMY material material (values recommended by Opensees and calculated by the formula in Table 8.2).

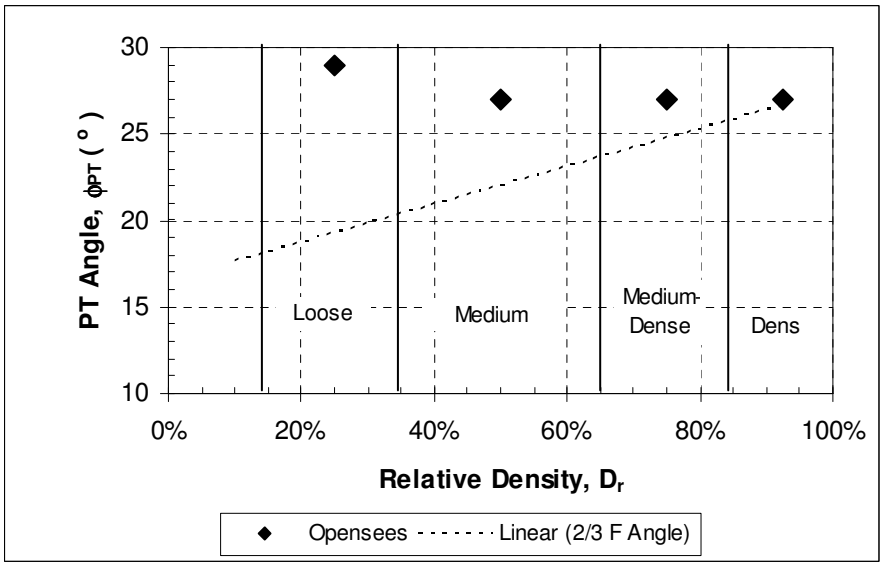

Figure 8.6 Relationship of phase transformation angle to relative density used to define the PDMY material (values recommended by Opensees and calculated by the formula in Table 8.2).

Table 8.2 includes the constitutive parameters description and the assumed value and the comparison with reference. This research dealt with unbiased loading, which typically produces equal straining in both directions along the axis of loading so the liquefaction parameter y_4 (or l_3).was not needed.

Table 8.3 Constitutive parameters

Paramaters	Values	Comments	Comparison
Contraction parameter (rate of contraction in phase 0-1) c_1	$c_1 = 10.394\exp(-6.0422 \cdot 0.45)$ for CSR<0.23 $c_1 = 1$ for CSR>0.23 (8.6)	Comparison with back calculated field and experimental results	Opensees reference $c = 0.0288 D_r^{-1.4172}$
Dilation parameter (rate of dilation above PT line phase 2-3) d_1	$d_1 = 1.147 D_r - 0.2454$ (8.7)	Match of reference	Opensees reference
Dilation parameter (rate of dilation above PT line phase 2-3 dependent on confinement) d_2	$d_2 = 6.9686 D_r - 1.7187$ (8.8)		
Liquefaction parameter (extension of the yield phase related to relative density) y_1	y_1 = 10 for Dr<65% (8.9) y_1 = -35.48D_r+32.5 (8.10) for Dr≥65%	Match of reference	Liquefaction parameter 1 (l_1)
Liquefaction parameter (extension of the yield phase related to cumulative damage) y_2	$y_2 = -0.0154 \ln D_r - 0.0012$ (8.11)	Match of reference	Liquefaction parameter 2 (l_2)
y_4	y_4 = 10 (8.12) for Dr<85% y_4 = 0 (8.13) for Dr>85%	Reference values	Liquefaction parameter 3 (l_3)

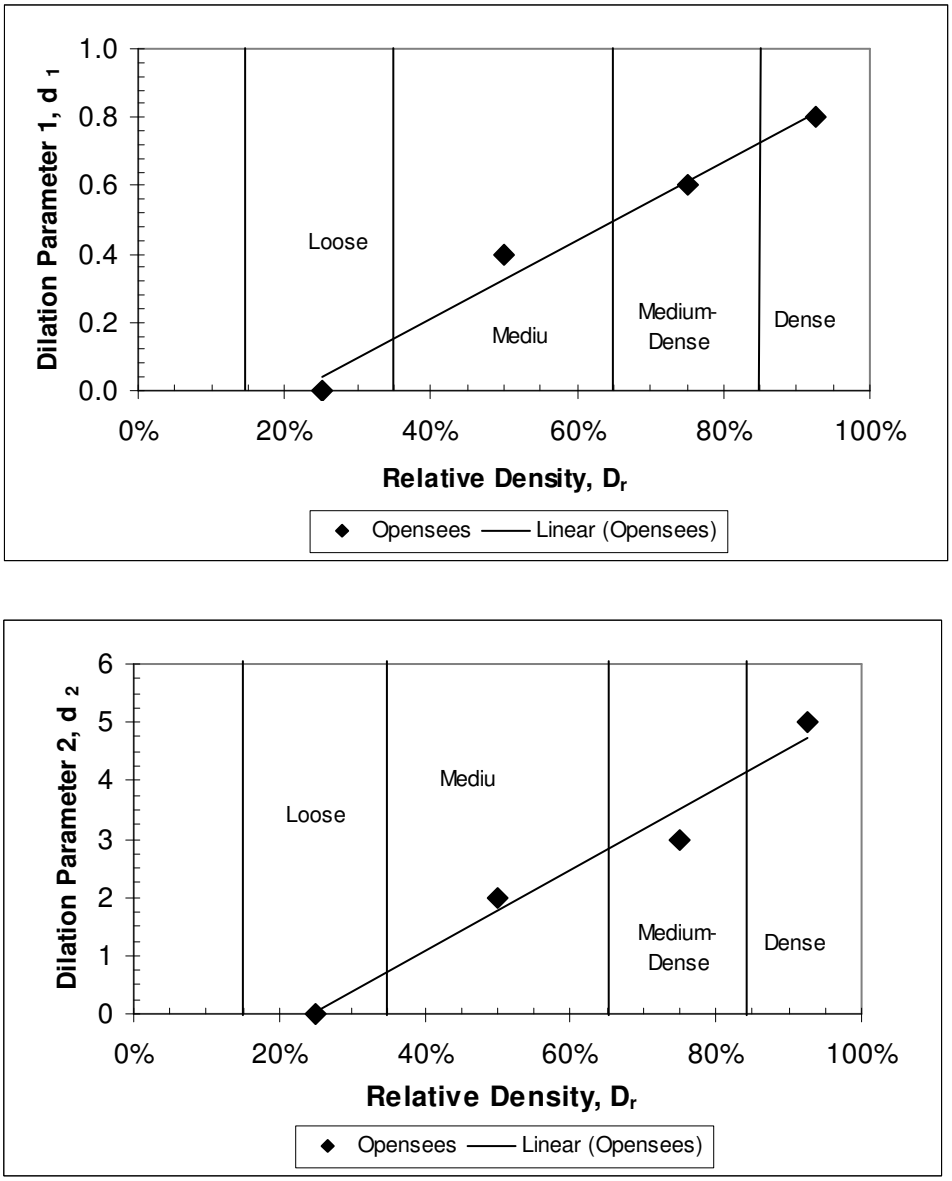

Figure 8. 7 Dilation parameters. (a) First dilation parameters comparion between reccommended values by Opensees and linear interpolation function (b) Second dilation parameter comparison bewteen reccommended values by Opensees and linear interpolation function.

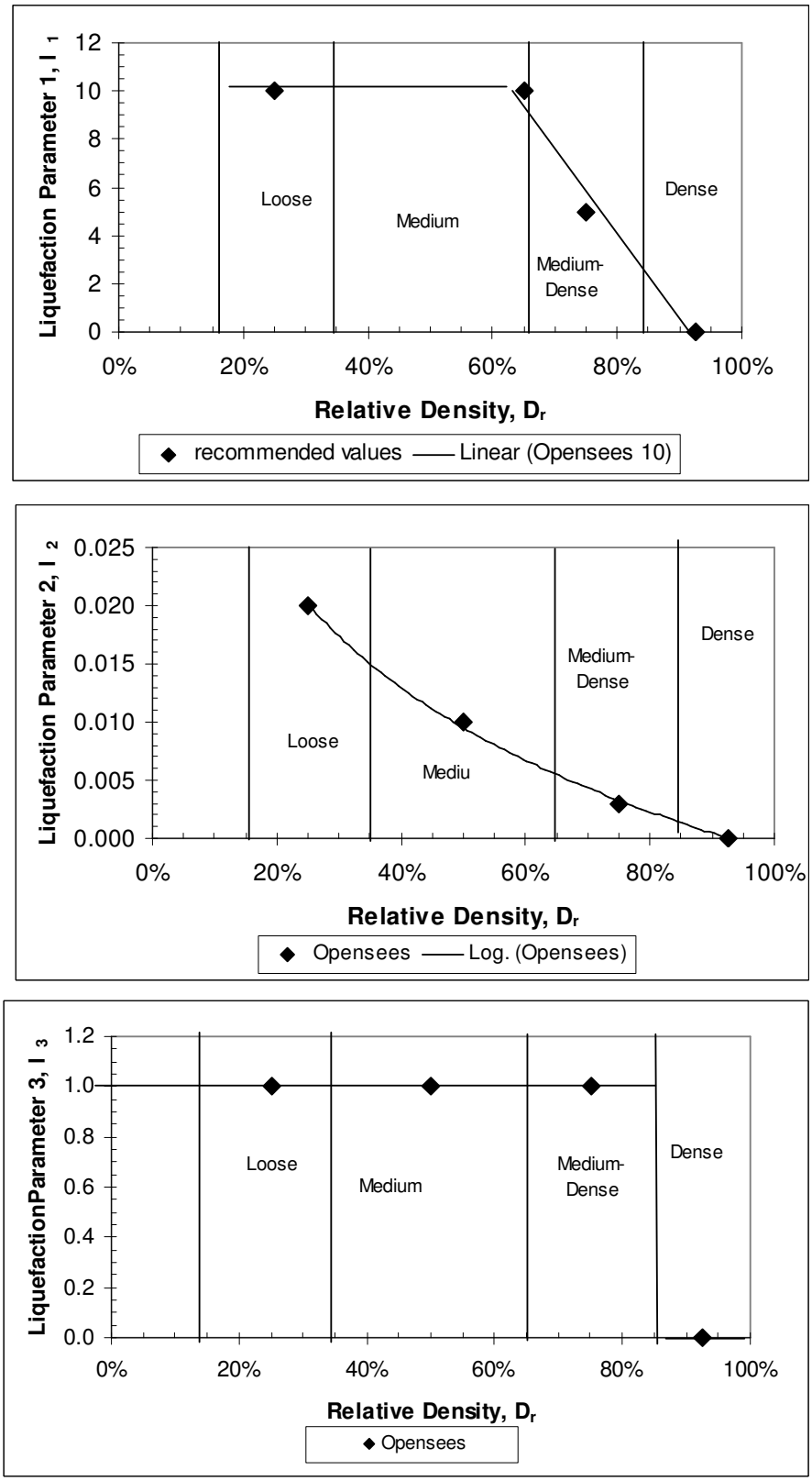

Figure 8. 8 Liquefaction parameters. Relationships between liquefaction parameters and relative density used to define PDMY material. Recommended values are represented by diamonds and Equations 8.9 to 8.13 are represented by lines.

Table 8. 4 Model constants

Paramater	Comments	Reference value
γ_{max}	maximum octahedral shear strain at soil failure at the reference mean effective confining pressure	Recommended by Opensees 0.1
p_r	confining pressure at which G_r, B_r, and γ_{max} are defined	80 kPa
d	positive constant that defines G and B as a function of the instantaneous effective confinement pressure, p' $G = G_r\left(\frac{p'}{p_r}\right)^d$ $B = B_r\left(\frac{p'}{p_r}\right)^d$	Recommended by Opensees 0.5

8.2 Saturated model calibration in OPENSEES

The first phase of testing involved the application of a stress-controlled cyclic load to a single element of undrained soil. The element was defined by four nodes: Nodes 1 and 2 were fixed, while nodes 3 and 4 were free to move both vertically and horizontally but laterally confined by equal movement in the x-direction

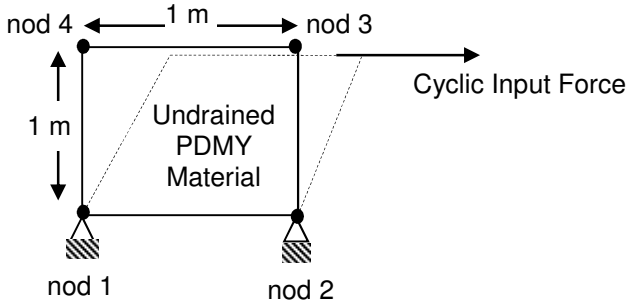

Figure 8. 9 single element model geometry

The cyclic component of the forcing function is a harmonic function with a period of 314 seconds, and time steps broken into one-second intervals ($\Delta t/T \approx 0.003$) (Figure 8. 10). These small time steps were used to avoid rapid loading of the "perfectly-undrained" element. The amplitude was increased gradually to minimize initial strong transient responses due to sudden loading, of the initially at rest element.

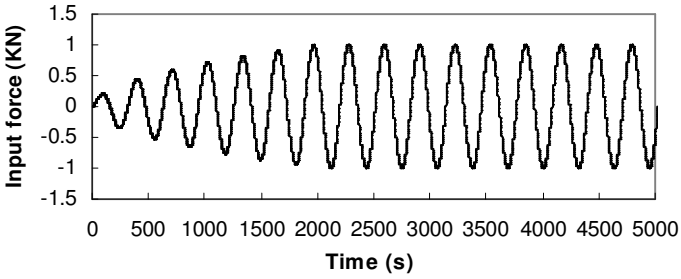

Figure 8. 10 Input cyclic force applied to top element under an effective confining pressure of 3.5 kPa

As noted earlier, the analyses were performed using the Newmark integration method, with time steps advanced using the Newton-Rhapson algorithm. The model's stress-strain behaviour was regulated by the modulus reduction curve, which gives the relationship between G/G_{max} and shear strain. The PDMY material uses an automatically-defined modulus reduction curve, unless the user specifies otherwise. Comparison of the automatically-defined modulus reduction curve and the curve proposed by Darendeli (2001) as shown in Figure 2.11 indicates that the curves are similar for deformations below 0.1%. Damping obtained using the automatic modulus reduction curve agrees reasonably well with damping projected by Darendeli

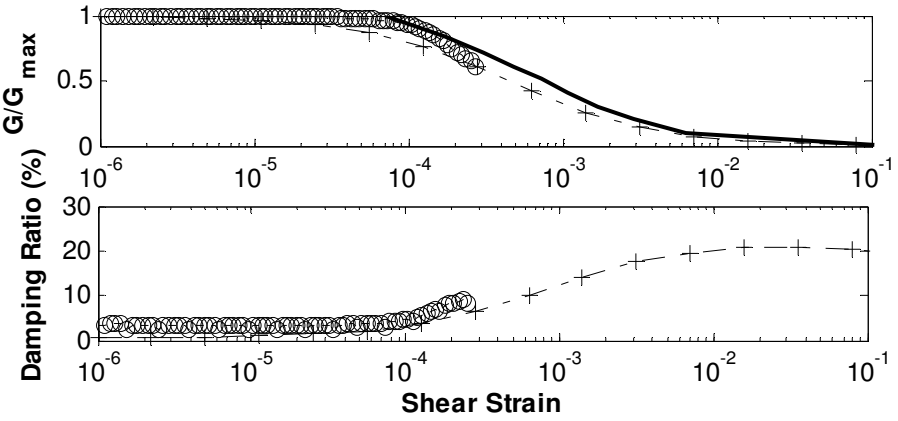

Figure 8. 11 Modulus reduction and damping curves for trial with automatic modulus reduction curve generation. The solid line represents the automatically-generated curve, crosses represent Darendeli's curve, and circles represent actual model behaviour.

As the analysis progressed, nodal and element recorders captured the displacement, stress, strain, and pore pressure at designated time intervals. Testing was performed for elements of varying relative density subjected to different cyclic stress amplitudes. For each test, the displacement at the top of the element and the development of excess pore pressure ratio with time were plotted, as well as hysteretic stress-strain diagrams and deviatoric stress versus confinement stress diagrams. From each data set, the cyclic stress ratio (CSR) and number of

cycles to liquefaction, N_L, were recorded and stored. Figure 8. 12 and Figure 8. 13 show the results obtained for CSR equal 0.23 and relative density equal 45% and 75%.

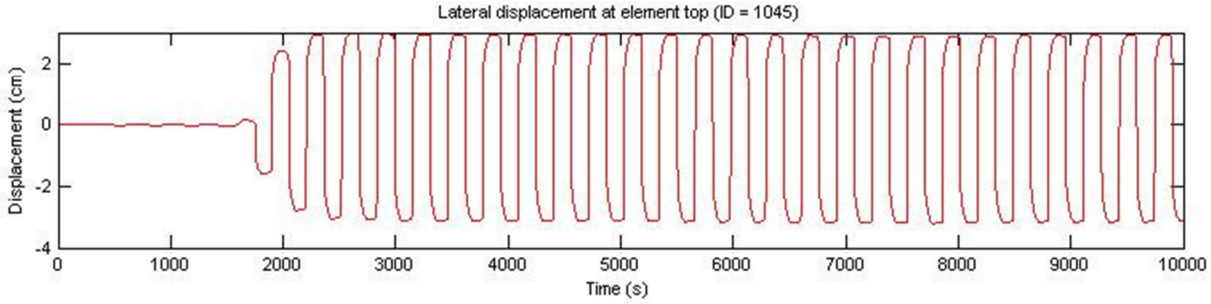

a)

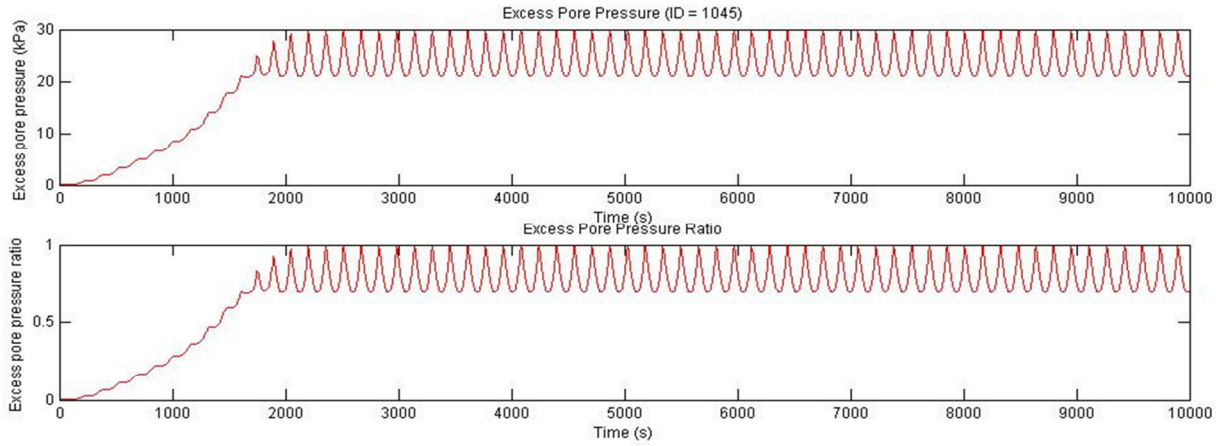

b)

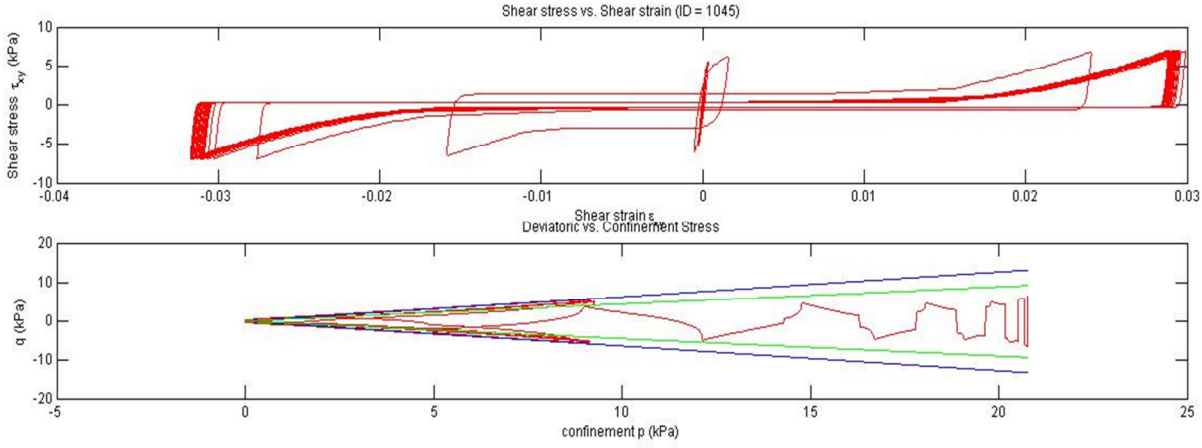

c)

Figure 8. 12 Results of a model execution with 0.23 CSR and 45% Dr; (a) displacement at element top (b) excess pore pressure ratio increase with time and (c) shear stress versus strain and deviatoric versus effective confining stress.

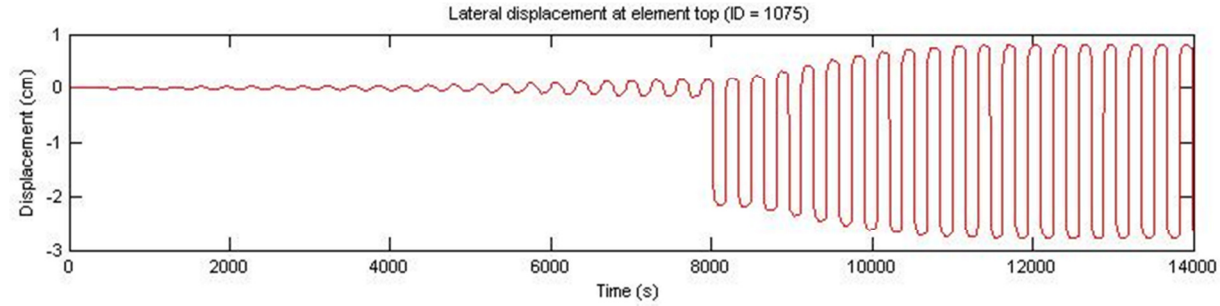

a)

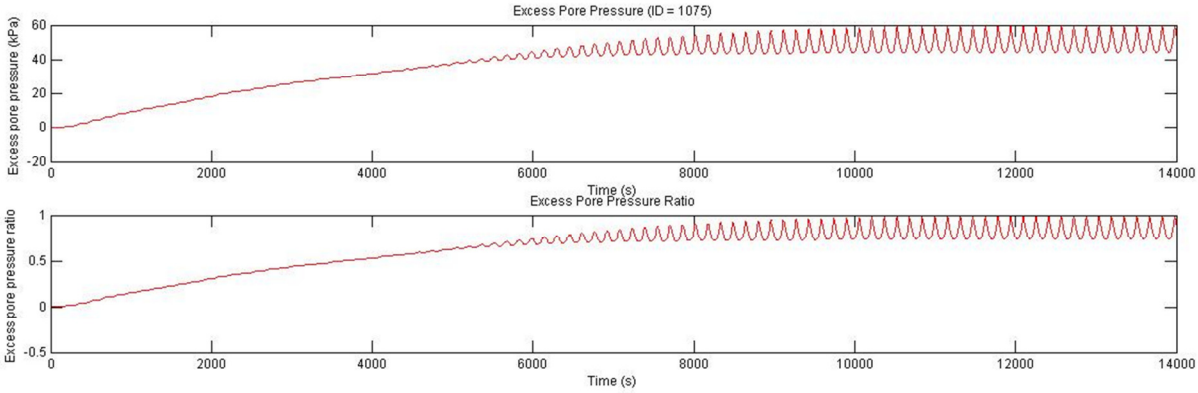

b)

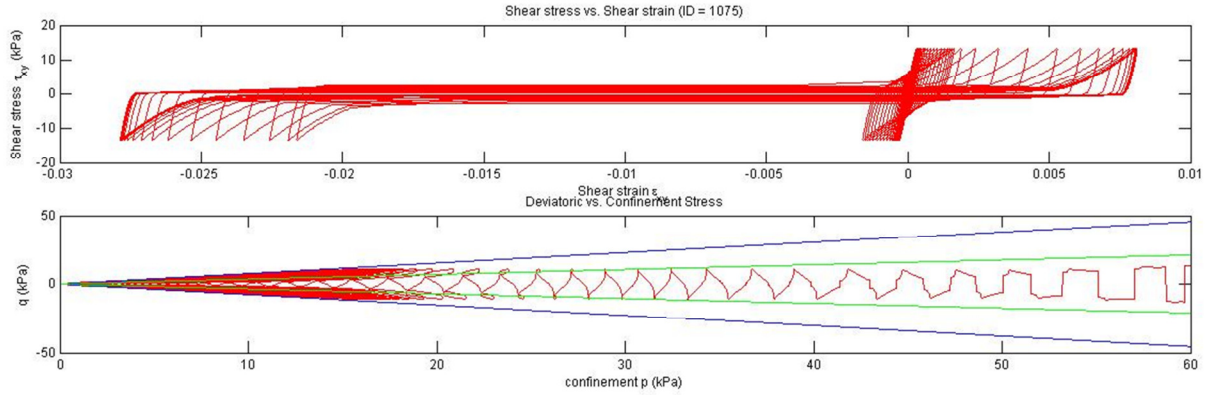

c)

Figure 8. 13 Results of a model execution with 0.23 CSR and 75% Dr; (a) displacement at element top (b) excess pore pressure ratio increase with time and (c) shear stress versus strain and deviatoric versus effective confining stress.

A summary table of the results for 45% and 75% relative density is included in the following Table:

Table 8.5 Results summary for Opensees element test.

Dr=45%		Dr=75%	
CSR	N_L	CSR	N_L
0.08	29		
0.1	21		
0.18	10	0.15	39
0.23	7	0.23	26
0.3	5	0.3	17
0.4	4	0.4	13
0.45	4		

8.3 Comparison of results to existing data

One of the possible comparisons between test element using the PDMY model and existing data is the relationship between the cyclic stress ratio and the number of cycles to liquefaction for soils of different densities. In order to determine this reference curves the following relationships are considered:

a) Field correlations to determine the cyclic stress ratio (Figure 2.4) required to produce liquefaction for a magnitude (M) 7.5 earthquake for a given soil density (expressed in terms of corrected standard penetration test SPT blow counts) (*Youd et al*, 2001) valid for $(N_1)_{60}<30$.

$$CRR_{7.5} = \frac{1}{34-(N_1)_{60}} + \frac{(N_1)_{60}}{135} + \frac{50}{[10\cdot(N_1)_{60}+45]^2} - \frac{1}{200} \qquad (8.1)$$

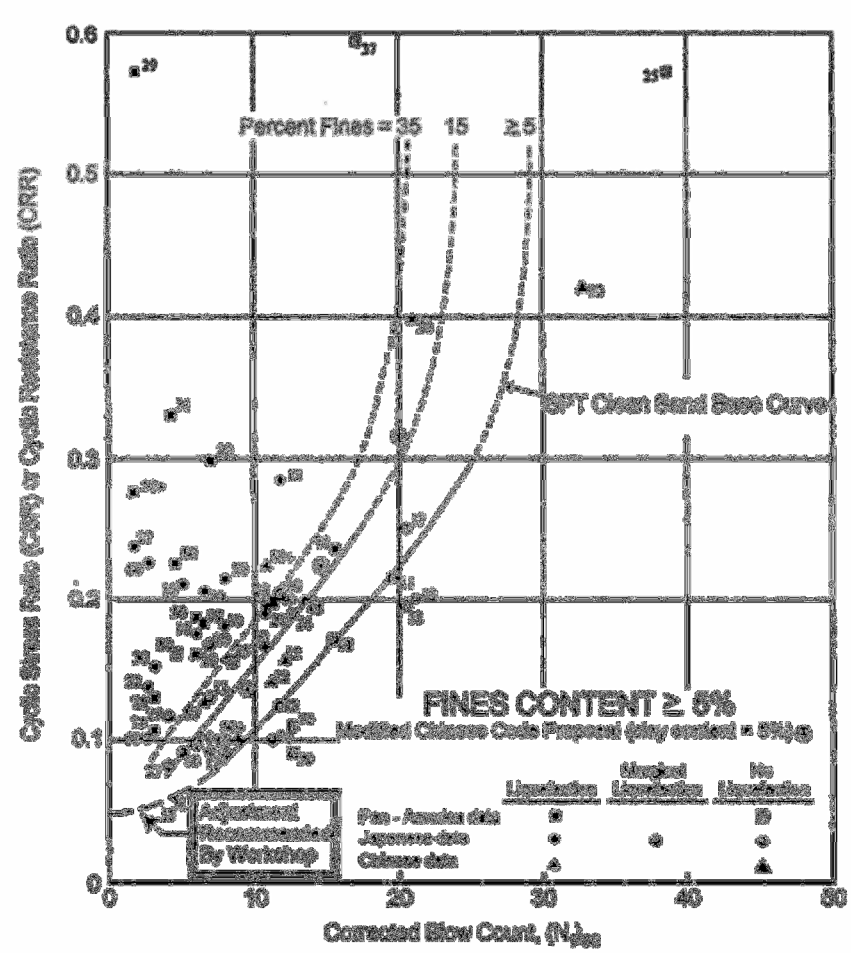

Figure 8. 14 SPT clean-sand base curve for magnitude 7.5 earthquake with data from liquefaction case histories (modified from *Seed et al.*, 1985) (*Youd et al.*, 2001)

b) Scaling factors to the CSRs to determine the CSR required to produce liquefaction for earthquakes of different magnitude M_w (*Youd et al*, 2001)

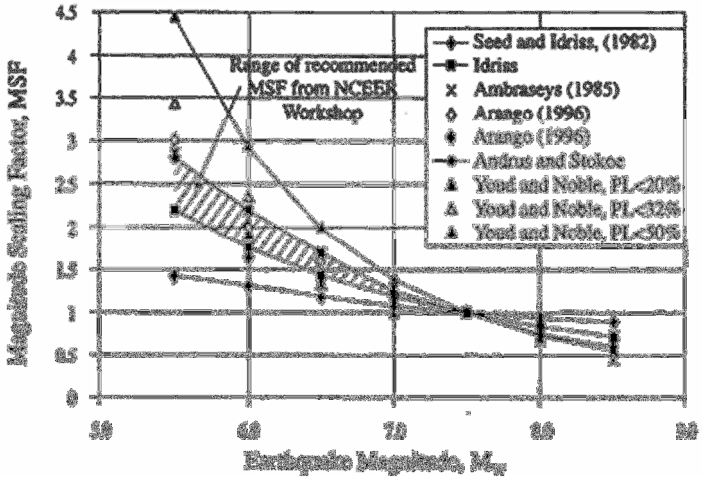

Figure 8. 15 Recommended magnitude scaling factors for earthquakes of varying magnitude. Values from the centre of the hatched area were used for this analysis (*Youd et al.*, 2001)

c) Laboratory relationships to correlate the earthquake magnitudes to an equivalent number of cycles to liquefaction.

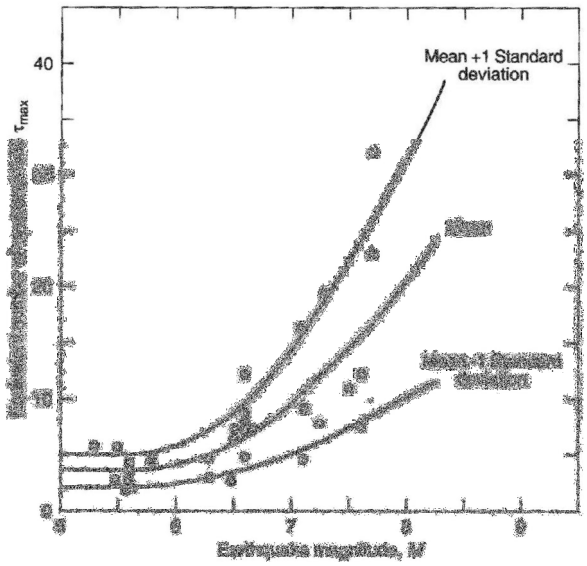

Figure 8. 16 Number of equivalent uniform stress cycles for earthquakes of different magnitude (*Seed et al.*, 1975)

Considering the correlation between SPT blowcounts and relative density (Kulhawy and Mayne (1990)) the correlations described above were used to derive the relationship between CSR and N_L for soils of varying density as shown in **Error! Reference source not found.** and compared to the results obtained by Opensees calibration as included in Table 3.1. As pointed out in Table 3.4 the trend of the contraction coefficient c_1 does not follow the same law for values of CSR higher than 0.23 for which it assumes a value close to unity.

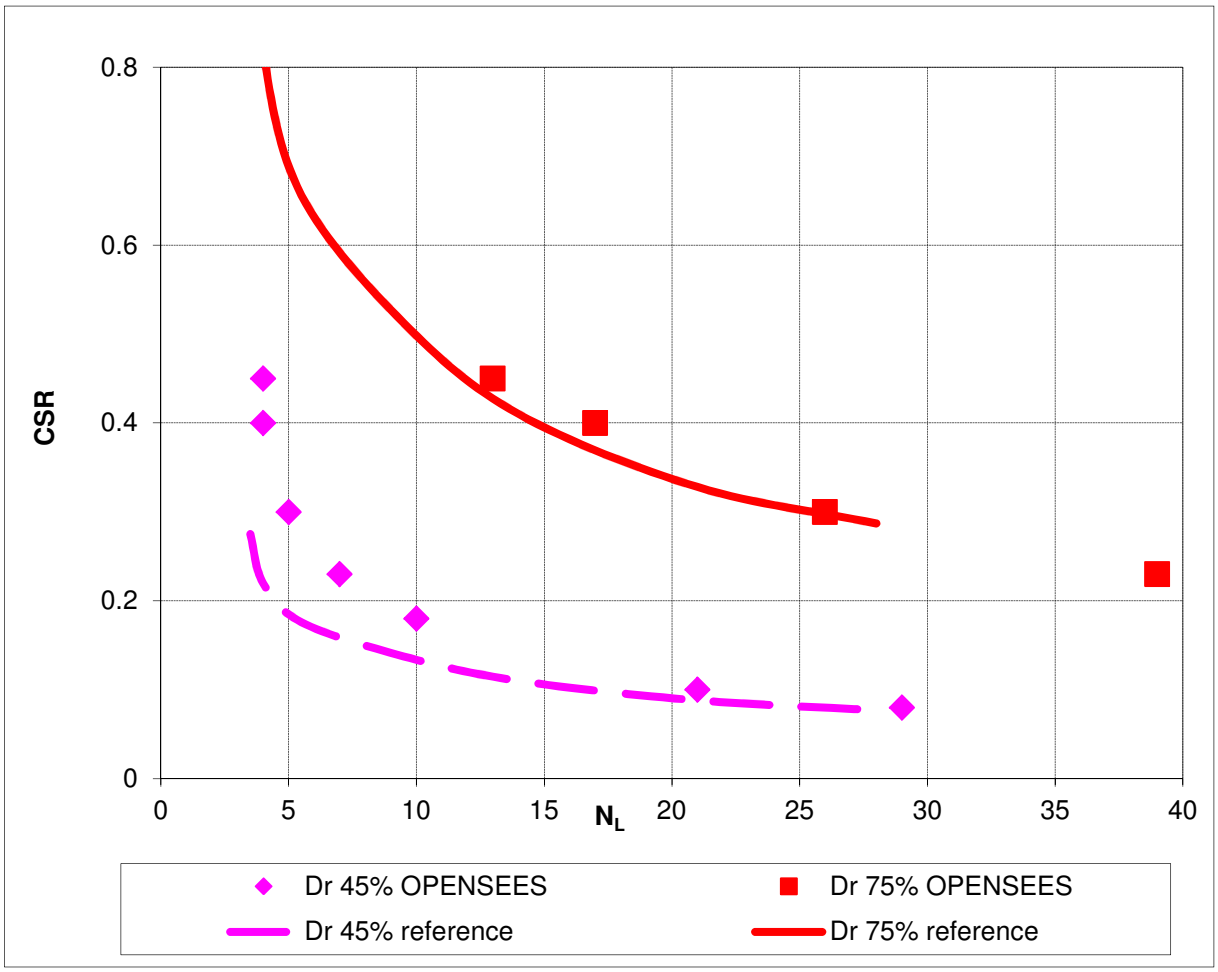

Figure 8. 17 Comparison between predicted relationship N_L/Dr and calculated by OPENSEES element test calibration process.

8.4 Calibration for Finn model in FLAC

The material constants in the Finn model that control pore pressure build-up are related to the volumetric response in a drained test. However, the relationship between number of cycles and cyclic stress ratio CSR can be modelled with *FLAC*, and the material constants can be deduced by comparing the *FLAC* results with the theoretical predictions.
A "shaking table" is modelled with *FLAC*—this consists of a box of sand that is given a periodic motion at its base. The motion of the sides follows that of the base, except that the amplitude diminishes to zero at the top (i.e., the motion is that of simple shear).
The frequency of loading is left unchanged and equal to 5Hz while the amplitude is modified in order to achieve a target CSR value (values between 5 and 30 mm). Vertical loading is by gravity only. Equilibrium stresses and pore pressures are installed in the soil, and pore pressure and effective stress (mean total stress minus the pore pressure) are monitored in a

zone within the soil. A column of only one zone width is modelled, since the horizontal variation is of no particular interest here.

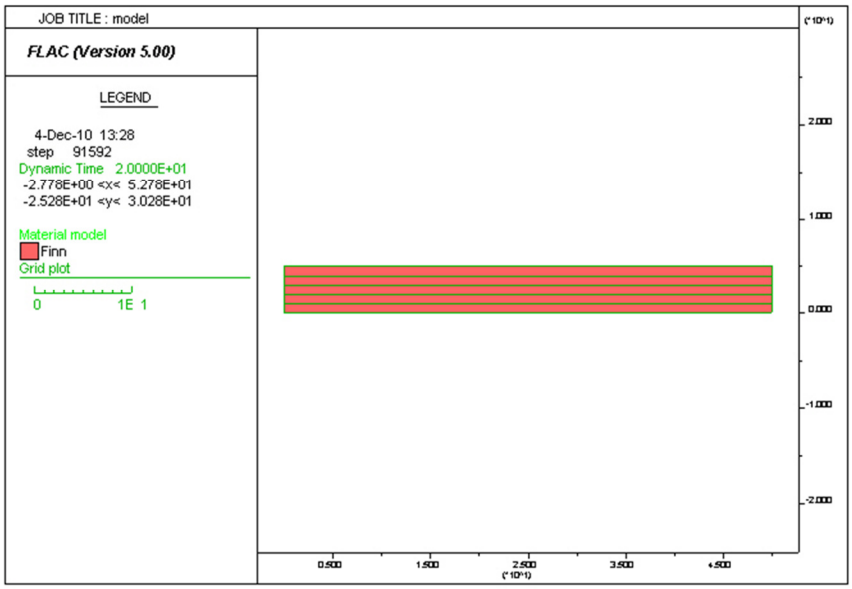

Figure 8. 18 FLAC geometry and grid for the shaking table test simulation.

The Byrne model parameters are correlated to the values of $(N_1)_{60}$=10 and the case $(N_1)_{60}$=30 corresponding to relative density of Dr 45% and 75% according to Kulhawy and Mayne (1990). By a trial and error procedure a curve fitting process can be carried out by monitoring the value of CSR and the effective stress value at a depth of 3.5m in the middle section of the model. When the effective stress value reaches the zero liquefaction has occurred and multiplying the time for the frequency (5Hz) provides the number of cycles for liquefaction N_L. The following results are obtained using $C_1=13.6\cdot(N_1)_{60}^{-1.25}$ for $(N_1)_{60}$=10 and $C_1=16\cdot(N_1)_{60}^{-1.25}$ for $(N_1)_{60}$=30. A plot comparing the expected reference curves and the one obtained by FLAC shaking table test is shown in

Table 8.6 Results summary for FLAC shaking table test.

Dr=45%		Dr=75%	
CSR	N_L	CSR	N_L
0.11	27.5		
0.17	11		
0.23	5		
0.3	2.5	0.3	33
0.4	2.5	0.4	11
0.44	2.5	0.45	6.5

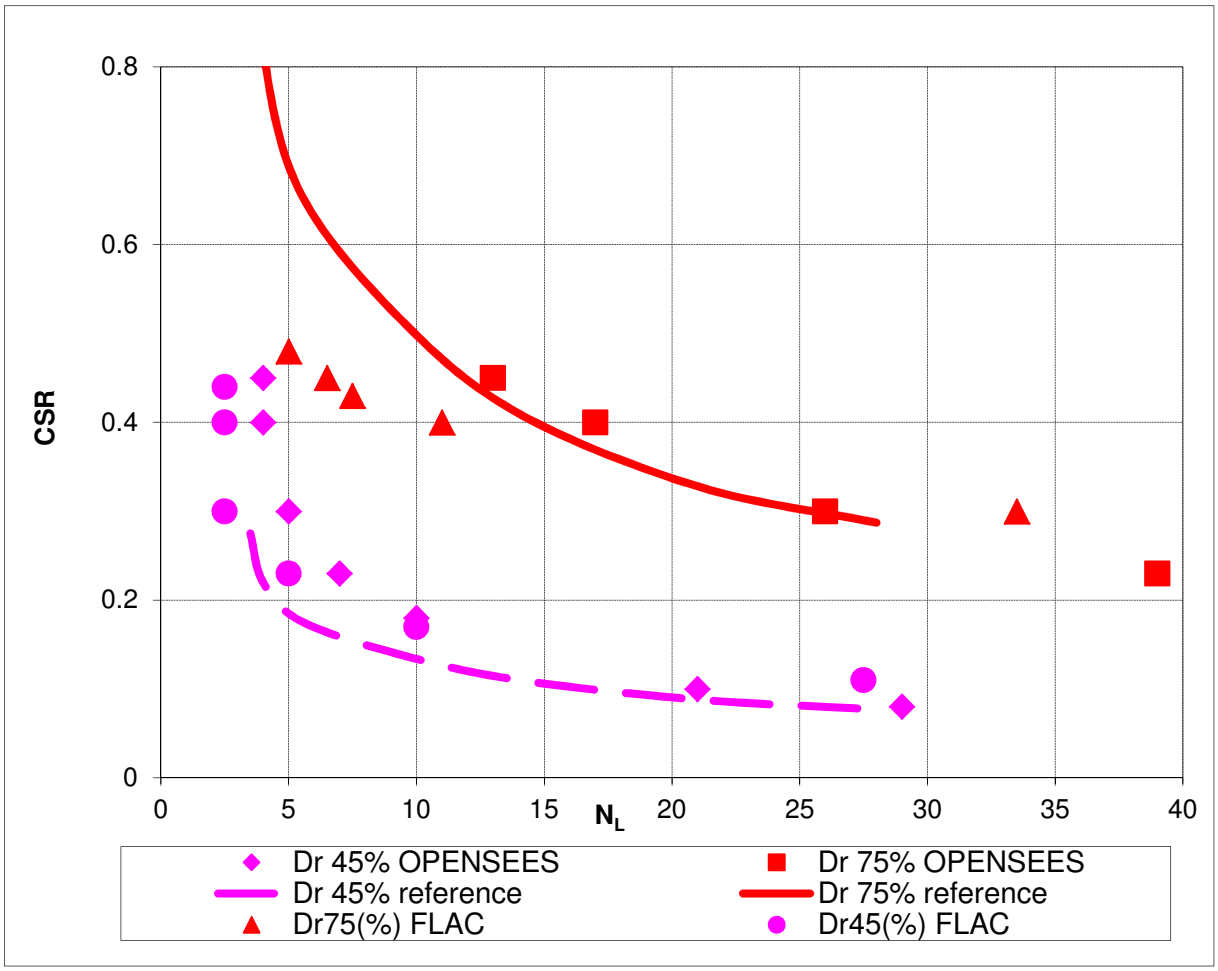

Figure 8. 19 Comparison between Opensees, FLAC and reference curves for number of cycles to liquefaction (N_L) and cyclis stress ration (CSR) for different values of relative density (Dr%).

Both Opensees and FLAC achieve a good agreement for lower Dr (more relevant for liquefaction). Nonetheless FLAC fitting is independent of CSR while, as already pointed out, the expression for C_1 parameter is not valid for CSR above 0.23 in Opensees. For this reason the fitting with FLAC is more satisfactory

8.5 Simplified predictions using Cyclic Stress Ratio (CSR) approach.

The cyclic stress required to cause liquefaction, $\tau_{cyc,L}$, is a function of soil density, the initial effective confining pressure, σ'_{vo}, and the earthquake magnitude (Kramer, 1996). It is expressed as

$$\tau_{cyc,L} = CSR_L \sigma'_{vo} \qquad (8.\ 2)$$

The cyclic stress ratio required to cause liquefaction (CSR_L) or the corresponding cyclic resistance ration (CRR) for a magnitude 7.5 earthquake is determined using the relationship, derived from field data, to the soil's density in terms of its corrected blow count (Figure 8. 14). A magnitude scaling factor (MSF) is used to convert the CSR to CSR_L for an earthquake of desired magnitude as (Figure 8. 15). Equation (8.2) shows that the resistance to liquefaction increases with effective confining pressure, or depth, and density.

The cyclic shear stress induced by the earthquake is estimated using the procedure developed by Seed and Idriss (1971). The stress at any depth is represented by (Kramer, 1996)

$$\tau_{cyc} = 0.65\ a_{max}\ \sigma_{vo}\ r_d \qquad (8.\ 3)$$

where a_{max} is the maximum ground surface acceleration in units of g and σ_{vo} is the total vertical stress at depth. The 0.65 factor is a scaling factor typically used to convert the maximum stress to an equivalent harmonic cyclic stress, and the stress reduction factor, $r_{d,}$ is used to estimate the reduction of stress with depth (Figure 4.12). The figure shows that the uncertainty in r_d increases with depth. A line of average values was estimated toward the centre of the shaded area for comparison and used for calculation in the following.

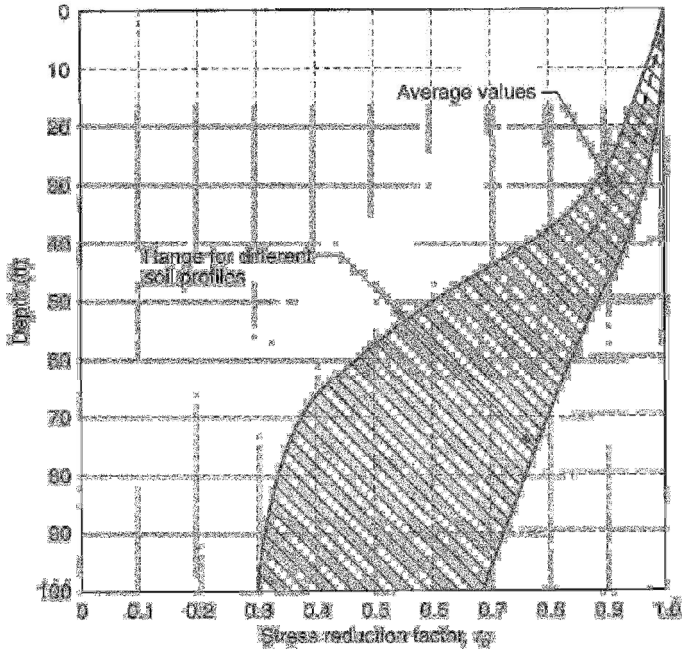

Figure 8. 20 Reduction factor to estimate the variation of cyclic shear stress depth below level or gently sloping ground surfaces (Kramer, 1996).

In addition to estimating the cyclic shear stresses and factor of safety at various depths, it is possible to predict the maximum excess pore pressure ratio. For a value of relative density the equivalent number of cycles at a given depth, N_{eq}, is estimated knowing the value of CRR from Figure 8. 14 and the scaling factor valid for the specific magnitude. In order to determine the number of cycles required for liquefaction for the acting value of CSR (lower than CRR if no liquefaction occurs) the same correlation can be used .The excess pore pressure ratio can be estimated using the relationship developed by Lee and Albaisa (1974) and DeAlba et al. (1975).

$$r_u = \frac{1}{2} + \frac{1}{\pi}\sin^{-1}\left[2\left(\frac{N_{eq}}{N_L}\right)^{1/0.7} - 1\right] \tag{8.4}$$

An hypothetical soil profile comprising a 23m thick layer of medium dense sand susceptible to liquefaction and a 32m thick layer of dense sand/till over stiff bedrock as shown in Figure 8. 21 is taken into consideration. Values of relative density, void index, vertical stresses and and cyclic stresses can be calculated using the relationships included in Table 3.1 The average value of shear wave velocity for the upper layer (as mentioned in 5.5) results being 186m/s therefore soil category type C (V_s threshold limit 180 m/s) therefore the soil amplification factor used to evaluate τ_{cyc} is 1.15 instead of 1.35.

Applying the simplified procedure based on CSR ratio described in paragraph 8.5 for the Tortona accelerogramm (Ms=4) and PGA equal to 0.15g and 0.25 it possible to evaluate the profiles of cyclic shear stresses, factor of safety against liquefaction and pore pressure ratios as shown in **Error! Reference source not found.** a) and b).

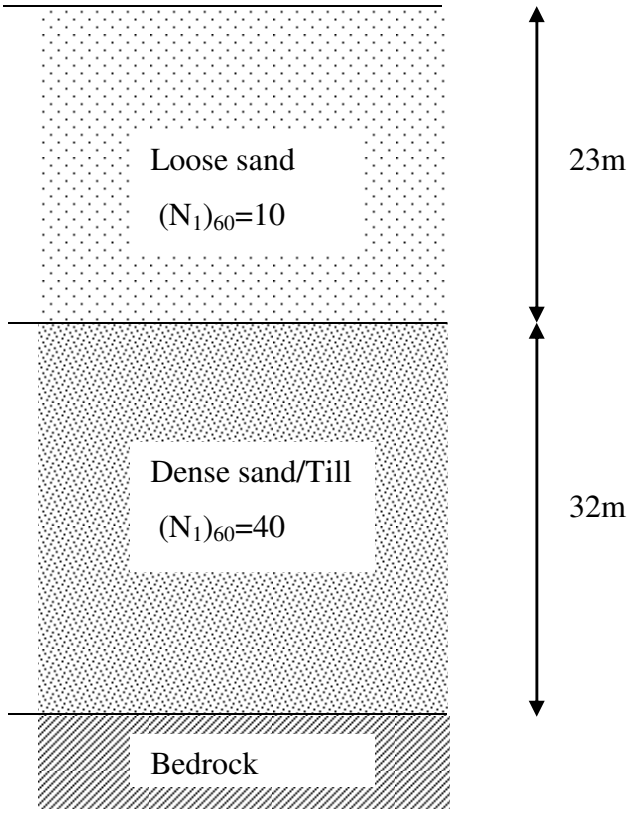

Figure 8. 21 Idealized soil profile used for comparison among analysis methods.

Table 8. 6 Estimated cyclic shear stresses, factor of safety, and excess pore pressure ratio with depth based on cyclic stress approach for a loose sand layer densities of $(N_1)_{60}$ = 10 for Tortona accelerogram scaled at a) 0.15g PGA, b) 0.25g PGA.

a)

Evaluation of Liquefaction Potential

Depth, m	Depth, ft	$(N_1)_{60}$	D_r	e	γ, kN/m^3	γ', kN/m^3	σ_{v0}, kPa	σ_{v0}', kPa	r_d	τ_{cyc}, kPa	CSR	$CRR_{M=7.5}$	MSF	CRR_L	$\tau_{cyc,L}$, kPa	FS_L	N_{eq}	N_L	r_u
0	0						0	0					tortonaMs4						0
1	3.28	10	0.443	0.736	19.397	9.597	19.4	9.6	0.995	2.2	0.23	0.12	2.5	0.31	3.0	1.37	2.846021	4.764612	0.486603
2	6.56	10	0.443	0.736	19.397	9.597	38.8	19.2	0.989	4.3	0.22	0.12	2.5	0.31	5.9	1.37	2.846021	4.808639	0.482618
3	9.84	10	0.443	0.736	19.397	9.597	58.2	28.8	0.984	6.4	0.22	0.12	2.5	0.31	8.9	1.38	2.846021	4.853323	0.47866
4	13.12	10	0.443	0.736	19.397	9.597	77.6	38.4	0.978	8.5	0.22	0.12	2.5	0.31	11.8	1.39	2.846021	4.901458	0.474491
5	16.4	10	0.443	0.736	19.397	9.597	97.0	48.0	0.971	10.6	0.22	0.12	2.5	0.31	14.8	1.40	2.846021	4.959737	0.469569
6	19.68	10	0.443	0.736	19.397	9.597	116.4	57.6	0.964	12.6	0.22	0.12	2.5	0.31	17.7	1.41	2.846021	5.019136	0.464687
7	22.96	10	0.443	0.736	19.397	9.597	135.8	67.2	0.956	14.6	0.22	0.12	2.5	0.31	20.7	1.42	2.846021	5.088831	0.459125
8	26.24	10	0.443	0.736	19.397	9.597	155.2	76.8	0.941	16.4	0.21	0.12	2.5	0.31	23.6	1.44	2.846021	5.220002	0.449112
9	29.52	10	0.443	0.736	19.397	9.597	174.6	86.4	0.927	18.1	0.21	0.12	2.5	0.31	26.6	1.47	2.846021	5.356684	0.439258
10	32.8	10	0.443	0.736	19.397	9.597	194.0	96.0	0.912	19.8	0.21	0.12	2.5	0.31	29.5	1.49	2.846021	5.499201	0.429556
11	36.08	10	0.443	0.736	19.397	9.597	213.4	105.6	0.888	21.3	0.20	0.12	2.5	0.31	32.5	1.53	2.846021	5.743146	0.414156
12	39.36	10	0.443	0.736	19.397	9.597	232.8	115.2	0.862	22.5	0.20	0.12	2.5	0.31	35.4	1.58	2.846021	6.040032	0.397193
13	42.64	10	0.443	0.736	19.397	9.597	252.2	124.8	0.834	23.6	0.19	0.12	2.5	0.31	38.4	1.63	2.846021	6.377189	0.37992
14	45.92	10	0.443	0.736	19.397	9.597	271.6	134.4	0.798	24.3	0.18	0.12	2.5	0.31	41.4	1.70	2.846021	6.855527	0.358385
15	49.2	10	0.443	0.736	19.397	9.597	291.0	144.0	0.763	24.9	0.17	0.12	2.5	0.31	44.3	1.78	2.846021	7.394163	0.337469
16	52.48	10	0.443	0.736	19.397	9.597	310.4	153.6	0.731	25.4	0.17	0.12	2.5	0.31	47.3	1.86	2.846021	7.928498	0.319478
17	55.76	10	0.443	0.736	19.397	9.597	329.7	163.1	0.701	25.9	0.16	0.12	2.5	0.31	50.2	1.94	2.846021	8.508603	0.30242
18	59.04	10	0.443	0.736	19.397	9.597	349.1	172.7	0.672	26.3	0.15	0.12	2.5	0.31	53.2	2.02	2.846021	9.115057	0.286804
19	62.32	10	0.443	0.736	19.397	9.597	368.5	182.3	0.643	26.6	0.15	0.12	2.5	0.31	56.1	2.11	2.846021	9.792348	0.271523
20	65.6	10	0.443	0.736	19.397	9.597	387.9	191.9	0.618	26.9	0.14	0.12	2.5	0.31	59.1	2.20	2.846021	10.46581	0.258164
21	68.88	10	0.443	0.736	19.397	9.597	407.3	201.5	0.599	27.3	0.14	0.12	2.5	0.31	62.0	2.27	2.846021	11.03772	0.248007
22	72.16	10	0.443	0.736	19.397	9.597	426.7	211.1	0.583	27.9	0.13	0.12	2.5	0.31	65.0	2.33	2.846021	11.52195	0.240133
23	75.44	10	0.443	0.736	19.397	9.597	446.1	220.7	0.570	28.5	0.13	0.12	2.5	0.31	67.9	2.38	2.846021	11.95136	0.233639
24	78.72	40	0.885	0.474	21.103	11.303	467.2	232.0	0.558	29.2	0.13	0.13	2.5	0.34	78.2	2.68	28.59768	145.8768	0.202179
25	82	40	0.885	0.474	21.103	11.303	488.3	243.3	0.547	30.0	0.12	0.13	2.5	0.34	82.1	2.74	28.59768	151.3342	0.196768
26	85.28	40	0.885	0.474	21.103	11.303	509.4	254.6	0.537	30.7	0.12	0.13	2.5	0.34	85.9	2.80	28.59768	156.8722	0.191623
27	88.56	40	0.885	0.474	21.103	11.303	530.5	265.9	0.527	31.4	0.12	0.13	2.5	0.34	89.7	2.86	28.59768	162.6395	0.186597
28	91.84	40	0.885	0.474	21.103	11.303	551.6	277.2	0.518	32.1	0.12	0.13	2.5	0.34	93.5	2.92	28.59768	167.9266	0.182261
29	95.12	40	0.885	0.474	21.103	11.303	572.8	288.6	0.510	32.8	0.11	0.13	2.5	0.34	97.3	2.97	28.59768	173.0662	0.178272

a)cont.

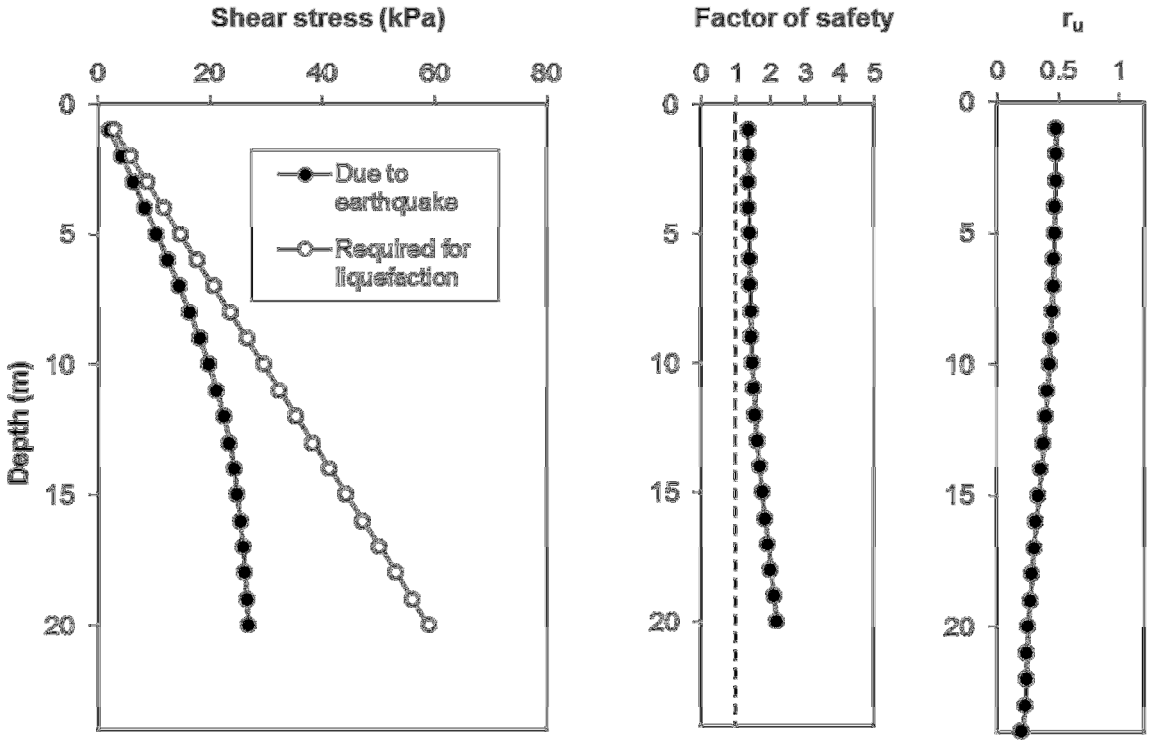
Shear stress (kPa)
Factor of safety
r_u
Depth (m)
Due to earthquake
Required for liquefaction

b)

Evaluation of Liquefaction Potential

Depth, m	Depth, ft	$(N_1)_{60}$	D_r	e	γ, kN/m^3	γ', kN/m^3	σ_{v0}, kPa	σ_{v0}', kPa	r_d	τ_{cyc}, kPa	CSR	$CRR_{M=7.5}$	MSF	CRR_L	$\tau_{cyc,L}$, kPa	FS_L	N_{eq}	N_L	r_u
0	0						0	0					tortonaMs4						
1	3.28	10	0.443	0.736	19.397	9.597	19.4	9.6	0.995	3.6	0.38	0.12	2.5	0.31	3.0	0.82	2.846021	2.046763	1
2	6.56	10	0.443	0.736	19.397	9.597	38.8	19.2	0.989	7.2	0.37	0.12	2.5	0.31	5.9	0.82	2.846021	2.065676	1
3	9.84	10	0.443	0.736	19.397	9.597	58.2	28.8	0.984	10.7	0.37	0.12	2.5	0.31	8.9	0.83	2.846021	2.084871	1
4	13.12	10	0.443	0.736	19.397	9.597	77.6	38.4	0.978	14.2	0.37	0.12	2.5	0.31	11.8	0.83	2.846021	2.105549	1
5	16.4	10	0.443	0.736	19.397	9.597	97.0	48.0	0.971	17.6	0.37	0.12	2.5	0.31	14.8	0.84	2.846021	2.130584	1
6	19.68	10	0.443	0.736	19.397	9.597	116.4	57.6	0.964	21.0	0.36	0.12	2.5	0.31	17.7	0.85	2.846021	2.1561	1
7	22.96	10	0.443	0.736	19.397	9.597	135.8	67.2	0.956	24.3	0.36	0.12	2.5	0.31	20.7	0.85	2.846021	2.18604	1
8	26.24	10	0.443	0.736	19.397	9.597	155.2	76.8	0.941	27.3	0.36	0.12	2.5	0.31	23.6	0.87	2.846021	2.242387	1
9	29.52	10	0.443	0.736	19.397	9.597	174.6	86.4	0.927	30.2	0.35	0.12	2.5	0.31	26.6	0.88	2.846021	2.301103	1
10	32.8	10	0.443	0.736	19.397	9.597	194.0	96.0	0.912	33.1	0.34	0.12	2.5	0.31	29.5	0.89	2.846021	2.362325	1
11	36.08	10	0.443	0.736	19.397	9.597	213.4	105.6	0.888	35.4	0.34	0.12	2.5	0.31	32.5	0.92	2.846021	2.467118	1
12	39.36	10	0.443	0.736	19.397	9.597	232.8	115.2	0.862	37.5	0.33	0.12	2.5	0.31	35.4	0.95	2.846021	2.594653	1
13	42.64	10	0.443	0.736	19.397	9.597	252.2	124.8	0.834	39.3	0.31	0.12	2.5	0.31	38.4	0.98	2.846021	2.739487	1
14	45.92	10	0.443	0.736	19.397	9.597	271.6	134.4	0.798	40.5	0.30	0.12	2.5	0.31	41.4	1.02	2.846021	2.94497	0.859903
15	49.2	10	0.443	0.736	19.397	9.597	291.0	144.0	0.763	41.5	0.29	0.12	2.5	0.31	44.3	1.07	2.846021	3.176355	0.751134
16	52.48	10	0.443	0.736	19.397	9.597	310.4	153.6	0.731	42.4	0.28	0.12	2.5	0.31	47.3	1.11	2.846021	3.405892	0.684395
17	55.76	10	0.443	0.736	19.397	9.597	329.7	163.1	0.701	43.2	0.26	0.12	2.5	0.31	50.2	1.16	2.846021	3.655092	0.630624
18	59.04	10	0.443	0.736	19.397	9.597	349.1	172.7	0.672	43.8	0.25	0.70	2.5	1.75	302.3	6.90	0.160608	3.915609	0.065148
19	62.32	10	0.443	0.736	19.397	9.597	368.5	182.3	0.643	44.3	0.24	0.70	2.5	1.75	319.1	7.20	0.160608	4.206557	0.061886
20	65.6	10	0.443	0.736	19.397	9.597	387.9	191.9	0.618	44.8	0.23	0.70	2.5	1.75	335.9	7.50	0.160608	4.495862	0.059006
21	68.88	10	0.443	0.736	19.397	9.597	407.3	201.5	0.599	45.6	0.23	0.70	2.5	1.75	352.7	7.74	0.160608	4.741539	0.0568
22	72.16	10	0.443	0.736	19.397	9.597	426.7	211.1	0.583	46.5	0.22	0.70	2.5	1.75	369.5	7.94	0.160608	4.949551	0.05508
23	75.44	10	0.443	0.736	19.397	9.597	446.1	220.7	0.570	47.6	0.22	0.70	2.5	1.75	386.3	8.12	0.160608	5.134017	0.053656
24	78.72	40	0.885	0.474	21.103	11.303	467.2	232.0	0.558	48.7	0.21	0.70	2.5	1.75	406.1	8.34	1.876772	62.66518	0.052008
25	82	40	0.885	0.474	21.103	11.303	488.3	243.3	0.547	49.9	0.21	0.70	2.5	1.75	425.8	8.53	1.876772	65.00954	0.050658
26	85.28	40	0.885	0.474	21.103	11.303	509.4	254.6	0.537	51.1	0.20	0.70	2.5	1.75	445.6	8.71	1.876772	67.38853	0.049372
27	88.56	40	0.885	0.474	21.103	11.303	530.5	265.9	0.527	52.3	0.20	0.70	2.5	1.75	465.4	8.91	1.876772	69.866	0.048112
28	91.84	40	0.885	0.474	21.103	11.303	551.6	277.2	0.518	53.4	0.19	0.70	2.5	1.75	485.2	9.08	1.876772	72.13723	0.047023
29	95.12	40	0.885	0.474	21.103	11.303	572.8	288.6	0.510	54.6	0.19	0.70	2.5	1.75	505.0	9.25	1.876772	74.34509	0.04602

b) cont.

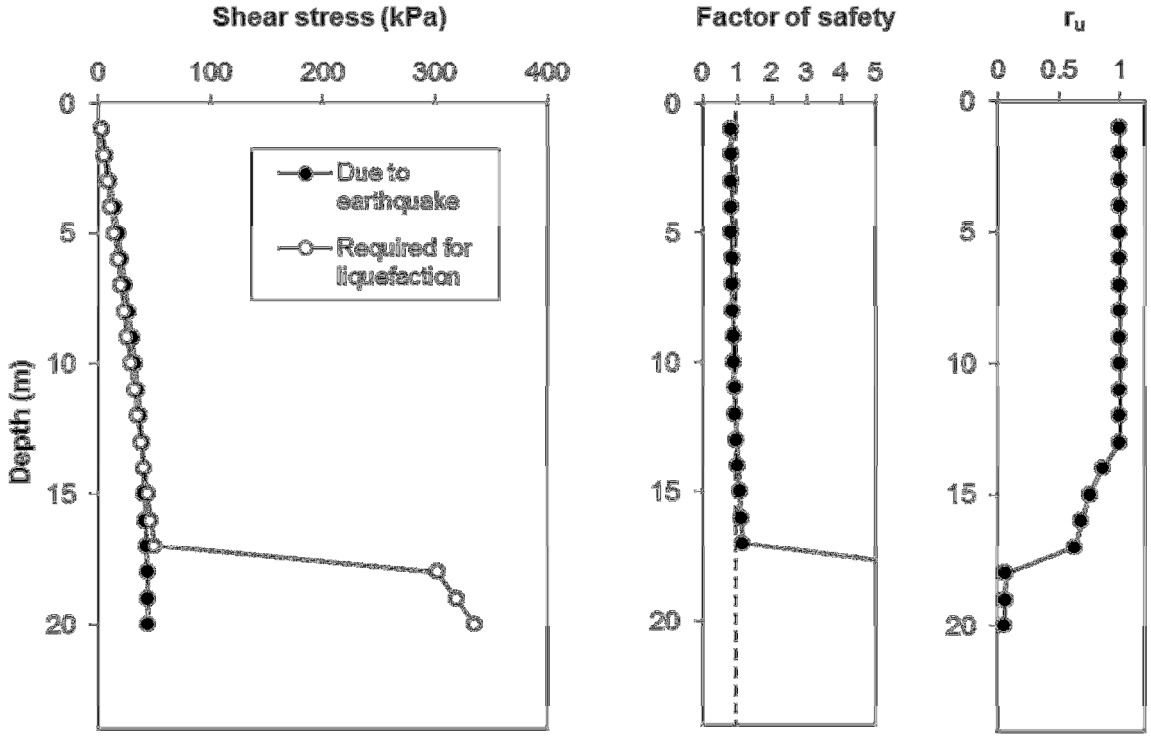
Shear stress (kPa)
Factor of safety
r_u
Depth (m)
Due to earthquake
Required for liquefaction

8.6 Numerical analysis and comparison with simplified methods.

Based on the results of the pseudostatic wall design described in 5.5, for the threshold PGA value of 0.25g and pore pressure ratio of 30% a wall length of 23m is evaluated. The model geometry is left unchanged as the one considered for the benchmark case shown in Figure 2.4 except for the wall length and inertia moment. Soil stiffness and strength properties for the two layers are evaluated on the base of the relationships shown in Table Table 3.1 and correspond to the average value of mean effective stress in the layer and to mean values of V_{s0}=186m/s for the upper layer and V_{s0}=266m/s for the lower layer. Flac model geometry is shown in Figure 8. 22.

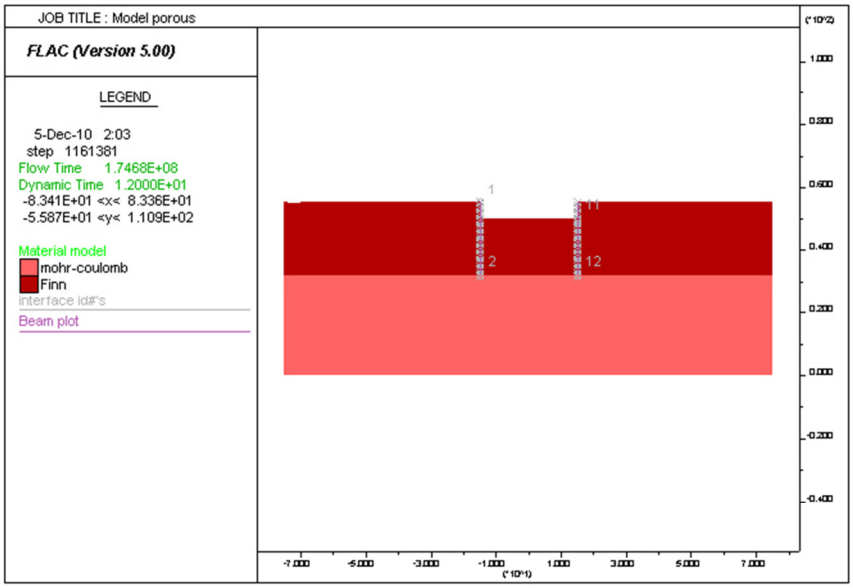

Figure 8. 22 FLAC model grid for the saturated case study.

Comparison between the predicted pore pressure ratio according to the CSR method and the FLAC analyses is shown in Figure 8. 24.

There is a good agreement in terms of pore pressure ratio distribution between the simplified CSR method and the FLAC results with the case 0.15PGA not leading to liquefaction and that 0.25g leading to liquefaction for both cases.

However if the cyclic shear stress in the CSR method would have been evaluated using a more precise value for in a_{max} in formula (8.3) as for example from a site response analysis, a better agreement between the FLAC and the CSR method could have been achieved. However formula (8.3) is considering a free field condition so= the presence of the excavation and the wall and its influence on the pore pressure build up during earthquake shaking can be taken into accoiunt only by mean of numerical modelling such as with FLAC.

Results in terms of maximum bending moments shown on Figure 8. 25 show a good agreement between pseudostatic and dynamic results. As expected displacement profiles (b) Figure 8. 26) are showing a strong increase for the case with PGA 0.25g in which liquefaction occurs, comparing to the case 0.15g where liquefaction does not occur.
A comparison between the dry case and the saturated case in terms of maximum displacements and bending moments is summarized in Figure 8. 23 for the static values and the peak values for Tortona 0.15g scaled earthquake. Since the structural stiffness is different between the dry and the saturated case, it is not meaningful to compare the absolute values but rather the increment between the static and the dynamic cases for saturated or dry case.

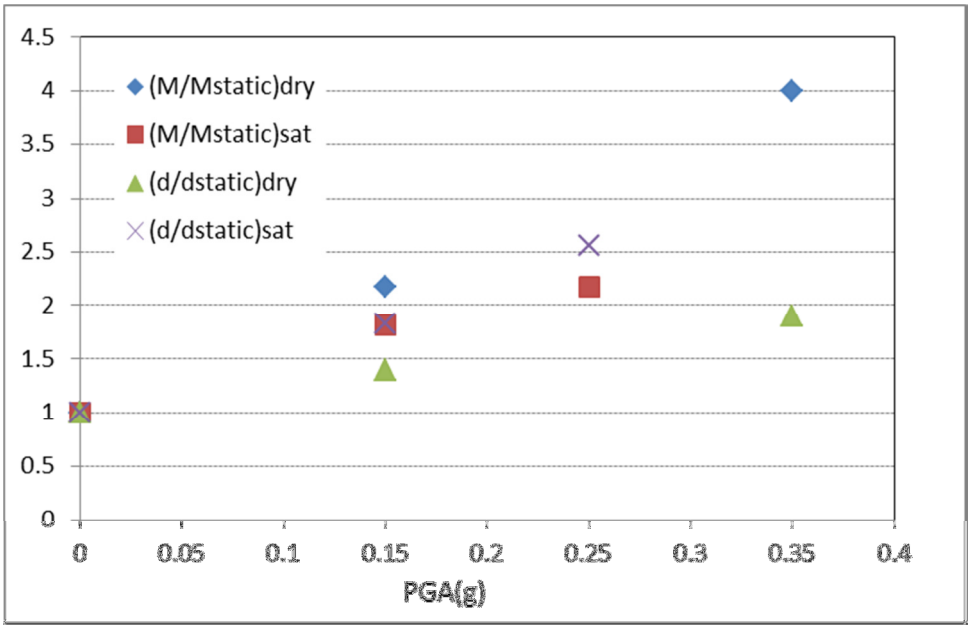

Figure 8. 23 Relative increments in displacement and bending moments for dry and saturated cases.

For increasing acceleration (zero acceleration corresponding to static loading) for the wet case the increment in displacement is higher than for the static case due to liquefaction whereas the increment in bending moments is lower.

a)

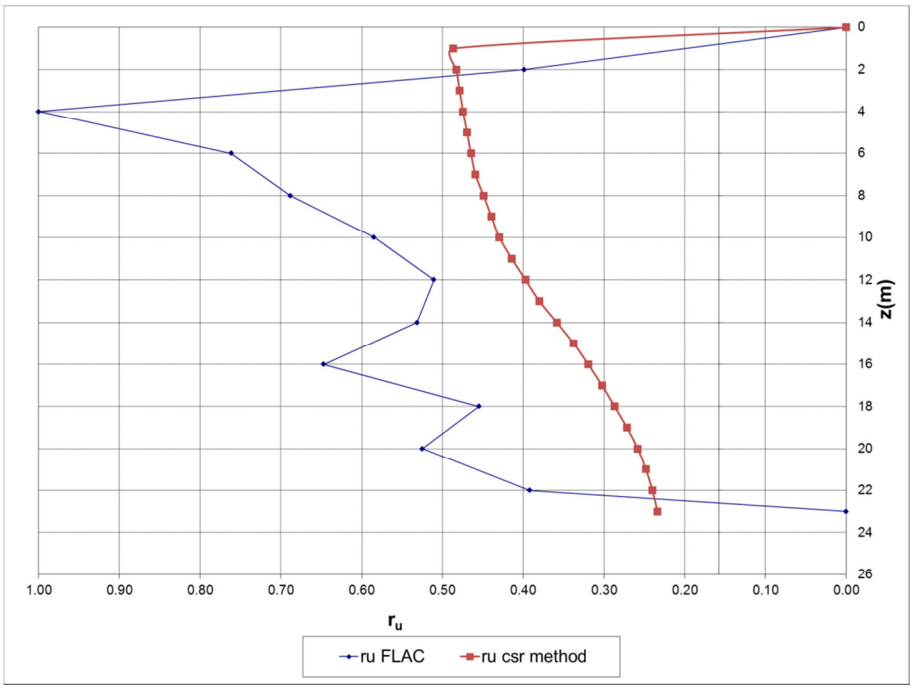

b)

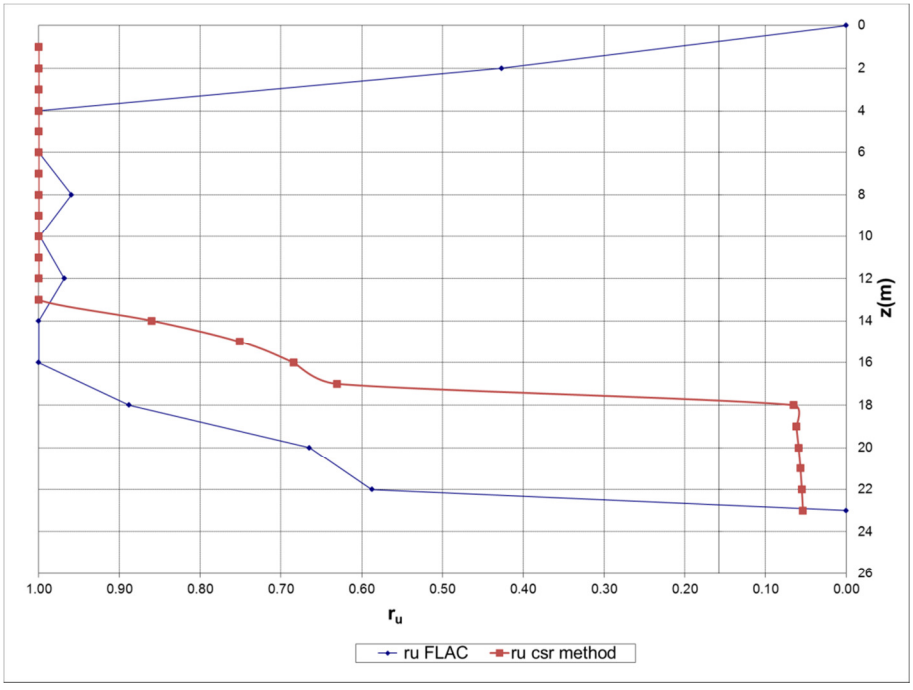

Figure 8. 24 Comparison between pore pressure ratio r_u prediction using CSR method and FLAC for Tortona earthquake scaled to PGA equal 0.15g a) and 0.25g b).

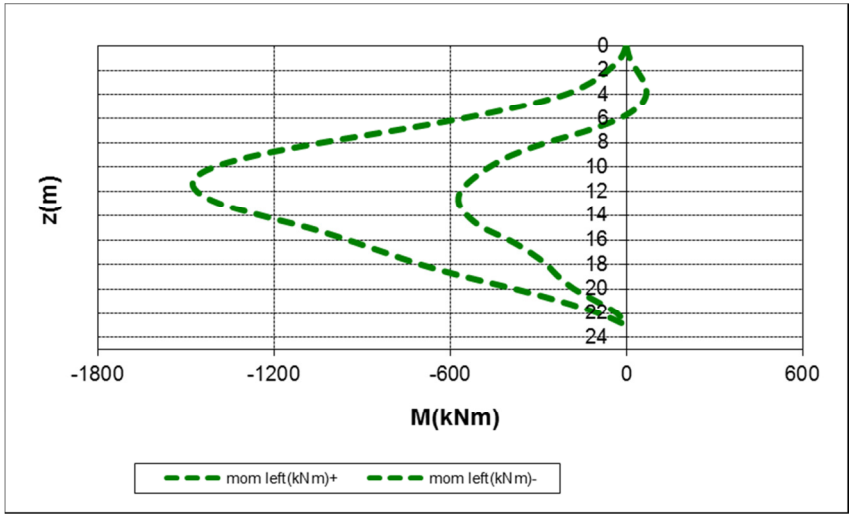

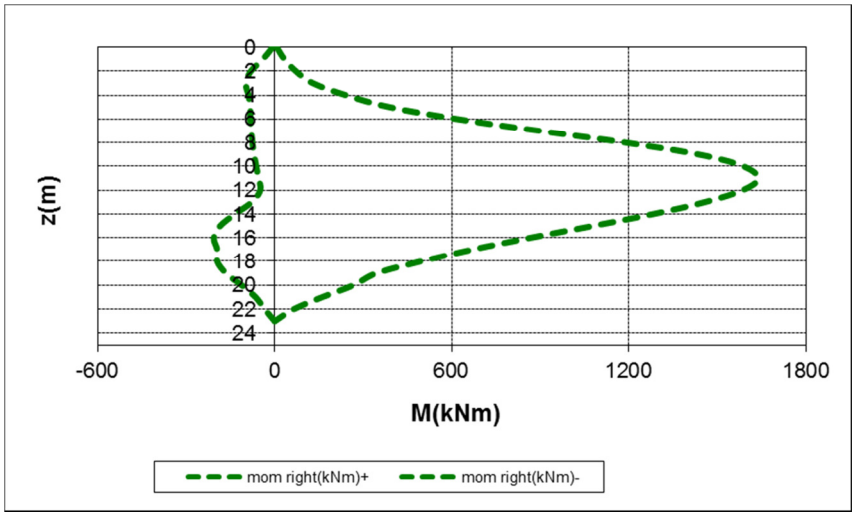

a)

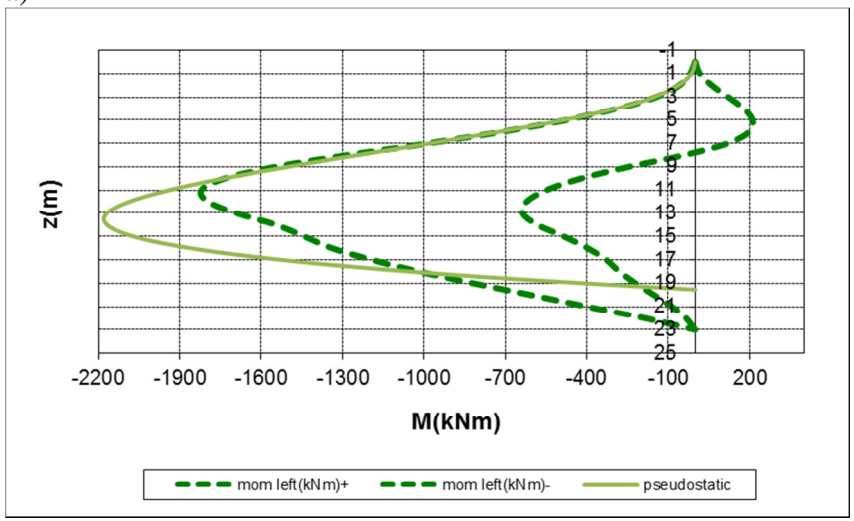

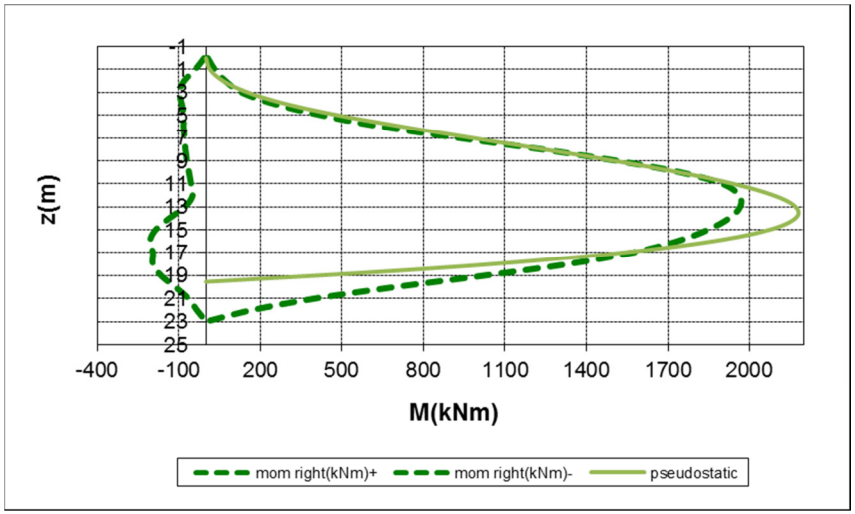

b) Figure 8. 25 Maximum bending moments along left and right wall for Tortona 0.15g PGA a) and 0.25g PGA b) from FLAC and pseudostatic analyses.

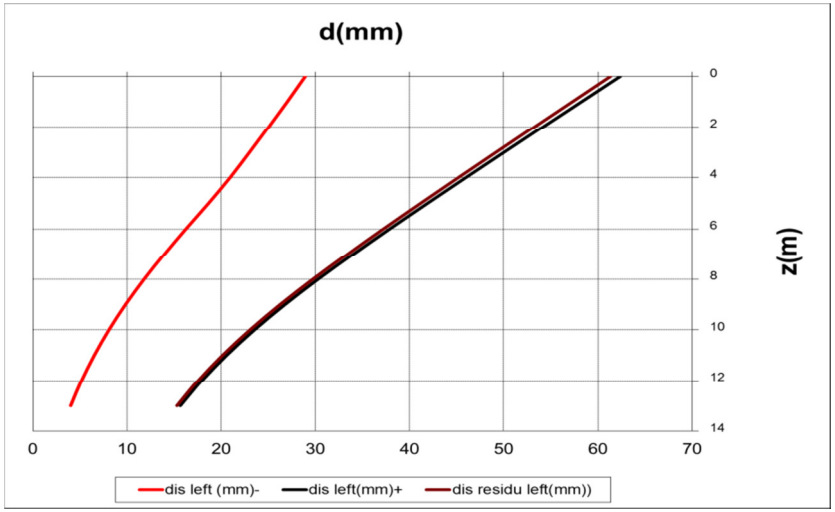

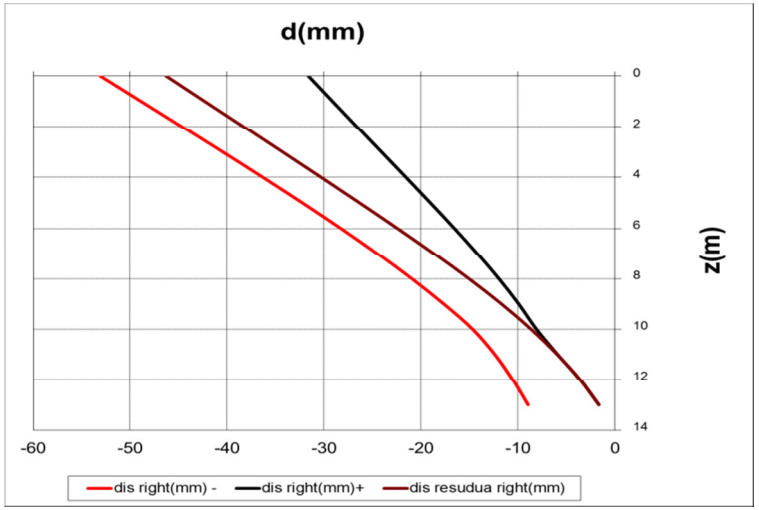

a)

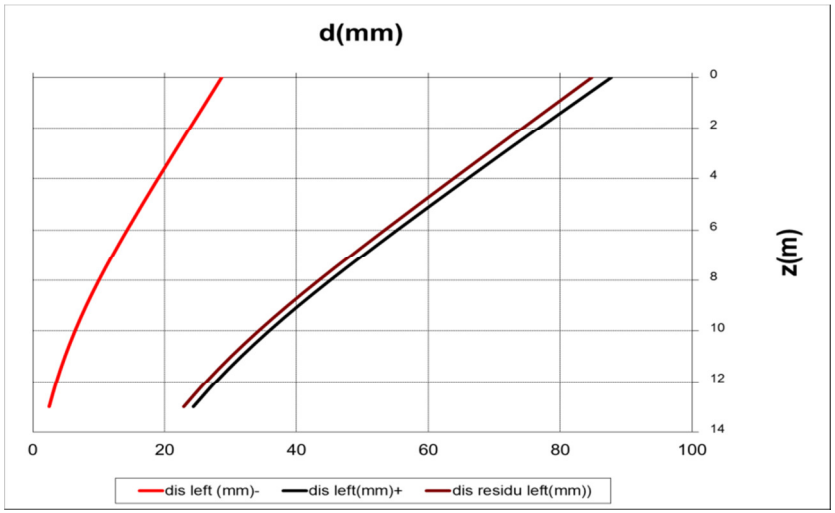

b)

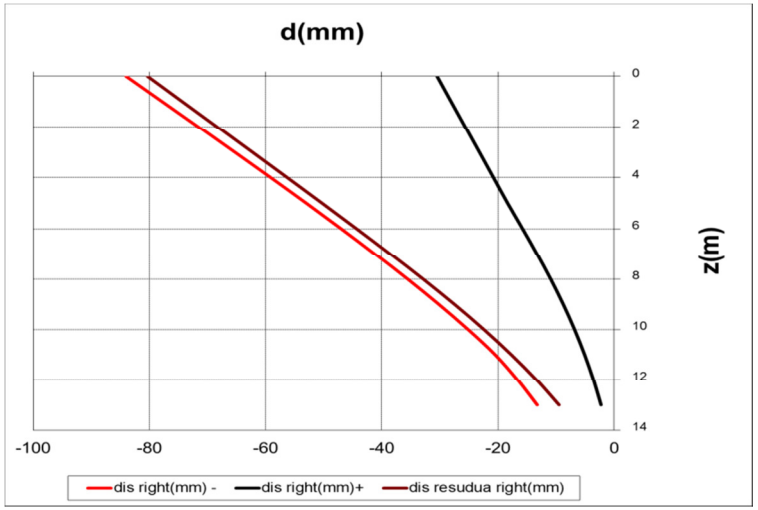

b) Figure 8. 26 Maximum wall displacements along left and right wall for Tortona 0.15g PGA a) and 0.25g PGA b) from FLAC analyses

8.7 Conclusions.

The analyses carried out have pointed out the importance that liquefaction can have in strongly increasing structural displacements comparing to the dry or non liquefied case.
The comparison between the simplified methodology for evaluation of liquefaction potential and the results of the numerical analyses have pointed out a generally good agreement. Despite this, the simplified methodology maybe improved, and a closer agreement may be reached if a more realistic value of peak acceleration is evaluated, for example, carrying out a site response study rather than the crude approximation based on code provisions.
Finally it was observed that the simplified procedure was developed for free field conditions and that therefore the effect of the wall and the presence of the excavation cannot be incorporated as it is in the numerical model.

9 CONCLUSIONS

The work presented is based on the comparison between different methodologies, characterized by increasing level of sophistication, for the design and analysis of flexible embedded cantilever walls under seismic loading including the case of saturated backfill and soil liquefaction.
An introductory part related to case histories and literature review has served the purpose to show that codes based simplified design/analysis approaches are not always successfully applied as maybe the case of saturated granular backfills [Gazetas *et al*, 2005].
A review of available approaches for design/analysis of flexible retaining structures has introduced non linear numerical time histories analysis and pointed out limitations and strengths of different available approaches [Pott and Zdravkovic, 1999].
Three numerical packages [Itasca, 2005; Prèvost, 2006, Elgamal *et al*, 2003] have been described along with the fundamental numerical approaches (Finite Elelement and Finite Differences) and features they are based on.
Critera of choice of the input accelerograms and several other topics related to non linear, time history earthquake geotechnical analysis have been illustrated.
Four different approaches were analysed and applied to a benchmark design case of cantilever wall in incoherent soil and some of the results/conclusions obtained are briefly summarised as follows:

- The application of pseudostatic methods currently adopted by most of design codes requires care in selecting a suitable methodology to deal with passive earth resistance [Lancellotta, 2007]. A suitable methodology provides a safe value but is not more conservative than others.
- The second method is a numerical approach (finite difference or finite elements) based on static and pseudostatic application of the load. Comparison of results in the first static phase for the numerical approaches has shown comparable displacements and forces. Comparable force values were also obtained for the pseudostatic case. The modelling approach for the interface between soil and wall shows a significant influence on such results. Included wall flexibility in the numerical models leads to lower forces in the wall than those calculated by code based paseudostatic analysis.

Moments obtained by such method imply a significant reduction compared to those obtained by the previous methods due to effect of including wall flexibility.

- The third approach is based on time history dynamic analysis using a "Mohr-Coulomb" elastic perfectly plastic constitutive models and one horizontal component for each one of three seismic events. Results for different PGA and different seismic excitation have shown that the average and the standard deviation of both forces and displacements are proportional to the PGA. The increasing dispersion in the values of forces cannot be accounted for by pseudostatic methods.
- Overestimation of pseudostatic code based method compared to maximum moment calculated by dynamic analysis is around 30% while agreement is closer for numerical based pseudostatic methods which therefore appears to be a more suitable design approach.
- Influence of polarization of the accelerograms on the wall forces is important (low coefficient of correlation between moments in the right and left wall) while it has less importance on the displacement values.
- Influence of modelling material non linearity implies a significant difference (30% at PGA_{design}) in calculated bending moments and increases for increasing PGA and non linear deformation
- Code based pseudo static analysis relies on a crude approximation of reality. The numerical analysis performed have underlined the effects of neglecting the following effects:
  - frequency content of the input motion and natural vibration frequency of the wall-soil system
  -wall flexibility
  -polarization (or asymmetry) in seismic excitation polarization
  All these approximation lead, for the case considered, to an overestimation of the wall force of the order of 30% comparing to results coming from more sophisticated analysis. A better approximation of the results obtained using non linear dynamic time history analysis is given by numerical based pseudostatic approach. Considering the simplicity of its implementation this design methodology is therefore advised for design purposes especially for those situations when a PSHA study and suitable spectrum compatible accelerograms are not available.
- The simplified procedure applied for the benchmark case has achieved a relatively good match with numerical modelling however in order to achieve a more reliable estimate it is suggested that at least a site response study is carried out.
- It is pointed out also that to account for the interaction of the earthquake shaking and the structure and to allow an estimation of the final structural displacement and residual settlements more complex type of modelling such as that with FLAC is suggested.

10 REFERENCES

Abrahamson, N.A. (1998). "Non-stationary spectral matching program RSPMATCH", PG&E Internal Report.

Ballantyne, D., R., Borcherdt, I., Bucle, T. O'Rurke and A. Schiff "The Hashin-Awaji earthquake on January 17, 1995. Performance of lifelines : performance of highways and bridges."

Bardet, J. P.,T. Tobita, (2001), A computer program for Nonlinear Earthquake site Response Analyses of layered soil deposits (NERA), April, University of Southern California, Civil Engineering Department

Boore, D.M. (2002). SMSIM – Fortran programs for simulating ground motions from earthquakes: version 2.19. A Revision of OFR 96–80–A. U.S. Geological Survey, 56 pp.

Byrne, P. [1991] "A Cyclic Shear-Volume Coupling and Pore-Pressure Model for Sand," in *Proceedings:Second International Conference on Recent Advances in Geotechnical Earthquake Engineering and Soil Dynamics*, St. Louis, Missouri, Paper No. 1.24, pp. 47-55.

Caquot, A. and Kerisel, J. [1948], *Tables for the Calulation of Passive Pressure, Active Pressure and Bearing Capacity of Foundations*, Gautiers-Villars, Paris

Clough RW, Penzien J.[1994] Dynamics of Structures. McGraw Hill: New York, 344{351

Chen, W. F., and Liu, X.L. [1990] *Limit analysis in soil mechanics*. Elsevier, Amsterdam

CIRIA, [1995] *Special publication 95. The design and construction of sheet piled cofferdams.* Tohmas Telford, London

Clough, G. W. and Duncan, J. M. 1991. Chapter 6: Earth Pressures, in *Foundation Engineering Handbook*, Second Edition, edited by Van Nostrand Raynold, NY, pp. 223-235.

Coulomb, C. A. [1776] "Essai sur une Application des Régles de Maxims et Minimum à quelques Problemes de Statique Relatifs à l'Architecture," *Mem. Acad. Roy. Des Sciences, Paris*; Vol. 3, pag. 38.

Cundall, P. A., and R. D. Hart. "Numerical Modeling of Discontinua," *Engr. Comp.*, ***9***, 101-113, 1992.

Das, B., M., [2007] *Principles of Foundation Engineering*, Thomson

Dismuke, T.D., [1991] *Retaining structures and excavations*, in Foundation Engineering Handbook, Van Nostrand Reinold, New York, U.S.A.

Dobry, R., Ladd, R.S., Yokel, F. Y., Chung, R.M., and Powell, D. [1982] "Prediction of pore water pressure buildup and liquefaction of sands during earthquakes by the cyclic strain method", *NBS Building Science Series 138*, National Berau of Standards, Gaithesburg, Maryland, 150 pp

DYNAFLOW, [2005] User's Manual, v02, Princeton University

Ebeling, R. E., and Morrison, E. E., Jr. [1992] "Seismic Design of Waterfront Retaining Structures," Technical Report ITL 92-11 U.S. Army Engineer Waterways Experiment Station, Vicksburg, MS.

Elgamal, A., Yang, Z., Parra, E., Ragheb, A. [2003]. "Modeling of cyclic mobility in saturated cohesionless soils," *International Journal of Plasticity*, Vol.19, pp. 883-905.

Faccioli, E et al. [1996] *Seismic behaviour and design of foundations and retaining structures*, Prenormative research in support of Eurcide 8, Edited by Ezio Faccioli and Roberto Paolucci, Milano

Fardis, M. N. et al. [2005] *Designers' Guide to EN 1998-1 and 1998-5. Eurocode 8: Design Provisions for Earthquake Resistant Structures,* Thomas Telford Ltd, London.

Felippa and Park, C. A., and Park, K. C.,[1980] *Staggered transient analysis procedures for coupled dynamic systems: formulation*, Comp. Meths. Mech. Engrg., 24, 61-112.

Finn W., D., Kwok W., L., Martin G., R., "An effective stress model for liquefaction", *Journal of Geotechnical Engineering Division*, ASCE, Vol. 103, n^{o} GT6.

Gasparini D., Vanmarcke E. (1976). "SIMQKE – A program for artificial motion generation, user's manual and documentation", Department of Civil Engineering, Massachusetts Institute of Technology.

Gazetas, G., Dakoulas, P., and Dennehy, K. 1990. "Emperical Seismic Design Method for Waterfront Anchored Sheetpile Walls," Proceedings of ASCE Specialty Conference on Design and Performance of Earth Retaining Structures, Geotechnical Special Publication No. 25. , pp. 232-250.

Gazetas, G., Psarropoulos, P.N., Anastasopoulos, I., and Gerolymos, N [2004]. "Seismic behaviour of flexible retaining systems subjected to short-duration moderately strong excitation" J.Soil dynamic and earthquake engineering vol.24, 537-550

Gomez, J. E., Filz, G. M., and Ebeling, R. M. [2000]. "Development of an improved numerical model for concrete-to-soil interfaces in soil-structure interaction analyses; Report 2, Final study," *ERDC/ITL TR-99-1,* U.S. Army Engineer Research and Development Center, Vicksburg, MS.

Green, R.A., and Ebeling, R.M., (2002). "Seismic analysis of cantilever retaining walls, Phase I, ERDC/ITL TR-02-3, Information technology laboratory, US army corps of engineers, Engineer research and development center, Vicksburg, MS.

Hardin, B., O., Drnevich, V. P. [1972] "Shear modulus and damping in Soils: measurement and parameter effects" *Journal of Soil Mechanics and Foundation Division*, ASCE, Vol.98, No. SM6.

Hardin, B., O., Drnevich, V. P. [1972] "Shear modulus and damping in Soils: design equations and curves" *Journal of Soil Mechanics and Foundation Division*, ASCE, Vol.98, No. SM7.

Hardin, B., O. [1978] "The Nature of Stress Strain Behaviour of Soils" State of the Art, *International Conference on Earthquake Engineering and Soil Dynamics*, Pasadena, California, 1978.

Hayashi, S., T., Katayama [1970] "Damage to harbour structures by the Tokachioki Earthquake" , *Soils and foundations,* Vol.10, No.2 ,pp. 83-102.

Hill, R., [1950] *The mathematical Theory of Plasticity,* Clarendon Press, Oxford,

Huang, C. (1996). ''Plastic analysis for seismic stress and deformation fields,'' PhD dissertation, Dept. of Civ. Engrg., SUNY at Buffalo, Buffalo, N.Y.

Hughes, T. J. R.,[1987] *The Finite Element Method, Linear Static and Dynamic Finite Element Analysis,* Prentice-Hall, Englewood Cliffs, NJ, pp 232-237.

Ishibashi, I., and Fang, Y. [1987] "Dynamic Earth Pressures with Different Wall Modes", *Soils and Foundations,* Vol.27.No. 4, pp 11-22

Ishibashi, I. L., and Zhang, X. [1993] "Unified dynamic shear moduli and damping ratios of sands and clay," *Soil and Foundations,* Vol.33.No1, pp 182-191

ITASCA Consulting Group Inc. [2005], FLAC 5.0- *User's Manual*, Minneapolis

Iwan W. D.[1967] On a Class of Models for the yielding behaviour of continuos and composite systems, *Journal of Applied Mechanics*, ASME, Vol. 34, n^{o}E3

Jennings P. C. "Periodic Response of a general yielding structure" , *Journal of the Engineering Mechanics division*, Vol. 90, n^{o}EM2, 1964

Kawakami, F., A., Asada [1966] "Damage to the ground and earth structures by the Niigata Earthquake of June 16, 1964" , *Soils and foundations,* Vol.6, No.1 ,pp. 14-30.

Kimura M. [1996] "Damage statistics", Special Issue, *Soils and foundations*.

Kitajima, S., and Uwabe, T. 1979 (Mar). "Analysis on Seismic Damage in Anchored Sheet-Piling Bulkheads," Report of the Japanese Port and Harbor Research Institute, Vol. 18, No. 1, pp. 67-130. (in Japanese).

Koseki, J., Tsutsumi, Y., Kiyota, T., Nakajima, S. and Maqbool, S. [2005] "Damage to earth structures caused by the 2004 Niigata-ken Chuetsu earthquake", *Bulletin of ERS*, No. 38

Kramer, S.L. [1996]. *Geotechnical Earthquake Engineering*, Prentice Hall, Inc.

Kramer, S.L. and A.W. Elgamal (2001). "Modeling soil liquefaction hazards for performancebased earthquake engineering," *PEER Rept 2001/13*, Pacific Earthquake Engineering Research Center, Richmond, California Saddle River, New Jersey, 653 pp.

Kuhlemeyer R., L.,and Lysmer, J., [1973] "Finite elements accuracy for wave propagation problems" *Proceedings 8th World Conference on Earthquake Engineering* , San Francisco, pp 90-98

Kuhlemeyer, R. L., and J. Lysmer [1973] "Finite Element Method Accuracy for Wave Propagation Problems," *J. Soil Mech. & Foundations, Div. ASCE*, ***99***(SM5), pp 421-427.

Kumar, J. [2001] "Seismic passive earth pressure coefficients for sand", *Can. Jeotech. J.,* Vol.38., pp 876-881

Lambe, T.W., Whitman, V. W. [1979] *Soil Mechanics, SI Version*, John Wiley & Sons, New York, U.S.A.

Lai C.G. Strobbia C., Dall'Ara (2005). "Elaborazione di Raccomandazioni e di Linee Guida per la Definizione dell'Input Sismico e delle Modellazioni da Adottare nei Territori

della Regione Toscana nell'Ambito del Progetto di Ricerca "VEL" ai Sensi della Nuova Normativa Sismica (Ordinanza PCM n° 3274 del 20/3/2003 e Successivi Aggiornamenti)". Parte 1 – Definizione dell'Input Sismico, pp. 58.

Lancellotta, R. [1997] *Geotecnica.* Zanichelli Editore S.p.A., Bologna

Lancellotta, R. [2002] "Analytical solution of passive earth pressure" *Géotechnique 52,* No. 8, pp 617-619

Lancellotta, R. [2007] "Lower bound approach for seismic passive earth resistance" *Géotechnique,* Vol. 57, No. 3, pp1-3

Li X., [1999], "Dynamic Analysis of Rigid Walls considering flexible foundations," *Journal of Geotechnical and Geoenvronmental Eng*., Vol. 125, No. 9, pp. 803-806, May

Loret, B. "Formulationd'une loi de comportement elastoplastique del milieux granulaires". Laboratoire de Mechanicque des Solides. Ecole Polytechnique, Palaiseau.

Lysmer, J., and R.L. Kuhlemeyer [1969], "Finite Dynamic Model for Infinite Media," *Journal of the Engineering Mechanics Division*, ASCE, 95(EM4), 859-877.

Lysmer, J. and Wass, G. [1972] "Shear waves in plane infinite structures", *Journal of the Engineering Mechanics Division*, ASCE, vol. 98, , pp 85-105

Madhabushi and Zeng [2007], "Simulating Seismic Response of Cantilever Retaining Wall" *Journal of Geotechnical and Geoenvronmental Eng*., ASCE, Vol. 133, No. 5, pp. 539-549, May

Madhabushi and Zeng [2007], "Seismic Response of Cantilever Retaining Walls with dry backfill" *Geomechanics and Geoengineering an International Journal*., ASCE, Vol. 1, No. 4, pp.275-289 ,Dec

Martin, P., P., *Non linear methods for dynamic analysis of ground response*, Ph.D. Thesis University of California, Berkeley.

Martin, G. R.,W. D. L. Finn and H. B. Seed, [1975] "Fundamentals of Liquefaction under Cyclic Loading," *J. Geotech., Div. ASCE*, pp 423-438.

Masing G., [1926] Eigensprannung und Verfestigung beim Messing, *Proceedings International Congress of Applied Mechanics.*

Matsuoka, H. and T. Nakai, [1985] "Relationship Among Tresca, Mises, Mohr-Coulomb and Matsuoka-Nakai Failure Criteria," *Soils and Foundations*, Vol.5, No. 4, pp123–128.

Menon, A., Lai, C.G., Macchi, G. [2004] Seismic hazard assessment of the historical site of Jam in Afghanistan and stability analysis of the minaret, Journal of Earthquake Engineering, Vol.8, Sp. 1, pp. 251-294.

Mononobe, and H. Matsuo [1929]: "On Determination of Earth Pressure During Earthquakes", *Proc. World Engineering Congress*, Tokyo, Japan.

Morrison, E., E., Jr., and Ebeling, R. M. [1995] "Limit equilibrium computation of dynamic passive earth pressure" *Canadian Geotechnical Journal*, Vol.32, No. 1, pp.481-487.

Mroz A., "On the description of anisotropic workhardening" *Journal of the Mechanics and Physiscs of Solids,* Vol.15, 1967

Müller-Breslau H., [1906] Erddruck auf Stutzmauern, Alfred Kroner, Stuttgart.

Nandkumaran, P [1973] "Behavior of Retaining Walls Under Dynamic Loads," *PhD Thesys*, Roorkee University, Roorkee, India.

Newmark, N. [1965] “Effect of earthquakes on dams and embankments,” *Geotechnique,* Vol. 15, No. 2, pp. 139-160.

Osinov, V., A., [2003] “Cyclic shearing and liquefaction of soil under irregular loading: an incremental model for the dynamic earthquake-induced deformation”, Soil Dynamics and Earthquake Engineering, Vol. 23, No.7, pp.535-548

Prévost, J. H. [1981], DYNAFLOW: A nonlinear transient finite element analysis program. Dept. of Civil Eng. And Op. Research, Princeton University, Last Update 2005

Prevost, J.H. [1985]. “A simple plasticity theory for frictional cohesionless soils,” *Soil Dyn.Earthquake Eng*., 4(1), 9-17

Palmieri [2005], Tesi di Dottorato, Politecnico di Torino

Pamuk, A., H. I. Ling, D. Leschchinsky, E. Kalkan, A. Korhan, [2004] ,"Behavior of reinforced wall system during the 1999 Kocaeli (Izmit), Turkey, earthquake" in *Proceedings: Fith International Conference on Case Histories in Geotechnical Engineering*, New York, NY, pp. 122-130.

Puller, M. [1996] *Deep Excavation. A Practical Manual.* Tohmas Telford, London

Parra, E. (1996). “Numerical modeling of liquefaction and lateral ground deformation including cyclic mobility and dilation response in soil systems” *PhD Thesis*, Dept. of Civil Engrg., Rensselaer Polytechnic Institute, Troy, NY

Pastor, M., Zienkiewicz, O. C., and Leung, K. H. [1985] “Simple model for transient soil loading in earthquake analysis. II: Nonassociative models for sands” *Int. J. Numer. Alyt. Meth. Geomech*, Vol. 9, pp.477-498

Pecker, A. [1984] *Dinamique des Sols.*Presses Ponts et Chaussées., Paris

Potts and Zdravcovic,. [1999] *Finite elements analysis in Geotechnical Engineering.* Thomas Telford, London

Prakash S. and S. Saran [1966] “Static and Dynamic Earth pressures Behind Retaining Walls”, *Proc. Third Symposium on Earthquake Engineering*, Roorke, Vol. 1, pp. 277-288, November.

Prakash, S., and P., Nandkumaran [1973] “Dynamic Eart Pressure Distributionon Rigid Walls, Proc. Symposium on Earth and Earth Structures Subjcted to Earthquakes and other Dynamic Loads, Roorke, Vol. 1, pp 11-16, March

Prakash, S., [1981] *Soil Dynamics*, Wiley & Sons

Prévost, J., H. [1978], “Plasticity theory for soil stress-strain behaviour,” *Journal of*

the Engineering Mechanics Division, Vol. 104, EM5.

Prévost J., H.,[1980] “Constitutive Theory for Soils”, Proceedings of the Workshop on Limit Equilibrium Plasticity and Generalised Stress-Strain in Geotechnical Engineering, ASCE, Mac Gill University.

Prévost, J., H. [1985] "A simple plasticity theory for frictional cohesionless soils" *Soils Dynamic and Earthquake Eng.*, 4:9–17 Reinold, New York, U.S.A.

Prévost, J., H. [2006] DYNAFLOW, - *User’s Manual*, Princeton, New Jersey

Psarropoulos, P.N., Klonaris.G., and Gazetas.G. [2005], “Seismic earth pressures on rigid and flexible retaining walls” J.Soil dynamics and earthquake engineering vol.25, 795-809.

Pyke, R., M., [1979] "Non linear soil models for irregular cyclic loadings ", Journal of Geotechnical Engineering Division, ASCE, Vol. 105, n^{o}GT6

Doctoral Thesys in Geotechnical Engineering, G. Li Destri Nicosia

Ramberg, W. and Osgood, W. R. [1943] ”Description of Stress-Strain curves by three parameters”, *Technical Note* 902, National Advisory Committee for Aeronautics, Washington D.C.

Richard, R., and Elms, D. [1979] “Seismic Behaviour of Gravity Retaining Walls,” ASCE, *Journal of the Geotechnical Engineering Division, ASCE*, Vol.*105* (GT4), pp 449-464

Richards, R. Jr., Elms, D. G., and Budhu, M. (1990). ‘‘Dynamic fluidization of soils.’’ *J. Geotech. Engrg.*, ASCE, 116(5), 740–759.

Richards, R., and Shi X. [1999] “Seismic Lateral Pressures in Soils with Cohesion” *J. Geotech. Eng.*, ASCE, Vol. 120, No. 7,, pp.1231-1251

Richard, R., Huang, C. and Fishman, K., [1999] “Seismic Earth Pressures on Retainig Structures” *Journal of Geotechnical and Geoenvironmental Engineering*, Vol.*125,* No.9, pp 771-464

Rowe, P. W., [1957] *Limit Design of Flexible Walls*, Midland, S.M.F.E., Society – Proc. Vol 1

Sabetta, F., Pugliese, A. (1996). “Estimation of Response Spectra and Simulation of Nonstationary Earthquake Ground Motions”, Bulletin of Seismological Society of America, Vol. 86, No. 2, pp. 337-352.

Schfield, A., N., WrothC. P., *Critical State Soil Mechanics*, Mac Graw Hill, 1968

Scott, R. F., [1973]. “Earthquake-induced earth pressures on retaining walls” *Proc., 5th World Conference on Earthquake Engineering*, International Association of Earthquake Engineering, Tokyo, Japan, II, 1611-1620

Seed, H. B., and R. V. Whitman [1970]: “Design of Earth Retaining Structures for Dynamic Loads”, *Proc ASCE Specialty Conference on Lateral Stresses in the Ground and Design of Earth Retaining Strucutres*, Ithaca, N.Y., pp 103-147

Seed, H. B. and I. Idriss, [1969] “Influence of soil conditions on Ground Motion During Earthquakes” *J. Soil Mech. Found., Div.* ASCE, pp 99-137

Seed, H. B., Idriss, I. M. [1970] “Soil Moduli and Damping factors for dynamic response analysis” Report EERC 70-10, Earthquake Engineering Research Center, Univesrity of California, Berkeley

Sherif, M., Ishibashi, I., and Lee, C. [1982], “Earth Pressure Against Rigid Retaining Walls”, ASCE, *Journal of the Geotechnical Engineering Division,* Vol.108.No. GT5, pp 679-695

Sherif, M., and Fang, Y. [1983] “Dynamic Earth Pressure on Walls Rotating About the Top”, ASCE, *Soils and Foundations,* Vol.24.No. 4, pp 109-117

Siller. T. J., Christiano, P. P., and Bielak, J. [1991]. “Seismic response of tied-block retaining walls” Earthquake Engrg. And Struct. Dyn. 20(7), 605-620

Silva, W.J. and Lee, K. (1987). WES RASCAL code for synthesizing earthquake ground motions, State-ofthe- Art for Assessing Earthquake Hazards in the United States, Report 24, U.S. Army Engineers Waterways Experiment Station, Misc. Paper S-73-1. Abrahamson, N.A. (1998). “Non-stationary spectral matching program RSPMATCH”, PG&E Internal Report.

Silvestri, F., [2005] “Comportamento meccanico dei terreni sotto azioni sismiche” Cap. 2, of *Aspetti Geotecnici della progettazione in zona sismica*, AGI

Sokolovskii, V.V. [1965] *Statics of granular media*, Pergamon, Oxford.

Doctoral Thesys in Geotechnical Engineering, G. Li Destri Nicosia

Soubra, A., H. [2000] “Static and seismic passive earth pressure coefficients on rigid retaining structures”, *Can. Jeotech. J.,* Vol.37., pp 463-478

Subba Rao, K.S., and Choudhury, D. [2005]. “Seismic passive earth pressures in soils” *J.Geotechnical and geoenvironmental engineering*, Vol. 131, No 1, 131-135.

Susumu, I., Kameoka, T. [1993] “Finite Element Analysis of Earthquake induced damage to anchored sheet pile quay walls” *Soils and Foundations*, Vol.33, No. 1, pp.71-91.

Technical Report NCEER-95-0015, National Center for Earthquake Engineering Research, State University of New York at Buffalo, November 1995, pp 7.22-7.73.

Terzaghi, K. [1943] *Theoretical soil mechanics.* John Wiley and Sons, New York

Towhata, I., and Islam, S [1986]. “Prediction of lateral displacement of anchored bulkheads induced by seismic liquefaction” Japanese society of soil mechanics and foundation engineering.

Tsatsanifos C., [2007]. “Contribution of Geotechnical Engineering in the rehabilitation of buildings and infrastructures” *Proc., European conference of Soil Mechanics and Geotechnical Eng*, ECSMGE 2007, Madrid , Spain

Veletsos, A. S., and Younan, A.H [1994a]. “Dynamic soil pressure on rigid vertical walls” *Earthquake Eng. And Struct. Dyn.*,Vol. 23, pp. 275-301.

Veletsos, A. S., and Younan, A.H [1994b]. “Dynamic modeling and response of soil-wall systems” *J.Geotech. Engrg*.,ASCE, 120 (12) 2155-2179.

Veletsos, A. S., and Younan, A.H [1997]. “Dynamic response of cantilever retaining walls” *J.Geotech Engineering.*, ASCE, 123 (2) 161-172

Veletsos, A. S., and Younan, A.H [2000]. “Dynamic response of flexible retaining walls” *J.Earthquake Engineering and Structural Dyn.*, 29, 1815-1844.

Vecchietti S., Cecconi, M., Pane, V., [2006]. “Metodi per la valutazione degli spostamenti di strutture di sotegno in presenza di sisma” *Proc., Incontro Annuale dei Ricercatori di Geotecnica*, IARG 2006,Pisa , talia, 1611-1620

Vucetic, M. and Doubry, R., [1991] “Effect of Soil Plasticity on Cyclic Response”, *Journal of Geotechnical Engineering*, ASCE, Vol. 117, No. 1, pp 89-107

Westergaard, H. [1931] “Water pressure on dams during earthquakes”, *Transaction of ASCE* Paper No, 1835, pp 418-433

Wood, J. H., [1973]. “Earthquake-induced soil pressures on structures” Rep. EERL 73-05, *Earthquake Engineering Research Laboratory*, California Inst. of Technol., Pasadena, Calif.

Yang, Z. (2000). “Numerical modeling of earthquake site response including dilation and liquefaction,” *PhD Thesis*, Dept. of Civil Eng. and Eng. Mech., Columbia University, NY, New York

Younan, A.H., and Veletsos, A.S., [2000]. “Dynamic response of flexible retaining walls” *J.Earthquake Engineering and Structural Dynamics* vol.29, 1815-1844

Yang, Z., A. Elgamal and E. Parra (2003). “Computational model for cyclic mobility and associated shear deformation,” *J. Geotech. and Geoenvir. Eng.*, ASCE, 129(12), 1119-1127.

Youd, T.L., Idriss, I.M., Andrus, R.D., Arango, I., Castro,G., Christian, J.T., Dobry, R., Finn, W.D.L, Harder, L.F., Hynes, M.E., Ishihara, K., Koester, J.P., Liao, S.S.C., Marcuson, W.F., Martin, G.R., Mitchell, J.K, Moriwaki, Y., Power, M.S., Robertson, P.K, Seed,

Doctoral Thesys in Geotechnical Engineering, G. Li Destri Nicosia

R.B, Stokoe, K.H. (2001). "Liquefaction resistance of soils: summary report from the 1996 NCEER and 1998 NCEER/NSF workshops on evaluation of liquefaction resistance of soils," *Journal of Geotechnical and Geoenvironmental Engineering*, Vol. 127, No. 10, pp. 817-833.

Zarrabi, K. [1973] "Sliding of Gravity Retaining Wall During Earthquake Considering Vertical Acceleration and Changing Inclination of Failure Surface", Thesis, Department of Civil Engineering MIT, Cambridge